Magnetic tuning of organic solar cell performance

Dissertation

von

Daniel Moseguí González

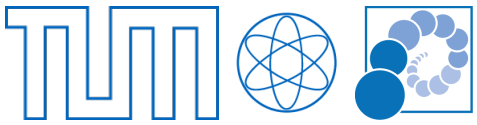

Technische Universität München
Physik-Department
Lehrstuhl für Funktionelle Materialien

3rd August 2017

TECHNISCHE UNIVERSITÄT MÜNCHEN

Physik-Department
Lehrstuhl für Funktionelle Materialien

Magnetic tuning of organic solar cell performance

Daniel Moseguí González

Vollständiger Abdruck der von der Fakultät für Physik der Technischen Universität München zur Erlangung des akademischen Grades eines

Doktors der Naturwissenschaften (Dr. rer. nat.)

genehmigten Dissertation.

Vorsitzender: Prof. Dr. Martin Zacharias

Prüfer der Dissertation: 1. apl. Prof. Dr. Peter Müller-Buschbaum
2. Prof. Jonathan J. Finley, Ph.D.

Die Dissertation wurde am 03.08.2017 bei der Technischen Universität München eingereicht und durch die Fakultät für Physik am 12.10.2017 angenommen.

This work is dedicated to Noa López Moseguí.

"Rien n'est plus puissant qu'une idée
dont l'heure est venue."

Victor Hugo

Abstract

The aim of this thesis is to explore the performance improvement of organic solar cells via tuning the efficiency of exciton Intersystem Crossing. The potential control of the excitonic spins is approached, on the one side, via the temperature-resolved study of a novel heavy element-containing spin-orbit coupling-enhancing macromolecule. Moreover, its performance in various types of solar cells is investigated. On the other side, exciton spin rephasing in solar devices is attempted via introduction of superparamagnetic nanoparticles. The influence of the nanoparticle coercive field on the solar cell performance is parametrized for different concentrations. Moreover, the influence of additional external magnetic fields is investigated. We finally characterize the effect of the nanoparticles on the aging behavior of modified cells via advanced scattering techniques. In particular, the link between material morphology and device performance is addressed.

Zusammenfassung

Das Ziel dieser Dissertation ist es, die Leistungsverbesserung von organischen Solarzellen mittels Anpassung des exzitonischen Intersystem Crossing zu erforschen. Einerseits wird die potenzielle Kontrolle der exzitonischen Spins durch die temperaturauflösende Studie eines Makro-Moleküls, das aus Spin-Bahn Kupplung verstärkenden schweren Elementen besteht, addressiert. Außerdem wird dessen Leistung in verschiedenen Solarzellenarten erforscht. Andererseits wird das exzitonische Spin-Rephasing in Solarzellen durch Einfügen von superparamagnetischen Nanopartikeln getestet. Der Einfluss des Nanopartikel-Koerzitivfeldes wird für verschiedene Nanopartikel-Konzentrationen parametrisiert. Der Einfluss von zusätzlichen externen Magnetfeldern wird außerdem erforscht. Wir charakterisieren abschließend den Effekt von Nanopartikeln auf das Degradierungsverhalten von modifizierten Solarzellen mittels fortgeschrittenen Streuungstechniken. Insbesondere wird der Zusammenhang zwischen Materialmorphologie und Solarzellenleistung untersucht.

List of symbols and abbreviations

A:	Electron acceptor or absorbance
a_0:	Bohr radius $a_0 = 5.2917721067 \cdot 10^{-11}$ m
α:	Fine structure constant $\alpha^{-1} = 137.035999139$
α_i, α_t, α_c:	Incident, transmitted and critical angles
$\alpha(\lambda)$:	Absorption coefficient
$\vec{B}$, B	Magnetic flux density
BHJ:	Bulk heterojunction
c:	Speed of light in vacuum $c = 2.99792458 \cdot 10^8$ $^{\mathrm{m}}/_{\mathrm{s}}$ or concentration
CB:	Chlorobenzene
CTE:	Charge transfer exciton
D:	Electron donor
D/A, D-A:	Donor/Acceptor, Donor-Acceptor
DESY:	Deutsches Elektronen Synchrotron
DF:	Delayed fluorescence
DFT:	Density functional theory
DI:	Deionized (water)
DOS:	Density of states
DSSC:	Dye-sensitized solar cell
DWBA:	Distorted-wave Born approximation
E:	Energy or electric field
ε	Relative dielectric permittivity or energy of hopping sites
EIA:	Effective interface approximation
Fe_3O_4:	Iron (II,III) oxide
FF:	Fill factor
FWHM:	Full-width at half-maximum
g:	Landé g-factor
GISAXS:	Grazing-incidence small-angle x-ray scattering
GIWAXS:	Grazing-incidence wide-angle x-ray scattering
GIXS:	Grazing-incidence x-ray scattering

H:	Magnetic field intensity
$\mathcal{H}$:	Hamiltonian
HOMO:	Highest occupied molecular orbital
I:	Intensity
IEA:	Independent electron approximation
ISC:	Intersystem crossing
ITO:	Indium-doped tin oxide or indium-doped tin oxide-coated glass slide
I-V:	Current-bias
$\vec{J}$, $\vec{j}$	Total angular momentum
J, J_{SC}	Current density, short-circuit current density
k, $\vec{k}$:	Wave vector
$\vec{L}$, $\vec{l}$	Orbital angular momentum
$L_{h,k,l}$:	Crystallite grain size along crystal direction {h,k,l}
l:	Azimuthal quantum number
λ:	Wavelength
LCAO:	Linear combination of atomic orbitals
LMA:	Local monodisperse approximation
LUMO:	Lowest unoccupied molecular orbital
$\overline{M_n}$:	Number average molar mass
$\overline{M_w}$:	Weight average molar mass
MPP:	Maximum-power point
μ_0:	Magnetic permeability of vacuum $\mu_0 = 4\pi \cdot 10^{-7}$ $^{\mathrm{H}}/_{\mathrm{m}}$
μ_B:	Bohr magneton $\mu_B = \frac{e\hbar}{2m_e} = 9.274009994 \cdot 10^{-24}$ $^{\mathrm{J}}/_{\mathrm{T}}$
μ_r:	Relative magnetic permeability
N:	Degree of polimerization or number of scattering centers
n:	Number of atoms or molecules, refractive index, principal quantum number or diode ideality factor
NP:	Nanoparticle
OA:	Oleic acid
OFET:	Organic field-effect transistor
OLED:	Organic light-emitting diode
OSC:	Organic solar cell
OPV:	Organic photovoltaics
ω:	Energy per interaction between monomers or angular velocity
P:	Power or power density
P3HT:	Poly(3-hexylthiophene-2,5-diyl)
PA:	Poly(acetylene)

PBST3HT:	Poly-(3-hexyl-2(3-(4-hexylthiophene-2-yl)-4,5-butylselenophene-1-yl)-5-(4,5-butyltellurophen-1-yl)thiophene)
PCBM:	Phenyl-C_{61}-butyric acid methyl ester
PCDTBT:	Poly(N-9'-heptadecanyl-2,7-carbazole-alt-5,5-(4,7-di-2-thienyl-2',1',3'-benzothiadiazole)]
PCE:	Power conversion efficiency
PDI:	Polydispersity index
PEDOT:PSS:	Poly(3,4-ethylenedioxythiophene):poly(styrenesulfonate)
PF:	Prompt fluorescence
PL:	Photoluminescence
PTFE:	poly(tetrafluoroethylene)
PVC:	Poly(vinil chloride)
ψ	Wavefunction or azimuthal scattering exit angle
$\vec{q}$, q:	Momentum transfer
q_x, q_y, q_z, q_r:	Components of the momentum transfer vector
r.p.m.:	Revolutions per minute
R_S:	Series resistance
R_{SH}:	Shunt resistance
RT:	Room temperature
S:	Entropy or singlet state
SAXS:	Small-angle x-ray scattering
SDD:	Sample-to-detector distance
SLD:	Scattering length density
σ_{RMS}:	Root mean squared roughness
T:	Temperature, triplet state or transmission
TTA:	Triplet-triplet annihilation
t, τ:	Time
TL:	Toluene
θ:	Diffraction angle or backbone torsion angle
UFF:	Universal force field
UV:	Ultra-violet
UV/Vis:	Ultra-violet/visible spectroscopy
V:	Bias, electric potential or volume
V_{OC}:	Open-circuit voltage
WAXS:	Wide-angle x-ray scattering
wt.%	Weight percentage
XRD:	X-ray diffraction
XRR:	X-ray reflectivity

χ: Reciprocal lattice angle about the direction of incoming x-ray radiation

χ_{p-p}: Polymer-polymer interaction parameter

z: Virtual lattice coordination number, height or Cartesian spatial coordinate

Contents

Chapter 1

Introduction

Our ever-ongoing process of industrialization, automation and electrification is resulting into a steadily-growing demand for energy that is not reaching saturation in the foreseeable future. The usage of energy has become engine and proxy of our economic activity and growth. Currently, a large share of our energy demand is still met by fossil or non-renewable sources. In particular, fossil fuels represent above 80 % of our energy mix.[1] Not only the fact of being limited is a drawback for fossil resources, but also they are linked to the rise of high environmental hazards, such as acid rain, air and water pollution, thermal pollution or the emission of greenhouse gases.

One of the current main alternatives to fossil fuels are renewable energy sources. Renewables currently account for approximately 11 % of the total energy mix, and are experiencing a swift increase.[1] In the end of the year 2016 the International Energy Agency forecast a substantial increase the renewables growth for the years 2017-2021 in light of the key political support in several countries and substantial cost reductions.[2] Currently, roughly three quarters of the produced renewable energy come from hydropower, amounting to approximately 0.5 TW worldwide.[1] Nevertheless, most of the viable locations for hydropower have been already exploited, limiting the growth capacity of this technology. Some prospects point to a plateauing value of $\approx$ 1 TW.[3] Another significant renewable technology is wind energy. Wind energy has developed very rapidly within the last couple of years, profiting from cutting-edge technological advances that dramatically increased efficiencies at the same time that lowered the costs. However, even though the amount of energy available in the form of wind would be enough for satisfying the global energy demand, this technology is expected to reach a limit of around 6 TW.[4] In a similar way, prospects of geothermal or tidal power generation establish power capacity ceilings of around 1 TW and 0.2 TW, respectively.[5,6] Overall, these renewable technologies named above, plus the contribution of some other sources, like biomass, are expected to end up

summing around 8 TW, falling far short of the forecast 30 TW energy demand by 2050.[1]

The only known renewable source able to close the gap between forecast demand and renewable generation is solar energy. Indeed, taking the average solar irradiance striking the earth, rough calculations considering a land mass surface coverage of 1 % and a prudential 12 % average device power conversion efficiency (PCE) estimate a yield of around 34 TW electrical power output, enough for meeting the estimated 30 TW demand by 2050.

Currently, the photovoltaic market is dominated by silicon in its three main device forms: monocrystalline, polycrystalline and amorphous (c-Si, p-Si and a-Si, respectively). Other commercially available technologies are cadmium telluride (CdTe) and copper indium gallium diselenide (CIGS). In decreasing module efficiency order, c-Si is the leader, followed by p-Si, CIGS, CdTe, and a-Si.[7,8] Nevertheless, other parameters need to be considered when addressing commercial viability. For instance, a-Si and CdTe are thin film technologies, which drastically reduces the transport and installation costs and, in turn, reduces payback times and makes them financially attractive.

Other novel approaches, like dye-sensitized solar cells (DSSCs) and organic solar cells (OSCs) are currently close to commercial relevance. Organic photovoltaics (OPV) is a thin-film technology and, as opposed to most traditional inorganic technologies, they present several advantages, like light-weight, semi-transparency, mechanical flexibility, and comparatively better performance under indirect light conditions or partial shadowing.[9] OSCs present a low cost per kWh and are compatible with simple, scalable and cost-effective fabrication processes, like roll-to-roll printing. OSCs have experienced a tremendous boost in efficiencies within the last few years, from the state-of-the-art 4 % in the beginning of the 2000's to today's values of 12 % PCE.[10] With increasing presence in industry, they arrive to open new uses of photovoltaic energy, and to add the yet missing degree of versatility that the traditional PV industry, based on massive and heavy rigid panels, is lacking.

Two of the main challenges that still remain for OPV are closing the PCE gap that still exists between OPV and its aforementioned competitors, and improving the device service life in order to make it comparable to inorganic technologies. Many estimates set the commercial competitiveness threshold for OPV at 7 % efficient modules with lifetimes beyond five years.[11–13] So far, these efficiencies have been achieved and surpassed in lab-scale devices, whereas commercial OPV modules still lie a long step behind.[7] As a common denominator for overcoming both challenges, further fundamental understanding

of devices and the materials and layers composing them is needed.

The goal of this thesis is to explore the room available for device PCE increase via one particular mechanism. This mechanism is the switch of the excitonic spins, known as Intersystem Crossing (ISC). The majority of the excitons excited in the active layer of an OSC are singlet excitons. Since the ground state of most organic molecules is a singlet, singlet excitons rapidly decay again to the ground state via fluorescence. Nevertheless, ISC favors triplet spin switch, thereby reducing the efficiency of the radiative decay and, consequently, elongating the average exciton diffusion length. Longer exciton diffusion lengths result in reduced device charge carrier recombination, which reverts positively on the OSC performance. The rate of ISC can be controlled via magnetic effects in the photoactive materials of the solar device. The main approaches consist of the control of the molecular spin-orbit coupling, which blurs the distintion between triplet and singlet, and the use of external magnetic fields, which through the Zeeman effect induce excitonic singlet-to-triplet spin rephasing.

To address the influence and potential of the mentioned ISC-control pathways, two main approaches are presented in the present thesis. On the one hand, the properties, potential and device behavior of a chemically-tailored heavy element-containing macromolecule (poly-(3-hexyl-2(3-(4-hexylthiophene-2-yl)-4,5-butylselenophene-1-yl)-5-(4,5-butyltellurophene-1-yl)thiophene), PBST3HT) are tested. On the other hand, a strategy based on the introduction of superparamagnetic nanoparticles (NPs) in OSCs yields significant device improvements. Our work about the effect of NPs in enhancing OSCs efficiencies,*"improved power conversion efficiency of P3HT:PCBM organic solar cells by strong spin-orbit coupling-induced delayed fluorescence"*[14], published in the beginning of 2015, was pioneer in the field and constituted the first comprehensive report on NP-assisted OSC efficiency enhancement.

In-depth study of the influence of the NPs on the OSC aging behavior yields comprehensive insight into the different phases of device degradation. The research outcome highlights the influence of the materials' and layers' morphology in the device performance, a topic of paramount significance in OPV that is present throughout the whole thesis. In this regard, the use of high-resolution morphology-tracking techniques enabled the observation of the *"codependence between crystalline and photovoltage evolutions in P3HT:PCBM solar cells probed with in-operando GIWAXS"*[15], or the in-situ tracking of the *"bandgap-tuning in triple-chalcogenophene polymer films by thermal annealing"*[16], which are presented and discussed in detail within this thesis. The logic behind the presented work as a whole and

the interrelations between topics are graphically summarized in figure 1.1. In this regard, some of the questions addressed in this thesis are:

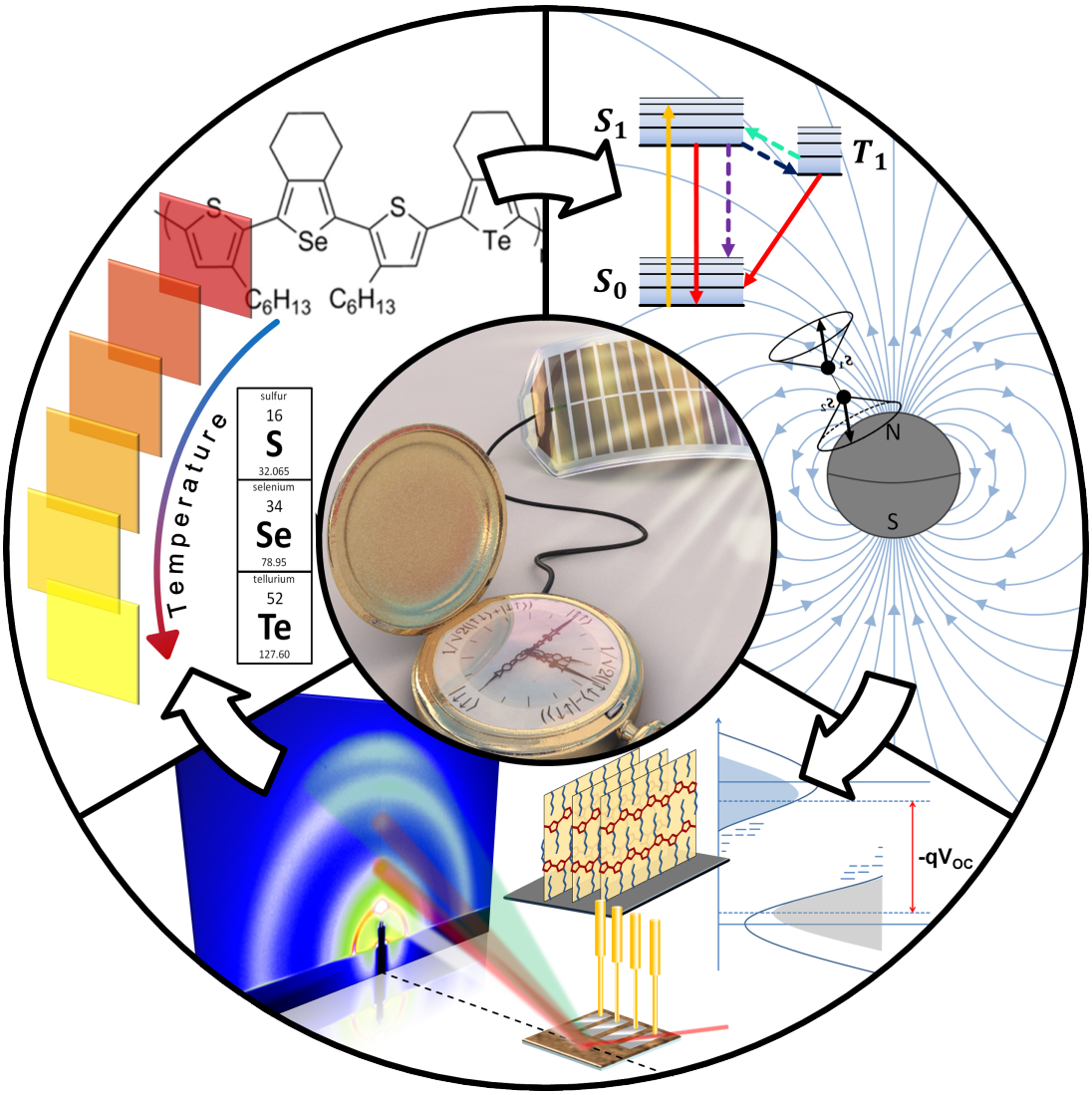

Figure 1.1: *Graphical abstract of the present thesis. The central idea of the thesis is the improvement of the device power conversion efficiency through elongation of the average exciton diffusion length. This is accomplished via adjustment of the ISC of the exciton spin statistics. First, characterization of chemically-engineered ISC-favoring materials yield striking morphological/crystalline properties that affect and allow control of their energetic and optoelectronic landscape, and, in turn, of the resulting device properties. Despite their promising behavior, device implementation requires further technology maturing. Thus, we pursue the same effect through easier, industry-friendlier processes, involving superparamagnetic nanoparticles. OSC modification and related tests are successful and yield significant performance improvement. Finally, deeper research into the effect of nanoparticles during device functioning leads to real-time investigation of the structure-performance relation via in-operando methods. Interesting insight into the morphology-performance relation in device functioning is gained, which connects again with the morphology-performance link of the initial stage. Adapted from references [14], [15] and [16]. Central image by Christoph Hohmann, Nanosystems Initiative Munich (NIM).*

- Does PBST3HT present advantageous morphological and optical properties for use in OSCs?
- Does PBST3HT help in bringing heavy period-five (semi)metals close to application in polymer-based OSCs?
- Can super-paramagnetic nanoparticles lead to a simple pathway to achieve enhanced ISC in photoactive systems that avoids the natural bottlenecks of engineered chemical synthesis?
- Does nanoparticle addition have an impact on the degradation of solar devices?
- How do morphological changes in the photoactive layer affect photovoltaic parameters?

The work included in this thesis is structured as follows. Chapter 2 collects the main theoretical background behind the current work, including the introduction of main concepts of polymer thermodynamics, solar cell functioning, exciton spin tailoring and x-ray scattering. Chapter 3 describes the characterization methods used in this thesis, their working principles as well as the technical details and parameters adjusted for our particular setups. Chapter 4 describes in detail all the materials and protocols of sample preparation used in the fabrication of samples, including substrate cleaning, film deposition, and full solar cell assembly. The band gap-tuning and device behavior of PBST3HT is discussed in chapter 5. Chapter 6 describes in detail the effect of superparamagnetic NPs on poly(3-hexylthiophene-2,5-diyl):phenyl-C_{61}-butyric acid methyl ester (P3HT:PCBM) OSCs, the gain in efficiency, as well as the effect of additional external magnetic fields. The influence of the NPs in the degradation behavior of the OSCs and their active layers, as well as the fundamental in-operando observation of the above-mentioned structure-function link is presented in chapter 7. Finally, chapter 8 collects the main conclusions and future prospects of the presented work.

Chapter 2

Theoretical background

The most relevant theoretical concepts for understanding the scientific content of this thesis are presented and discussed in this chapter. Advanced readers in search for discussion in greater detail are referred to the external sources provided throughout the discussion. Being consistent with the previously presented link between materials' structure and device performance, a significant part of the theoretical discussion is centered in the characteristics, thermodynamics and behavior of polymers, as well as their study using scattering techniques. Moreover, the working principle, layout, working regimes and loss mechanisms of organic solar cells are introduced, along with the theoretical background and physical channels approaching ISC control and exciton spin tuning.

The chapter opens with section 2.1 about basic concepts of polymers, including definition and characteristics, as well as a brief discussion of the main thermodynamic models describing phase separation and aggregate formation. Section 2.2 introduces the formalism describing conductivity in polymers, featuring band formation, charge carrier and conduction mechanisms in organic media. Moreover, the main steps of photon-to-charge-carrier conversion in OSCs (exciton formation, transport, separation, etc.) are described. The section includes a brief discussion on the working regimes of OSCs and the main device loss mechanisms and degradation pathways. The theoretical background of the core work of this thesis is described in section 2.3, which discusses the most relevant features of exciton spin and its tailoring through increased ISC, as well as possible mechanisms to achieve it. Lastly, section 2.4 discusses in detail the fundamentals of scattering, as well as it presents the mathematical and physical frameworks of the methods used.

2.1 Basic concepts of polymer physics

Over the past years polymers or macromolecules have become a topic of increasing interest due to their widespread range of applications, such as in plastics, fibers, electronics or food industry; as well as owing to their practically unlimited potential of tuning their physical and chemical properties. Polymers can be custom-tailored in an extensive variety of features like e.g. hardness (compare carbon fiber vs. glue), electrical conductivity or heat-response.

Polymer industry as such can be considered to have started in the middle of the 19th century with the vulcanization of rubber by Charles Goodyear. However, it was not until 1907 that Bakelite appeared. Bakelite is considered to be the first completely synthetic polymer ever manufactured. Nowadays, 110 years later, polymers are present in our daily lives, in fields such as the car or packaging industries, food, medicines, cleaning and cosmetics, amongst many others.

2.1.1 Definitions and characteristics

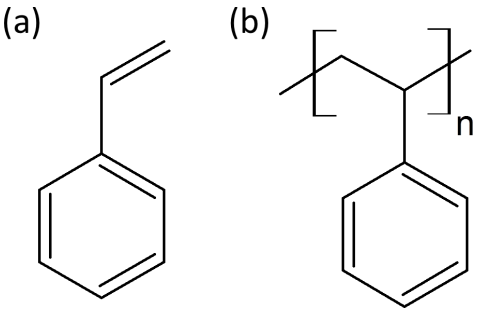

Figure 2.1: *Chemical formulae of a) styrene and b) polystyrene*

Polymers are constructed as a concatenation of *monomers*, featuring mainly carbon and other light atoms, such as hydrogen, oxygen or sulfur. The monomers are small molecular units which are linked together via covalent bonds. Polymers feature a *backbone chain*, which constitutes the core of the molecule, attached to which are the *side groups*, as it is the case for the phenyl ring in polystyrene, depicted in figure 2.1. The amount of monomers chained together determines the *degree of polymerization*. The degree of polymerization depicts the ratio between the molecular weight of the macromolecule and that of the monomer, to account for the amount of chained monomers units. Large molecular weights give rise to polymers, whereas short macromolecules are called *oligomers*. Generally, as a thumb rule, a molecular weight of 10 $^{\mathrm{kg}}/_{\mathrm{mol}}$ = 10 kDa is taken as the threshold between oligomer and polymer. The main difference between them consists of the fact that in the mathematical parametrization of polymers the effect of chain ends, which are chemically different from the rest of the monomers, can be neglected. This way polymers with large molecular weights behave in general in accordance with the used thermodynamic models. In the case of oligomers, due to the higher relative importance of the chain ends compared to the

whole, the quality of the agreement between experiments and polymer models is generally lower.

The process of attaching monomers to fabricate polymers is named *polymerization*. Polymers usually present a molar mass distribution, rather than a unique molar mass, i.e. a unique chain length. Therefore, polymers are normally characterized by a *number average molar mass*, given by:

$$\overline{M_n} = \int_0^\infty p(M) M dM \tag{2.1}$$

and a variance:

$$\left\langle \Delta M^2 \right\rangle = \int_0^\infty p(M)(M - \overline{M_n})^2 dM = \int_0^\infty p(M) M^2 dM - \overline{M_n}^2 \tag{2.2}$$

The remaining integral in equation 2.2 normalized to the number average molar mass is called *weight average molar mass*:

$$\overline{M_w} = \frac{\int_0^\infty p(M) M^2 dM}{\int_0^\infty p(M) M dM} \tag{2.3}$$

and allows for writing of the variance calculated in equation 2.2 as $\left\langle \Delta M^2 \right\rangle = \overline{M_w}\ \overline{M_n} - \overline{M_n}^2$, which allows for calculation of the *polydispersity index (PDI)*:

$$PDI = 1 + \frac{\left\langle \Delta M^2 \right\rangle}{\overline{M_n}^2} = \frac{\overline{M_w}}{\overline{M_n}} \tag{2.4}$$

ranged between one and infinity. Usually, polymer samples used for industrial applications present high polydispersity indexes, yet low production costs. On the other hand, for scientific purposes, in which narrow mass distributions and precise parametrization are generally required, polydispersity indexes generally present lower values.

Polymerization is usually conducted by two main processes, *step polymerization* and *chain polymerization*. The former class consists of attaching already linked monomer groups, whereas in the latter reactive centers that react exclusively with monomers are shifted to the new end of the chain as the number of attached monomers increase. These two polymerization routines lead to different polymer mass distributions. In the step polymerization approach, the resulting distributions are normally broad, whereas chain polymerization usually yields narrow weight distributions. Figure 2.2 exemplary displays the Schulz-Zimm and the Poisson polymer mass distributions associated to step and chain polymerization processes, respectively.

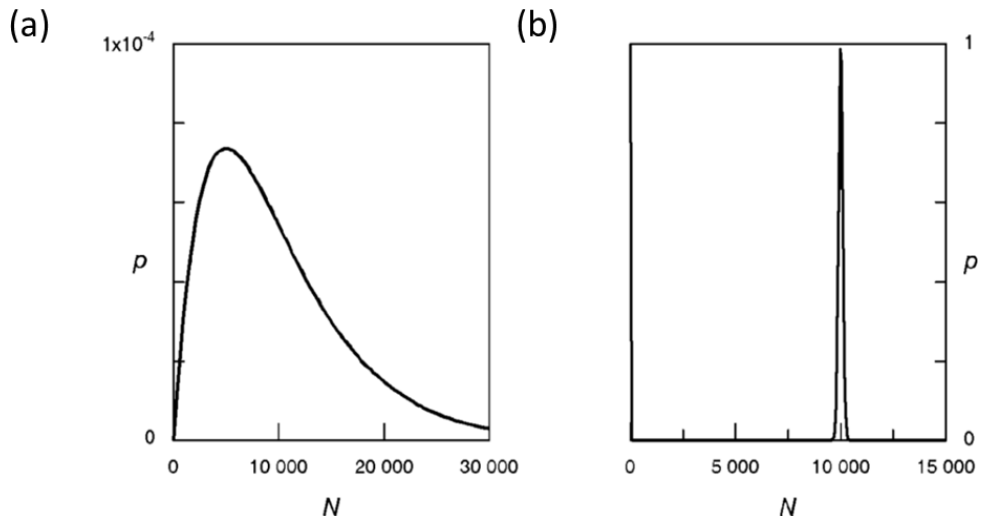

Figure 2.2: *Exemplary mass distributions for a) step and b) chain polymerization methods. Figure taken from [17].*

The mass (and mass distribution) of polymers has a strong influence on their thermodynamic, mechanical and electronic properties. Another feature of polymers that has a strong influence on the mechanical properties of polymers regards the arrangement of the side groups along the backbone chain. This feature is known as *tacticity*. Tacticity is defined by the International Union of Pure and Applied Chemistry (IUPAC) as "The orderliness of the succession of configurational repeating units in the main chain of a regular macromolecule, a regular oligomer molecule, a regular block, or a regular chain".[18] Depending on the arrangement pattern of the side groups in the polymer they are classified in *isotactic*, *syndiotactic*, *atactic* and *eutactic*. These different configurations are achieved via different polymerization procedures. In isotactic polymers, the side groups are positioned in the same side with respect to the backbone along the whole chain, as it is schematically depicted in figures 2.3a and b for the case of poly(vinyl chloride) (PVC). In the case of syndiotactic polymers (figure 2.3c) the side groups are alternatively distributed along the backbone chain, whereas in atactic polymers (figure 2.3d) the arrangement of the side groups is random. In eutactic macromolecules, the substituents occupy specific (although potentially complex) sequences of positions. Hence, isotactic and syndiotactic polymers are particular cases of the more general family of eutactic polymers.

Tacticity of polymers is of special importance in vinyl polymers of the type $-H_2C-CH(R)-$ and it has a major effect in properties such as crystallinity. Whereas isotactic and syndiotactic polymers are in general partially crystalline due to the high degree of order within the chains, the random arrangement of side groups in atactic macromolecules causes them to be generally amorphous. Tacticity also determines some further polymer properties, such as miscibility, glass transition temperature or phase behavior, amongst

others.[19,20]

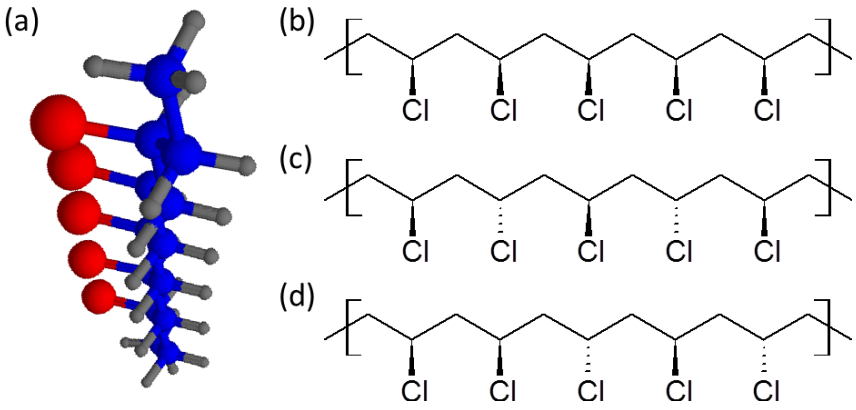

Figure 2.3: *a) 3D representation of an isotactic PVC chain. Blue spheres represent carbon atoms, whereas gray and red balls represent hydrogen and chlor atoms, respectively. Natta representations of a) isotactic, b) syndiotactic and c) atactic PVC.*

Another property of polymers that has also major impact in polymer aggregates, such as crystallinity or conjugation length, is the *regioregularity*. The regioregularity refers to the tendency of the polymer chains to be formed from the same isomer. Polymers with high indexes of regioregularity are desirable in applications like OSCs, since regioregular macromolecules present more favorable rates of light absorption and charge transport.[21,22] In the particular case of thiophenes, the asymmetry of the 3-substituted monomers results in three possible coupling modes between linked units, provided that they link in the 2- and the 5- positions. These possible coupling modes are named $2,5'$, or head-tail (HT) coupling, $2,2'$, or head-head (HH) coupling, $5,5'$, or tail-tail (TT) coupling. Thus, the relative presence of each of these monomer coupling modes defines the overall regioregularity of the polymer chains. Figure 2.4 depicts the four possible triads resulting from the possible couplings between the 3-substituted thiophenes. Generally, very high regioregularities are desired in polymer-based optoelectronic applications.

2.1.2 Polymer blends and the semicrystalline state

Not only in the field of OSCs, but in general, polymer blends are of capital interest, since they enable the combination of different material properties in one single composite. They can for instance combine stiffness with resistance to fracture, two properties that are normally hard to implement a homopolymer material, since, in general, an increase in stiffness (Young modulus) implies also an increase in brittleness. Likewise, in some applications related to organic electronics, such as OSCs, an efficient device functioning is guaranteed through the blend of the so-called donor and acceptor materials.

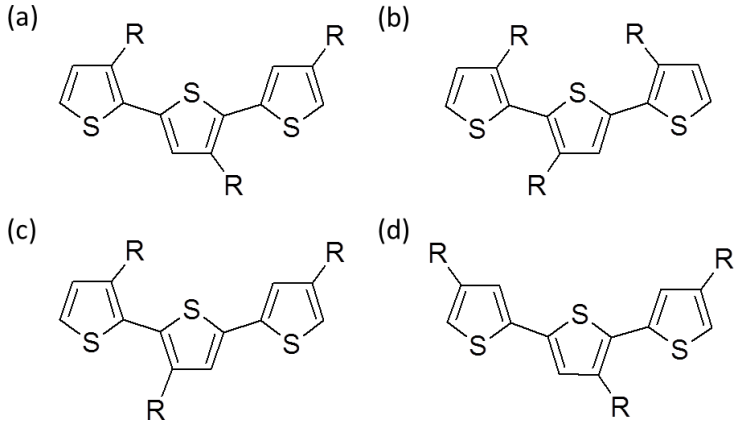

Figure 2.4: *Possible atttaching configurations of three thiophene units. For long polymerized chains, the different configurations give rise to different regioregularities. a) head-to-tail-head-to-tail (HT-HT), b) HH-TH, c) HH-TT, d) TT-HT.*

Moreover, and especially in the case of OSCs, the understanding and eventual control on the demixing behavior of polymer blend is of paramount importance. Therefore, insight into the conditions necessary for polymer blends to either form homogeneous mixtures or form two-phase structures is of special interest.

2.1.2.1 Flory-Huggins theory and phase diagrams

The Flory-Huggins theory is a thermodynamic model that describes the mixing and demixing behavior of polymer blends or of molecules in solution. The model takes as main parameters the size of the modeled molecules, i. e. the degree of polymerization of the corresponding chains in the case of polymers, and the volume fractions of the species present in the mixture. As a result, we obtain an expression for the molar *Gibbs free energy of mixing*, denoted as ΔG_m:

$$\Delta G_m = -T\Delta S_m + \Delta H_m \tag{2.5}$$

where $T\Delta S_m$ accounts for the molar entropy of mixing and ΔH_m is a molar enthalpic contribution that accounts for the interactions between molecules of the same and of different species in the mixture.

Although the model is in general able to deal with either monomer-monomer interactions, as well as with monomer-polymer and polymer-polymer interactions, we will focus on the latter case. The model provides basic understanding of polymer blend phase diagrams as a function of the molar masses and of the temperature. Although we will make some simplifying assumptions, it yields useful information for interpreting experiments and for understanding the behavior of polymer mixtures in general terms.

For the calculation of the term corresponding to the entropy of mixing $T\Delta S_m$ we imagine that our monomers are placed in a lattice, like it is shown in figure 2.5 for the case of polymers, in which each monomer of the chain is sitting on one position of the bidimensional lattice. For the calculations that follow, besides assuming that we deal with a mixture of two monomers (for the simplicity of the calculations without any loss of generality), we make three assumptions: there is no interaction between particles, it is not allowed to have two particles in the same lattice position, and it is as well forbidden to have empty positions in the lattice (so that $n = n_1 + n_2$). Thus, the increase in entropy of the mixture $\Delta S = S_{12} - (S_1 + S_2)$ is calculated via the Boltzmann's entropy formula. Given that the separate subsystems 1 and 2 can only access one microstate (and, therefore, $S_1 = S_1 = 0$), we have:

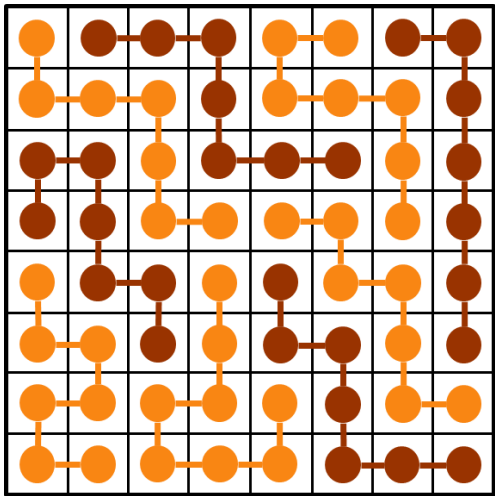

Figure 2.5: *Schematic representation a polymer mixture for construction of the Flory-Huggins formalism. The dimension and arrangement of the lattice defines the coordination number z.*

$$\Delta S = S_{12} = k_B \ln \Omega \tag{2.6}$$

where S is the entropy, k_B the Boltzmann constant, and Ω the total number of microstates that our system can access. In our case:

$$\Omega = \frac{n!}{n_1! n_2!} \tag{2.7}$$

where n accounts for the total number of molecules, whereas n_1 and n_2 denote the amount of molecules of the two different organic species present in the system. We shall now merge the equations 2.6 and 2.7 and rewrite them without factorials using the Stirling approximation:

$$\ln n! \approx n \ln n - n \tag{2.8}$$

Assuming exact equality of expression 2.8 and that the monomers of both species occupy the same volume, the entropic contribution to the Gibbs free energy of mixing can be written as follows:

$$\Delta S = k_B (n_1 \ln n + n_2 \ln n - n_1 \ln n_1 - n_2 \ln n_2) \tag{2.9}$$

Now we introduce the expressions for the volume fractions ϕ_1 and ϕ_2 of the two species:

$$\phi_1 = \frac{n_1}{n_1 + n_2} \qquad \phi_2 = \frac{n_2}{n_1 + n_2} \tag{2.10}$$

Yielding an expression for the entropy of mixing of one mol of particles mixed in ideal conditions that depends only on the volume fraction of the two species:

$$\Delta S_m = -R(\phi_1 \ln \phi_1 + \phi_2 \ln \phi_2) \tag{2.11}$$

where $R = N_A k_B$ is the ideal gas constant. The case presented above corresponds to the easiest scenario in which the molecules being mixed are just monomeric. However, more elaborated cases covered by the Flory-Huggins theory comprise also the monomer-polymer and the polymer-polymer interactions (polymer in solution and polymer blends, respectively). In these cases the possible arrangements of the monomers of the same type are less, since they are chained to one another due to the polymerization process. In these cases, the calculation of the entropy of mixing deals as well with the coordination number of each proposed lattice and the availability of lattice positions as a virtual polymerization reaction goes on. For the polymer blend case (polymer-polymer interaction, see figure 2.5) the final expression of the entropy of mixing also includes the respective degrees of polymerization of the two species N_1 and N_2. It reads:

$$\Delta S_m = -R\left(\frac{\phi_1}{N_1} \ln \phi_1 + \frac{\phi_2}{N_2} \ln \phi_2\right) \tag{2.12}$$

As it can be seen, the entropic term of the Gibbs free energy of mixing is always negative and therefore always favors mixing. For the case of polymer mixtures, the entropic term is strongly reduced in modulus due to the polymerization process. This latter consideration accounts for the fact that long chains have lower entropy of mixing and therefore demixing or phase separation is more likely in long polymerized chains.

We also need to consider the enthalpic contribution to the Gibbs free energy of mixing (equation 2.5). This contribution ΔH_m parametrizes the different interactions present in the mixture, between either molecules of species 1 or 2 between themselves, or between molecules of species 1 and 2 (not the covalent bonding, but the interaction between different chain sections). We generally represent these interactions by the coefficients ω_{11}, ω_{12} and ω_{22}. Unlike for the entropic contribution to the Gibbs free energy of mixing, the enthalpic part can either favor mixing or demixing, depending on the nature of the different interaction coefficients. In general, for van der Waals forces, attractive interactions between monomers of the same species are stronger than those between monomers of type 1 and 2, thus favoring demixing.[17] Since each of the interaction coefficients increases at

expenses of the average of the remaining two, the increment in energy per interaction between monomers of different species is:

$$\Delta\omega = \omega_{12} - \frac{1}{2}(\omega_{11} + \omega_{22}) \tag{2.13}$$

If we now account for all the interactions in the system we come to a total increment in enthalpy of:

$$\Delta H = (z-2)\Delta\omega N_2 n_2 \phi_1 \tag{2.14}$$

where z is the (virtual) lattice coordination number and, therefore, $z-2$ are the available positions around the monomer to potentially be filled by the opposite species. Hereby, the volume fraction of the species ϕ_1 indicates the probability for the $z-2$ available positions around the type 2 monomers to be filled with type 1 molecules assuming homogeneity in the mixture. According to:

$$N_2 n_2 \phi_1 = \frac{N_2 n_2 N_1 n_1}{N_2 n_2 + N_1 n_1} = n\phi_1\phi_2 \tag{2.15}$$

we can rewrite equation 2.14 in its molar version as:

$$\Delta H_m = RT\chi_{p-p}\phi_1\phi_2 \tag{2.16}$$

where now χ_{p-p} is the so-called *polymer-polymer interaction parameter*. The interaction parameter compares the energy gained by the interaction with monomers of either the same or the opposite species to the thermal energy. Its formal expression reads:

$$\chi_{p-p} = \frac{(z-2)\Delta\omega}{k_B T} \tag{2.17}$$

Finally, by introducing the equations 2.12 and 2.16 in 2.5 we come to a final expression for the molar Gibbs free energy of mixing:

$$\Delta G_m = RT\left[\frac{\phi_1}{N_1}\ln\phi_1 + \frac{\phi_2}{N_2}\ln\phi_2 + \chi\phi_1\phi_2\right] \tag{2.18}$$

Besides the formal expression for χ_{p-p} presented in equation 2.17, approaching the values of χ_{p-p} that successfully reproduce the entropy of mixing of two particular materials follows diverse pathways. When dealing with polymer solutions, the interaction parameter can be estimated from the *Hildebrand solubility parameters* δ_1 and δ_2:[23]

$$\chi_{p-p} = \frac{V_{seg}(\delta_1 - \delta_2)^2}{RT} \tag{2.19}$$

where V_{seg} stands for the volume of a polymer segment. For polymer solutions, the dependence of the interaction parameter with the temperature as $\chi_{p-p} \propto 1/T$ is generally

sufficient. Nevertheless, when dealing with more complex scenarios, like polymer blends, solvation, D-A complexes, etc. some corrections in the interaction parameter need to be made. The "Tanaka modification", the "model of Bawendi and Freed" [24] or the "model of Mumbi and Sher" are just few examples of models deploying more complex descriptions of the interaction parameter χ_{p-p}. These feature in some cases $\chi_{p-p} \propto T$ or demixing at both low and high temperatures, amongst others. A deeper treatment of the Flory-Huggins theory and more detailed calculations are presented elsewhere.[17,25,26]

2.1.2.2 Blend demixing: phase diagrams and decomposition mechanisms

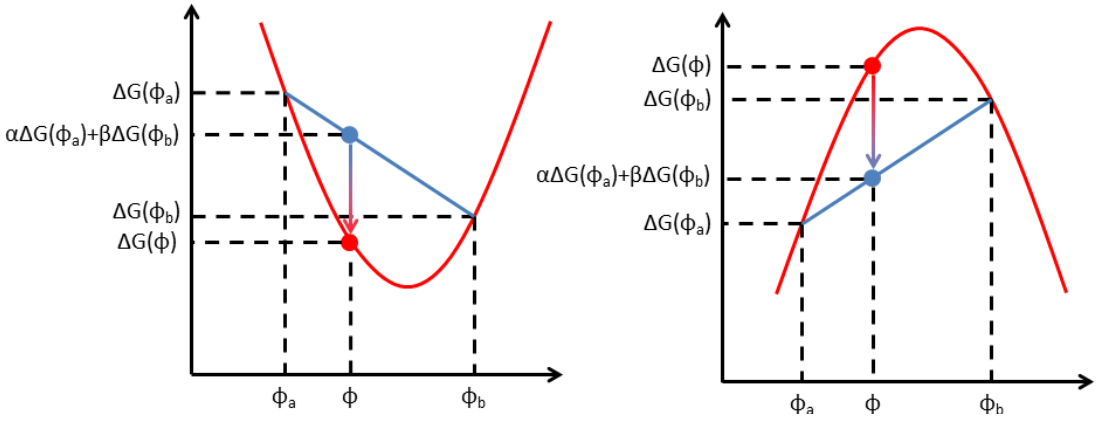

Figure 2.6: *Sketch of the mixing-demixing behavior of a polymer mixture in an a) stable and b) unstable regions of the phase diagram. In the stable region, the energy of the mixed phase is lower than for the two separate components. In the unstable region, the systems accomodates at lower overall energy by demixing into two phases.*

In general, systems remain in the minimum of their Gibbs energy of mixing. Thus, the demixing of the two phases will not occur if the Gibbs energy of the mixture is lower than the Gibbs energies of the two single components weighted by their relative amounts α and β:

$$\Delta G_m(\phi) < \alpha \Delta G_m(\phi_a) + \beta \Delta G_m(\phi_b) \tag{2.20}$$

where ϕ corresponds to the composition of the mixture in terms of a and b and ϕ_a and ϕ_b the pure phases. This phenomenon is schematically depicted in figure 2.6, in which the red lines indicate the Gibbs free energy of the mixtures as a function of the volume ratios of the a and b components, and the blue lines the averaged contributions of the two components to the Gibbs free energy in a demixed state. In the case of figure 2.6a the Gibbs free energy of the mixture is convex. In this case, we say that the solution is stable, since demixing would increase the Gibbs free energy of the system, and therefore

it does not occur spontaneously. On the contrary, figure 2.6b depicts the case of an unstable solution, in which the Gibbs free energy curve for the mixture is concave. Hereby, demixing of the blend components leads to a more favorable energetic state and, thus, the system undergoes phase separation.

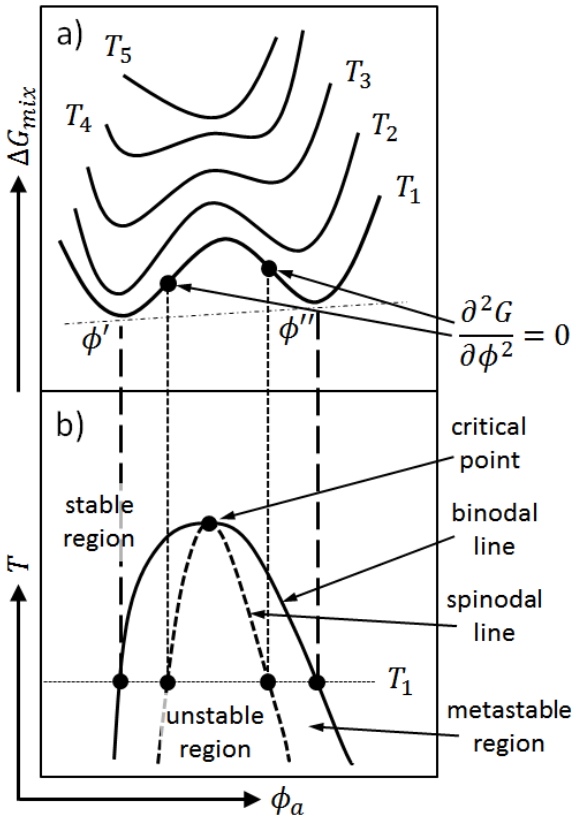

Figure 2.7: *a) Gibbs free energy as a function of the polymer blend composition for different temperatures. The temperature increases from T_1 to T_5. b) Temperature phase diagram for different blend compositions obtained from the first and second derivatives of the Gibbs free energy function for multiple temperatures. The upper critical point is obtained through the third derivative.*

In general, these diagrams of Gibbs free energy of mixing as a function of the composition of the mixtures are a key feature for constructing the phase diagrams of polymer mixtures. An example of the construction of a polymer blend phase diagram using the Gibbs free energy ΔG_m of mixing for multiple temperatures is displayed in figure 2.7. The maxima and the minima of the ΔG_m as a function of the blend composition defines stable, metastable and unstable regions of the phase diagrams, meeting at the binodal and spinodal lines, repectively (see figure 2.7b). In the stable region we find a single phase corresponding to the mixture of the two polymers, whereas in the unstable region the two polymers demix into two phases. In the metastable region, phase separation does not occur spontaneously but it needs a nucleation step, usually triggered by the presence of impurities. In general it is possible to obtain analytical expressions for the binodal and the spinodal lines.[17] Finally, the point of the phase diagram in which binodal and spinodal lines meet each other is called *critical point*. This point of the phase diagram depicts a second-order transition and corresponds to a phase-separated state of the mixture in which each of the two components form a continuous structure.[17]

Phase diagrams of polymer blends allow for anticipation of sample morphologies, which is of capital importance for each desired application. Furthermore, the decomposition

mechanism triggered in the system also depends on the region of the phase diagram the system is at, and it also affects the sample morphology. Two of the main decomposition mechanisms for polymer mixtures are known as *nucleation and growth* and *spinodal decomposition*.

The former arises when a temperature change shifts the system from homogeneous mixture to the metastable region of the phase diagram (see figure 2.7). In this case, the system remains stable against small concentration fluctuations. However, when concentration fluctuations or even impurities are big enough they bring the system out of its metastable equilibrium, so that the new phase grows around the original nucleus and, hence, it is called nucleation and growth. On the contrary, when a jump in temperature brings the mixed system into the unstable region of the phase diagram, it becomes automatically unstable, so that any small fluctuation in concentration leads automatically to a scenario in which the system phase-separates into two phases, each of them with the composition corresponding to the two nearest minima of the $\Delta G_m(\phi_A)$ curve. Unlike in the case of nucleation and growth, in which diverse lengths are present in the system, in spinodal decomposition only a rather narrow gap of concentration fluctuation length scales survives, since long fluctuation length scales imply transporting material through long distances and short fluctuation wavelengths trigger a severe energy penalty due to strong composition gradients. As a result, systems that demix through a spinodal step present a bicontinuous interpenetrating matrix of the two phases displaying a narrow range of typical size scales.

In organic electronics in general, and OSCs in particular, the morphology and length scales present in demixed polymer blends are of capital importance, as it will be discussed in the following. In spin coated films, the development of the morphology freezes prior to reaching thermodynamic equilibrium. This has as well an effect on the performance of subsequent devices, and several treatments (thermal and solvent annealing, solvent additives, etc.) are used for achieving optimal blend morphologies.

2.1.2.3 Formation and growth of polymer aggregates

Besides the behavior of polymer mixtures regarding phase separation, which plays a determining role in the performance of the final organic semiconductor devices, other features that drastically condition their functioning are the amount, size, orientation, etc. of the crystalline regions within the polymers composing the OSC. One of the most accepted models explaining polymer crystallization, featuring the formation of nucleation centers, followed by thickness and lateral growths, is the multistage model proposed by Strobl.

The reader is referred to the literature for comprehensive discussion.[17,27]

Owing to their morphology, featuring entangled chains and a mesh-like structure, polymers usually exist in a semicrystalline state. This means that polymer samples present crystalline regions separated by amorphous regions of the same material. The reason for this is that complete crystallization is associated to the high entropic cost of disentangling chains. Moreover, in the process of aggregate formation, other features that hinder crystal formation are expelled into the amorphous phase, like impurities, chain ends and other defects.

The first stage in the crystallization of polymers is the formation of nucleation centers. These are small regions of high inner order formed due to thermal fluctuations. Depending on their size, they either disappear again or stabilize into a nuclei, from which the crystallization starts. The crystallization rate is proportional to the volume of the crystallizable region, and it is an exponential function of the temperature.[28,29] Two main mechanisms assist the intial aggregate nucleus stabilization and growth: intramolecular crystallization, a fast process in which one single chain folds, forming the nucleus of the polymer aggregate, or intermolecular crystallization, in which different chains are involved in the initial thermal fluctuation and stabilization, featuring much slower nucleation rates.[30] Once the nucleation centers are formed, they start to grow forming crystalline regions. The aggregate formation is pictured as forming from the crystalline core towards the outside. In the framework of the multistage model, different phases are considered, each of them associated to a control temperature. The control temperatures very much define the final thickness of the crystalline domains. However, the lateral growth, characterized by the merger of crystalline blocks, is, in principle, unlimited.

The formation and development of crystallites and polymer aggregates regions plays an important role in the performance of OSCs, since they strongly influence parameters such as the efficiency of charge carrier transport or the shape of the molecular density of states (DOS). Greater insight on the link between crystallinity and device perormance is provided in chapter 7.

2.2 Organic semiconductors and solar cells

In this section, we first discuss the main features participating in the electrical conductivity of polymers and, more generally, organic materials. The formation of delocalized conducting states and their packing in pseudo-bands is discussed together with the most

relevant aspects of exciton and charge carrier transport in organic media. Secondly, the working principle of organic solar cells and their main operation features are discussed, including charge carrier generation, transport, operation regimes and main recombination mechanisms.

2.2.1 Conducting polymers

2.2.1.1 Band formation in organic semiconductors

In spite of the broad versatility of polymers with regard to mechanical and thermodynamic properties, polymers have traditionally been regarded as generally good insulators. However, the chemical composition of some polymers enables charge transport under certain conditions. This was first observed in the simple polymer polyacetylene (PA) by A. Heeger, A. MacDiarmid and H. Shirakawa in the year 1977. They observed an increase in electrical conductivity of seven orders of magnitude upon exposure of PA to iodine vapor, reaching conductivity values comparable to many semiconductors. For this contribution the three scientists were awarded with the Nobel prize in chemistry in the year 2000.

The simple chemical structure of PA makes it a useful case study for understanding the more general properties of conducting polymers, as well as which are the main features of charge transport in organic media. It is the presence of so-called conjugated bonds that confers polymers semiconducting properties.

The process of hybridization in carbon yields three co-planar sp^2 orbitals, whereas the original $2p_z$ orbital remains unchanged. Thus, carbon atoms with sp^2 hybridized orbitals come together, forming strongly localized σ bonds between the nuclear centers, giving rise to a long chain-like macromolecule. The remaining non-hybridized p_z orbitals overlap above and below the carbon chain, forming so called π bonds. This repeated overlap of π bonds along the chain gives rise to delocalized electronic probability waves through which electric charges can be transported over long distances. These delocalized electron probability clouds over many units of a hydrocarbon chain are called conjugated bonds, and, although the actual carbon-carbon bond distance in such conjugated systems lies between that of the single and the double bonds, in the Lewis representation they are depicted as a chain of alternating single and double bonds. As a result of the long sequence of conjugated bonds, a 1-dimensional crystal is obtained in which each carbon atom contributes with one electron to the π delocalized cloud. The binding between each pair of carbon atoms gives rise to a lower-energy bonding (π) and a high-energy antibonding (π^*) molecular state. Thus, the chaining of multiple carbon atoms leads, in the limit of

infinite chained atoms, to a quasi-continuum of energy states, as schematically depicted in the upper half of figure 2.8. In the polymerization process the number of available states doubles the number of contributed electrons in the π conjugated orbitals. Thus, the formed energy band is filled up to the half, as highlighted in red in figure 2.8.

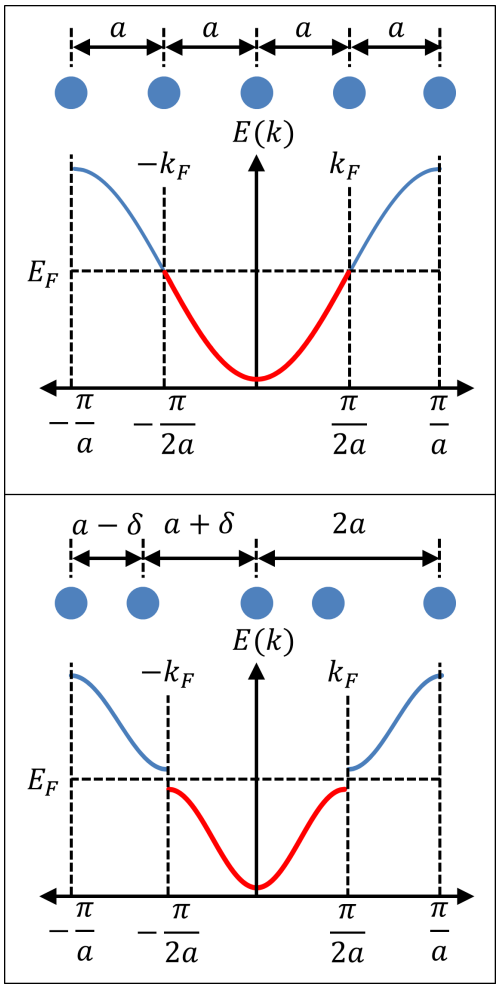

Figure 2.8: *a) Energy diagram of a perfect one-dimensional lattice. The red section of the line indicates the filled states up to the Fermi energy. b) According to the Peierls theorem, such unstable structure distorts, enlarging the size of the unit cell. This reduces the size of the first Brillouin zone and induces the appearance of an energy gap, reducing the overall energy of the crystal.*

According to the Peierls' transition theorem, a one-dimensional equally spaced chain with one electron per ion is unstable. Such a 1D crystal undergoes a distortion along the chain by a magnitude δ, as depicted in the lower panel of figure 2.8. This distortion doubles the size of the unit cell. Accordingly, the size of the first Brillouin zone shrinks by half, whereby the energy function $E(k)$ at the edges of the new first Brillouin zone plateaus. This leveling off causes small energy savings in the vicinity of the edges of the new first Brillouin zone $|k| = \pm k_F = \pm\pi/2a$ (compare the filled states in both cases depicted in red in figure 2.8). Hereby, the overall energy of the crystal is reduced, making the distortion energetically favorable. At the same time, this induces the appearance of a band gap in the material, which will conform the base of the semiconducting properties of the polymer. This effect is commonly referred to as *metal-insulator transition.*

The appearance of the band gap defines, in analogy to classical inorganic semiconductors, two energy bands. According to the theoretical benchmark of the Linear Combination of Atomic Orbitals (LCAO), the overlap of each two p_z orbitals yields two different solutions to the corresponding Schrödinger equation, called bonding (π) and antibonding (π^*), as discussed above (n=1 case in figure

2.9). As the process of polymerization proceeds, each carbon atom undergoes this process twice, once for each of the two neighboring carbons. Consequently, the number of states double that of the contributed electrons by each carbon atom. As the number of chained units increase, a sequentially closer-packing of bonding and antibonding states separated by a gap forms (compare increasing n cases in figure 2.9). The π electrons occupy the lowest energy states, i.e. the bonding states located below the gap. Consequently, the energetic states located immediately below and above the gap are referred to as *Highest Occupied Molecular Orbital (HOMO)* and *Lowest Unoccupied Molecular Orbital (LUMO)*, respectively. As the polymerization proceeds to very large numbers of chain monomeric units, the energy states eventually become so closely packed that appear like a quasi-continuum of occupied states below the gap. Similarly, an empty energy band of states above the band gap E_g appears, analogous to inorganic semiconductors.

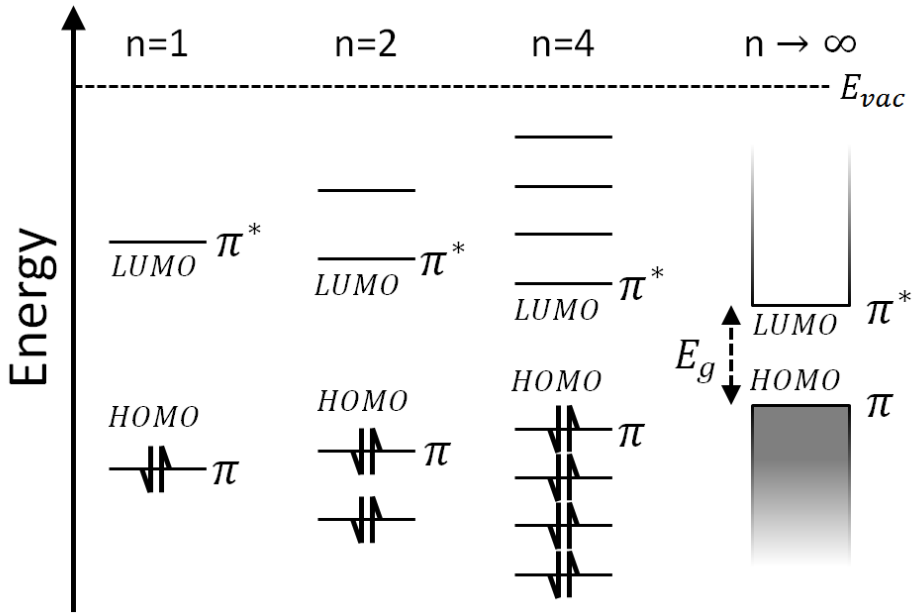

Figure 2.9: *The Schrödinger equation for two bound carbons (n=1) yields two solutions, a bonding (π) and an antibonding (π^*) one. The addition of further carbon atoms yields more allowed energy states, defining the HOMO and LUMO levels. In the limit of $n \to \infty$, they form a quasi-continuous band of allowed energy states with a forbidden gap in between E_g.*

Modeling of the band formation in organic media through formalisms like the metal-insulator transition or the LCAO framework provides good understanding of the basic physics involved. However, organic media present very substantial differences compared to inorganic environments, like being mechanically less rigid, presenting lower dielectric coefficients, or being structures formed on the basis of covalent but not metallic bonds. These and further features introduce qualitative differences related to e.g. material en-

ergetic landscape or charge carrier formation and transport that do not allow physical treatment based on conventional, crystalline inorganic semiconductor physics.

2.2.1.2 Charge carriers and transport in polymers

The natural appearance of charge carriers in polymers featuring conjugated bonds is mainly based on the presence of bonding irregularities, kinks, chemical defects, etc. An example of this natural occurrence of charge carriers in polymers is usually depicted with the case of PA, although the principle is as well valid for all polymers featuring conjugated backbones, such as those used in this thesis.

PA consists of a conjugated chain with two energetically equivalent ground state configurations. The switch between the two is generally thermally excited. When the two configurations meet within the same chain, the carbon atom at the junction is bound to its two neighboring carbon atoms and to one hydrogen. This requires three out of the four carbon valence electrons, thereby leaving an unpaired valence electron, as depicted in figure 2.10. Thus, this unpaired radical possesses a spin and an electric charge, and is able to move along the chain, creating a deformation in the chain in its path. This combination of radical and the associated deformation forms a quasi-particle known as *neutral soliton (S^0)*. Energetically, the neutral soliton is an exicted state and, according to the SSH theory (named after Su, Schreiffer and Heeger), its energy level lies within the bandgap, increasing the overall conductivity of the polymer.[31] The neutral soliton does not have a charge (since the negative charge of the radical plus the positive charge of the corresponding carbon nucleus cancel out) but has spin $1/2$, the spin of the unpaired electron. Removal of the unpaired electron by e.g. an oxydizing agent leaves in the polymer chain a net positive charge with no spin (since there are no unpaired electrons remaining). This is knwon as *positive soliton (S^+)*. Similarly, the reunion of a neutral soliton and an additional unpaired radical (from another neutral soliton or provided by a reducing agent) results in a *negative soliton (S^-)*, which also has spin zero. On average, the mass of a soliton is around six time the mass of the electron, and due to the low soliton activation energy ($2\ \text{meV} << k_bT$) they are widely present at room temperature (RT).[31]

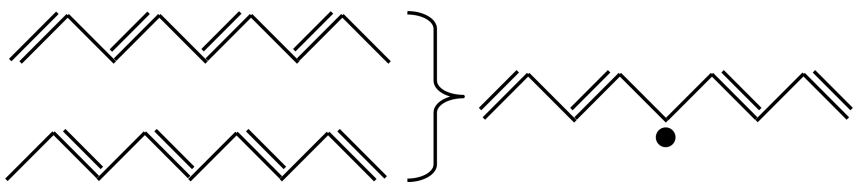

Figure 2.10: *Lewis representation of the formation of a neutral soliton via junction of the two degenerated ground states of a PA chain.*

As solitons move through the polymer chain, they can combine with each other, forming another quasi-particle called *polaron*. In contrast to solitons, polarons can only be either positive (P^+) or negative (P^-), formed by the combination of a neutral soliton with a positive or negative one, respectively. Both types of polarons P^+ and P^- have spin ½ (see figure 2.11). Furthermore, same-charge polarons can merge forming the third kind of charge carrier in polymeric media, the *bipolaron*. Bipolarons are also always charged (B^+ and B^-) and have spin zero. A graphical representation of the whole quasi-particle zoo, their energetic location in the material and their spins can be found in figure 2.11.

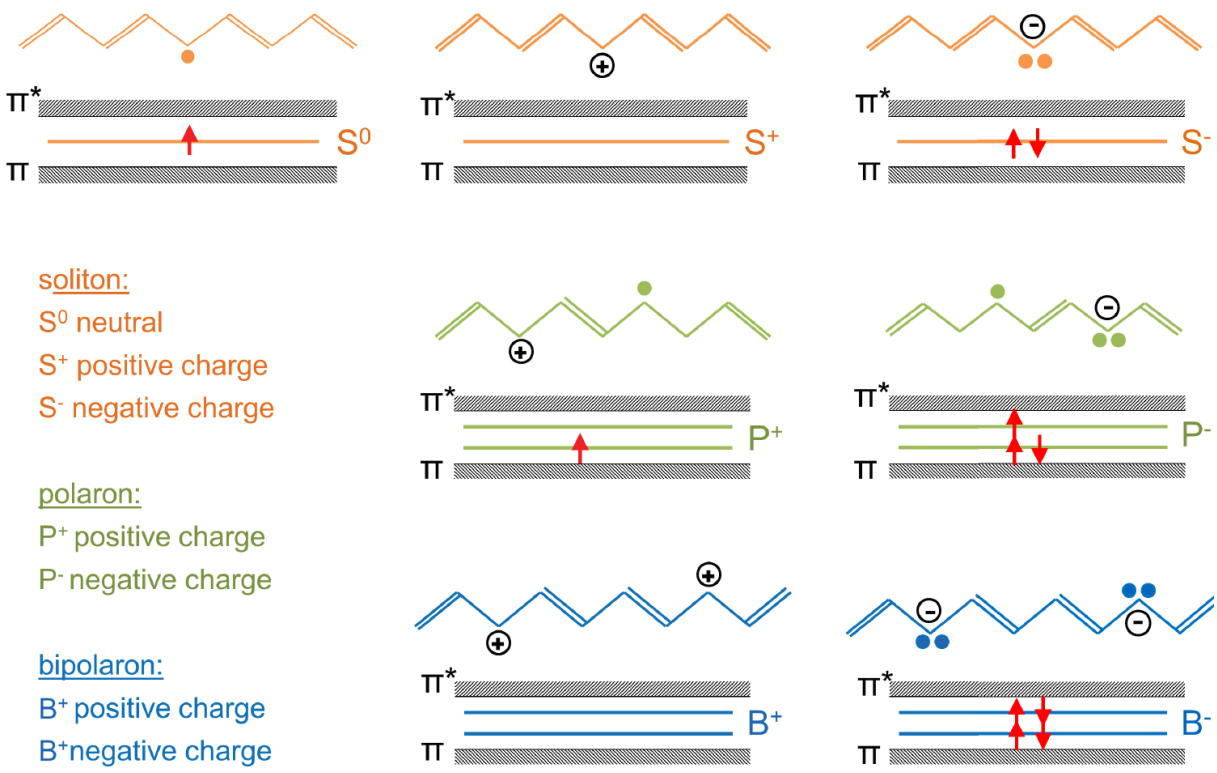

Figure 2.11: *Summary chart of the main charge carriers present in organic semiconductors, including their composition, electric charge, spin and energetic position within the band gap. Extracted from* [32].

Solitons, polarons and bipolarons travel along polymer chains carrying significant chain deformations. For this reason, amongst many others, it is complicated to describe the transport of charge carriers in organic media using mathematical formalisms of inorganic solid state physics. Typically, solitons formed in a PA chains span over several carbon atoms for polymer segments displaying long conjugation lengths.

In general, charge carriers in polymeric environments need to be transported along one chain as well as between different chains, i.e. both inter- and intra-chain transport occur. Band-like transport along conjugated polymer backbones and ordered crystals is success-

fully described by the SSH model, in which higly delocalized quasi-particles move freely. Similarly to the case of inorganic semiconductor, the efficiency of this type of transport mechanisms decreases with temperature, as the interactions between the charge carriers and the phonons (lattice vibrations) disturb the coherent transport, giving rise to phonon scattering events and reducing the quasi-particle delocalization.

In contrast to the band-like transport, characteristic of intra-molecular transport or motion of carriers in highly-ordered aggregated polymer regions, inter-molecular charge transport in amorphous polymer regions is dominated by the so-called *hopping* transport, which sets to a large extent the conductivity bottleneck for most organic materials. Hopping transport becomes the main mechanism as soon as the static disorder (i.e. localized charge carriers) has an important contribution to the description of the energetic landscape of the material, as it is the case for polymer amorphous regions, or regions concentrating high densities of defects, chain ends, etc. In these cases, the energetic landscape of the photoactive medium is characterized by locally-defined HOMO and LUMO energetic levels, varying from spot to spot depending on chain features like crystallinity, defect concentration, local ring coplanarity, etc. This results into a Gaussian distribution of isolated yet close energetic states. When moving throughout the material, carriers need to overcome small energetic barriers in order to hop from state to state. Hence, this kind of transport is known as hopping.

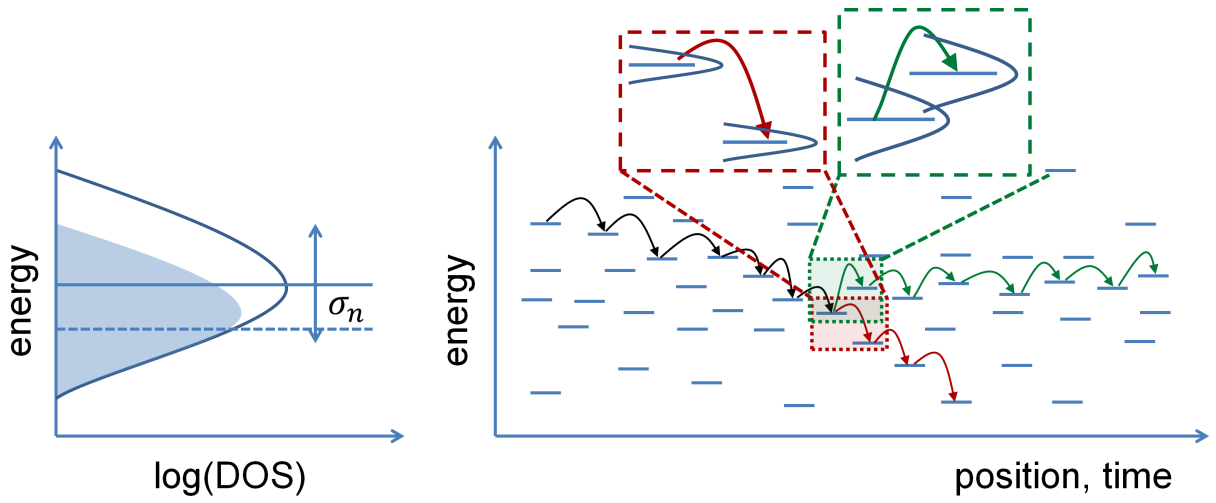

Figure 2.12: *Left: Density of states of an organic molecule presenting energetic Gaussian disorder. The blue-shaded area represents the occupied states compared to the available total. Right: Relaxation and transport of a photogenerated polaron via hopping. The red path depicts a relaxation to the bottom of the band ($T = 0$). The green path, at $T > 0$, possesses sufficient energy for granting spatial transport.*

Hopping is based on the tunneling probability between energy states, which is in turn

determined by the strength of the thermal fluctuations. The probability of hopping between energetic states is parametrized via a so-called hopping rate ν, first introduced by Marcus.[33,34] Miller and Abrahams proposed a similar approach:[35]

$$\nu_{ij} = \nu_0 e^{-2\gamma\Delta R_{ij}} \begin{cases} exp\left(-\frac{\varepsilon_j - \varepsilon_i}{k_b T}\right) & ;\ \varepsilon_j > \varepsilon_i \\ 1 & ;\ \varepsilon_j \leqslant \varepsilon_i \end{cases} \tag{2.21}$$

Hereby, amongst other factors, the hopping probability scales with the negative exponential of the spatial distance between hopping sites R_{ij}. It can be seen that between sites featuring increasing energy ($\varepsilon_j > \varepsilon_i$) the tunneling probability increases with temperature. In contrast, the downward hopping rate ($\varepsilon_j \leqslant \varepsilon_i$) is independent of the temperature. Therefore, in the case of hopping transport, the conductivity increases with increasing temperature. For low temperatures charge carriers relax to the bottom of the DOS, where they become trapped. In contrast, higher temperatures increase the tunneling probability due to a higher overlap of the wave functions of the individual states. This aids the hopping between energetic states and drives the macroscopic transport throughout the material. The macroscopic transport of charge carriers via hopping is commonly described by the Bässler model.[36]

2.2.2 Light absorption, exciton generation and diffusion

In order for a photon to be absorbed, its energy must be larger than energy of the band gap of either of the components of the photoactive layer $E_{photon} \geqslant E_{LUMO} - E_{HOMO}$, whereby in the mixture P3HT:PCBM the main absorber is P3HT. The wavelength-dependent light absorption of polymer films is described by the Lambert-Beer law (see section 3.2.1). For a photon of sufficient energy interacting with the absorbing material, the excited electron experiences a vibronic transition. Vibronic transitions are simultaneous changes in electronic and vibrational levels, and the intensity (probability) of their occurrence is described by the Franck-Condon principle.[37] This model was explored particularly in depth for H-aggregated polymers by Frank Spano.[38–41] The Franck-Condon principle asserts that, during the electronic transition upon photon absorption, the overlap between the initial vibrational wave functions of the ground and excited states determines the likelihood for transition between specific vibrational levels. Thus, despite the fact that the configurational order of the polymeric chain changes upon photon absorption (it was discussed in the previous section 2.2.1.2 that charge carriers in organic media carry significant deformations of the polymer chains), the intensity of a specific vibronic transition depends on the initial overlap of vibronic wave functions. This occurs due to the fact that the absorption of the photon happens at a much shorter time scale than the modification of the configurational coordinate, i.e. the relative spatial arrangement between electronic

orbitals. This is schematically depicted in figure 2.13.

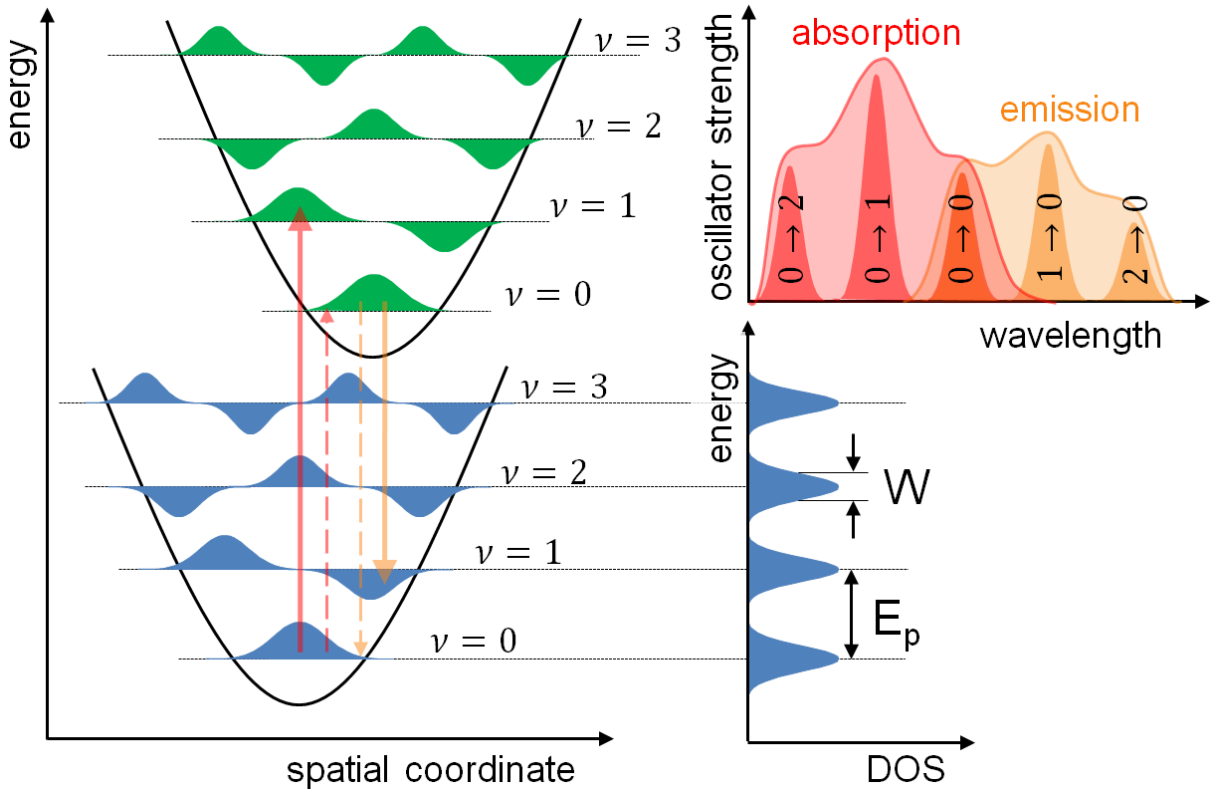

Figure 2.13: *Schematic representation of the Franck-Condon pinciple and the formation of absorption and emission bands. a) The two electronic states, represented by the two parabolas, depict a fine structure of vibronic states, whose overlap determines the probability of transition. b) The resulting transition probabilities give rise to stronger or weaker absorption/emission bands. c) Representation of the energetic broadness W of each vibronic level.*

Thus, the obtained absorption spectrum results from the superposition of the intensities (probabilities) of all allowed vibronic transitions/bands. The vibronic transitions in the absorption spectrum present a so-called *exciton bandwidth (W)*, which is a measure for the degree of polymer aggregation, since the sharpness of the vibronic transitions is determined by the degree of energetic disorder. Since the disorder affects all transitions to the same extent, all vibronic transitions present the same broadness. For the case of P3HT, Frank Spano suggested a relation between the $0 \rightarrow 0$ and the $0 \rightarrow 1$ transitions that allow calculation of W:

$$\frac{A_{0-0}}{A_{0-1}} \approx \frac{n_{0-0}}{n_{0-1}} \left(\frac{1 - 0.24\frac{W}{E_p}}{1 + 0.073\frac{W}{E_p}} \right) \tag{2.22}$$

where n_{i-j} indicates the refractive index of the material at the wavelength of the corresponding transition, and E_p is the energy of the vibrational ground state of the harmonic

oscillator, which for P3HT is $E_p = \hbar\omega_0 = 0.2\ eV$. Upon promotion of an electron to the LUMO excited state, the ground HOMO is left with a missing electron, hence displaying a net positive charge. This is described as a so-called hole. In organic semiconductors the excited electron and the hole are coulombically bound, forming an *exciton*. The binding energy of an exciton in a specific environment depends upon the material's dielectric constant as $E_{bind} \propto {}^{1}/_{\varepsilon_r^2}$. Hence, in inorganic semiconductors, where the dielectric constants are high ($\varepsilon_{r,Si} \approx 11.68$) the electrical screening is efficient and, thus, the excitons, with a large exciton radius, can be splitted by thermal energy at RT ($\approx 25\ meV$),[42] immediately turning into separated free charge carriers. These are known as Wannier-Mott excitons.

In contrast, the low dielectric constants of most organic media ($\varepsilon_{r,org} \approx 3-4$) render the photoactive medium limited electrostatic screening properties. Thereby, excitons in polymeric environments, known as Frenkel excitons, require the energy level offset present at the donor-acceptor (D-A) interface in order to split. As it happens for all excited states, excitons present a certain lifetime after which they recombine, decaying again to the ground state. Thus, depending on their lifetime and their mobility within the material, excitons have a characteristic diffusion length. The average exciton diffusion length in organic materials lies in the order 10 nm.[42–44] After exciton recombination, the energy of the incoming photon is again irradiated and cannot be used for electricity generation. For this reason, parameters like the exciton diffusion length or the D-A demixing scale are of paramount importance in the performance of photovoltaic devices.

2.2.3 Exciton splitting and polaron transport

As discussed above, once formed, excitons need to diffuse to a D-A interface in order to split, given that the average thermal energy is not enough for overcoming the exciton binding energy E_{bind}. When an exciton reaches the interface between the donor (D) and the acceptor (A) phases, the negative polaron is transferred to the acceptor and the overall exciton energy decreases. Due to deeper electron affinity of the acceptor, the negative polaron finds in the acceptor a more favorable energy state. In contrast, the shallower ionization potential of the donor makes the positive polaron to stay at the donor's HOMO. This lower-energy exciton in which each polaron is in either of the pohotoactive phases is known as *charge transfer exciton (CTE)* or *exciplex*. Subsequently, the two components of the exciton at the D-A interface experience electrical forces in opposite directions due to the strong local electric field present as a result of the sharp gradient between energy levels. If the electric forces associated to this energy HOMO/LUMO offset between D and A phases are large enough to overcome E_{bind}, the exciton splits and gives rise to two separated and opposedly charged polarons. The process of exciton dissociation is

described by the Braun-Onsager model.[45]

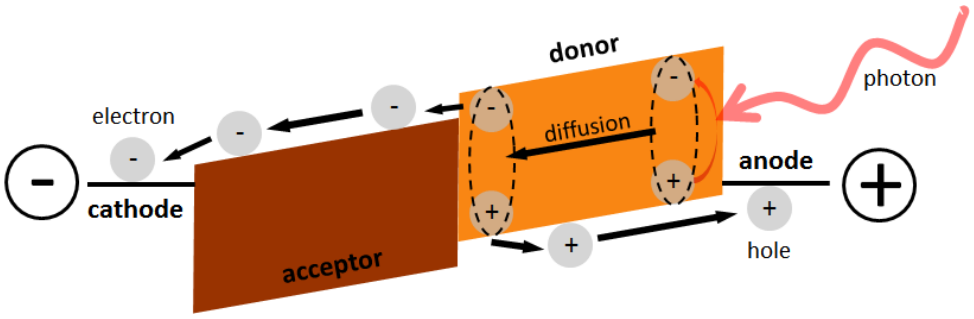

Figure 2.14: *Representation of the exciton generation, diffusion and splitting, and of the subsequent drift of charge carriers in an OSC heterojunction.*

Once the exciton is split, the two polarons live in the corresponding material phase of the photoactive layer, where they are majority carriers. The polarons need to be subsequently transported to their correspondent device electrodes. Hereby, the macroscopic transport is not only driven by diffusion, as it was the case for excitons, since they are electrically neutral. In contrast, polarons also respond to drift forces in the material, affecting the system differently depending on the spot of the current density-bias (J-V) curve at which we are at, i.e. depending on the bias the device is subjected to. The process of exciton diffusion, separation and polaron transport is schematically depicted in figure 2.14.

2.2.4 Organic solar cells: energy picture and device working principle

After the exciton is split into two independent polarons, they need to be transported throughout the device to the corresponding electrode or transport layer. Under operation of an OSC the prevailing transport-driving forces are different depending on the external bias. Thus, the different points of the J-V curve are associated with different transport-driving mechanisms and different energetic equilibrium.

When all the layers composing the OSC are stacked together and the device electrodes are connected through an external circuit, the device is at the *short-circuit* position of the J-V curve (figure 2.15a). In this scenario, the now externally connected OSC electrodes with different work functions align in order to keep one Fermi energy throughout the whole device. This creates an internal electric field E_{int} that makes the HOMO and LUMO energies to depend on the especific spatial position between the electrodes, making the energy bands to "look bent" when moving from anode to cathode (see figure 2.15a). As a result, the photogenerated charge carriers being released at the D-A interface are

transported by two forces acting simultaneously upon them. On the one hand, the electric field E_{int} generated by the energy alignment of the two electrodes and the D-A energetic offsets generates a drift current that drags the polarons in opposite directions, as they have opposed charges (see figure 2.15a). Moreover, the high concentration of polarons at the interfaces compared to the bulk of each of the two photoactive phases causes the polarons to move due to the strong gradient in chemical potential, thereby giving rise to a diffusion current. In short-circuit both current contributions point in the same direction and result macroscopically in a combined reverse current.

If now a bias starts to be applied in the forward direction, the electric field generated within the device by the external bias acts against E_{int}, flattening the energy bands. At some point the system reaches the *flat-band condition*, in which the difference in work function of the device electrodes is compensated by the external bias (figure 2.15b). In this situation, the drift current is suppressed, and the motion of the polarons is diffusion-driven. Thus, all charge carriers arriving to the device electrodes in flat-band conditions are photogenerated. In BHJ cells, since the diffusion current pushes the polarons away from the interfaces, but there is no force pointing them specifically towards the electrodes, the device is especially sensitive to recombination at this stage. In flat-band condition, the outcome of the competition between diffusion and recombination currents is of major importance determining the ideality factor, i.e. the "squareness" of the J-V curve and, hence, has a major impact on the device fill factor (FF).

Further appliance of forward bias leads to a bending of the energy bands in the reverse direction (figure 2.15c). From this point on, the drift and diffusion currents flow in opposite directions, reducing the current outcome continuously as the external bias grows. Moreover, the strong reverse bending of the energy bands narrows the energy barrier for the charge carriers in the electrodes to penetrate again in the photoactive medium and move dragged by the net electric field. Consequently, the charge carrier tunneling probability from the electrodes to the active layer increases, giving rise to an injection current of both, positive and negative polarons, that adds up to the drift current. For a certain bias conditions all the currents present are exactly compensated, giving a nil outbound current density. This position of the J-V curve is known as the *open-circuit*, and the bias at which this happens is called the *open-circuit voltage*.

Further discussion on how the mentioned stages affect the J-V curve and the associated parameters, as well as on how to use particular spots of the J-V curve to calculate e.g. efficiencies or characteristic resistances are provided in section 3.2.3.

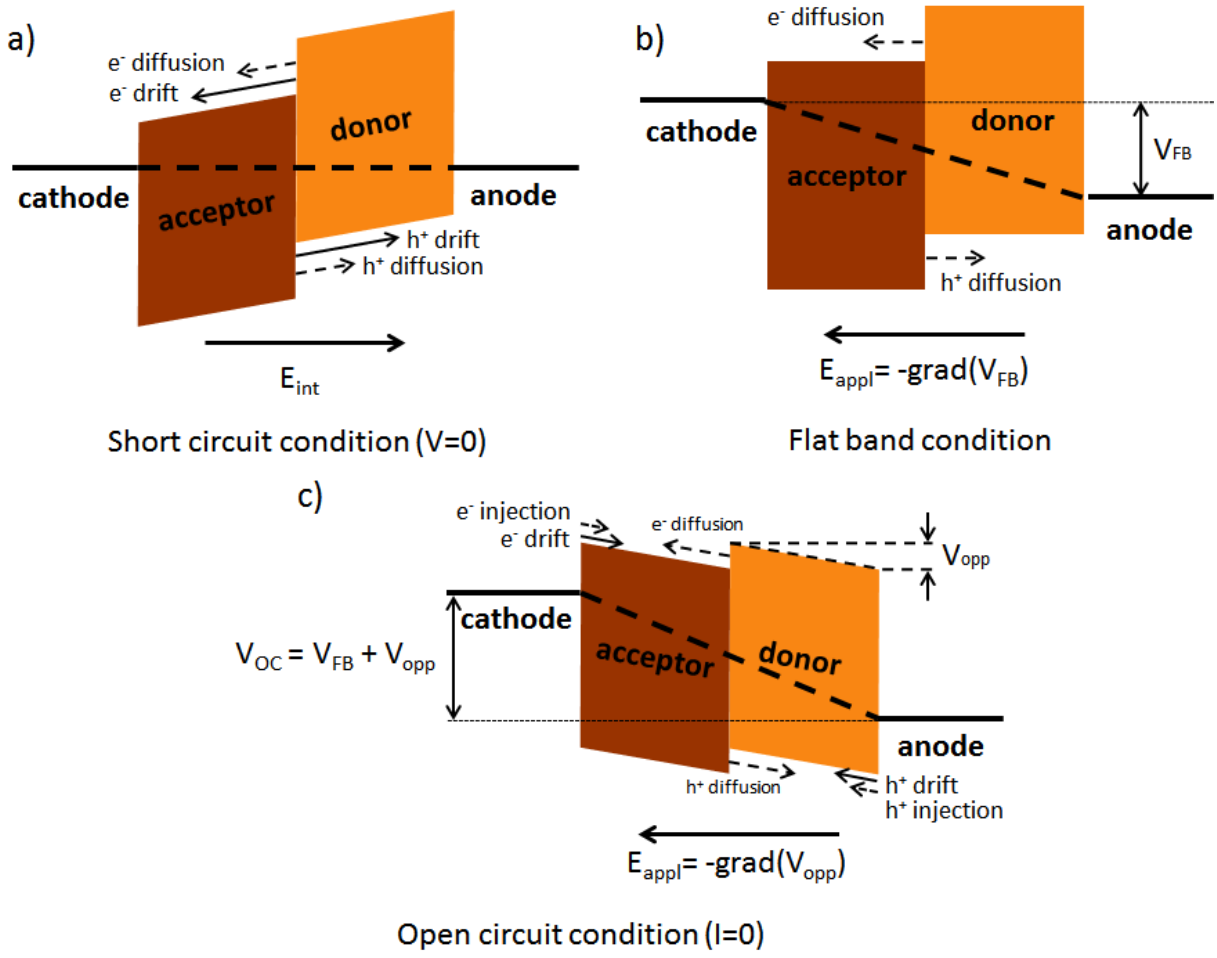

Figure 2.15: *Energy level diagrams of a bi-component OSC for different bias conditions. a) Short-circuit condition. b) Flat-band condition. c) Open-circuit condition.*

2.2.5 Organic solar cells: recombination and degradation

In order to have better understanding of the operation of OSCs, it is useful to shortly revise some of the factors that can hinder their performance. In this section we mostly focus on charge carrier recombination (either exciton decay or recombination of separated polarons). Different cases of charge carrier recombination are listed according to the nature of their occurrence or the region of the device in which they take place.

a. Decay of an exciton within its lifetime. In order to generate an electric current out of every photon absorbed by the material, the exciton needs to meet a D-A interface within its diffusion length. Otherwise the excited state relaxes back to the ground state and the energy provided by the photon is radiated away (figure 2.16a).

b. Recombination of dissociated or dissociating excitons. This type of recombination event is generally subdivided in two different cases. On the one hand, an exciton

that has arrived to the D-A interface starts the splitting process by forming a CTE. As a result, a polaron forms at each of the photoactive phases. If the rupture of the Coulomb bond between the two polarons by the electric field at the D-A interface is not fast enough, the polarons recombine. This recombination process is known as *field ionization of the geminate CTE*, or geminate recombination for short. On the other hand, two already separated polarons dragged through the device by diffusion or drift forces can hit a D-A interface and fortuitously meet a polaron of opposite charge. This second case is called *non-geminate recombination of the CTE* or just non-geminate recombination. Non-geminate recombination is a bi-molecular process, since it happens between already independent positive and negative polarons. Thus, as illumination increases, chances for polarons of pairing with polarons of opposite charge grow quadratically with polaron population, becoming an important recombination route. In contrast, in geminate recombination, exciplex separation has not yet occurred and each positive polaron is linked to its unique negative counterpart. Hence, geminate recombination grows linearly with polaron concentration. Both processes are represented by figure 2.16b.

c. Polaron spatial confinement. Especially in the case of BHJ active layers, some regions of photoactive material form islands lacking percolation pathways that ultimately connect them to an electrode or transport layer, hindering their extraction. Polarons accumulate in these islands, acting as recombination centers (figure 2.16c)

d. Polaron recombination at the wrong electrode. Strong diffusion forces can force polarons to move against the electric field, eventually making them reach the wrong electrode, recombining with an opposite charge carrier. Usually, polaron diffusion against the electric field is only significant when working close to flat-band conditions. Therefore, this mechanism has an influence on the diode region of the J-V fill factor, but does not significantly affect the curve throughout the entire bias range. Morevoer, this recombination path can be hindered to a large extent through the use of blocking layers (figure 2.16d). Further insight into this mechanism is provided in [46].

e. Trap states. Impurities, chemical and physical defects of the materials composing the OSC can induce the appearance of so-called trap states, i.e. states lying deep within the material band gap, spatially and energetically isolated, thereby hindering the hopping to neighboring states. This effect can usually happen between crystalline and amorphous polymer regions, at the D-A interface or at the organic-metal interface. This latter case is particularly known as *surface recombination* and detailed discussion can be found in [47].

The recombination mechanisms present in an OSC depend mainly on the materials chosen, the fabrication route and the BHJ morphology. In addition, the materials forming the OSC and the layer stack itself degrade during operation. Some degradation mechanisms regard the physical and or chemical deterioration of the device metallic contacts, such as the oxidation of the metallic cathode in non-inverted OSCs, or the fracture of brittle transport conducting-oxide layers, like indium-doped tin oxide (ITO. See section 4.2) in flexible devices.[48]

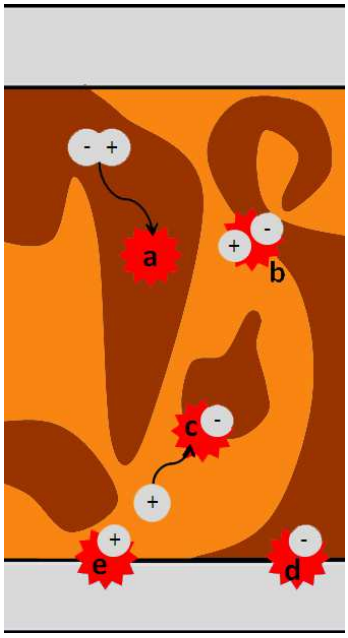

Figure 2.16: *Illustration of the main recombination mechanisms in a BHJ OSC. Electrodes are depicted in gray, donor material in orange and acceptor material in brown. The different listed types of recombination events are labelled from a to e.*

Other important degradation pathways are related to the chemical degradation of the materials composing the photoactive layer, often referred to as photobleaching. Polymer photobleaching is triggered by light, although atmospheric agents such as oxygen or water content can substantially accelerate the process. While P3HT is reported to be relatively resistant against each of these factors separately, their combination seem to have a significant worsening effect on the material degradation.[49–56] Photobleaching in P3HT leads to absorbtion-reducing effect, such as the reduction of the polymer conjugation length, or the detachment of light units, like C-S units or hexyl chains.[57]

Moreover, device aging is as well closely linked to physical degradation of the active layer. Especially under exposure to elevated temperatures and prolonged illuminations, physical degradation of the bulk heterojunction (BHJ) can appear in the form of D-A domain coarsening, or disintegration of polymer aggregates. Coarsening of the active layer morphology at the mesoscale was thoroughly investigated by Schaffer et al.[58], and the relation between crystallinity and device performance during aging experiments will be discussed in chapter 7. More comprehensive discussion on degradation mechanisms in OSCs is provided in references [59], [60] and [61].

2.3 Intersystem crossing tailoring

In this section we discuss the theoretical aspects of the core of this thesis. They mainly correspond to exciton spin configuration, its statistics, its effect on exciton lifetime and on the exciton diffusion length. Moreover, the theoretical background behind the ways explored in this thesis to approach its tuning are also discussed.

2.3.1 Intersystem crossing via spin-orbit coupling

As discussed previously in section 2.2.5, the need for excitons to reach a D-A interface in order to dissociate makes the exciton relaxation one of the main mechanisms of OSC performance loss. In order to improve that, many research efforts focus on the tuning of the D-A demixing morphology, trying to tune it down to the nanometer scale. This is approached via several pathways, including nanostructuring, solvent annealing, or use of solvent additives.[44,62–64] Nevertheless, tuning the BHJ nanomorphology at such small length scales is challenging, and the desired scales of the order of 10 nm are still very difficult to achieve in a tailored way. Hence, the reverse approach has been gaining interest, namely attempting to elongate its lifetime and, consequently, its diffusion length within the material.[65,66] This can be achieved by controlling the spin state of the photogenerated excitons within the device, as explained in the following.

The ground state of most molecules is electrically neutral and with all spins in the molecular orbitals paired, i.e. of singlet spin configuration. Thus, in systems where spin-orbit coupling is negligible, photon absorption can only excite singlet excitons. Upon absorption of a photon with energy in the visible range by an atom, the wavelength of the incoming radiation is significantly larger than the size of the atom itself. This makes the atom to experience a directional uniform electric field that induces a dipolar redistribution of charge. Hence, the process of absorption of visible light is usually treated in the frame of the *dipolar approximation*.

Calculation of the electric dipole matrix element yields transition probabilities depending on the n, l and m_l quantum numbers. Under the dipole approximation, the electric dipole matrix elements vanish under some conditions determined by the parity of the involved quantum numbers n, l and m_l. Consequently, calculation of the electric dipole matrix elements yields some constraints on the changes in quantum numbers that lead to allowed transitions, known as *selection rules*. In the particular case of the dipole approximation:

$$\Delta l = \pm 1 \qquad \Delta m_l = 0, \pm 1 \qquad \Delta m_s = 0 \tag{2.23}$$

In this case no operators appear that can change the spin. Therefore, the spin angular momentum must be conserved $\Delta m_s = 0$. This means that a dipolar electric field does not couple with magnetic moments. Thus, it implies that, upon absorption of a photon by an atom, which is mainly governed by the electric dipolar order of the electromagnetic field, a change or flip in electron spin is forbidden or, for real systems, very unlikely.

Similarly to the presented case of the hydrogen-like atom, a spin-flip is also forbidden upon photon absorption in chromophores of light elements (C, S, H), as it the case for most organic molecules. The hamiltonian under consideration in this case is not that of a single electron in an atom, but rather the hamiltonian of an exciton. Both positive and negative polarons are follow the Fermi statistics and have spin $s = 1/2$. Within the exciton, their spins are coupled via exchange interaction. Thus, the coupling of the two fermionic spins yields four exciton spin states, one singlet and three triplets.

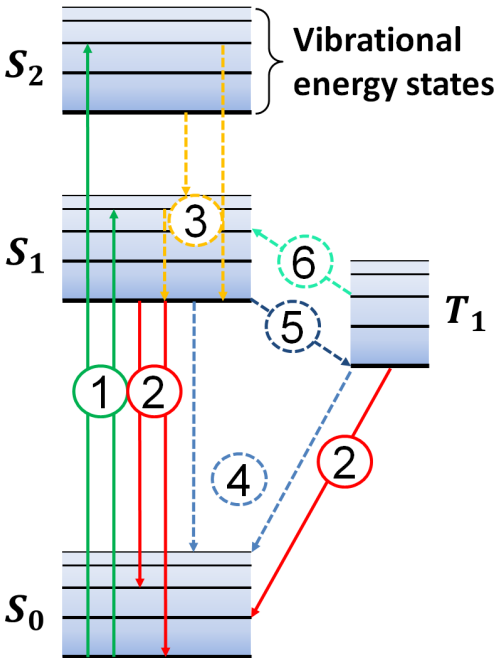

Figure 2.17: *Jablonski diagramm of the vibronic transitions in organic semiconductors. The label subindices indicate excited states, with S_0 as the ground state. The vibronic states are grouped laterally by spin multiplicity. 1) Absorption. 2) Fluorescene/phosphorescence. 3) Internal convertion and vibrational relaxation. 4) Non-radiative relaxation. 5) Intersystem Crossing. 6) Delayed Fluorescence (Intersystem crossing).*

According to the previously introduced spin selection rules, radiative recombination as a decay mechanism is only efficient (formally: electric dipole spin-allowed) if it starts from the singlet excited state. Thus, if triplet photogenerated excitons could be obtained, these would present longer lifetimes and, thus, longer diffusion lengths. Experimentally, singlet excitons present reported lifetimes in the range of 400 ps, corresponding to a diffusion length of less than 10 nm. In contrast, triplet excitons present much longer lifetimes, yielding effective diffusion lengths in the order of 100 nm.[67–71] When referring to materials or macromolecules, the highly efficient radiative recombination process that does not require spin flip is known as *fluorescence*, whilst *phosphorescence* accounts for the radiative decay from the triplet excited state to the singlet ground state. This decay mechanism requires a spin flip and is, therefore, much

less efficient, yielding excited states, like excitons, of much longer lifetimes. Other internal exciton conversion processes are of importance, such as *delayed fluorescence*. Delayed fluorescence corresponds to singlet excitons that decay on significantly longer timescales compared to prompt fluorescence, since they can elongate their average lifetime through the facilitated access to the triplet spin manifold, allowing back-and-forth conversions. These and other internal exciton processes are summarized in figure 2.17.

So far we have referred to electrons experiencing central nuclear potentials. In order to approach the real atomic or molecular energetic landscapes, in which the spin selection rules can be violated, we need to take into account several corrections that are applied to the system Hamiltonian and their mathematical and quantum-mechanical implementation. This is of special interest in the case of multielectronic atoms or, as it is our case, positive-negative polaron pairs in organic molecules. In multielectronic atoms, the actual Hamiltonian of the system reads:

$$\mathcal{H}_0 = \sum_{i=1}^{N}\left(-\frac{\hbar^2}{2m_e}\nabla_i^2\right) + \sum_{i=1}^{N}\left(-\frac{Ze^2}{r_i}\right) + \sum_{i<j}\frac{e^2}{r_{if}} \tag{2.24}$$

whereby $m_e = 9.1093826 \cdot 10^{-31}$ kg indicates the electron mass and $\hbar$ is the reduced Planck constant $\hbar = {}^{h}/_{2\pi} = 1.054571800 \cdot 10^{-31}\ {}^{\mathrm{Js}}/_{\mathrm{rad}}$. The Hamiltonian features a nuclear potential based on two components. The first term of the potential $\sum_{i=1}^{N}\left(-\frac{Ze^2}{r_i}\right)$ depicts the summed interaction between the electrons and the charged nuclei, whereas the second $\sum_{i<j}\frac{e^2}{r_{if}}$ indicates the electric interaction between electrons. Except for some special cases, the existence of the second term implies the non-centrality of the potential. Nevertheless, the real Hamiltonian 2.24 is in most of the cases not analytically solvable, and it is approximated. Indeed, a common approach is the *central field approximation*. We consider an effective potential:

$$V_{eff}(r) = -\frac{Ze^2}{r} + \mathcal{F}(r) \tag{2.25}$$

that includes the interaction with the nuclei and an effective function $\mathcal{F}(r)$, which accounts for the radial part of the interaction between electrons. Thus, the Hamiltonian of each electron within the system reads:

$$\mathcal{H}_{eff} = -\frac{\hbar^2}{2m_e}\nabla^2 + V_{eff}(r) \tag{2.26}$$

And the Hamiltonian of the system is composed of the sum of each individual electronic Hamiltonian:

$$\mathcal{H}_{IEA}(x_1, ..., x_n) = \sum_{i=1}^{N} \mathcal{H}_{eff}(x_i) \tag{2.27}$$

This is known as the *independent electron approximation (IEA)*, and the difference between $\mathcal{H}_{IEA}$ and the real Hamiltonian $\mathcal{H}_0$ is given by:

$$\mathcal{H}_{re} \equiv \mathcal{H}_0 - \mathcal{H}_{IEA} = \sum_{i=1}^{N} \left(-\frac{Ze^2}{r_i} \right) + \sum_{i<j} \frac{e^2}{r_{if}} - \sum_{i=1}^{N} V_{eff}(r_i) \tag{2.28}$$

$\mathcal{H}_{re}$ is the main correction to the central field approximation (electrostatic correction). The correction for spin-orbit interaction is also one the most important ones, and the formalism used for describing its contribution to the system Hamiltonian depends on the relative magnitudes of $\mathcal{H}_{re}$ and $\mathcal{H}_{S-O}$. The spin-orbit term of the Hamiltonian reads:

$$\mathcal{H}_{S-O} = \sum_{i=1}^{N} \xi(r_i) l_i \cdot s_i \qquad \xi(r_i) = \frac{\hbar^2}{2m_e^2 c^2} \frac{1}{r} \frac{dV}{dr} \tag{2.29}$$

where c is the speed of light in vacuum $c = 2.99792458 \cdot 10^8$ m/s. In light atoms or molecules, $\mathcal{H}_{re} >> \mathcal{H}_{S-O}$, i.e. the spin-orbit coupling, is a weak effect. Therefore, the system is described by the Schrödinger equation in the electrostaic approximation, with Hamiltonian $\mathcal{H}_{ES} = \mathcal{H}_{IEA} + \mathcal{H}_{re}$. In this case, since the Hamiltonian does not contain spin-orbit terms, it commutes separately with $\vec{L}^2 = \left(\sum_i \vec{l_i} \right)^2$ and $\vec{S}^2 = (\sum_i \vec{s_i})^2$, indicating that the total spin module $\vec{S}$ (singlet or triplet in the case of our polaron pair) is a constant of motion in the absence of external torque, magnetic fields, or multipolar transitions, i.e. stays unchanged. Afterwards, the contribution to the Hamiltonian of the spin-orbit interaction $\mathcal{H}_{S-O}$ is applied as a perturbation in the basis of the eigenstates of $\mathcal{H}_{ES}$. This approach is known as L-S coupling or Russell-Saunders approximation.

In heavy atoms the spin orbit interaction is much more important than the electrostatic correction ($\mathcal{H}_{S-O} >> \mathcal{H}_{re}$). Hence, the independent particle model Hamiltonian $\hat{\mathcal{H}}_{IEA}$ is constructed as the sum of the individual Hamiltonians, each of which include the contribution of the spin-orbit interaction between each electron's orbital and spin momenta:

$$\hat{\mathcal{H}}_{IEA} = \sum_{i=1}^{N} \mathcal{H}_{eff+ls}(x_i) \tag{2.30}$$

$$\mathcal{H}_{eff+ls}(x_i) = -\frac{\hbar^2}{2m_e} \nabla_i^2 + V_{eff}(r_i) + \xi(r_i) \vec{l_i} \cdot \vec{s_i} \tag{2.31}$$

In this case, the Hamiltonian depends explicitly on the product $\vec{l} \cdot \vec{s}$. Therefore, $\vec{L}^2$ and $\vec{S}^2$ do not commute with the Hamiltonian. The individual orbital and spin angular momenta are first coupled together, yielding an electronic total angular momentum ($\vec{j_i} = \vec{l_i} + \vec{s_i}$), afterwards combining in $\vec{J} = \sum_i \vec{j_i}$. The resulting scheme displays a total angular momentum $\vec{J}$, and $\vec{J}^2$ does commute with the Hamiltonian. In this scenario the once degenerated energy levels split according to their J value, each of them degenerated in M_J. Thus, the transition between electronic states with equal M_J (but not necesarily equal spin) can happen without energy cost. This is known as j-j coupling.

In other words, in heavy atoms the wave function spinors and spheric harmonics are mixed together due to the strong interaction between orbital and spin magnetic momenta. In this case, the distinction between triplet and singlet is significantly blurred. As an example, the energetic contribution of the L-S interaction to the Hamiltonian in monoelectronic atoms reads:

$$E_{S-O} = \frac{Z^4 \alpha^2}{2a_0^3 n^3} \left(\frac{j(j+1) - l(l+1) - s(s+1)}{2l(l+1/2)(l+1)} \right) \tag{2.32}$$

where $a_0 = \hbar/m_e c\alpha == 5.2917721067 \cdot 10^{-11}$ m is the Bohr Radius and α the fine structure constant $\alpha^{-1} = 137.035999139$. It can be seen how the strength of the interaction grows with Z^4, but only with n^3. Thus, as discussed before, the spin-orbit interaction is significantly larger for atoms that are located further down a specific column of the periodic table. Generally, pure L-S or pure j-j couplings are uncommon. Most atoms present intermediate couplings as combination of both schemes. Carbon (Z=6) is well described by L-S. Lead is well described by j-j (Z=82). The splitting of the ^1P and ^3P terms for the carbon group is depicted in figure 2.18 and shows the transition between coupling regimes. Te (Z=52), the heteroatom responsible for the spin-orbit coupling-enhancing molecule tested in this thesis, is expected to present a decently relaxed spin selection rule, thereby substantially enabling ISC.

2.3.2 Magnetic field-assisted intersystem crossing

According to the quantum mechanical model presented above, in absence of spin-orbit coupling, ISC is forbidden. It is worth noting that this is an approximation. For real systems based on light atoms, ISC is just an inefficient mechanism, yet the transition probability is not exactly zero. The reason is that the spin-orbit interaction is not zero and, moreover, other weaker contributions, like dipolar interactions, spin-spin coupling or hyperfine coupling, have been neglected in the presented mathematical treatment. In the following we discuss the influence of external magnetic fields that couple to polaronic

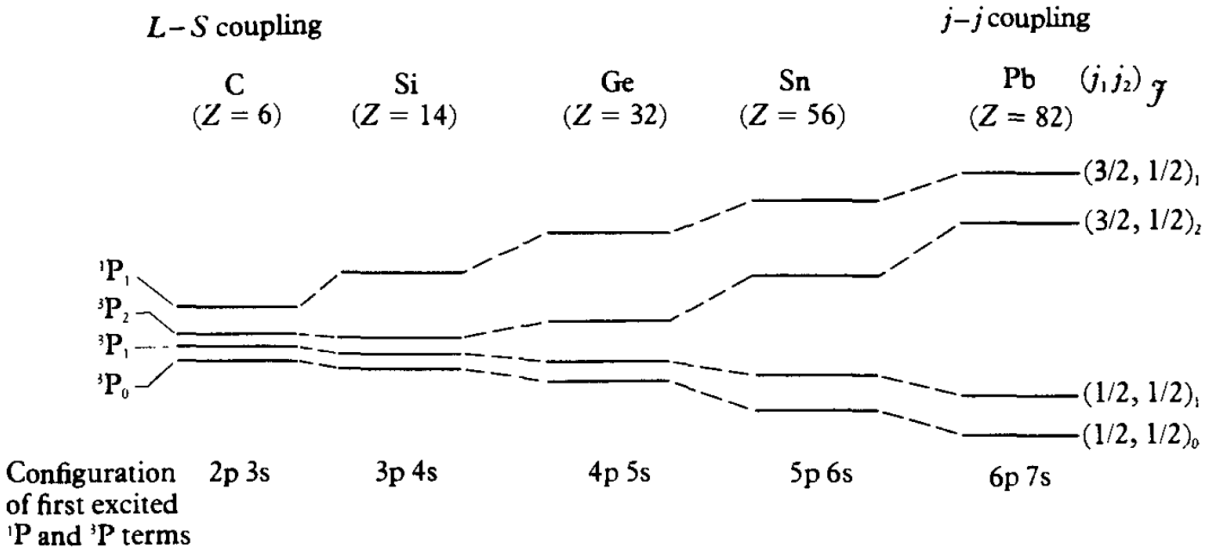

Figure 2.18: *Configuration of the* ^1P *and* ^3P *terms for the carbon group. Extracted from* [72]

spins and can favor ISC. Essentially, the argument is that significant inhomogeneities in magnetic flux density over the extent of an exciton can make the two polarons precess at different Larmor frequencies, thereby inducing a singlet-to-triplet spin rephasing.

The evolution of a single spin under an homogeneous external magnetic field $\vec{B}$ is described by the Schrödigner equation:

$$i\hbar\frac{\partial\psi}{\partial t} = -\frac{g\mu_B}{\hbar}\vec{B}\cdot\vec{S}\psi \tag{2.33}$$

where $\vec{S}$ is the electron spin $\vec{S} = \frac{\hbar}{2}\vec{\sigma}$ and $\vec{\sigma}$ the Pauli matrix. The solution to equation 2.33 is $\psi(t) = U(t)\psi_0$, where $U(t)$ is a rotation operator:

$$U(t) = \begin{pmatrix} cos(\omega_L t/2) + ib_z sin(\omega_L t/2) & (ib_x + b_y)sin(\omega_L t/2) \\ (ib_x - b_y)sin(\omega_L t/2) & cos(\omega_L t/2) - ib_z sin(\omega_L t/2) \end{pmatrix}$$

$\psi(t)$ describes a rotation of the electronic spin within the Bloch sphere about the direction of $\vec{B}$ with the Larmor frequency $\omega_L = \frac{g\mu_B|\vec{B}|}{\hbar}$, and being $b_i = \vec{B}\cdot\hat{i}/|\vec{B}|$ the projection of the magnetic field along each corresponding Cartesian direction. If now a pair of spins subjected to different magnetic fields is considered, the Hamiltonian reads (omitting higher-order contributions, such as spin-spin coupling $\vec{s_1}\cdot\vec{s_2}$):

$$\mathcal{H}_{mag} = -\frac{\mu_B g}{\hbar}\left(\vec{B_1}\cdot\vec{s_1} + \vec{B_2}\cdot\vec{s_2}\right) \tag{2.35}$$

which can be rewritten as:

$$\mathcal{H}_{mag} = -\frac{\mu_B g}{2\hbar}\left[\left(\vec{B_1}+\vec{B_2}\right)\cdot(\vec{s_1}+\vec{s_2}) + \left(\vec{B_1}-\vec{B_2}\right)\cdot(\vec{s_1}-\vec{s_2})\right] \tag{2.36}$$

Similarly to the case in the previous section 2.3.1 of strong spin-orbit coupling (j-j coupling), now coupled field-spin scalar products appear in the Hamiltonian. Therefore, $\vec{S} = \vec{s_1} + \vec{s_2}$ is not a motion constant. Regarding the probability of transition between singlet (S) and triplet (T), the interest lies on the second addend on the right side of equation 2.36 $\left(\vec{B_1}-\vec{B_2}\right)(\vec{s_1}-\vec{s_2})$. The reason is that the second addend has an antisymmetric contribution to the transition probability integral $\langle T|\mathcal{H}_{mag}|S\rangle$. Combined with the fact that T is spin-symmetric and S spin-antisymmetric, it follows that only the antisymmetric part of $\mathcal{H}_{mag}$ yields a non-zero contribution once integrated over the whole space (symmetric range).

The solution to the corresponding Schrödinger equation for two spins yields as well a rotating solution for each spin. Thus, the two-spin time evolution operator U_{Tot} is constructed as the direct product of each of the rotation operators:

$$U_{Tot} = U_1 \otimes U_2 \tag{2.37}$$

We start with an initial singlet spin configuration $|\psi_0\rangle = {}^1\!/\!\sqrt{2}(|\uparrow\downarrow\rangle - |\downarrow\uparrow\rangle)$ and construct the initial density matrix $\rho_0 = |\psi_0\rangle\langle\psi_0|$. Thus, we can calculate the time-dependent density matrix for the two-spin system:

$$\rho(t) = U_{Tot}\rho_0 U_{Tot}^{\dagger} \tag{2.38}$$

With this we are able to calculate the probability for the two-spin system to be in a singlet state as a function of time $P_S(t) = Tr[Q_S\rho(t)]$, where Q_S is the singlet projection operator $Q_S = {}^1\!/_4 - {}^{\vec{\sigma_1}\cdot\vec{\sigma_2}}\!/_4$. The resulting time-dependent singlet probability reads:

$$P_S(t) = \left[cos(\omega_{L1}t/2)cos(\omega_{L2}t/2) + \frac{\vec{B_1}\cdot\vec{B_2}}{|\vec{B_1}||\vec{B_2}|}sin(\omega_{L1}t/2)sin(\omega_{L2}t/2)\right]^2 \tag{2.39}$$

It can be seen from equation 2.39 that when $\vec{B_1} = \vec{B_2}$, $P_S(t) = 1$ for all times, indicating that an homogeneous magnetic field cannot induce spin rephasing and, consequently, ISC. In order for ISC to happen, the two spins need to accumulate a phase shift of 180 °. This happens in a time $\tau_{ISC} = {}^{\pi}\!/_{\Delta\omega_L}$. Using a semiclassical approach and taking into account that within an exciton the Landé g-factors of the positive and negative polarons differ, an ISC transition rate can be obtained:[73]

$$\tau_{ISC}^{-1} \approx \frac{\mu_B}{\pi\hbar}(B\Delta g + g\Delta B) \tag{2.40}$$

being g the Landé g-factor , and $\mu_B = 9.274009994 \cdot 10^{-24}$ J/T the Bohr magneton. This estimation of τ_{ISC} is accurate under the consideration that other magnetic coupling effects, like exchange interactions between polarons, spin-orbit coupling, or dipolar interactions, can be ignored. A treatment in full detail is provided in references [74] and [75].

Thus, in order to improve the ISC rate τ_{ISC}^{-1} it is important to implement a field gradient between the two components of the exciton, as opposed to coupling to an external constant field. In an exciton, the average rephasing rate τ_{ISC}^{-1}, displayed in equation 2.40, shows two main sources of phase shift. One of the sources scales with the difference in magnetic flux density for the two polarons ΔB, and the other comes from the intrinsic difference in Landé factors for positive and negative polarons Δg, and scales linearly with the field intensity. In organic molecules, Δg typically amounts to $\approx 10^{-3}$.[76] More specifically, positive and negative polarons present g-factors of 2.0017 and 1.9996 in P3HT and PCBM, respectively, according to light-induced and transient paramagnetic resonance experiments.[77,78] Thus, taking a $\Delta g \approx 10^{-3}$ and a flux density of 1 T, the obtained rephasing time is $3 \cdot 10^{-8}$ s.[73] Compared to the much shorter singlet exciton lifetimes in the range of 400 ps,[79] it follows that the term $\Delta g B$ alone is insufficient for significantly improving ISC in organic systems.

When looking for physical effects that can take advantage of the term $g\Delta B$ of equation 2.40, the main effects that can carry out the described spin rephasing are the Zeeman effect and the hyperfine couplings.[80–84] The hyperfine coupling is a weak effect and, in absence of external fields, it is the main responsible for the existing low rates of ISC, mixing the four possible spin states together.[73] The hyperfine interactions of the electrons with the surrounding nuclei can translate into flux densities of 0.1 to 3 mT, leading to mean transition times of $\tau_{ISC} = 10^{-6} - 10^{-8}$ s.[73,85] As in the previous case of the $\Delta g B$ term of equation 2.40, the resulting transition time due to hyperfine interaction is generally insufficient compared to the short singlet exciton lifetimes. In contrast, strong magnetic field gradients can be achieved with magnetic NPs. NPs cause strong field inhomogeneities over nanometric distances due to their round shape and small size. In particular, simple calculations show that the inhomogeneities in flux density produced by some magnetic nanostructures can surpass those created by hyperfine fields by up to two orders of magnitude.

Thus, a rephasing of a singlet spin pair into a triplet can be induced if the local field intensities (and, hence, the Larmor rotation frequencies) differ for each of the polarons forming the exciton. If the applied external field is deployed along the z-direction, the two

spins will display a relative phase shift, inducing a $S-T_0$ transition. Moreover, significant magnetic field components in the x- and y- directions can induce s_1 spins turning into s_2 and vice-versa, thereby enabling the $S-T_{+1}$ and $S-T_{-1}$ transitions. In particular, in systems like P3HT, triplet exciton energy lies below the singlet one (spin-spin, dipolar, exchange interactions considered).[86] Thus, the energy level splitting induced by the Zeeman effect caused by the field generated by the NPs shifts the T_{+1} upwards. Hereby, the energetic overlap between the S and the T_{+1} increases and, with it, the likelihood of $S-T_{+1}$ transition upon magnetic field components in the x- and y- directions.

2.4 X-ray scattering

Previously, the importance of the morphology of polymer phases and of its characterization in organic electronic devices, and specially in OSCs, has been discussed. Most imaging techniques allow morphology characterization only of the sample surface or offer only local information. Further characterization of the sample bulk often imply some degree of destruction or irreversible manipulation of the samples under investigation.

X-ray scattering allows by-passing of such setbacks, since they offer morphology information averaged over large sample areas at the same time that they non-destructively probe the whole sample volume. X-ray scattering techniques achieve Angs-trom resolutions, only comparable to some highly complex microscopy techniques, such as scanning tunneling microscopy (STM) or atomic force microscopy (AFM) in very special cases, such as $2D$ materials, highly ordered monolayer arrays, under high vacuum and with monoatomic-sharp measuring tips. Hereby, nevertheless, the problem of locality inherent to microscopy techniques cannot be overcome.

In this section we discuss the fundamental physics of elastic x-ray scattering. The presented techniques allow for characterization of structures ranging in size from few Angstroms to hundreds of nanometers both in bulk samples as well as in thin films. First, section 2.4.1 discusses fundamental aspects such as the definition of elastic scattering or the formation of scattering contrast. Afterwards, sections 2.4.2 and 2.4.3 present and discuss in detail the theoretical formalisms used for understanding the formation of scattering/diffraction patterns in both small and large outbound q regimes. Subsequently, the physical and mathematical treatment for scattering experiments suited for thin film investigation is presented. X-ray reflectivity as a specular technique is introduced in section 2.4.4 and subsection 2.4.5 will discuss the adaptation of the diffuse-scattering formalisms

introduced in section 2.4.2 and 2.4.3 to thin film geometry.

2.4.1 Basic concepts

X-ray scattering techniques reveal physical material information such as morphology, crystalline structure, or even dynamic phenomena, like diffusion coefficients or relaxation timescales.

In the present thesis, we focus on elastic scattering, in which the kinetic energy is conserved, i.e. in which the module of the scattering wave vectors $\vec{k_f}$ and $\vec{k_i}$ remains unchanged. The incident photons propagate with a wave vector $k_i = \left|\vec{k_i}\right| = \left|\vec{k_f}\right| = \frac{2\pi}{\lambda}$, where λ is the wavelength of the radiation. In its time-independent form, the electric field $\vec{E}(\vec{r})$ associated to the propagating radiation can be expressed as a plane wave:

$$\vec{E}(\vec{r}) = \vec{E_0} e^{i\vec{k_i}\cdot\vec{r}} \tag{2.41}$$

where $\vec{E_0}$ describes the amplitude and the polarization of the beam. The electric field expressed as in equation 2.41 is the solution of the time-independent wave equation, which mathematically can be expressed as a Helmholtz equation:

$$(\nabla^2 + k^2 n^2(\vec{r}))\vec{E}(\vec{r}) = 0 \tag{2.42}$$

where $n(\vec{r})$ is the refractive index of the medium in which the beam propagates. In attenuating media, the refractive index can be described with a real and an imaginary part, corresponding to the dispersion and absorption of the material, respectively. In the range of energies of x-rays and extreme ultraviolet, the refractive index deviates slightly from unity and has a real part smaller than one. Therefore, for x-rays, the complex refractive index is generally defined as:[87]

$$n(\vec{r}) = 1 - \delta(\vec{r}) + i\beta(\vec{r}) \tag{2.43}$$

where the dispersion and absorption parts are respectively given by:

$$\delta(\vec{r}) = \frac{\lambda^2}{2\pi} r_e \rho(\vec{r}) \sum_{j=1}^{N} \frac{f_j^0 + f_j'(E)}{Z} = \frac{\lambda^2}{2\pi}\rho(\vec{r}) \tag{2.44}$$

and:

$$\beta(\vec{r}) = \frac{\lambda^2}{2\pi} r_e \rho(\vec{r}) \sum_{j=1}^{N} \frac{f_j''(E)}{Z} = \frac{\lambda}{4\pi}\mu(\vec{r}) \tag{2.45}$$

being $r_e{=}e^2/(4\pi\varepsilon_0 mc^2)$ the Lorentz radius, Z the total electron number, and $f^{'}(E)$ and $f^{''}(E)$ the real and imaginary corrections to the atomic scattering length, respectively.[88] $\rho(\vec{r})$ indicates the electronic density distribution and $\mu(\vec{r})$ the mass absorption coefficient of the material under investigation.

In order for scattering to occur it is required that the beam experiences changes in the optical density of the medium. More specifically, the quantity with which the scattered intensity in an experiment scales is called *scattering contrast* and it is given by:

$$\Delta\delta^2 + \Delta\beta^2 = (\delta_1 - \delta_2)^2 + (\beta_1 - \beta_2)^2 \tag{2.46}$$

whereby the subscripts 1 and 2 denote the two phases between which scattering occurs.

2.4.2 Small-angle x-ray scattering

Greater insight into the contents of this section is provided in references [88] and [89].

In elastic scattering, incoming photons interact with strongly-bound electrons without experiencing any energy transfer. The electrons coherently oscillate with the frequency of the impinging radiation and the scattered intensity distribution is recorded on the detector. The distribution of scattered intensity is studied as a function of the momentum transfer $\vec{q}$ to which, for a particular experimental setup, a given spot on the detector corresponds to. In SAXS experiments, the momentum transfer on the detector plane measured from the direct beam $q_r = \sqrt{q_y^2 + q_z^2}$ relates to the outgoing radiation angle via:

$$q_r = \frac{4\pi}{\lambda} sin(\psi/2) \tag{2.47}$$

where ψ corresponds to the exit angle of the scattered radiation measured in relation to the incoming radiation. In the regime of hard x-rays the fundamental magnitude that summarizes the interaction between matter and radiation and describes the scattered intensity distribution is the *scattering cross section*. It essentially describes the likelihood of a scattering event for a given set of materials and radiation parameters, yielding as well the angular distribution of scattered intensity. We assume our system to contain N_p domains, each of them containing N_i nuclei. We can define the position of each atom in the material $\vec{r_{ij}}$ with respect to the center of the domain it belongs $\vec{r_{ij}} = \vec{R_i} + \vec{X_j}$, whereby $\vec{R_i}$ is the center of each domain. Thus, the cross section can be expressed as:

$$\frac{d\Sigma}{d\Omega}(\vec{q}) = \frac{1}{V} \left\langle \left| \sum_{i=1}^{N_p} exp\left(i\vec{q}\cdot\vec{R_i}\right) \sum_{j=1}^{N_i} b_{ij} exp\left(i\vec{q}\cdot\vec{X_j}\right) \right|^2 \right\rangle \tag{2.48}$$

where V is the scattering volume and b_{ij} the coherent scattering length of the jth atom in the ith domain. The second summation over j on the right member of equation 2.48 represents the sum of the contributions of all N_j atoms in a domain i, and it allows us to define a property of each domain:

$$F_i(\vec{q}) = \sum_{j=1}^{N_i} b_{ij} exp\left(i\vec{q}\cdot\vec{X_j}\right) \tag{2.49}$$

Equation 2.49 is called the *form factor* of the domain. As we can see, this factor describes each individual domain in the sample, since it is constructed from each of the N_i individual atoms within one domain, the scattering length and the respective configuration of the atoms within the domain. In its integral form:

$$F_i(\vec{q}) = \int_i d\vec{r}(\rho_i(\vec{r}) - \rho_m) exp\left(i\vec{q}\cdot\vec{r}\right) \tag{2.50}$$

where $\rho_i(\vec{r})$ is the *scattering length density (SLD)* of the domain, ρ_m the SLD of the medium, and the integral extends to the volume of the ith domain. $\rho_i(\vec{r}) - \rho_m$ corresponds to the above-mentioned scattering contrast, in our case in which light absorption is neglected. The form factor, thus, accounts for domain properties related to its shape, size and composition, and its contribution to the scattering cross section scales with the difference in SLD between the domain and its environment. If we now re-write the cross section by inserting equation 2.49 in 2.48, we obtain:

$$\frac{d\Sigma}{d\Omega}(\vec{q}) = \frac{1}{V}\left\langle \sum_{i=1}^{N_p}\sum_{i'=1}^{N_p} F_{i'}^*(\vec{q})F_i(\vec{q}) exp\left(i\vec{q}\cdot(\vec{R_i} - \vec{R_{i'}})\right)\right\rangle \tag{2.51}$$

where now the summations cover all possible pairs of domains i and i' within the sample. Hereby, $F_{i'}^*(\vec{q})F_i(\vec{q}) = F(\vec{q})^2$, and the remaining contribution to the cross section in equation 2.51:

$$S(\vec{q}) = \frac{1}{N_p}\left\langle \sum_{i=1}^{N_p}\sum_{i'=1}^{N_p} exp\left(i\vec{q}\cdot(\vec{R_i} - \vec{R_{i'}})\right)\right\rangle \tag{2.52}$$

is a factor that accounts for the relative distances and arrangements between domains R_i and $R_{i'}$. This factor is known as the *structure factor* and it is the second main player in the description of the formation of scattering patterns. Thus, the scattering cross section can be expressed as a combination of the squared form factor $F(\vec{q})^2$, the density of scattering domains N_p/V and the structure factor $S(\vec{q})$:

$$\frac{d\Sigma}{d\Omega}(\vec{q}) = \frac{N_p}{V}F(\vec{q})^2 S(\vec{q}) \tag{2.53}$$

2.4.2.1 Polydispersity for characterization of organic systems

Organic systems, such as polymers, often correspond to systems in which scattering domains as well as their arrangement are irregular. Theferore, the main parameters describing the system introduced above need to be treated as distributions with certain deviations from their mean values. If we consider a system with irregularities or a distribution of form factors, equation 2.51 is not evaluated according to the product $F_{i'}^{*}(\vec{q})F_i(\vec{q})$ but according to its expected value. Therefore:

$$\frac{d\Sigma}{d\Omega}(\vec{q}) = \frac{1}{V}\left\langle \sum_{i=1}^{N_p}\sum_{i'=1}^{N_p} \langle F_{i'}^{*}(\vec{q})F_i(\vec{q})\rangle exp\left(i\vec{q}\cdot(\vec{R_i}-\vec{R_{i'}})\right)\right\rangle \tag{2.54}$$

where the expected value $\langle F_{i'}^{*}(\vec{q})F_i(\vec{q})\rangle$ can be expressed as:

$$\langle F_{i'}^{*}(\vec{q})F_i(\vec{q})\rangle = \left[\left\langle|F(\vec{q})|^2\right\rangle - |\langle F(\vec{q})\rangle|^2\right]\delta_{ii'} + |\langle F(\vec{q})\rangle|^2 \tag{2.55}$$

If now equation 2.55 is introduced in equation 2.54 we obtain an expression for the cross section:

$$\frac{d\Sigma}{d\Omega}(\vec{q}) = \frac{N_p}{V}\left[\left\langle|F(\vec{q})|^2\right\rangle - |\langle F(\vec{q})\rangle|^2\right] + \frac{N_p}{V}|\langle F(\vec{q})\rangle|^2 S(\vec{q}) \tag{2.56}$$

that differs from the equation 2.53 not only in the fact that the squared form factor is replaced by the square of its expected value, but moreover an additional term independent of the structure factor appears, contributing to the cross section with increasing polydispersity. Generally, organic systems do not grant the condition $|\langle F(\vec{q})\rangle|^2 = \left\langle|F(\vec{q})|^2\right\rangle$. Thus, a new parameter $\beta(\vec{q}) = |\langle F(\vec{q})\rangle|^2 / \left\langle|F(\vec{q})|^2\right\rangle$ is defined to tabulate the deviation of the system from ideality. Hereby, we can re-write the cross section as:

$$\frac{d\Sigma}{d\Omega}(\vec{q}) = \frac{N_p}{V}\left\langle|F(\vec{q})|^2\right\rangle\left[1-\beta(\vec{q})+\beta(\vec{q})S(\vec{q})\right] = \frac{N_p}{V}\left\langle|F(\vec{q})|^2\right\rangle\left[1+\beta(\vec{q})\left(S(\vec{q})-1\right)\right] \tag{2.57}$$

whereby $P(\vec{q}) \equiv \left\langle|F(\vec{q})|^2\right\rangle$ is the new form factor (*decoupling approximation*[90]) and $S'(\vec{q}) \equiv 1+\beta(\vec{q})\left(S(\vec{q})-1\right)$ is an apparent interparticle structure factor. Thus, in the cross section described for the polydisperse system the domain morphology-related term is not the squared form factor, but its expected value, given the fact that in polydisperse systems $F(\vec{q})$ becomes a distribution. The factor $\beta(\vec{q})$, initially defined for parametrizing the deviation from ideality of the form factor, enters the structure factor of the polydisperse system as a q-dependent term between 0 and 1 that dumps the oscillations of the "true" structure factor. Note that the apparent structure factor $S'(\vec{q}) = 1+\beta(\vec{q})\left(S(\vec{q})-1\right)$ becomes the regular $S(\vec{q})$ of the monodisperse system in case $\beta(\vec{q}) = 1$, i.e. in case

$\left\langle |F(\vec{q})|^2 \right\rangle = |\langle F(\vec{q}) \rangle|^2$. Finally, the cross section for polydisperse systems can be summarized:

$$\frac{d\Sigma}{d\Omega}(\vec{q}) = \frac{N_p}{V} P(\vec{q}) S'(\vec{q}) \tag{2.58}$$

in analogy to the monodisperse example. In this case, the differences between $\left\langle |F(\vec{q})|^2 \right\rangle$ and $|\langle F(\vec{q}) \rangle|^2$ arise from the variance of the distribution $f(\vec{r})$ and their calculations are given by:

$$\left\langle |F(\vec{q})|^2 \right\rangle = \int_{V_\infty} |F(\vec{q}, \vec{r})|^2 \, f(\vec{r}) d\vec{r} \tag{2.59}$$

$$|\langle F(\vec{q}) \rangle|^2 = \left| \int_{V_\infty} F(\vec{q}, \vec{r}) f(\vec{r}) d\vec{r} \right|^2 \tag{2.60}$$

whereby the integrals, extended to the whole space, equal in case $f(\vec{r}) = 1$, in accordance to the Cauchy-Schwarz inequality.

The discussed general formalism holds for characterizing many scales of our sample. Small and Wide-Angle X-ray Scattering (SAXS or WAXS) refer to the broadness range of this exit angle. SAXS is used for studying the morphology of samples in the poorly ordered mesoscale (few to few hundreds of nm), where domain sizes are broadly distributed and the arrangement among them is usually described with paracrystalline lattices. In our case, samples characterized with SAXS were fitted with the form factor of a spherical domain with a Gaussian size distribution, meaning:

$$f(\vec{r}) = f(R) = \frac{1}{\sigma\sqrt{2\pi}} exp\left(-\frac{(R - R_{avg})^2}{2\sigma^2} \right) \tag{2.61}$$

being R_{avg} the mean domain size of the distribution. Given the highly unordered nature of oligomeric and polymeric samples, data fitting was done in the limit of low domain concentration, whereby the structure factor $S'(\vec{q}) = S(\vec{q}) = 1$ (*Guinier limit*).

2.4.3 Wide-angle x-ray scattering

The contents of this section are discussed in greater detail in references [91] and [92].

WAXS, due to its experimental arrangement, enables study of samples in the sub-nanometer scale, accessing the aggregated polymer regions, where the degree of molecular order is generally higher and the scattering is dominated by the periodicity of the lattice. In these regions, polymers are sufficiently ordered in their packing for featuring lattice distances and crystalline grain sizes. Thus, the presented WAXS formalism applies to systems with

translational symmetry forming a lattice. For such systems, only specific $\vec{q}$ vectors complying with certain conditions of the lattice yield scattering peaks, being its amplitude zero for all other values. The complete set of wave vectors that yield scattering is known as the reciprocal lattice, which is the Fourier transformation of the direct (real-space) crystal lattice.

Crystals in real space can be described using their translational symmetry. In the reciprocal space this is done by the *primitive vectors of the reciprocal lattice*, $\vec{b_i}$, $\vec{b_j}$ and $\vec{b_k}$. With this set of primitive vectors, we can move to any node of the reciprocal lattice by building a vector $\vec{G}$ so that $\vec{G} = h\vec{b_i} + k\vec{b_j} + l\vec{b_k}$, where h,k and l are the integer *Miller indices*. $\vec{G}$ vectors are the reciprocal lattice vectors and their module is $|\vec{G}| = 2\pi n/d_{hkl}$, being d_{hkl} the distance between scattering planes along the (h,k,l) direction.

Upon elastic scattering the direction of the wave vector of the incoming x-rays changes and gives rise to a momentum transfer vector $\vec{\Delta k} = \vec{k'} - \vec{k}$. In order for constructive interference to occur and, thus, to obtain a Bragg Peak, $\vec{\Delta k}$ must coincide with a reciprocal lattice vector $\vec{G}$. This is generally referred to as *Laue condition* or diffraction condition.

In a crystal, the incoming and the scattered beams acquire upon scattering a certain difference in optical path that may or may not give rise to constructive interference. We can generally calculate the amplitude of the scattered wave F via:

$$F = \int_V dV \rho(\vec{r}) exp\left(i(\vec{k} - \vec{k'}) \cdot \vec{r}\right) = \int_V dV \rho(\vec{r}) exp\left(i\vec{\Delta k} \cdot \vec{r}\right) \tag{2.62}$$

where the concentration of electrons $\rho(\vec{r}) = \sum_{\vec{G}} \rho_{\vec{G}} exp\left(i\vec{G} \cdot \vec{r}\right)$ is a periodic function with the periodicity of the lattice. By plugging $\rho(\vec{r})$ into equation 2.62 the scattering amplitude becomes:

$$F = \sum_{\vec{G}} \int_V dV \rho_{\vec{G}} exp\left(i(\vec{G} - \vec{\Delta k}) \cdot \vec{r}\right) \tag{2.63}$$

where the integral extends to the whole scattering volume. $exp\left(i(\vec{G} - \vec{\Delta k}) \cdot \vec{r}\right)$ is a phasor that cancels the integral for $\vec{\Delta k}$ vectors significantly different from $\vec{G}$. For $\vec{\Delta k} = \vec{G} \Rightarrow F = V\rho_{\vec{G}}$, resembling the Laue condition. By taking equation 2.62 and setting $\vec{\Delta k} = \vec{G}$, the amplitude of the scattered wave becomes:

$$F = \int_V dV \rho(\vec{r}) exp\left(-i\vec{\Delta k} \cdot \vec{r}\right) = N \int_{V_{cell}} dV \rho(\vec{r}) exp\left(-i\vec{G} \cdot \vec{r}\right) = NS_{\vec{G}} \tag{2.64}$$

where $S_{\vec{G}} = \int_{V_{cell}} dV\rho(\vec{r})exp\left(-i\vec{G}\cdot\vec{r}\right)$ is called the *structure factor* and it depicts the contribution to the scattering amplitude of one cell of the crystal.

Within the unit cell, the electronic distribution at each point $\vec{r}$ can be understood as the sum of the contributions of each jth atom within the cell to $\vec{r}$. Therefore, we can express the electronic density as $\rho(\vec{r}) = \sum_j n_j(\vec{r}-\vec{r_j})$. By introducing this into the expression for structure factor we obtain:

$$\begin{aligned} S_{\vec{G}} &= \sum_j \int_{V_{cell}} dV n_j(\vec{r}-\vec{r_j})exp\left(-i\vec{G}\cdot\vec{r}\right) \\ &= \sum_j exp\left(-i\vec{G}\cdot\vec{r_j}\right)\int_{V_{cell}} dV n_j(\vec{r}-\vec{r_j})exp\left(-i\vec{G}\cdot(\vec{r}-\vec{r_j})\right) \end{aligned} \tag{2.65}$$

The *atomic form factor* is defined as the Fourier transform of the electron density:

$$f_j = \int_{V_{cell}} dV n_j(\vec{r}-\vec{r_j})exp\left(-i\vec{G}\cdot(\vec{r}-\vec{r_j})\right) \tag{2.66}$$

It describes the electron contributions of each atom in the unit cell to each of its inner points. Therefore, the structure factor can be written:

$$S_{\vec{G}} = \sum_j f_j exp\left(-i\vec{G}\cdot\vec{r_j}\right) \tag{2.67}$$

As it was the case in section 2.4.2, it can be seen how the form factor f_j is a property of the scattering object. In this case it is a combination of the atomic properties of the scattering atoms within the unit cell. In contrast, in the structure factor the geometric arrangement of the atoms within the cell plays as well a role in shaping the scattering intensity distribution.

In general the Laue condition can be expressed as $\Delta\vec{k} = \vec{G} \Rightarrow \vec{k} + \vec{G} = \vec{k'}$, whereby for elastic scattering $|\vec{k}| = |\vec{k'}|$. By squaring each side of the equality, we obtain $|\vec{k}|^2 + |\vec{G}|^2 + 2\vec{k}\cdot\vec{G} = |\vec{k}|^2$. With it we obtain another expression for the Laue condition with a simpler geometric interpretation (depicted in figure 2.19a):

$$2\vec{k}\cdot\vec{G} = |\vec{G}|^2 \tag{2.68}$$

This new form of the Laue condition can be re-written as $\vec{k}\cdot(\vec{G}/2) = |\vec{G}/2|^2$, which means that every wave vector $\vec{k}$ that goes from the origin pointing to any point of a bisecting plane of any vector of the reciprocal lattice $\vec{G}$ satisfies the Laue condition. We can further develop equation 2.68 by explicitly calculating the dot product:

$$\frac{1}{2}|\vec{k}||\vec{G}|cos(\phi) = \frac{1}{4}|\vec{G}|^2 \Rightarrow |\vec{k}|cos(\phi) = \frac{1}{2}|\vec{G}| \tag{2.69}$$

By recalling that $|\vec{G}| = \frac{2\pi n}{d_{hkl}}$ and $|\vec{k}| = \frac{2\pi}{\lambda}$, and by taking $\theta = 90° - \phi$ we obtain:

$$2d_{hkl}sin(\theta) = n\lambda \tag{2.70}$$

Equation 2.70 is known as *Bragg's law*, and it predicts the positions of the scattering maxima for a particular crystalline family (h,k,l). As mentioned before, the difference in the directions of the incoming and the scattered beams introduces a certain difference in the optical path $\Delta\lambda$ between different regions of the beam's wavefront. Bragg's law establishes that when $\Delta\lambda$ is a multiple of the wavelength, constructive interference occurs. A schematic depiction of Bragg's law is presented in figure 2.19b. In the analysis of scattering data, Bragg's law is used in its q-form (by introducing equation 2.47 in 2.70) for reading out the lattice distances of the diffracting crystalline families.

$$d_{hkl} = \frac{2\pi n}{q} \tag{2.71}$$

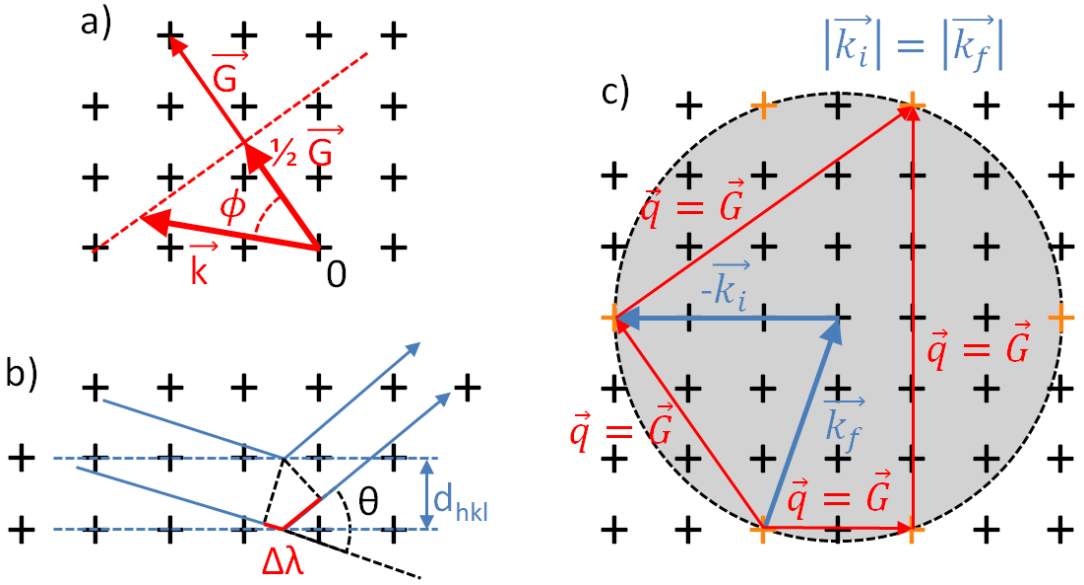

Figure 2.19: *a) Every wave vector going from the origin to any point of the bisecting plane of a vector of the reciprocal lattice satisfies the diffraction condition (reciprocal space. See equation 2.69). b) Schematic depiction of the Bragg's law (real space). The incoming beam scatters at a plane (h, k, l) with an angle θ. The optical path difference between two regions of the beam $\Delta\lambda$ is highlighted in red. c) Construction of the Ewald's Sphere (reciprocal space). Red momentum vectors satisfy the Laue condition.*

The elastic nature of the scattering $|\vec{k_i}| = |\vec{k_f}|$ allows us to define a sphere, called the *Ewald's sphere*, within which every single possible pair of vectors $|\vec{k_i}|$ and $|\vec{k_f}|$ of equal module in the reciprocal lattice are inscribed (see figure 2.19c). By taking their difference,

which equals to the momentum transfer $\vec{q} = \vec{k_f} - \vec{k_i} = \vec{G}$, we define the set of all accessible momentum transfers with a given wavelength λ. All these vectors $\vec{q}$ have their start and their end at some point of the sphere's surface. However, the Laue condition establishes that only those $\vec{q}$ that coincide with a vector of the reciprocal lattice $\vec{G}$ will indeed yield scattering (highlighted in orange in the example of figure 2.19c). This allows us to reformulate the diffraction condition by saying that "only the intersection between the Ewald's sphere and the reciprocal lattice is resolvable for a given setup". Thus, the $\vec{q}$ vectors satisfying the diffraction condition $\vec{q} = \vec{G}$ will generate a Bragg peak, in accordance with equations 2.71 and 2.67.

2.4.3.1 Finite crystallite size in polymer systems

In contrast to a theoretical infinite crystal or to macroscopic monocrystalline materials, for which the above-discussed formalism would determine at which $\vec{q}$-position and with which intensity would infinitely sharp Bragg peaks appear, in organic materials, like polymers, which are just semi-crystalline and feature crystallites of few nanometers size, Bragg peaks present a certain broadness. This allows for estimation of the crystallite size L with aid of the Scherrer equation:

$$L_{hkl} = \frac{K\lambda}{\beta_{\theta,hkl} cos\theta_{hkl}} \tag{2.72}$$

where L is the mean size of ordered crystalline domain and K is the so-called *shape factor* that accounts for the degree of spherical symmetry of the crystallites. θ_{hkl} is the Bragg angle in radians for a given family (h, k, l) and $\beta_{\theta,hkl}$ is the corresponding peak broadening at half intensity (FWHM) after subtracting the instrumental broadening. In its q-form, the Scherrer equation reads:

$$L_{hkl} = \frac{2\pi K}{\beta_{q,hkl}} \tag{2.73}$$

where $\beta_{,hkl}$ is the FWHM expressed in inverse distance. It is worth noting that the Scherrer equation reveals a lower limit of L_{hkl}. More comprehensive treatment of diffraction in amorphous systems and imperfect crystals can be found in the literature.[93]

2.4.4 Reflectivity

As discussed in section 2.4.1, in the x-ray regime the real part of the refractive index for all materials is smaller than one. Thus, taking into account that the refractive index of air (or vacumm) is exactly one, it follows, according to Snell's law, that there is an angle of incidence below which the beam will become totally reflected, thereby enabling the total

reflection from air to a material, known as *total external reflection*. This contrasts with the total internal reflection with visible light, in which the reflection only occurs going from a medium into vacuum or air. According to Snell's law:

$$cos(\alpha_i) = n_{mat} cos(\alpha_t) \tag{2.74}$$

being α_i and α_t the incident and transmitted angles with respect to the media interface, respectively. n_{mat} is the optical density of the probed material. For an incident angle equal to the critical angle of the material an evanescent wave parallel to the surface of the material is formed, ergo $cos(\alpha_{t,crit}) = 1$. Therefore:

$$cos(\alpha_c) = n_{mat} \tag{2.75}$$

with α_c as the critical angle of the material and $n_{mat} = 1 - \delta < 1$. By developing $cos(\alpha_c)$ in Taylor series:

$$cos(\alpha_c) = 1 - \frac{\alpha_c^2}{2} + ... = 1 - \delta \tag{2.76}$$

It follows the approximation of the critical angle α_c:

$$\alpha_c \approx \sqrt{2\delta} \tag{2.77}$$

The total external reflection in x-rays is very important because it enables the study of polymer thin films in reflection configuration. An important application of such a physical property is the technique x-ray reflectivity (XRR).

XRR is a specular scattering technique ($\alpha_i = \alpha_f$) and the beam is always in the vertical plane formed by the incident beam and the direction perpendicular to the sample surface ($\psi = 0$). Thus, the q-vector of the recorded signal contains exclusively vertical component ($|\vec{q}| = q_z$), given by:[94]

$$q_z = \frac{4\pi}{\lambda} sin(\alpha_i) \tag{2.78}$$

Therefore, the information accessible with this technique corresponds to structures along the vertical direction of the sample, i.e. perpendicular to the sample plane, such as film thickness, roughness or vertical composition gradient.

The incident beam arrives at the interface between two phases, e.g. air and polymer film. It becomes partially reflected and partially transmitted. The amplitudes of the transmitted and reflected parts of the electromagnetic wave can be calculated via the Fresnel coefficients:[87]

$$t^F = \frac{2sin(\alpha_i)}{sin(\alpha_i) + \sqrt{n^2 - cos(\alpha_i)^2}} \tag{2.79}$$

$$r^F = \frac{sin(\alpha_i) - \sqrt{n^2 - cos(\alpha_i)^2}}{sin(\alpha_i) + \sqrt{n^2 - cos(\alpha_i)^2}} \tag{2.80}$$

The reflectivity is defined as $R_F = \left|r^F\right|^2$ and can be expressed as:[87]

$$R_F = \frac{(\alpha_i - p_+)^2 + p_-^2}{(\alpha_i + p_+)^2 + p_-^2} \tag{2.81}$$

whereby:

$$p_\pm^2 = \frac{1}{2}\left(\sqrt{(\alpha_i^2 - \alpha_c^2)^2 + 4\beta^2} \pm (\alpha_i^2 - \alpha_c^2)\right) \tag{2.82}$$

Modeling of films in XRR requires consideration of at least two interfaces, the air-film and the film-substrate interface, which will according to their respective properties yield an overall reflectivity pattern, featuring so-called Kiessig fringes that allow for thickness determination.[95] In practice, however, films peresent certain vertical composition inhomogeneities or gradients, and finer description of polymer films requires modeling of a stack of several layers with optical densities $n_j(z)$ and thicknesses d_j. Parrat developed a recursive formalism featuring these calculations, in which each interface of the stack is characterized by the ratio between reflectivity and transmittivity as calculated for each layer from the Fresnel coefficients $X_j = R_j/T_j$:[96]

$$X_j = \frac{R_j}{T_j} = exp\left(-2ik_{z,j}z_j\right)\frac{r_{j,j+1} + X_{j+1}\exp\left(2ik_{z,j+1}z_j\right)}{1 + r_{j,j+1}X_{j+1}\exp\left(2ik_{z,j+1}z_j\right)} \tag{2.83}$$

whereby:

$$r_{j,j+1} = \frac{k_{z,j} - k_{z,j+1}}{k_{z,j} + k_{z,j+1}} \tag{2.84}$$

being $k_{z,j} = k(n_j^2 - cos(\alpha_i)^2)^{1/2}$ the z-component of the wave vector in the layer j. Further approximation in the description to real systems includes taking into account the roughness between two layers j and $j+1$, parametrized as:

$$\sigma_{rms} = \sqrt{\frac{1}{N_{\sigma_{rms}}}\sum_{i=1}^{N_{\sigma_{rms}}}\Delta z_i^2} \tag{2.85}$$

The effect of the roughness of each interface is accounted in the model by adding a correction in the calculation of the optical density of each layer, which ultimately results

in a correction in the Fresnel reflection coefficient, and thus in the reflectivity. This correction function is known as the Névot-Croce factor, and it is described in the literature in greater detail.[97]

2.4.5 Grazing-incidence x-ray scattering

In the previous sections we have introduced diffuse scattering techniques that allow characterization of bulk samples in transmission, as well as a specular technique suited for thin films that allows sample study along the vertical direction (XRR, section 2.4.4). Other techniques that offer comprehensive thin film characterization present features of both of the already presented types.[94,98,99] Amongst the most powerful, grazing-incidence x-ray scattering (GIXS) techniques have proven to be best suited for thin films. They are diffuse scattering techniques, like those presented in sections 2.4.2 and 2.4.3, that scatter on thin film-samples by impinging with an x-ray beam under very shallow angles, taking advantage of the introduced total external reflection phenomenon present in x-ray energies. Moreover, small incident angles ensure large footprints on the sample, granting statistic data averaged over large sample areas, as well as they provide high-intensity signals due to large sample scattering volume despite nanometric film thicknesses. The theoretical background for GIXS is analogous to that discussed in sections 2.4.2 and 2.4.3 in terms of generation of a contrast, definition of a scattering cross section, as well as regarding the different treatments associated to semi-ordered scattering phases and highly crystalline regions, or the extra considerations added for polydisperse or partially crystalline systems. However, in contrast to the bulk samples studied in SAXS and WAXS (sections 2.4.2 and 2.4.3) the thin film fashion of GISAXS and GIWAXS samples will make the theoretical formalisms to require of some elements of XRR (section 2.4.4), like the concepts of critical angle of the Fresnel coefficients.

In GIXS experiments, the isotropy and the spherical symmetry observed for SAXS and WAXS is broken due to the presence of a preferential direction introduced by the plane of the sample substrate. This symmetry breaker allows, in general, differentiated study of patterns and features parallel and perpendicular to the plane of the sample substrate, as well as it allows study of the orientation of sample elements with respect to it. In grazing-incidence configuration, the expression that establishes the relation between q-values and the real-space exit angles reads:

$$\vec{q} = \frac{2\pi}{\lambda} \begin{pmatrix} cos(\psi_f)cos(\alpha_f) - cos(\alpha_i) \\ sin(\psi_f)cos(\alpha_f) \\ sin(\alpha_i) + sin(\alpha_f) \end{pmatrix} \tag{2.86}$$

2.4.5.1 Grazing-incidence small-angle x-ray scattering (GISAXS)

As it was the case for SAXS (section 2.4.2), GISAXS is best suited for exploring thin film structures in the mesoscale, especially lateral structures within thin-film samples. These usually feature heterojunction demixing at the nanometer scale and up, material clustering, film roughness, etc. Generally, the GISAXS setup implies large sample-to-detector distances (SDD), which translates in small exit angles. This allows for small-angle description of $\vec{q}$. By approximating the sine and cosine functions in equation 2.86 to their Taylor development to first order, it becomes:

$$\vec{q} = \frac{2\pi}{\lambda} \begin{pmatrix} 0 \\ \psi_f \\ \alpha_i + \alpha_f \end{pmatrix} \tag{2.87}$$

This approximation allows for establishment of a bijective dependence between real-space and q-directions, being q_y and q_z clearly separately identifiable as the horizontal and vertical directions on the detector. Hereby, in GISAXS experiments, the q_x component, perpendicular tot he detector plane, is always negligible[98,100]

One major difference in the conformation of the scattering data introduced by the presence of the substrate is the variety of types of scattering events. Indeed, in grazing-incidence configuration, four different types of scattering events are accounted (see figure 2.20b): (1) x-ray scattering on the bulk sample material, (2) reflection on the sample substrate prior to scattering, (3) scattering followed by reflection on the substrate, and (4) a combination of the two last points featuring a reflection on the sample substrate, followed by scattering and followed by another substrate reflection. Mathematically, this is modeled in the frame of the *distoted-wave Bron approximation (DWBA)*, where the incoming radiation is a superposition of direct and reflected waves and the outgoing radiation is a combination of directly scattered and reflected waves, giving rise to the introduced four terms. DWBA is a first-order perturbation theory that takes a perfectly flat layer as the unperturbed system, and the roughnesses between layers are added as the corresponding perturbation. Simulation of GISAXS patterns in the frame of the DWBA is resource-demanding. Therefore in this thesis, a further approximation is used. It is called the *Effective Interface Approximation (EIA)*[98,100] and it consists of disregarding vertical correlations in the film. Hereby, lateral GISAXS cuts are fitted considering only the film lateral structure. Within the DWBA, the scattering cross-section can be approximated as:

$$\frac{d\Sigma}{d\Omega}(\vec{q}) = \frac{A\pi^2}{\lambda^4}(1-n^2)|t_i^F|^2|t_f^F|^2 P_{diff}(\vec{q}) \tag{2.88}$$

being A the illuminated sample area, $|t_i^F|$ and $|t_f^F|$ the Fresnel transmission coefficients

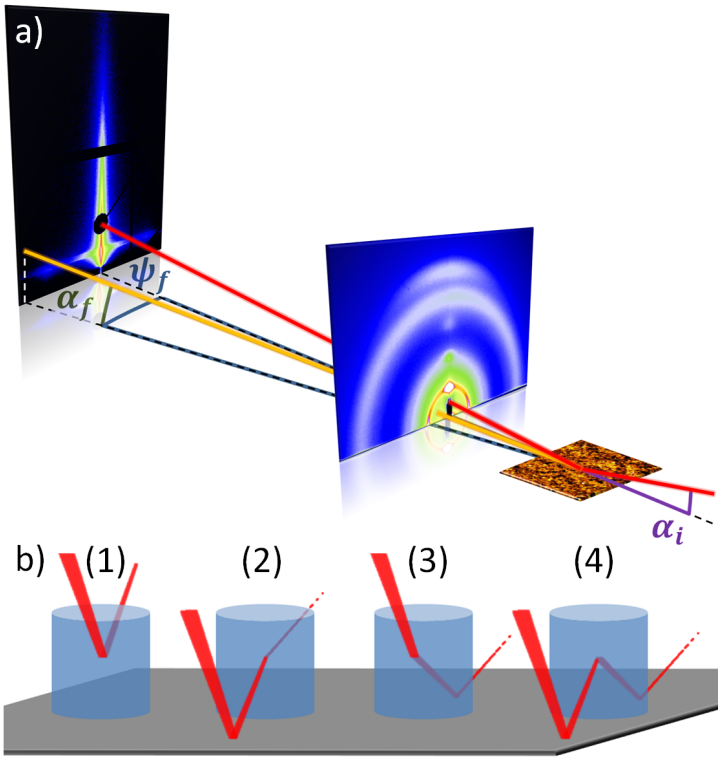

Figure 2.20: *a) Schematic depiction of the GISAXS and the GIWAXS setups. The difference in SDD allows for access of different length scales. The incoming beam impinges under a shallow angle α_i. The scattered beam subtends from the detector an horizontal angle ψ_f and a vertical angle α_i. b) Exemplary depiction of the four types of scattering events accounted in the DWBA.*

for the incoming and the scattered beam, respectively, and $P_{diff}(\vec{q})$ the diffuse scattering factor.[100] Both $|t_i^F|$ and $|t_f^F|$ reach a maximum at the critical angle of the probed material, hence giving rise to a material-sensitive intensity maximum, which is known as *Yoneda Peak*.[101] Since the Fresnel coefficients top at the Yoneda position, GISAXS lateral cuts are usually performed there, given that at this position the scattering between domains in heteromixtures is dramatically enhanced.

The diffuse scattering factor $P_{diff}(\vec{q})$ is, as seen for regular SAXS (see section 2.4.2) a combination of a form factor, parametrizing the scattering centers, with an assumed homogeneous electronic density, and a structure factor that describes their arrangement ($P_{diff}(\vec{q}) \propto F(\vec{q})^2 S(\vec{q})$). However, as in section 2.4.2, the polydisperse nature of polymer systems turns $P_{diff}(\vec{q})$ into a combination of size distributions. There exists several approaches to account for the cross-coupling between different structures. One of the classic treatments is the decoupling approximation[90], where all domains scatter with all others regardless of the size. This approach shows good behavior for spherical systems with low polydispersity. However, the model presents also breakdowns.[89] Another common

approach is the *Local Monodisperse Approximation (LMA)*. The LMA assumes regions in which domains of the same size are spatially grouped together. Hereby, only scattering from domains of the same size is allowed, and coupling between different structures is disregarded.[102] In this work, multiple form factors and their corresponding structure factors based in the LMA are assumed. Owing to the effect of polydispersity, the form and structure factors are assumed to be Gaussian-distributed and to span over and beyond several tens of nanometers. Hereby, the scattering intensity is modeled as the incoherent superposition of the local monodisperse domains:

$$P_{diff}(\vec{q}) \propto \sum_k N_k P_k(\vec{q}) S'_k(\vec{q}) \tag{2.89}$$

whereby $P_k(\vec{q}) = \left\langle |F_k(\vec{q})|^2 \right\rangle$ as it was the case for SAXS. Details on the nature of $\left\langle |F(\vec{q})|^2 \right\rangle$ and $S'(\vec{q})$ are discussed in detail in section 2.4.2.

In the present work, domain modeling of GISAXS data is performed with standing cylinder-shaped form factors:[102,103]

$$F_{cyl}(\vec{q}, R, H) = 2\pi R^2 H \frac{J_1(q_r R)}{q_r R} sin\left(q_z \frac{H}{2}\right) exp\left(i q_z \frac{H}{2}\right) \tag{2.90}$$

where R and H are the radii and heights of the cylinders, respectively, and $J_1(q_r R)$ is the first kind Bessel function of first order. Neverhteless, within the EIA, in which the vertical structure of the scattering domains is neglected, the expression for a cylinder-shaped form factor breaks down to :

$$|F_{cyl}(q_y, R)|^2_{q_z \approx 0} \approx \left(R \frac{J_1(q_y R)}{q_y}\right) \tag{2.91}$$

Regarding the arrangement of the cylindrical form factors, the description in polymer films often consists of a one-dimensional paracrystalline lattice (1DDL), i.e. a semi-ordered structure with in-plane isotropy featuring a Gaussian distribution of inter-domain distances with average value d and standard deviation σ:[102–104]

$$S(q_y, d)|_{q_z \approx 0} \approx \frac{1 - exp\left((\pi(\sigma d q_y)^2)^2\right)}{1 + exp\left((\pi(\sigma d q_y)^2)^2\right) - 2exp\left((\pi(\sigma d q_y)^2)\right) cos(q_y d)} \tag{2.92}$$

Hereby, the standard deviation σ induces $S(q_y)|_{q_z=0}$ to lose definition with increasing q_y, thereby decreasing dramatically the long-range order of the domain arrangement. This is a characteristic feature of paracrystals.

A very comprehensive review on the theoretical background as well as the technical and analytical details of GISAXS is provided in [102].

2.4.5.2 Grazing-incidence wide-angle x-ray scattering (GIWAXS)

In the wide angle regime, the small-angle approximation is no longer valid, and we recover the expression for $\vec{q}$ given in 2.86. In this case, it can be seen how the different angles of the outgoing radiation are no longer decoupled from each other along the different $\vec{q}$-directions. Basically, for the large q-values aimed to be observed in GIWAXS, the curvature of the Ewald's sphere with respect to the flat (h, k, l) crystalline planes cannot be neglected, which is precisely the assumption made in the small-angle approximation that leads to the GISAXS description of $\vec{q}$ (equation 2.87).

A schematic 2D example is shown in figure 2.21a. As discussed in section 2.4.3, the Ewald's sphere is formed with center at the $\vec{q}$-position of the scattering event, and only those vertices of the reciprocal lattice cut by the surface of the Ewald's sphere can contribute to the obtained scattering intensity, highlighted in green in figure 2.21a. As it is shown in the example of the wave vector $\vec{q}$, displayed in red, all momentum transfer vectors that accomplish both conditions for observable scattering, i.e. 1) having its start and its end on the surface of the Ewald's sphere, which means being resolvable for a given wavelength, and 2) having its start and its end on two green vertices, which means satisfying the Laue condition $\vec{q} = \vec{G}$, have at least two non-zero components within its overall $\vec{q}$. The red $\vec{q}$ vector in figure 2.21a shows that even for its most vertical position it has a non-negligible q_x component. If we now resemble all possible orientations of this q-value, which means rotating the vector $\vec{q}$ about the $\vec{k_i}$ axis (which gives the dotted circle highlighted in green), we obtain for each orientation a vector with a certain balance of q_y and q_z components, for none of which q_x is zero or negligible.

After the scattering event, the scattered x-rays hit onto a flat detector perpendicular to $\vec{k_i}$, what allows us to distinguish between the q_y and q_z directions, but both with a certain q_x contribution in them. Therefore, the GIWAXS image obtained on the detector is not directly a $\vec{q}$ map, since it contains a distortion originated by the conflict between the spherical and flat hypersurfaces of the Ewald's sphere and the flat crystalline planes. For displaying a $\vec{q}$ map, only one of the three q-directions can be decoupled from the other two, and usually it is q_z the one that is shown independently in q_z vs. q_r maps, where $q_r = \sqrt{q_x^2 + q_y^2}$. The situation is equivalent to that of projecting maps of the earth on flat canvaes. Further details on the nature of this so-called χ-*correction* can be found in the literature.[32,105]

An exemplary GIWAXS $\vec{q}$ map after the reshaping is shown in figure 2.21b, in which the impossibility of observing $\vec{q}$ vectors with less than a certain q_x-component induces the

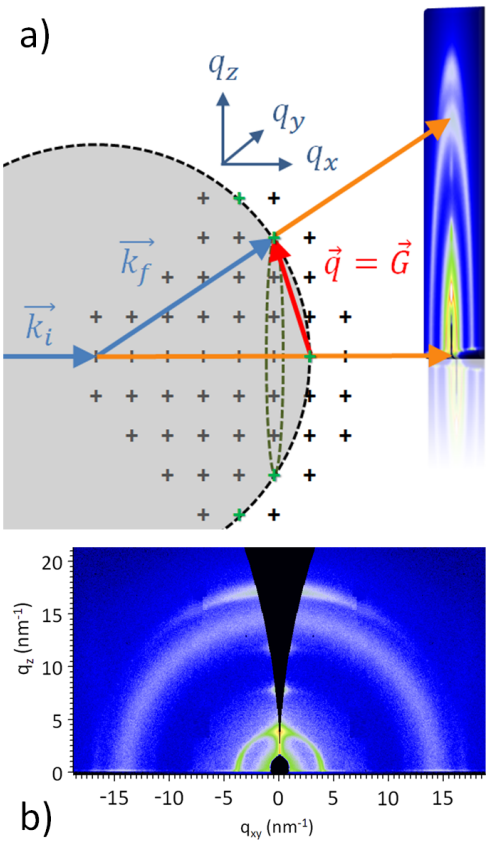

Figure 2.21: *a) Example of a scattering event. The incoming x-ray scatters at one vertex of the reciprocal lattice, giving rise to the Ewald's Sphere. The momentum transfer $\vec{q} = \vec{G}$, in red, satisfies the Laue condition and gets projected onto the detector. b) Exemplary $\vec{q}$ map of a GIWAXS measurement. The χ-correction enables q_z vs. q_r representation and causes the appearance of the central missing wedge.*

appearance of the central black missing wedge. Comparing figures 2.21a and 2.19, it can be geometrically seen that the minimum observable polar angle is again the Bragg's angle θ_{hkl}, which is given by:

$$\begin{aligned} \theta_{hkl} &= arctan\left(\frac{q_z}{\sqrt{q_x(q_z)^2 + q_y(q_z)^2}}\right) \\ &= arctan\left(\frac{q_z}{q_r(q_z)}\right) \end{aligned} \tag{2.93}$$

where the particular dependence of $q_r(q_z)$ is determined by the specific geometry of the reciprocal lattice and of the Ewald's sphere. On the other hand, decoupling q_z from the other two momentum transfer directions enables something very important, which is the differentiation of scattering vectors according to their orientation with respect to the sample substrate, the system's symmetry breaker. The example of figure 2.21b shows the GIWAXS pattern of a P3HT:PCBM BHJ. On the one hand, a ring-shaped feature at a q-radius of about 15 nm^{-1} can be seen, corresponding to PCBM and representing aggregation with a certain degree of crystalline order, but with no preferred orientation with respect to the substrate. On the other hand, we can see at the two sides of the missing wedge several footprints of vertically-oriented Bragg peaks, corresponding to crystalline P3HT. Study of the crystallite orientation with respect to the substrate is very important in polymer science and, especially, in organic electronics, provided that the electrical conductivity in organic crystals is usually highly anisotropic. This way, for some applications, such as for organic field-effect transistors (OFETs), a high degree of horizontal conductivity along the sample plane is desired, in contrast to, for example, some types of OSCs. Further discussion on the study of crystallite orientation is provided in section 3.1.4.

Besides of the above-discussed χ-correction, extraction of reliable intensity distributions and comparison of absolute intensities require other corrections, some of them again related to the geometry of the experiment setup. The most important of the additional corrections feature the *efficiency corrections* (photons scattered to detector pixels away from the direct beam experience a longer air path and, consequently, more air absorption, yielding lower intensities), the *solid angle correction* (the solid angle subtended by detector pixels located at the edge is smaller compared to pixels closer to the spot of the direct beam) and the *polarization correction* (the strongly polarized synchrotron light favors scattering with a certain crystallite orientation to detriment of the rest). These and further corrections are discussed in the literature in greater detail.[106,107]

Chapter 3

Characterization methods

One main focus of this work is the attainment of a deeper understanding of the link between morphology and performance of solar devices. To achieve this goal, information from both sides, structural and electronic, is necessary in order to achieve a broader overview and, with it, a more comprehensive understanding.

The following chapter introduces the characterization methods employed for conducting the research presented in the present thesis from a technical point of view. The description of the methods is divided in two main groups: spectroscopic/optoelectronic and structural methods. The spectroscopic methods feature the characterization of absorption and emission properties of the investigated materials as well as the behavior of complete solar devices. The structural methods feature microscopy and scattering techniques suitable for the characterization of both bulk and thin film samples. Recent innovations in the sample characterization associated with in-situ sample and device tracking using scattering methods are discussed as well.

3.1 Structural characterization methods

The morphological arrangement of thin films composing organic electronic devices determines their behavior and properties to a great extend. In the following, we introduce the characterization methods that have helped to picture both the surface and the inner morphology of the studied systems, as well as the effect of the conditions they were exposed to. They feature real space (SEM) as well as reciprocal space (XRR, SAXS/WAXS, GIXS) techniques.

3.1.1 Scanning electron microscopy

Scanning electron microscopy (SEM) is indicated for measuring the surface of solid-state samples with sub-nanometer resolution. This improved resolution compared to classical optical microscopy stems from the wave-particle duality first introduced by De Broglie in the beginning of the 20th century. In microscopy, the resolution is limited by the wavelength of the beam impinging on the sample. According to the particle-wave duality, electrons present for the same energy much shorter wavelengths than photons, thereby providing a much lower limit for the spatial resolution. Moreover, the resolution can be further tuned with the electron accelerating voltage. The wavelength of the electrons can be expressed through the De Broglie relativistic wavelength as:

$$\lambda_e = \frac{h}{m_e v} = \frac{hc}{\sqrt{(Ve)^2 + 2m_e c^2 Ve}} \tag{3.1}$$

where V is the accelerating voltage.

An SEM is basically composed of an electron source, a set of electromagnetic lenses and an electron detector. The electron beam is focused on the sample surface, which emits secondary electrons detected by the detector. The number of electrons detected depends on the changes across the sample surface, thereby enabling the reconstruction of the surface topography.

According to the wave-particle duality, the theoretical spatial resolution of an electron microscope is unlimited, whereby practically resolutions are limited to the Angstrom scale. Limitations in resolution appear due to technical constraints related to the lens systems.

SEM measurements shown in this thesis were carried out on an NVision40 field emission SEM from CarlZeiss AG, located at the *Zentrum für Nanotechnologie und Nanomaterialien* of the Technical University of Munich.

3.1.2 X-ray reflectivity

XRR is a scattering technique used to investigate the vertical structure and composition of thin film samples in reflection geometry. In an XRR experiment, the incoming x-ray beam impinges onto the sample under an incident angle that always equals the measuring exit angle ($\alpha_i = \alpha_f$). The setup is schematically depicted in figure 3.1a. Hence, XRR is a specular scattering method. Once the incident angle is above the critical angle of the sample material, the x-ray beam starts penetrating the film. There, the x-ray radiation experiences multiple reflections and refractions at different heights inside the film sample,

giving rise to an overall reflectivity pattern.

The internal vertical structure of the probed films can be modeled as a stack of layers, each of them with its characteristic dispersion $\delta(\lambda)$ and absorption indices $\beta(\lambda)$, and, therefore, its characteristic complex refractive index and critical angle $\alpha_c(\lambda)$. This defines different Fresnel reflection and transmission coefficients (r^F and t^F) at the interfaces between these stacked layers, according to which (and to the differently transmitted and reflected intensities at each interface) an overall reflectivity profile arises. The resulting reflectivity function depends on all features along the z-direction (vertical, perpendicular to the sample surface) such as layer thickness, vertical composition gradients, enrichment layers, roughness, etc.. Discussion on the theoretical aspects of XRR is provided in section 2.4.4.

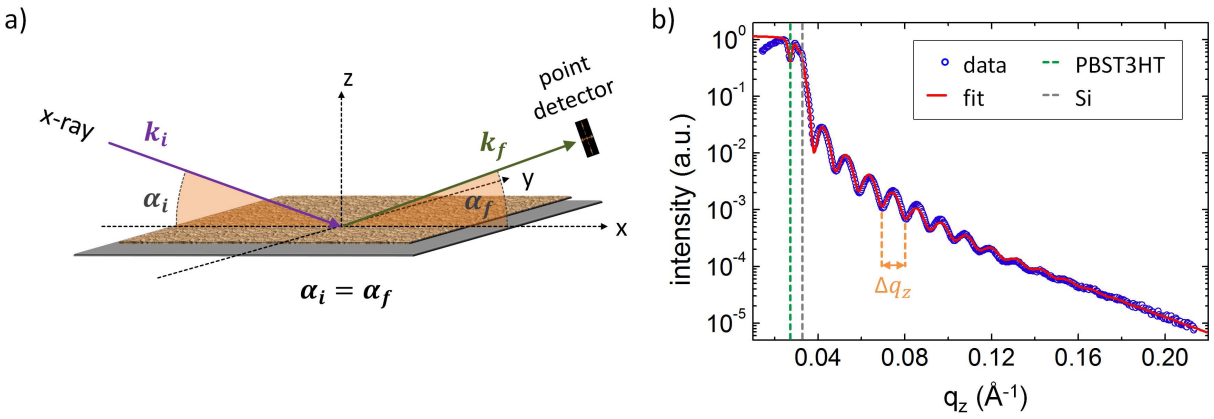

Figure 3.1: *a) Schematic setup of scattering in reflection geometry with incident and scattered beams $\vec{k_i}$ and $\vec{k_f}$. Both beams lie throughout the whole scattering event within the XZ plane. In the case of specular scattering, like in XRR, $\alpha_i = \alpha_f$. b) Exemplary XRR curve of a PBST3HT film on a Si substrate, showing the critical angles for PBST3HT and Si, as well as the Kiessig fringes, which allow for film thickness determination.*

XRR measurements are carried out at RT at a Bruker D8 ADVANCE diffractometer. In order to measure the specularly reflected intensity, measurements are performed in a coupled θ–2θ configuration, where the sample remains on an horizontal holder, whilst both the x-ray source and the detector move along a circumference (with the center at the sample) keeping the same angle with the plane defined by the sample (α_i=α_f). The x-ray beam is generated at a copper cathode (Cu-K$_\alpha$ line, $\lambda = 0.1541$ nm). The beam is monochromized and focused with the help of a Goebel mirror and further shaped with slits placed before the sample. The sample lies right under a knife edge that avoids over-illumination at shallow angles due to large footprint sizes and thereby protects the detector from saturation. Organic samples for XRR characterization are fabricated on

precleaned silicon substrates.

XRR data are fitted with the software package *Motofit* for *IGOR Pro* (by *Wavemetrics Inc.*).[97] Samples are modeled as multilayers and their thicknesses, SLDs and roughnesses are fitted. The combination of the resulting SLDs for each sublayer resembles the sample SLD profile, and the Kiessig fringes (see figure 3.1b) present in the XRR measurement provide information on the total film thickness, given by:

$$d \approx \frac{2\pi}{\Delta q_z} \tag{3.2}$$

3.1.3 Small/wide-angle x-ray scattering

Further comprehensive description of polymer systems requires as well characterization of lateral structures. Information only about the vertical direction is not enough for providing comprehensive insight into the sample's morphology. In contrast to XRR, where only the specular scattering along the vertical direction with respect to the sample surface can be probed, other x-ray scattering methods additionally provide access to the lateral information of bulk samples.

SAXS/WAXS methods are non-destructive and indicated for the characterization of bulk samples. They provide lateral-structure information of samples in the meso- and nanoscale with good sample statistics. With adjustment of the measuring parameters, such as the SDD, we can access real-space data of domains and crystalline structures with sizes ranging from several nanometers all the way down to the upper Angstrom threshold. SAXS and WAXS are also elastic scattering techniques. However, in contrast to XRR, SAXS and WAXS measurements are performed in transmission (i.e. the beam impinges perpendicularly onto a thick film of several μm and is elastically scattered in the film volume). In this configuration there is no reflected beam and, thus, no specular scattering. The scattered intensity forms usually symmetric ring-shaped maxima (in absence of preferred orientation within the sample) that are azimuthally integrated, yielding lateral cuts that provide information on the relevant length scales and can be interpreted with appropriate models (discussion in greater detail is provided in section 2.4.2).

In the analysis of the obtained SAXS radial cuts, the curves are usually described with models that account for the shapes, sizes and arrangement of the scattering objects present. These models usually consist of the convolution of two real-space terms: one is called the form factor, which accounts for the shape and the size of the scattering objects as well as for its size distribution. The second is called structure factor and de-

scribes the arrangement (distances between neighbors, lattice type) in space between the scattering objects. The model is further refined with scaling parameters related to the concentration of scattering domains or the contrast between scattering phases. A more detailed discussion on the nature of the modelling as well as of the nature of scattering pattern formation is given in section 2.4.2. This allows us to model the data and to extract the relevant system information. In this work, SAXS modeling consists of spherical scattering objects (see section 2.4 for further details).

WAXS probes wide exit angles, which translates into shorter SDDs. The technique can access data regarding crystalline structures, lattice distances and crystallite grain sizes, thus covering a size range from a few nanometers to the Angstrom regime. WAXS data usually present Bragg peaks that can be fitted with mathematical (Gaussian, Lorentzian, etc.) distributions, whose properties (center, full-width-at-half-maximum or relative center positions between higher orders) allow for the extraction of crystallite parameters such as lattice distances, grain sizes and crystalline structures (see section 2.4 for further details).

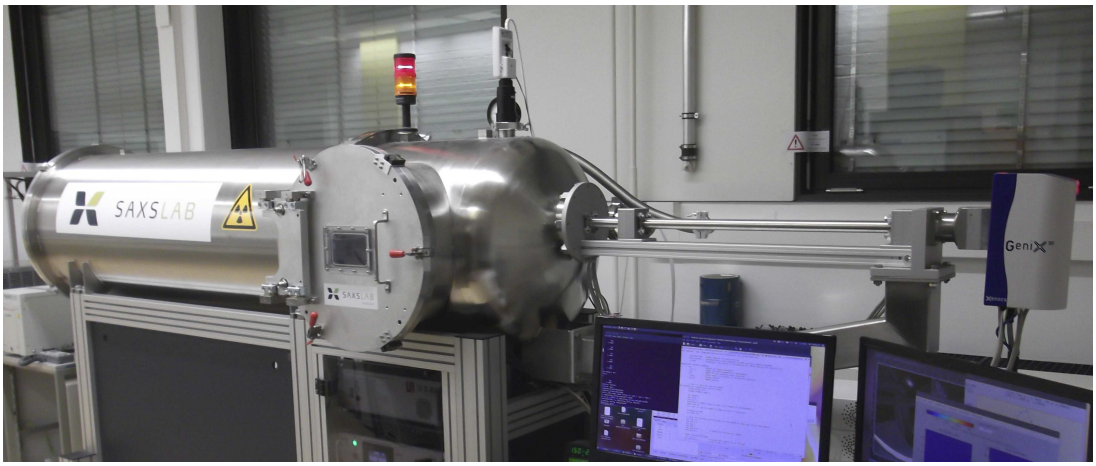

Figure 3.2: *Lab-scale Ganesha 300XL SAXS-WAXS instrument (SAXSLAB).*

In the present thesis, all SAXS and WAXS measurements are performed at a Ganesha 300XL SAXS-WAXS system (SAXSLAB ApS, Copenhagen, Denmark; shown in figure 3.2). The whole system (x-ray source, sample stage, detector) is kept in vacumm (10^{-3} mbar) to avoid air scattering. The x-ray source consists of a Cu anode ($\lambda_{K_\alpha} = 1.542$ Å) operated at 50 kV accelerating voltage and a current of 0.6 mA. The bulk samples are sandwiched between two mica windows, sealed in a Linkam holder (shown in figure 3.3) and put into the Linkam stage. The stage offers full sample temperature control (via a temperature-controlled air flow) ranging from approximately -20 °C to 150 °C, if assisted

by active liquid N_2 cooling.

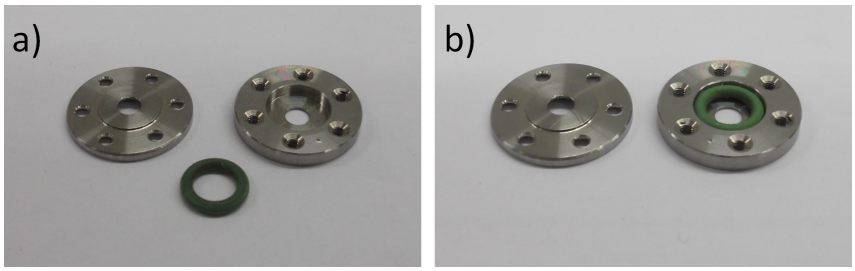

Figure 3.3: *Open Linkam holder for SAXS and WAXS characterization. Thick films are fabricated between two mica windows and laterally contained by the rubber ring. Afterwards, the sample is sandwiched between the two screwed metallic parts which, when pressed against the ring, ensure an air-tight environment.*

Before each scattering measurement, the total sample transmission is measured using a pin diode, and the transmission reference measurement is done by measuring the empty beam. The scattered beam is recorded on a Pilatus 300K detector with a pixel size of 172×172 μm^2. During the scattering measurements, the direct beam is blocked with a circular beamstop to avoid saturation of the detector. The available SDDs range from 101.35 mm to 1501.35 mm.

Prior to the azimuthal averaging about the direct beam position, unwanted areas of the 2D data files, like the inter-modular gaps of the detector or dead pixels, are masked out. The masking is done with the help of the software Fit2D. After the masking, the azimuthal integration of the 2D files is performed and the resulting curves are ready for fitting or modeling. Measurements accessing different q-ranges are recorded via different SDDs. Generally, these are merged together to yield master curves that account for the sample under study for the whole available q-range.

3.1.4 Grazing-incidence x-ray scattering

GIXS techniques represent a combination of some of the principles seen for SAXS/WAXS (section 3.1.3) as well as for XRR (section 3.1.2). They present a set of advantages. Similar to XRR, GIXS techniques are suited for the investigation of thin films, since they make use of the grazing incidence principle, which drastically increases the scattering volume compared to regular transmission measurements, as seen in section 3.1.3. Besides being able to probe the whole sample volume and not only the surface, the methods are non-destructive and they offer information statistically-averaged over large sample areas.

Unlike in XRR, GIXS methods are based on diffuse scattering, like SAXS/WAXS. The specular scattering is typically hidden behind a beam stop in order to avoid detector

saturation. In GIXS, as it was the case for the transmission configuration, the accessible q-range and, therefore, the resolvable length scales are determined mainly through the SDD. In the following, the GISAXS and GIWAXS methods are introduced. As it happens for regular SAXS and WAXS, the main difference between GISAXS and GIWAXS is the length scales they can access. GISAXS is indicated for sample characterization in the mesoscale, while GIWAXS allows for probing of sub-nanometric crystalline phases. The theoretical physical background behind these two methods can be found in section 2.4.5. A detailed description of the main GIXS techniques and their advantages can as well be found in the literature.[108]

The data presented in this thesis were obtained in experiments performed at either the beamline P03, PETRA III of the Deutsches Elektronen Synchrotron (DESY) in Hamburg, Germany[109,110] or a the AUSTRIAN SAXS beamline of the Elettra Sincrotrone in Trieste, Italy.

3.1.4.1 Grazing-incidence small-angle x-ray scattering (GISAXS)

GISAXS features SDDs between about 1.5 to 4 m, thus operating in the low q-range (for hard x-rays), which confers it resolution of structures between approximately 1 nm and 1 μm. The recorded diffuse scattering allows for the study of both vertical (along the direction perpendicular to the sample substrate) as well as lateral (parallel to the substrate) structures within the film. A schematic depiction of the GISAXS setup can be found in figure 2.20.

The GISAXS measurements discussed in this thesis correspond to experiments conducted at DESY (see details above). The x-ray beam energy was 13 keV. The incident angle was 0.35°, which is above the critical angle of the probed materials to ensure the full penetration of the film with a footprint smaller than the sample size. The SDD was 2.55 m and the signal was recorded on a noise-free Pilatus 1M Detector by Dectris, with a 981×1043 pixel array and a pixel size of 172×172 μm^2. The direct and specular reflections were shielded behind beamstops to avoid the saturation of the detectors.

The GISAXS data analysis is mainly based on the fitting of the so-called *out-of-plane cuts*, i.e. horizontal cuts characterizing lateral structures along the direction parallel to the sample substrate. The cuts are performed at the Yoneda position of the investigated materials. The cuts are performed with the software DPDAK.[111] As explained in section 2.4.5 in greater detail, GISAXS lateral cuts are fitted within the DWBA and the EIA, following a combination of form factors of cylindrical shaped based on the LMA. The

scattering centers are located on a 1D paracrystal. Both cylinders' lateral sizes as well as neighboring distances along the paracrystal are Gaussian-distributed. The number of different form and structure factors required depends on the exact case, whereby in the presented cases the amount is two or three. A Lorentzian resolution function always accounts for the resolution limit of the experimental setup.

3.1.4.2 Grazing-incidence wide-angle x-ray scattering (GIWAXS)

As explained in greater detail in section 2.4.5, GIWAXS accesses thin film information in the sub-nanometer scale, like crystalline lattice distances, crystallite grain sizes, or crystallite orientation. As explained in the theoretical part, the symmetry break in GIWAXS experiments allows for the determination of crystallite orientation with respect to the sample substrate, which is of high importance for optoelectronic devices.[32] Bragg peaks from oriented crystallites appear along the direction connecting coherent scattering planes, extending along one direction for highly oriented crystals, and yielding ring-like maxima for random crystallite orientation. A visual explanation is depicted in figure 3.4, as extracted from reference [32]. A schematic depiction of the GIWAXS setup is displayed in figure 2.20. Further details on GIWAXS can be found elsewhere.[99,112]

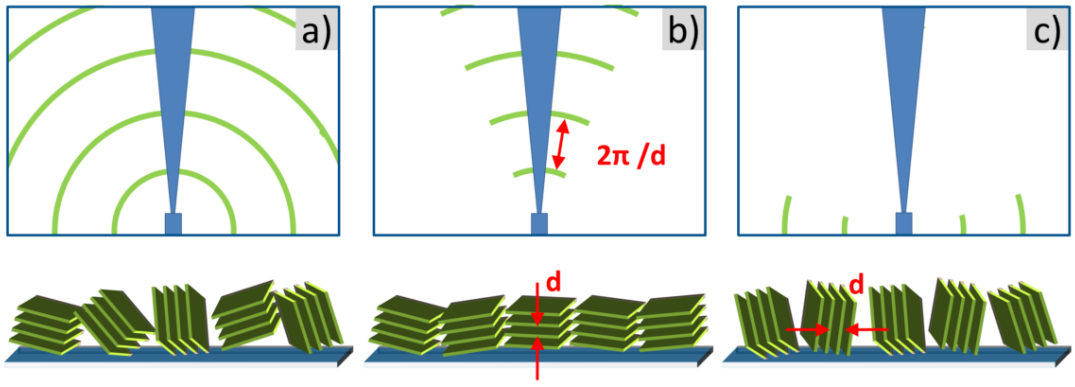

Figure 3.4: *Qualitative example of the GIWAXS pattern obtained depending on the mean crystallite orientation. a) random orientation. b) preferential vertical lamella stacking. c) preferential horizontal lamella stacking. Figure extracted from [32].*

In GIWAXS the incident angle is chosen to be between the critical angle of the probed materials and below the generally higher critical angle of the sample substrate. This way crystalline contributions of the substrate to the overall GIWAXS signal can be avoided, since the beam will experience total reflection at the sample-substrate interface. Unlike in GISAXS, where the substrate does not contribute due to the scattering intensity lack of any lateral structures, in GIWAXS the crystalline structure of the substrate can give a strong contribution if measuring above its critical angle. Moreover, amorphous substrates

eventually add large backgrounds.

In this work, GIWAXS experiments were conducted both at DESY and Elettra synchrotrons (see details above). In DESY experiments, the incident angle was set to 0.15° and the SDD to 153 mm. The beam energy was 13 keV and the signal was collected on a Pilatus 300K by Dectris (487 × 619 pixel array, pixel size 172 × 172 μm^2). In Elettra experiments, a beam energy of 8 keV was used. The SDD was set to 244 mm and the grazing-incident angle to 0.44°. The signal was recorded on a Pilatus 1M Detector (Dectris. Pixel array 981 × 1043. Pixel size of 172 × 172 μm^2).

In the analysis of GIWAXS data, two main types of cuts are performed. On the one hand, sector cuts, i.e. azimuthally-integrated cuts for a certain angle range, are performed along different orientation with respect to the sample substrate in order to determine lattice distances and grain sizes (see section 2.4.5). Sector cuts are performed between the χ angles 1° and 11° for examining the P3HT face-on orientation and between 85° and 95° for the edge-on orientation, unless explicitly stated otherwise. Note that $90° - \theta_B$ is the z-most resolvable direction (highlighted in purple in figure 3.5a. Detailed explanation in section 2.4.5). The intensity-versus-q profiles resulting from the azimuthal integration of the performed sector cuts (figure 3.5b) are subjected to a background subtraction of the type $bg(q) = aq^{-b} + c$. The resulting flat-background intensity profiles (figure 3.5c) are fitted with Gaussian curves to extract lattice distances and crystallite sizes, according to the formulae introduced in section 2.4.5.

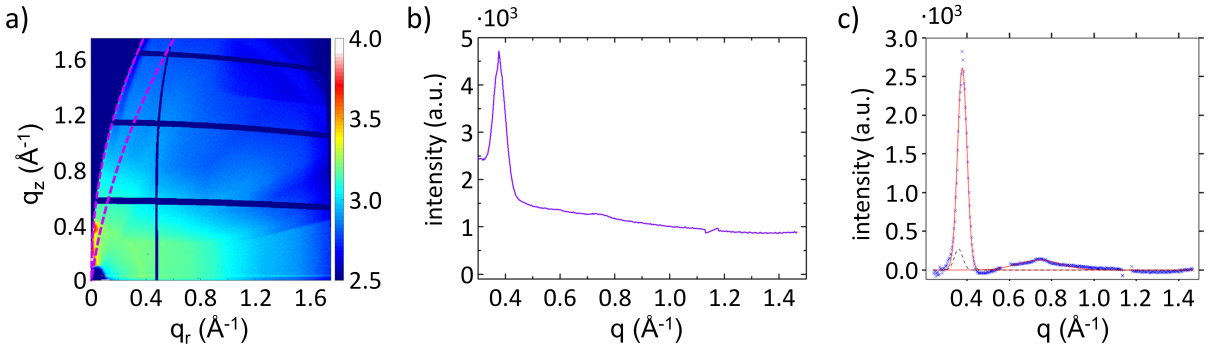

Figure 3.5: *a) Example of a GIWAXS $\vec{q}$ map. The violet slice represents a sector cut along z-most resolvable direction, forming an angle θ_B with the perpendicular to the substrate. b) azimuthally-integrated 1D profile prior to background subtraction. c) Background-subtracted cut and Gaussian fit. Figure taken from [15].*

On the other hand, tube cuts, i.e. radially-integrated cuts for a certain q-range, are performed in order to study the ratio of the edge-on to face-on orientations. Tube cuts

are performed for various q-values and generally for the whole accessible χ range (0° to $90° - \theta_{Bragg}$). The face-on to edge-on ratio is determined by comparing the lateral to central integrated intensities on the performed tube cuts. Multiple interval choices are taken into account in order to guarantee independence of the obtained results of a particular interval choice.

Aside from the cuts, a certain set of corrections needs to be done on GIWAXS raw data in order to obtain $\vec{q}$ maps with reliable intensities, as explained in section 2.4.5. The corrections and the cuts have been mostly done with help of the software GIXSGUI.[106,107]. Cuts have as well been performed with self-written Genplot macros.[113]

3.1.5 In-situ & in-operando grazing-incidence x-ray scattering

One important feature of synchrotron radiation compared to in-house x-ray devices is the much higher intensity of the x-ray beam, i.e. the much higher photon density. This feature brings along an important advantage about performing experiments at a synchrotron, which is a much higher time resolution. Actually, the time resolution for synchrotron GISAXS and GIWAXS experiments is already high enough that it enables characterization of physical phenomena *in-situ* or *in-operando*, meaning the tracking of one or multiple system parameters with time resolutions better than one second. This opens new ways of understanding how polymer systems and devices behave, since it is now possible to observe in real time how films behave upon various tailored conditions, like temperature, atmosphere composition, ultra-violet (UV) radiation, etc. Some examples are already available in literature.[15,58]

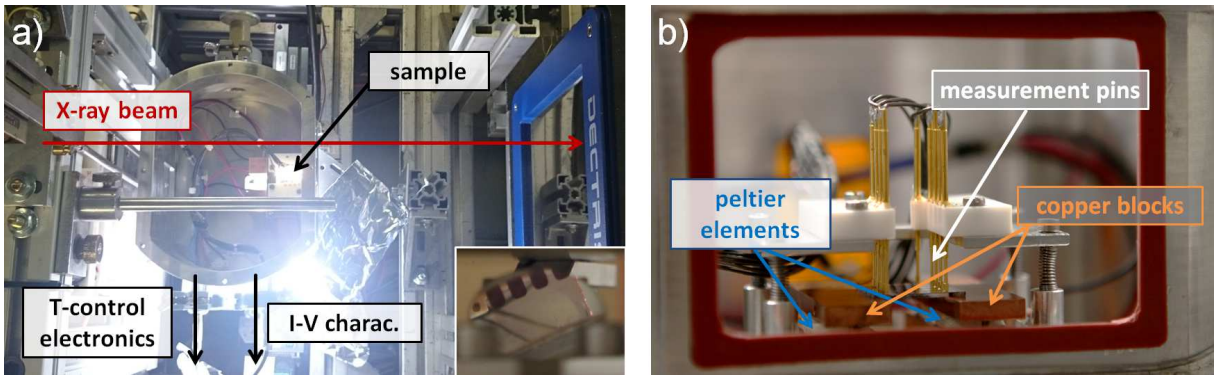

Figure 3.6: *a) In-operando setup placed in the beamline. Close to the exit window of the chamber an illuminated area indicates the place where the sample and the measurement pins are mounted. b) Sample holder and measuring pins seen through the exit window without the Kapton® foil fixed. Figure taken from [15].*

In the present thesis, one major in-operando experiment was performed, based on the observation of full OSCs during operation with GIWAXS. Hereby, the evolution of the crystalline behavior at the same time as that of the solar cell parameters was tracked, providing insight on the causes of device degradation. The in-operando GIWAXS measurements were performed at the AUSTRIAN SAXS beamline at Elettra. Further details on the obtained results are presented in chapter 7.

In order to allow for simultaneous GIWAXS and optoelectronic characterization, an in-operando chamber was designed by J. Schlipf. The chamber, as shown in figure 3.6, enables paths for x-rays and GIWAXS characterization through two large Kapton windows along the beam propagation direction. The large Kapton exit window allows for an exit angle of up to 55° (see figure 3.6b), thereby enabling the tracking of the main crystalline families of a vast variety of polymer systems.

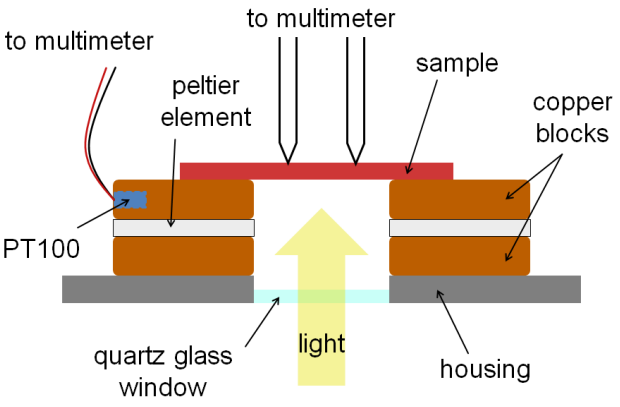

Figure 3.7: *Sketch of the sample holder as seen along the direction of x-ray propagation. Figure taken from* [15].

The floor of the chamber is equipped with a quartz window to allow illumination of the sample from below with a solar simulator through a 45° mirror placed below the entrance quartz window (compare figure 3.6a, also inset, and figure 3.7). The entrance illumination window at the floor of the chamber is made of quartz to ensure that the window itself does not absorb the UV radiation of the incoming simulated solar spectrum. Inside the chamber, the sample is mounted on a holder consisting of two copper plates at the sides of the quartz window (enabling a path for the solar radiation to reach the sample lying on top) whose temperature can be read out and actively controlled by means of Peltier regulators. The sample is placed on top of the copper holder and the solar cell contacts are contacted from above with gold-capped test pins. The solar simulator consists of a Perkin Elmer PX5 150 W lamp. A picture of the sample holder is shown in figure 3.6b and a schematic depiction of all parts is displayed in figure 3.7.

The OSCs were tracked for approximately 20000 s (5.5 h). For the photovoltaic characterization, current-bias (I-V) curves were continuously swept and recorded every 16 s with help of a Keithley SourceMeter. Further details on I-V characterization are provided in section 3.2.3. In contrast, x-ray probing was discrete, in order to ensure that no radiation

damage affects the sample. During the first 4 min, one GIWAXS pattern was taken every 30 s. Afterwards, one GIWAXS image was recorded every 60 s up to 15 min after the start. From 15 to 26 min, one GIWAXS pattern was taken every 120 s, and, subsequently and until the end of the experiment, one further GIWAXS image was obtained every 600 s, since all tracked parameters reached a stable regime. Characterization of the solar device in-situ during illumination is completed with a control experiment in the dark. This is performed in absence of both illumination and I-V sweeps. The control experiments help to ensure that all crystalline changes observed for the functioning are indeed related to the functioning of the OSC during illumination. Moreover, monitoring of the GIWAXS intensity in control experiments help to guarantee that the samples do not experience any x-ray radiation damage. For each of the experiments the GIWAXS measurements were performed at the same sample spot to ensure that the intensity changes observed did not correspond to local heterogeneities of the film.

One big issue with which in-operando device tracking experiments always confront is the preliminary degradation to which the devices are subjected in the process of transporting the finished devices from the fabrication laboratory to the synchrotron beamline, a process there is not straight-forward way to avoid.[58] In our case, this process from fabrication to actual measurement can take up to few days. For transporting, the samples are individually sealed in small air-tight KF flange steel containers. The process of sealing is carried out at a glovebox under N_2 atmosphere to ensure absence of oxygen and water. Nevertheless, long-time storage of the OSCs within the small gas-tight environment has after few days a negative effect on the J-V characteristics of the device, especially affecting the short-circuit current density J_{SC} and the fill factor FF.

3.2 Spectroscopic and optoelectronic characterization methods

The investigation of the electrical and optical properties of polymeric materials as well as a deeper understanding of their role in devices require spectroscopic and electronic characterizations. The study of material intrinsic properties, such as light absorption or emission, allow for understanding the effect of treatments, dopings or system modifications on the polymer behavior. Similarly, they provide optoelectronical information with which the anticipation and understanding of the behavior of the resulting full devices are facilitated. In the following, three methods will be presented. Two of them, UV/Vis and photoluminescence spectroscopy, describe the intrinsic interaction of matter with light and give some hints on the system's crystalline structure and energetic landscape. Fi-

nally, the characterization of complete solar devices themselves is introduced.

3.2.1 UV/Vis spectroscopy

UV/Vis spectroscopy is used to study the absorption of light by polymer films with wavelength resolution. A monochromatic beam of a controlled wavelength is sent to the thin film sample. Incoming photons with an energy higher than that of the optical band gap of the respective material interact with it and are absorbed, promoting valence electrons to excited electronic, vibrational and rotational states. Photons with an energy below the optical band gap will just travel through the sample without interacting with it. For each wavelength of the incoming light, matter and radiation interact to a different degree, i.e. the absorption of light for each wavelength is intrinsically differently intense. Hereby it is possible to extract information on the energetic landscape of the probed material.

In polymer films, the absorption is described with the help of the so-called Lambert-Beer Law. According to it, the differential light intensity lost by the beam when passing through a material depends on a few intrinsic parameters of the system and the total light intensity at that point:

$$dI(\lambda) = -\alpha(\lambda)I(\lambda)dx \tag{3.3}$$

If we take the integral form and perform the calculation for a film of total thickness d, we obtain:

$$I_T(\lambda) = I_0(\lambda)e^{-\alpha(\lambda)d} \tag{3.4}$$

where $I_0(\lambda)$ and $I_T(\lambda)$ are the total and the transmitted light intensities, respectively, and $\alpha(\lambda)$ is the *absorption coefficient* which, as it can be seen from equation 3.4, is the only parameter that describes the intrinsic behavior of the probed material, since it is decoupled from the measurement setup and film thickness. Further development of equation 3.4 allows for the calculation of $\alpha(\lambda)$:

$$log_{10}\left(\frac{I_T(\lambda)}{I_0(\lambda)}\right) = log_{10}(T(\lambda)) = -\alpha(\lambda)d\ log_{10}(e) \Rightarrow \alpha(\lambda) = \frac{-1}{d}\ \frac{log_{10}(T(\lambda))}{log_{10}(e)} \tag{3.5}$$

Introducing the *absorbance* $A(\lambda) \equiv -log_{10}T(\lambda)$, which is a magnitude commonly used by spectrometers, we can express the absorption coefficient either as a function of the absorbance or the transmission:

$$\alpha(\lambda) = \frac{1}{d}\ \frac{A(\lambda)}{log_{10}(e)} = \frac{-ln(T(\lambda))}{d} \tag{3.6}$$

where *ln* indicates the natural logarithm.

The measurements presented in this work where carried out on a Lambda 35 spectrometer by PerkinElmer. The spectrometer is controlled by the software UV-Winlab, as well developed by PerkinElmer. The spectrometer consists of two lamps: a tungsten halogen lamp covers the near infrared and the visible spectrum range, and a deuterium lamp covers the UV range. Overall, the spectrometer is capable of accessing wavelengths from 190 nm to 1100 nm. The generated beam passes an optical grating, thereby becoming monochromatic. The monochromatic beam is subsequently divided with aid of a half-mirror. One of the resulting beams will be used for probing the sample, whilst the other one will serve as reference measurement. The measurements are performed in transmission. Therefore, samples for UV/Vis spectroscopy are fabricated on glass substrates. The beams transmitted through the sample and through the reference are individually detected by two photodiodes. Thus, the data obtained by the photodiodes correspond to $I_0(\lambda)$ and $I_T(\lambda)$, and thereby, calculation of $T(\lambda)$, $A(\lambda)$ and $\alpha(\lambda)$ is enabled. The UV/Vis measurements were conducted with a slit width providing a wavelength resolution of 1 nm and a scan speed of 120 $^{\mathrm{nm}}/_{\mathrm{min}}$.

3.2.2 Photoluminescence spectroscopy

Another important indicator of the energetic landscape of a material is given by its photoluminescence (PL) response. PL refers to the capacity of a given system to emit light (luminescence) after being excited by incoming electromagnetic radiation (photoexcitation). In PL measurements, materials are excited with photons capable of being absorbed by the sample (usually specific absorption transitions are targeted, for which the excitation is slightly more energetic than the corresponding absorption maximum). In the simplest cases, the PL intensity obtained for a given energy is generally interpreted as the amount of incoming radiation exciting a transition in the material with the given energy. While this is generally true for simple systems, like atoms or small molecules in the gas phase, the PL response of complex environments, like macroscopic crystals, polymers or, in general, many-body systems include other phenomena and can be at least partially approached by the *semiconductor luminescence equations*.[114,115] In these more complex sample environments the PL signal also develops as a result of additional effects, like charge carrier-phonon interaction or the influence of dielectric environments, amongst others.

Two main photoluminescence mechanisms are distinguished: *fluorescence* and *phospho-*

rescence. The prior is usually a fast process in which a portion of the absorbed energy is released prior to the photon emission via non-radiative mechanisms, such as energy transfer between ions, phonon relaxation in crystalline regions, and more generally eventually fracton relaxation.[116] This process induces energetic relaxation down to the edge of the optical band gap and, as a result, the emitted photons are red-shifted (have lower energy) compared to the excitation. Phosphorescence, on the other hand, implies a change in the spin multiplicity of the generated excitons, which undergo ISC, usually to a triplet state. Phosphorescence displays much longer decay times to the ground singlet due to the low efficiency of the decay mechanism imposed by the quantum selection rules (detailed discussion in section 2.3). In general, PL measurements on BHJs of photoactive materials help gaining insight on the recombination rate, since less PL emission corresponds to a higher exciton quenching, which usually correlates with higher rate of exciton separation into charge carriers (polarons).

Unlike for UV/Vis measurements, samples for PL are generally fabricated on silicon wafers, since glass presents itself a PL contribution in the visible range due to its boron content. The PL measurements presented in this thesis are conducted on a LS55 fluorescence spectrometer by PerkinElmer. The illumination is provided by a Xenon discharge lamp with a pulse FWHM shorter than 10 μs. The signal is detected with a Hamamatsu R928 photomultiplier under an angle of 90°. The spectral scan speed is set to 500 $^{\text{nm}}/_{\text{min}}$ and the slit width resolution to 10 nm. The setup is controlled by the software FL-Winlab, developed by PerkinElmer as well.

3.2.3 Current-bias solar cell characterization

Aside from the different approaches to characterize the outer and inner film structure as well as the optoelectronic properties of materials used for organic solar cell fabrication, an important approach is the probing of the solar cells themselves. Solar cells are composed of many layers (more details in section 2.2), amongst which the most important one is the photoactive layer, generally in the form of a BHJ. The BHJ is composed of two materials, identified as donor and acceptor, according to their relative ionization potential and electron affinity. The fact that they are composed of a bicontinuous D-A mixture resembles in a way the inorganic P-N junction. Thus, organic solar cells present as well a diodic behavior. The current flowing through the device in the dark as a function of the applied bias is, ideally, well described by the Schockley diode equation:

$$J_D(V) = J_S \left(e^{\frac{eV}{nk_BT}} - 1 \right) \tag{3.7}$$

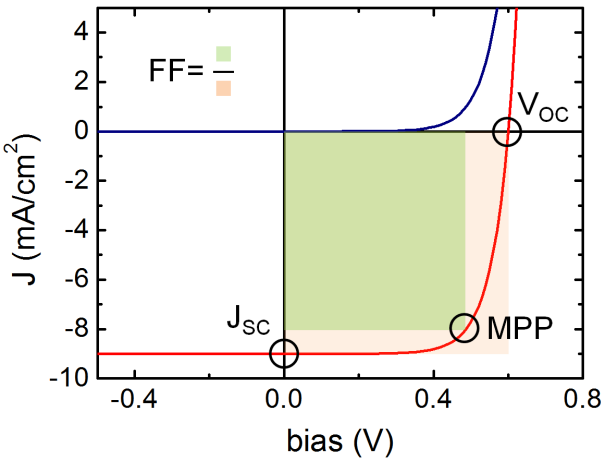

Figure 3.8: *Dark (blue solid line) and light (red solid line) exemplary J-V curves of a solar cell. The J_{SC}, V_{OC} and MPP points are indicated. The FF corresponds to the ratio between the green and orange higlighted areas.*

where J_S is the saturation current density in reverse bias and n the diode ideality factor. Under illumination, the photogenerated charge carriers add up to those electrically pulled in and out of the device. Thereby, in the easiest level of description, the J-V curve experiences a shift and can be described by:

$$J_I(V) = J_S\left(e^{\frac{eV}{nk_BT}} - 1\right) - J_{ph} \tag{3.8}$$

where J_{ph} indicates the photogenerated current. Both the dark and the illuminated cases are indicated in figure 3.8 by the blue and red lines, respectively. Under illumination, the point at which the J-V curve meets the current density axis ($V = 0$) is called *short-circuit current density (J_{SC})*:

$$J_{SC} = J_I(V = 0) = -J_{ph} \tag{3.9}$$

whereas the intersection between the J-V characteristics under illumination and the bias axis is known as *open-circuit voltage (V_{OC})*:

$$V_{OC} = V(J_I = 0) = \frac{k_BT}{e} ln\left(1 + \frac{J_{SC}}{J_S}\right) \tag{3.10}$$

This way, each point of the J-V curve under illumination located between the J_{SC} and the V_{OC} corresponds to the power density ($P = V \cdot J_I$) that the solar device is able to yield under illumination for the corresponding bias (compare figure 3.8). Thus, at least one of the points along that section of the curve displays a maximum power output. This generic point is called *maximum power point (MPP)* and its associated power output is indicated in figure 3.8 by the green-colored area. The ratio between that maximum yielded power and the theoretical maximum withdrawable power (indicated in figure 3.8 by the orange-colored area) is as well an important photovoltaic indicator, known as the *fill factor (FF)*:

$$FF = \frac{P_{MPP}}{P_{ideal}} = \frac{J_{MPP}V_{MPP}}{J_{SC}V_{OC}} \tag{3.11}$$

Thus, by dividing the maximum power yielded by the real solar device through the irradiated power, we obtain the *power conversion efficiency (PCE)*:

$$PCE = \frac{P_{MPP}}{P_{irr}} = \frac{J_{MPP}V_{MPP}}{P_{irr}} = FF\ \frac{J_{SC}V_{OC}}{P_{irr}} \tag{3.12}$$

In the data presented in this thesis $P_{irr} = 100\ ^{\mathrm{mW}}/_{\mathrm{cm}^2}$, in reproduction of the most common calibration conditions, the global standard spectrum (AM1.5g).

The diode equations presented so far correspond to an ideal solar cell. However, a description closer to a real OSC requires additional ideality-breaking components, which account for recombination processes or, more generally, losses taking place in actual devices. One common approach is to complete the description of the ideal OSC with two additional resistances: one parallel shunt resistance (R_{SH}) and a series resistance (R_S). The corresponding equivalent circuit is depicted in figure 3.9. R_S accounts for the resistivity experienced by the charge carriers in the different materials composing the device, such as the resistivity of the device contacts, or low conductivities of polymeric materials. R_{SH} describes the leakage currents that appear in devices. These can correspond e.g. to partially short-circuited electrodes or charge carrier recombination at an interface. All these effects prevent the current flow through the branch of the equivalent circuit containing the diode (see figure 3.9). Inclusion of both resistances in the model leads to a more developed device equation:

$$J_I(V) = J_S\left(e^{\frac{eV - R_S J_I}{nk_BT}} - 1\right) + \frac{V - R_S J_I}{R_{SH}} - J_{ph} \tag{3.13}$$

Equation 3.13 is transcendental and thus cannot be solved algebraically, but is generally solved numerically. Both resistances R_S and R_{SH} can be obtained from the slope of the J-V curve at the V_{OC} and the J_{SC} points, respectively:

$$R_S = \left.\frac{dJ}{dV}\right|^{-1}_{V=V_{OC}} \tag{3.14}$$

$$R_{SH} = \left.\frac{dJ}{dV}\right|^{-1}_{J=J_{SC}} - R_S \tag{3.15}$$

Experimentally, the illumination of the solar cells is carried out with a solar simulator Solar Constant 1200 from K. H. Steuernagel Lichttechnik GmbH. Its lamp is halide-based and contains rare earth metals. The light of the lamp is directed with help of parabolic reflectors and passes through a borosilicate diffuser prior to arriving at the sample in order to ensure a spatially homogeneous illumination. The sample lies around 32 cm above the diffuser. To grant constant illumination throughout time, the solar simulator is switched

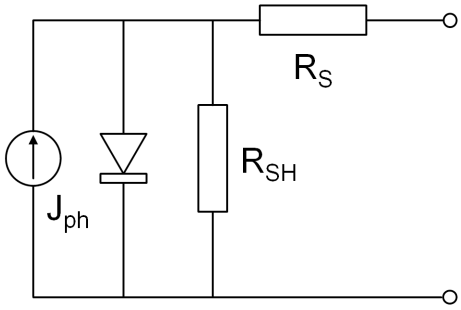

Figure 3.9: *Equivalent circuit of a solar cell with series (R_S) and shunt (R_{SH}) resistances.*

on, set to AM1.5g and heated up for about 45 min. Prior to the sample characterization, the spectrum is first calibrated to AM1.5g with two different reference silicon photodiodes, WPVS RS-ID3 and WPVS RS-ID-4 with a KG5 filter, both by CalLab-Fraunhofer ISE. The samples are measured through a voltage sweep from −1.0 V to +1.0 V (irrespective of the sweep direction) with a voltage step of 0.01 V carried out with a Keithley 2400 SourceMeter. The setup is controlled with the Labview-based software Testpoint V6 (CEC Capital Equipment). The program governs the Keithley, offering the possibility to tune all the above-mentioned parameters, as well as programming continuous loop measurements with waiting times that allow the study of time-dependent effects, e.g. device degradation.

One part of the present work consists of the study of the effect of magnetic fields on the OSC performance. To enable this sort of characterization, two different setups were designed and constructed. For low and finely-adjustable fields, a double coil mounted on a holder that fits the solar simulator measuring slot is constructed. For testing the effect of high magnetic fields, a sample holder for contacting the solar cells was designed, which allows the placement of a cuboid neodym permanent magnet. Detailed description of the two magnetic field-generating setups, of their construction, assembly and calibrations are provided in the appendix A and in the reference [117].

Chapter 4

Materials and sample preparation

The present chapter gives information about the main materials used, as well as the procedures followed for fabricating the samples characterized in the multiple experiments carried out in the frame of this thesis. In the first section, the main materials used are presented and their main properties are discussed. In a subsequent section, the types of substrates used to fabricate thin film samples are introduced, as well as their corresponding cleaning procedures. Afterwards all the steps followed for fabricating thin films are described in detail. Finally, the construction of organic solar cells as an assembly of several layers is described.

4.1 Materials

In the present section the main organic materials along with the nanoparticles, of capital importance in the present work, are introduced. The materials presented here constitute the main components of thin film samples or solar cells, featuring photoactive materials, as well as blocking layers/electrodes, or the solvents needed for enabling solution processing.

4.1.0.1 Poly(3,4-ethylenedioxythiophene):poly(styrenesulfonate) (PEDOT:PSS)

PEDOT:PSS is a polymer mixture of two ionomers (see figure 4.1), commonly used in organic electronics for its advantageous properties, like high electrical conductivity, transparency and ease of processing. PEDOT is the conducting component, consisting of a polythiophene-based conjugated polymer backbone that offers high values of electrical conductivity for positively-charged polarons. Especially after treatment of films with a variety of chemicals, PEDOT:PSS has shown conductivities on the same order of that of

traditional inorganic transparent electrodes, such as ITO. For this reason PEDOT is being established as prominent low-cost option for transparent, flexible and cheap electrode material in organic electronics.[118,119] PSS is the constituent that provides water-solubility to the mixture and makes it processable in solution via the sulfonyl groups, which tend to deprotonate and become negatively charged sulfonates.

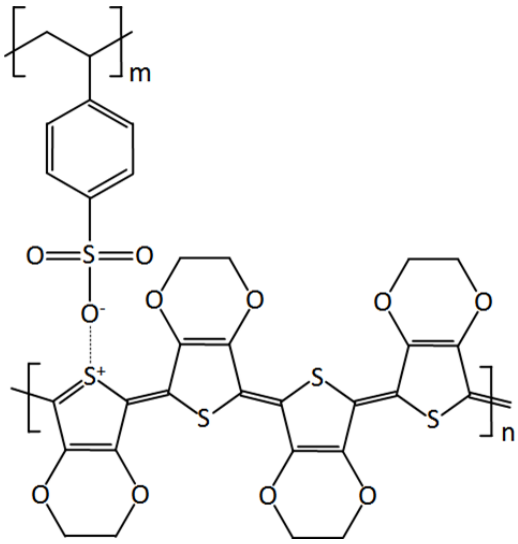

Figure 4.1: *Chemical structure of PEDOT:PSS.*

In standard OSCs, PEDOT:PSS is used as an electron blocking layer, preventing negative polarons to reach the device anode. The PEDOT:PSS mixture used in this work is PEDOT:PSS PH1000 by Ossila Ltd. (Sheffield, UK). The water-based solution contains 1.3 to 1.7 wt.% of PEDOT:PSS, both components mixed at a 1:2.5 ratio. The mixture is stored at low temperatures below 6 °C and protected from light.

4.1.0.2 Poly(3-hexylthiophene-2,5-diyl) (P3HT)

P3HT constitutes a cornerstone of the study of OSCs, being the main contributor to charge carrier generation in P3HT:PCBM devices and, together with PCBM, by far the most studied and well-characterized photoactive material for OSCs. P3HT is a conjugated polymer displaying conductivity for positive charge carriers along with other interesting properties for devices, like comparably high crystallinity and good processability in a wide range of organic solvents. Typically, P3HT presents a HOMO at around -5.0 eV and a LUMO at about -3.0 eV. Thus, it presents an optical bandgap of 2 eV, which yields and absorption onset at around 650 nm and and absorption maximum at about 500 nm. The P3HT used in this work is purchased from Rieke Metals, Inc., with a molecular weight of M_W = 53 kDa, regioregularity index of 92% and PDI = 2.3, according to the manufacturer. The chemical formula of P3HT is displayed in figure 4.2a.

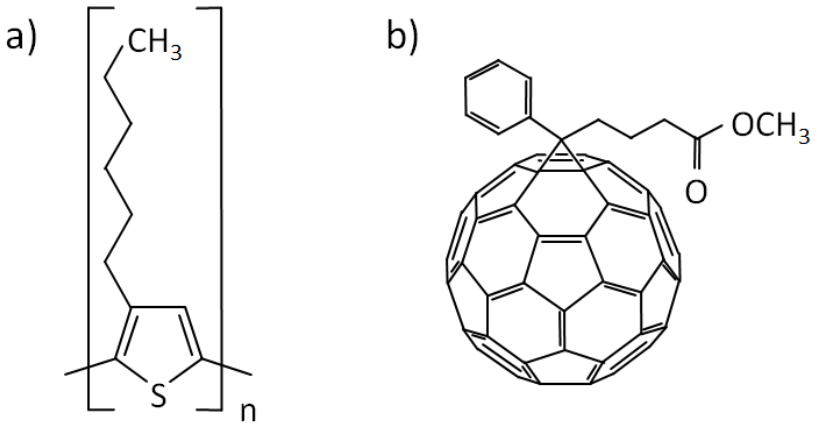

Figure 4.2: *Chemical structure of a) P3HT. b) PCBM.*

4.1.0.3 Phenyl-C_{61}-butyric acid methyl ester (PCBM)

PCBM is commonly used as electron acceptor in combination with P3HT and other donor polymers. It is a fullerene derivative of the C_{61} buckyball, showing electron accepting behavior and negative polaron conductivity. The geometry of the buckyball yields a highly delocalized π-orbital structure over all of its surface. It usually displays values for the electron mobility in the order of 10^3 cm^2/Vs and HOMO and LUMO levels around -6.5 ev and -4 eV, respectively, thereby presenting light absorption mainly in the UV range. Furthermore, its solubility in most organic solvents is of great importance for printable electronics device fabrication. PCBM from two different manufacturers is used in the scope of this thesis. On the one hand, PCBM is purchased from Nano-C Inc., with a purity >99.5%. On the other hand, >99% purity PCBM is supplied by Ossila Ltd. The chemical structure of PCBM is displayed in figure 4.2b.

4.1.0.4 Poly-(3-hexyl-2(3-(4-hexylthiophene-2-yl)-4,5-butylselenophene-1-yl)-5- -(4,5-butyltellurophen-1-yl)thiophene) (PBST3HT)

PBST3HT is a hexylthiophene-based conjugated oligomer with alternatively inserted butylselenophene and butyltellurophene units in the repeating unit. Its chemical structure is displayed in figure 4.3. The material presents a band gap at RT of around 2 eV, though it displays band gap-switching behavior when treated with temperature. The embedded selenium centers serve the purpose of drastically reducing the band gap, while the tellurium heteroatoms increase the degree of spin-orbit

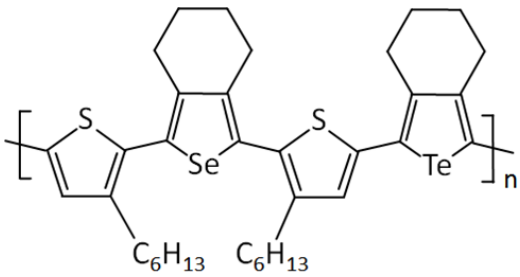

Figure 4.3: *Chemical structure of PBST3HT*

coupling in the delocalized π-bands. PBST3HT is a novel material in organic electronics and it is still not commercially available. The PBST3HT used in this work was synthesized by Prof. Eric Rivard's group at the University of Alberta, Canada, featuring a molecular weight of around $M_W \cong 4$ kDa.[120,121]. More detailed characterization of PBST3HT follows in chapter 5.

4.1.0.5 Iron(II,III) oxide nanoparticles (Fe_3O_4 NPs)

In the frame of the present thesis the effect of heavy metal nanoparticles and that of magnetic stress on OSCs is investigated. To address these issues, superparamagnetic iron(II,III) NPs are used. The NPs are purchased from Sigma Aldrich. They present a diameter of 10 nm with a size distribution of 10 ± 1 nm, according to the supplier). The NPs are purchased in toluene solution at 5 $^{mg}/_{mL}$. They are capped with oleic acid (OA) in order for them to be compatible with organic solvents (<1.0% stabilizing ligands). Further information related to the NPs can be found elsewhere.[122,123] The Fe_3O_4 NPs solution is stored in the fridge at temperatures below 6°C.

4.1.0.6 Solvents

The solvents used for processing of photactive material and, therefore, for assisting the fabrication of active layers are toluene (TL. Figure 4.4a) and chlorobenzene (CB. Figure 4.4b). Both organic, colorless, flammable and water-insoluble solvents are purchased from Carl Roth GmbH with a purity $\geqslant 99.5\%$. At 20 °C toluene has a density of 870 $^{g}/_{L}$ and chlorobenzene 1126 $^{g}/_{L}$. The boiling temperature for toluene is 111 °C, whilst for chlorobenzene it is 132 °C.

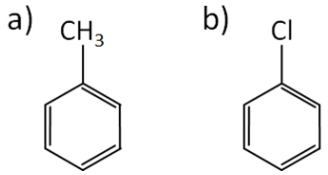

Figure 4.4: *Structures of: a) toluene. b) chlorobenzene.*

4.2 Substrates: types and preparation

This section introduces the types of substrates used to meet different experimental requirements. Moreover, the modification and cleaning procedures to which they are subjected are described in detail. Particularly complex is the ITO substrate patterning, which is necessary in order to comply with technical requirements of the solar cell layout.

4.2.1 Subtrate types

In the course of the investigations presented in this work, a variety of substrates were used. The use of one or another type of substrates stems from the nature of the samples that are

built or the methods that are used for characterization. For example, SEM and PL require conducting and non-fluorescent substrates, respectively. This usually means that samples fabricated for this characterization techniques are fabricated on silicon wafers. On the other hand, measurements like UV/Vis spectroscopy in transmission require transparent substrates, for example glass. The use of ITO-coated glass substrates is a requirement of the fabrication of solar cells, at least in the frame of the present thesis.

4.2.1.1 Glass slides

Glass slides are a common substrate and are mainly used for absorption measurements and for some of the scattering experiments, as indicated. 1 mm thick 26×75 mm^2 microscope slides are cut into the desired sizes. The microscope slides are purchased from Carl Roth GmbH. The required cleaning process prior to sample fabrication is described in detail in section 4.2.2.

4.2.1.2 Silicon wafers

In this thesis, p-doped silicon wafers are used as substrates for PL and SEM measurements, as well as for GIXS experiments. Round-shaped wafers with a diameter of 10 cm are purchased from two different suppliers: *Silicon Materials Inc.* (Thornburg, USA) and *SiMat* (Kaufering, Germany). The wafers are polished on one side and the polished side coincides with the $\langle 100 \rangle$ crystal direction. The wafers have a thickness of around 500 μm and a roughness of $\sigma_{RMS} < 0.5$ nm. Wafers are cut with a diamond pen into the desired samples sizes followed by a cleaning procedure (detailed in section 4.2.2) prior to film deposition.

4.2.1.3 Indium-doped tin oxide-coated glass slides

For OSC fabrication, ITO glasses are used. They are purchased from *SOLEMS* (Palaiseau, France) already cut in 22×22 mm^2 squared substrates. The ITO layer is around 80 nm thick and presents sheet resistances of 25 to 35 $\Omega/\square$. The ITO work function lies around -4.7 eV, matching the HOMO of P3HT and the polaron extraction energy of PEDOT:PSS (about -5 eV) very well. Prior to use in solar devices, ITO glass slides need to be patterned to successfully accomplish their role as electrode. Details on this patterning process and the subsequent cleaning procedure follow in section 4.2.2.

4.2.2 Substrate preparation

4.2.2.1 Cleaning of glass and Si substrates

After cutting the substrates (glass slides or silicon wafers) to the desired sample size, the substrates need to undergo a cleaning procedure that ensures complete removal of impurities. Substrate cleaning is very important and has a strong influence on the subsequent films, since their morphology is sensitive to many substrate conditions that can be adjusted with cleaning procedures, like substrate hydrophobicity or the presence of organic residues. Therefore, efficient cleaning procedures ensure reproducibility of the experiments and thereby enable systematic research.

For ensuring complete removal of organic traces, substrates are cleaned with an acid bath that resembles a modified piranha bath. The cleaning procedure is based on the ionic cleaning SC-2 step of the RCA silicon wafer standard cleaning protocol, common in semiconductor industry.[124] Prior to that, the substrates are rinsed with DI-water while held on an acid-resistant polytetrafluoroethylene (PTFE) holder. The holder with the substrates is then submerged for 15 min in a bath consisting of deionized water (DI-H_2O), hydrogen peroxide (H_2O_2, 30%) and concentrated sulfuric acid (H_2SO_4, 96%), mixed at a volume ratio of 16.1:25:58.9. The corresponding quantities of the different agents are poured in the mentioned order into a clean beaker that is held at constant 80 °C temperature. After the 15 min, the substrates are transferred to a pure DI-water bath, and after 5 min more, the latter step is repeated. From the second DI-water beaker the substrates are extracted one by one, thoroughly rinsed with DI-water and dried with N_2.

Besides of the surface cleaning, the acid bath has an additional effect on silicon substrates. Silicon has a strong tendency to oxidize. This happens when soaking it in H_2O_2, which is a strong oxidant. When both are in contact the oxidation of silicon induces the appearance of a silicon oxide layer, the thickness of which depends on the time of exposure. The reaction driving the Si oxidation ($2H_2O_2$+Si $\rightarrow$ $2H_2O$ + SiO_2) is carried out in an acidic medium provided by HCl. The acidic medium assists the protonation of the dangling oxigen bonds in the outer silicon oxide layer. OH groups are more stable than charged O^{-1} atoms and, therefore, the sulfuric acid speeds up the reaction, acting as a catalyst. On the other hand, all traces of organic materials in contact with the cleaning medium are also heavily oxidized, thereby becoming soluble in water or being released in the form of CO_2.

4.2.2.2 Patterning and cleaning of ITO glasses

The preparation of substrates for fabrication of solar cells is more complex. Solar cells are built as a stack of layers, with the topmost being the cathode, which in this work will be made of aluminum. Finished solar cells need to be contacted with metallic pins than can present sharp edges and, therefore, penetrate through the whole layer stack. Hence, this generally requires the ITO not to cover the whole substrate in order to avoid short-circuits. In this regard, prior to the cleaning procedure, the substrates for solar cells (ITO glasses, see above in section 4.2.1) are patterned to have the right shape for matching a certain device layout. The ITO areas of the substrate that are to be maintained are protected with scotch tape and the remaining areas are covered with a paste made out of deionized water (DI-H_2O) and zinc powder (Zn) mixed at a 1:1 volume ratio. Once applied, the water from the paste evaporates rapidly, leaving a thick and compact Zn layer on the ITO. Subsequently, hydrochloric acid (HCl, 37%) is mixed as well at a 1:1 volume ratio with DI-H_2O and the mixture is applied on the zinc, triggering the catalytic reaction that etches the ITO away. The samples are subsequently soaked in a DI-H_2O bath and thoroughly rinsed with DI-H_2O to remove all possible acid traces before removing the tape in order to avoid contamination of the underlying ITO.

In the work presented here, two different solar cell layouts are used, with 8 and 4 devices on each substrate, respectively. Figure 4.5 summarizes each step of the ITO etching process. Figure 4.5f displays only the patterned substrates with the corresponding OSC layout for showing how the final device array looks like. The OSC active areas under the cathodes for each corresponding layout are highlighted in orange. Further discussion on the solar cell assembly and the contact deposition is provided in section 4.4.

After removing the tape from the substrates, the patterned substrates are rinsed thoroughly with DI-H_2O again and are subsequently subjected to a four-step-solvent cleaning procedure based on ultrasonication. The substrates are put into a PTFE holder, soaked into a water-based solution of Alconox® (16 g/L, Sigma Aldrich) and are subjected to 10 min ustrasonication. The step is repeated for the solvents ehtanol (C_2H_6O, $\geqslant$ 99.8%, Carl Roth), aceton (C_3H_6O, $\geqslant$ 99.9%, Carl Roth) and, finally, isopropyl alcohol (C_3H_8O, $\geqslant$ 99.8%, Carl Roth), in the given order. Alconox® is used for removing oleaginous residues, ethanol for dissolving hydrohobic impurities, aceton dissolves tape glue traces, as well as residues from ethanol, and, lastly, isopropanol is used for removing aceton residues. Between two ultrasonication steps, a rinsing step with the outbound solvent followed by rinsing with the next one is inserted. After the last 10-minute ultrasonication, the substrates are thoroughly rinsed with 2-propanol and dried with N_2. The final

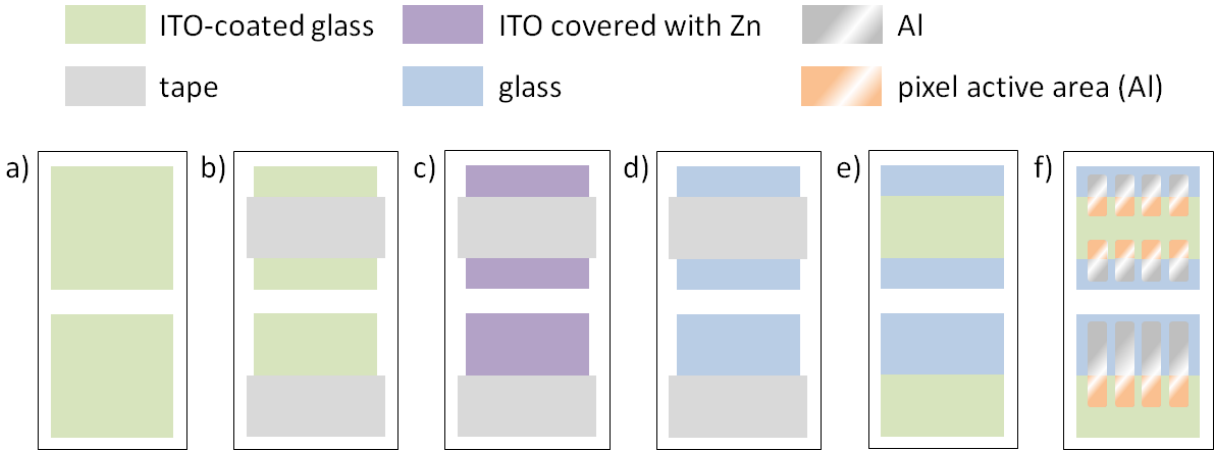

Figure 4.5: *ITO etching process. a) Initial ITO-coated glass slide. b) Scotch tape is applied to protect the wanted areas. c) The remaining areas are covered with Zn. d) The ITO under the Zn is removed with aid of HCl. e) The substrated is bathed in DI-water and thorougly rinsed. The tape is removed and the etching process is complete. f) Example of the resulting OSCs layouts and device active areas for each of the ITO patterns. The top and bottom sequences correspond to the two layouts used in the present thesis.*

step of the ITO cleaning procedure consists of an oxygen (O_2) plasma treatment. The plasma treatment consists of a high radio frequency that excites the O_2 gas at low pressure. When the O_2 molecules relax, the vacuum ultraviolet (VUV) radiation breaks very effectively most of organic bonds (i.e. C-H, C-C, C=C, C-O and C-N), thereby cleaning the substrates of any last organic trace from 2-propanol. The plasma cleaning is carried out at a Plasma-System-Nano device by Diener electronic GmbH for 10 minutes at a gas pressure of 0.4 mbar and a power or 240 W.

4.3 Fabrication of thin films

After substrate cleaning, the fabrication of thin film samples follows. Polymer thin films are usually processed from solution, meaning that they are dissolved and subsequently deposited on the clean substrates, in the case of the presented work, via spin coating or drop casting. In the following, the preparation of polymer solutions for different purposes is explained along with the description of the spin coating procedure. Lastly, the process of thermal deposition of the solar cell aluminum pixels is described along with the general annealing procedure of polymer thin film samples.

4.3.1 Solution preparation and deposition

The process of solution preparation and deposition for the different needed materials is described in the following.

4.3.1.1 Ultrasonication and filtering of PEDOT:PSS solution

PEDOT:PSS (introduced in section 4.1), purchased already in the form of a water-based solution, is stored in a fridge at a temperature below 6°C and protected from light. PEDOT:PSS tends to form large aggregates, reason for which prior to its spin coating it needs to be subjected to a purification process. For this purpose, PEDOT:PSS solution is poured into a welted glass and the solution is subsequently ultrasonicated in a water bath at RT for 15 min in order to break the eventually formed aggregates. Afterwards, the ultrasonicated solution is put into a syringe and filtered with a poly(vinyldifluoride) (PVDF) filter with a pore diameter of 0.45 μm. The PEDOT:PSS solution is afterwards ready for deposition. PEDOT:PSS solution (120 to 150 μL for a 22×22 mm^2 standard size substrate) is spin coated at 3500 revolutions-per-minute (r.p.m.) for 60 s time (acceleration parameter: 9, meaning 6 s ramping-up time). More details on the spin coating process are provided in section 4.3.2.

4.3.1.2 Organic solutions

As main constituent materials of OSCs photoactive layers, P3HT, PCBM (and blends of both) and PBST3HT films are especially closely studied. In the frame of this work, solutions of these materials are made with either CB or TL as a solvent (introduced in section 4.1). First, a welted glass along with a stirring bar is cleaned with the solvent in use and dried with N_2. The glass with the stirring bar in it and its cap is placed on a 0.01 mg-precision scale (BP210D by Sartorius) and their tare is subtracted from the total weight. Subsequently, the needed amount of solid-state polymer is put in the welted glass with a lab spatula cleaned with ethanol and dried with N_2. Subsequently, the weight of the polymer phase is controlled and the volume of solvent required for achieving a desired concentration is mixed in the welted glass. In the presented thesis, P3HT, PCBM and P3HT:PCBM solutions were prepared at a concentration of 16 $^{\text{mg}}/_{\text{mL}}$ unless stated otherwise. PBST3HT solutions are prepared at 18 $^{\text{mg}}/_{\text{mL}}$ for spin coated thin films and at 50 $^{\text{mg}}/_{\text{mL}}$ for drop-cast thick films.

Once the components of the solution (polymer and solvent) are mixed, the solutions are sealed with Parafilm® and the glasses are placed on an magnetic stirrer in order to improve the dissolution of the organic phase. Solutions are generally stirred for a period of time between 2 and 3 hours. In the case of CB-based P3HT, PCBM or P3HT:PCBM solutions, the stirring happens at RT. In the case of TL-based P3HT, PCBM and P3HT:PCBM solutions, due to the lower solubility of the organic phase, the solution is stirred while placed in a sand bath at a constant temperature of 45°C.

After the stirring time is over and the solution turns clear (though colored) and homogeneous, it is deposited onto the clean substrates. P3HT:PCBM solutions are spin coated (120 to 150 μL for substrate) at 2000 r.p.m. for 30 s (acceleration parameter: 9). Spin coated PBST3HT films are deposited at 1500 r.p.m. as well for 30 s (acceleration parameter: 9). Drop-cast PBST3HT thick films for SAXS/WAXS transmission measurements are fabricated by depositing 50 $^{mg}/_{mL}$ PBST3HT solution onto a mica window and let it dry in air atmosphere at RT for approximately 3 hours. In the case of P3HT:PCBM solutions, both P3HT and PCBM solutions are stirred under the above-mentioned solvent-dependent conditions for a time between 1 and 2 hours. Afterwards, the solutions are mixed at a 1:1 ratio and the resulting mixed master solution is sealed again in its glass with Parafilm® and further stirred for the remaining time.

Many experiments in the presented work discuss the effect of small superparamagnetic iron(II,III) oxide NPs (introduced in the materials section 4.1) on the performance of P3HT:PCBM OSCs. The NPs are purchased in TL solution. Hence, these studies are done with as well TL-based P3HT:PCBM solution. In order to incorporate the NPs into the master solution, the Fe_3O_4 NPs solution is first ultrasonicated for 10 min at RT for ensuring homogeneous disperson of the NPs in the solvent. Afterwards, the NPs solution is added stepwise to the P3HT:PCBM master solution prior to the spin coating of each desired NP wt.% sample, whereby the samples are spin coated in increasing order of NP concentration. The deposition starts with a known amount of P3HT:PCBM master solution, to which the corresponding amount of NP solution to achieve the desired NP wt.% is added. This already modified master solution is ultrasonicated again for 30 to 60 s to further ensure homogeneous distribution of the NPs in the master solution. Then, the sample is spin coated according to the above-mentioned parameters, and, with the (known) remaining amount of master solution and its current NP concentration, the complementary amount of NPs is added to achieve the next higher desired NP wt.%. The newly modified P3HT:PCBM master solution is ultrasonicated for between 30 and 60 s again, and the new sample is spin coated. This process is further repeated for all desired NP concentrations.

4.3.2 Spin coating

Spin coating is one of the most used coating techniques for lab-scale thin film fabrication. It enables attainment of homogeneous films with thicknesses of up to 1 μm. A substrate is placed on a rotatory plate, to which the substrate is generally fixed via vaccuum pulling from the back side through a pipe along the rotational axis of the plate. The whole substrate is covered with solution, and the rotation starts immediately thereafter. In

the beginning of the rotation, the excess solution is expelled from the substrate through centrifugal forces. The film forms assisted by convection, whereby the solute starts adhering to the substrate and accumulating. Finally, a homogeneous thin film forms and the remaining volatile solvent evaporates.

The thickness of spin-coated polymer films can be parametrized with the Schubert equation as long as the viscosity of the solution can be neglected:[125]

$$d = A \left(\frac{1950\ min^{-1}}{\omega}\right)^{\frac{1}{2}} \left(\frac{c_0}{20\ mg\ mL^{-1}}\right) \left(\frac{M_\omega}{100\ kg\ mol^{-1}}\right)^{\frac{1}{2}} \tag{4.1}$$

where ω corresponds to the angular velocity and c_0 to the concentration of the polymer in solution. A is a scaling parameter that depends on constraints like the specific spin coater used, or environmental factors, such as temperature or moisture. The spin coated films reported in this thesis are fabricated with a Delta 6 RC TT device by Süss MicroTec Lithography GmbH.

4.3.3 Thermal deposition

In the fabrication of solar cells the deposition of a back electrode (in the case of our work, where all solar cells are made in standard, non-inverted geometry, a cathode) is required. The cathode is pure aluminum and, hence, difficult to process and apply from solution, as opposed to previous layers. Therefore, Al contacts are deposited on the OSC layer stack directly from the gas phase via physical thermal deposition. Cathode evaporation is carried out at a custom-made evaporation setup designed by Robert Meier.[126] The setup consists of a closed evaporation chamber, at the bottom of which a tungsten boat (BD482000-T tungsten boats by Leybold Oerlikon) is fixed between two electrodes. This tungsten boat is subsequently filled with the required amount of aluminum, in our case 100 to 150 mg. Afterwads, an evaporation mask is placed about 30 cm above the boat. The masks contains eight slots for placing substrates upside down, and the floor of the mask has at each of the slots the desired OSC layout carved in it. Once the substrates are placed, the chamber is closed and the cathode deposition is carried out at a pressure of 1 to $3 \cdot 10^{-5}$ mbar. An electrical current is forced to flow through the tungsten boat until the generated elevated temperatures induce the evaporation of the aluminum, which ultimately adheres to the sample through the mask, thereby yielding the desired contact layout. The two layouts used in the present thesis are schematically depicted in figure 4.5f. The final contacts have a typical thickness of 60 to 100 nm.

4.3.4 Thermal annealing

Thermal annealing is an important processing step in the fabrication of OSCs. Annealing provides the polymer films sufficient energy for allowing them to relax to an equilibrium state, since films are not in equilibrium after the spin coating. This has in general an effect on the nanomorphology and on the crystallinity of the materials, also for P3HT:PCBM blends for OSC active layers.[127–129] Moreover, in the case of PEDOT:PSS films, annealing is key for extracting all remnant water stored in the film prior to deposition of another polymer film, making this an important impact on the performance of a final device. Annealing helps as well providing an improved contact between polymer film and aluminum layer after cathode deposition. Annealing is carried out at a RCT basic heat plate by IKA Werke GmbH & CO. A copper plate that ensures homogeneous temperature distribution is mounted on the plate. Active temperature control is enabled via a contact thermometer inserted into the copper block.

4.4 Assembly of solar cells

OSCs feature the most complex type of samples fabricated in the frame of this thesis, since they are composed of several layers following different fabrications procedures. The fabrication of OSCs gathers most of the procedures introduced along the whole chapter 4.

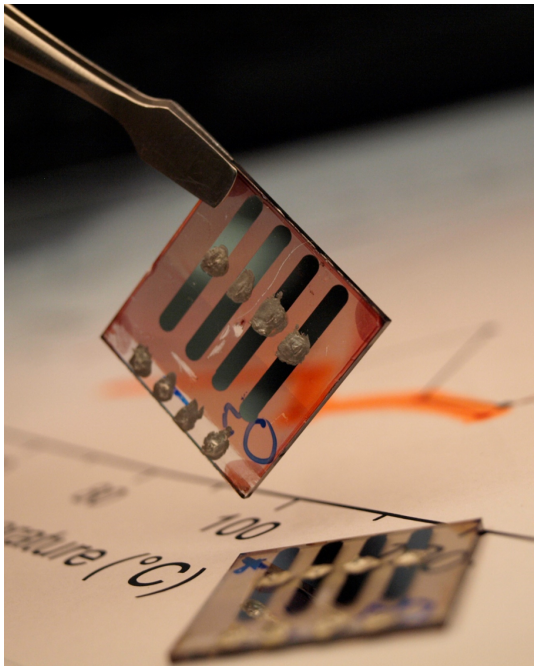

Figure 4.6: *Lab-scale OSCs fabricated on ITO glasses with a four-device layout.*

As previously stated, the stack of organic layers that builds up the solar cell needs to be fabricated on top of a transparent electrode, which in the case of our standard geometry OSCs serves as an anode. This anode needs to be transparent, since the sunlight first passes this layer before reaching the photoactive layer. In our work, ITO-glass slides are chosen. The substrates are generally of $22 \times 22 mm^2$ size and, in order to avoid short-circuit contacts between anode and cathode when characterizing them at the very end, the ITO coating is patterned according to the desired final cathode layout. The patterning is done via an acid etching process, driven by a catalytic reaction between zinc and hydrochloric acid (the devices are a couple

hundreds of nm thick, therefore the contacting with test pins could drill though the whole stack, leading to short-circuited contacts). The substrates are subsequently cleaned in a four-step-solvent process and a 10-minute plasma treatment. Detailed description on the process of ITO-glass patterning and cleaning is provided in section 4.2.2.

PEDOT:PSS solution is ultrasonicated and filtered during the last cleaning step of plasma treatment and spin coated on the clean ITO substrates (details on PEDOT:PSS solution preparation and spin coating in section 4.3.1. Details on spin coating as deposition method in section 4.3.2). The PEDOT:PSS films are afterwards annealed in air atmosphere for 10 minutes at 140°C (details on annealing in section 4.3.4). During the annealing, the substrates are partially covered in order to avoid dust particles adhering on the PEDOT:PSS film, but not completely covered in order to avoid the creation of a humid environment out of the water released by the film during the heating.

Afterwards, the active layer of the OSC is deposited on top according to section 4.3.1. The Al back contacts are subsequently evaporated (section 4.3.3). Finally, after deposition, the layer stack is annealed at 140°C for 10 minutes in a glovebox (N_2 atmosphere, < 0.1 ppm H_2O and O_2). After the annealing step, the OSCs are ready for subsequent I-V characterization (details in section 3.2.3).

Solar cells are contacted with specially designed holders (details in appendix A) featuring gold-capped test pins that grant homogeneous contact throughout all the OSCs fabricated on one substrate, which are contacted simultaneously. Homogeneous electrical contact is provided by the springs to which each test pin is attached. OSCs not measured using the mentioned holders are characterized using adjustable-height electrical pin holders, which contact each OSC individually and sequentially. In this cases, homogeneous contact is guaranteed by the use of conducting silver paste.

Chapter 5

Heavy-chalcogenophene-based oligomer for solar cell applications

Hereby, we open the results part of the present work, done within the framework of the broader topic of improving organic solar cell performance via control of the exciton diffusion length. The present chapter discusses the temperature-resolved characterization of a novel chemically-engineered heavy chalcogenophene-based oligomer. This material is designed in pursuit of tuning the charge carrier statistics, for ultimately improving device performance. The material presents an interesting behavior featuring a varying material band gap depending on the processing temperature. Furthermore, the first attempts to incorporate this oligomer as photoactive material in organic solar cells are presented, as well as the study of its behavior and properties within a real device. The article *Band gap-tuning in triple-chalcogenophene polymer films by thermal annealing*, published and cited in this thesis as reference [16], contains parts of the data discussed in this chapter.

5.1 Introduction

OSCs present many advantageous mechanical, optoelectronic, and even cost-related properties as compared to traditional inorganic counterparts. These have turned out not to be enough for warranting deployment of such technologies at an industrial and commercial level. As previously discussed, two of the main weak points are short device lifetimes and still relatively low efficiencies (champion lab devices surpassing 11 % and operational modules yielding around 10 %[8,130]). These bottlenecks hinder the spread of OPV despite a low price per kW and short payback times.[7] Hence, further breakthroughs in boosting efficiency values while keeping potentially competitive costs are the focus of numerous research groups.

One of the most important aspects to consider when approaching the increase in efficiency is the influence of the morphology of the layers composing the device. Especially to that of the photoactive layer. The introduction of the BHJ concept meant already a significant step forward compared to single-material or flat-interface OSCs.[131,132] In this configuration the donor and acceptor molecules of the device photoactive layer are mixed in solution yielding a nanoscale bicontinuous blend. However, the intermixing between donor and acceptor phases still sets a bottleneck on subsequent device performances, since the exciton diffusion length determines the optimal mean distance between donor (D) and acceptor (A) that ensures maximum splitting rate. The exciton diffusion length for model systems like P3HT lies somewhat below 10 nm.[43,44,133]

This has lead considerable research effort towards optimization of the D/A morphology, featuring various approaches to ensure exciton diffusion length-compatible D-A morphologies. Some of them include nanostructuring, tuning of the solvent composition, or introduction of solvent additives for morphology control, such as, e.g., diiodooctane or octanedithiol, amongst others.[62,63,134–140] Nevertheless, most of these techniques suffer from diverse setbacks. On the one hand, morphology-tuning approaches do not generally have direct control over the morphology, but rather try to improve it by trial and error, based on yet poorly understood physical and chemical processes. On the other hand, as is the case for nanostructuring, they face the technical challenges derived from trying to directly tailor the morphology at such short length scales, e.g. the fabrication of nanostamps.[63] Consequently, the opposite approach has been recently hauling increasing interest, i.e. to tune the exciton diffusion length to aid it matching a given active layer morphology.

Adjustment of the exciton diffusion length requires tuning of its lifetime. Its core idea is to influence the exciton spin statistics, taking advantage of the quantum selection rules. The aim is to favor the ISC of the excited singlet excitons into the triplet manifold, thereby lowering the decay rate. The recombination from the triplet excited state to the singlet ground is, in principle, forbidden, making phosphorescence a low-efficiency decay mechanism. The physical principles behind it are introduced and discussed in detail in section 2.3.

In practice, this is generally achieved with small organic molecules that contain heavy metallic atoms, and the process is long-known and established in organic light-emitting diode (OLED) research. They are commonly known as *triplet emitters*. OLEDs present exactly the opposite problem than OSCs. In order to illuminate featuring the highest efficiency possible, OLEDs try to maximize the recombination of positive and negative

polarons that are electrically pulled from the outside into the active layer. However, in the case of OLEDs, since the carriers are not optically excited, their distribution of spins follow the regular statistics: 75 % triplet and 25 % singlets. As previously discussed, only the singlet excitons are allowed to recombined radiatively, feature that limits the theoretical OLED efficiency to 25 %. Therefore, triplet emitters are incorporated into OLEDs to allow the rate of radiatively recombining excitons to exceed one quarter, via increasing the efficiency of the phosphorescence decay mechanism (see section 2.3 for the theoretical discussion).

Thus, the same principle is considered for OSCs in order to solve the opposite problem, i.e. to induce ISC from the singlet to the triplet manifolds of the 100 % singlet photogenerated excitons. This approach has been already used in OSCs, featuring modified active layers with low weight percentages of doping molecules that have yielded satisfactory results.[141–143] However, as mentioned above, phosphorescent agents successfully incorporated into OSCs are mainly featured by small molecules with coordinated heavy metallic atoms. These small molecules are used as dopants of OSC active layers otherwise fabricated with regular and well-known photoactive materials. Whilst their incorporation demonstrably contributes to the reduction of the device polaron pair recombination and to the elongation of excitons lifetimes, the desirable goal on a longer run is rather to achieve such effects in long macromolecules featuring high molecular weights. Thereby, instead of having sparsely distributed ISC-centers in organic devices, we can aim for long conjugation lengths with nanoscopic intra-molecular transport of triplet polarons. So far, partially successful work has been done in this area of introducing heavy main group elements in polymers, featuring mainly metals or metalloids from the groups 13 to 15 of the periodic table. So far these have mainly been germanium (Ge), tellurium (Te), tin (Sn) and gallium (Ga). Hereby, to date BHJ OSCs with active layers containing Ge and Se have delivered successful results, featuring efficiencies ranging from under 1 % up to 8.20 % in the case of Ge-containing macromolecules, and between 2 % and 4.5 % for Se-based polymers. All of them after device optimization and eventual use of solvent additives.[144] Nevertheless, Ge is still light compared to the metals that are known to carry significant degrees of L-S coupling.[145] In the longer run, attainment of macromolecules with transition-metal heteroatoms of the periods five or six is desirable, as it is currently the situation for triplet-emitting small molecules, which mostly present iridium (Ir) or platinum (Pt) metallic heteroatoms.

In pursuit of this goal, in the present chapter we study fundamental and operational properties of the novel triple chalcogenophene-based oligo poly-(3-hexyl-2(3-(4-hexylthio-

phene-2-yl)-4,5-butylselenophene-1-yl)-5-(4,5-butyltellurophene-1-yl)thiophene), or PBST-3HT for short. Te is a metalloid of the period five, situated already at the right height of the periodic table. Moreover, Te is about 76 % heavier than Ge, thereby presenting expectedly much higher rates of L-S coupling. PBST3HT consists of a repeating monomer formed by a hexylthiophene-butylselenophene-hexylthiophene-butyltellurophene sequence, featuring molecular weights in the oligomeric range. This feature, combined with the high ring coplanarity associated to polyselenophenes, enables potential for building long intramolecular π- conjugated bands, along which triplet polarons (ISC-crossed due to the presence of tellurium along the conjugated backbone) are transported. Spectroscopic as well as morphological characterization in section 5.2 reveals versatile band gap-adjusting properties as well as potential control of the material packing. Hereby, and in order to better understand the intrinsic molecular behavior, we combine the analysis of the morphological and crystalline evolutions with computationally optimized models that provide further insight into energetically favorable morphologies. Section 5.3 presents the first attempts to incorporate PBST3HT into organic solar devices. The main challenges still presented by the material will be identified from in-device performance, along with interesting aging-related effects that set possible benchmarks for further research on PBST3HT.

5.2 System characterization

PBST3HT presents heavy chalcogen atoms in a long conjugated backbone, i.e. in the region of most efficient charge transport. Selenium (Se) and tellurium (Te) heteroatoms contribute with various advantages that are expected to increase OSC performance.[146] On the one hand, polyselenophenes present generally narrower band gaps than the more common and far better characterized poly-(3-hexylthiophene-2,5-diyl) (P3HT), with the lighter chalcogen sulfur (S) as heteroatom. This comes as a result of the lower ionization potential of Se compared to S, as well as of a higher ring coplanarity, which allows π-delocalization over larger molecular regions. The two effects lead to narrower band gaps that result in improved light absorption properties.[120,147,148] On the other hand, tellurium, which is a semimetal, provides PBST3HT with organometallic properties, through e.g. metal-to-ligand bonds, which increase the spin-orbit (L-S) coupling in the delocalized π regions and, consequently, the ISC. Hereby, presence of Te helps tuning the average exciton lifetime through tailored spin statistics, arguably leading to a higher rate of triplet excitons. This approach aids the tuning of molecular singlet and triplet yields and is explored already for long time in OLED research.[149–152] The physics governing such phenomena are discussed in detail in section 2.3.

5.2.1 Spectral response of thin films to temperature

Figure 5.1 displays an energetically optimized arrangement of the PBST3HT monomer, according to simulations performed at the MM2 Force Field level of theory in the gas phase (simulations have been carried out by Prof. Alex Brown at the Chemistry Department of the University of Alberta, Canada). The results show the emergence of a dihedral angle θ between the central thiophene, with the S heteroatom displayed in yellow, and the selenophene, with the Se atom in red. This tendency is confirmed by further calculations performed at other levels of theory, like for the Universal Force Field (UFF) and the Density Functional Theory (DFT) frameworks. Besides the fact that the different formalisms yield different values for θ ($\theta_{MM2} = 50°$, $\theta_{UFF} = 110°$, $\theta_{DFT} = 69°$), the repeated attainment of a non-coplanar monomer poses questions on the availability of long delocalized π-conjugated regions. This twisted morphology could, moreover, clash with the highly attractive Te—Te interactions of the tellurophene units.[153–155] Thus, the potential competition between these effects adds uncertainty on the direction of the evolution towards equilibrium of the material morphology upon temperature treatment. Consequently, the characterization of PBST3HT is done with respect to temperature. Moreover, temperature-resolved characterization is important, since temperature is a key parameter in the OSC production process.

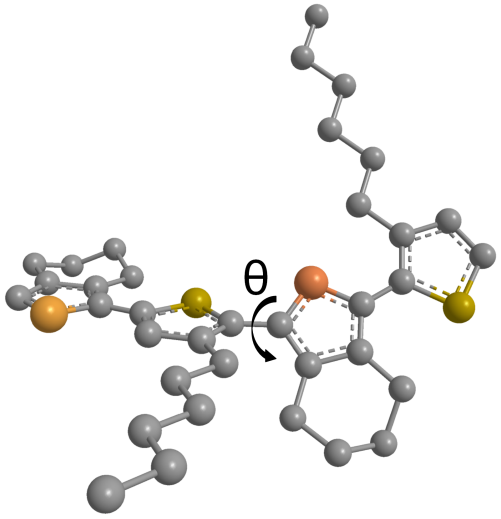

Figure 5.1: *3D representation of a BST3HT monomer displaying an energetically-optimized configuration according to MM2 force field calculations. The different colors represents different atomic species: yellow:S, orange:Te, red:Se, gray:C. H atoms are omitted for clarity of the presentation. Figure taken from* [16].

PBST3HT characterization is partly performed on thin film samples, since the solar devices are composed of stacked thin films. For their study, thin layer samples were fabricated according to the details given in sections 4.2 and 4.3. The absorption response as a function of the temperature of 60 nm-thin PBST3HT films has been investigated. The UV/Vis experiments are carried out with in-situ varying temperature, from RT to 150 °C and back to RT in steps of 10 °C.

Figure 5.2 displays the obtained optical behavior. The obtained absolute absorbance values are displayed in figure 5.2a. Figure 5.2b displays the absorbance curves artificially

shifted along the ordinate axis for clarity of the presentation. The absorbance presents an onset at around 650 nm and two additional transitions at 460 and 500 nm. The absorption spectrum remains unchanged up to approximately 80 °C, presenting the mentioned absorption onset that corresponds to a band gap of around 2 eV, giving the samples their characteristic red color.

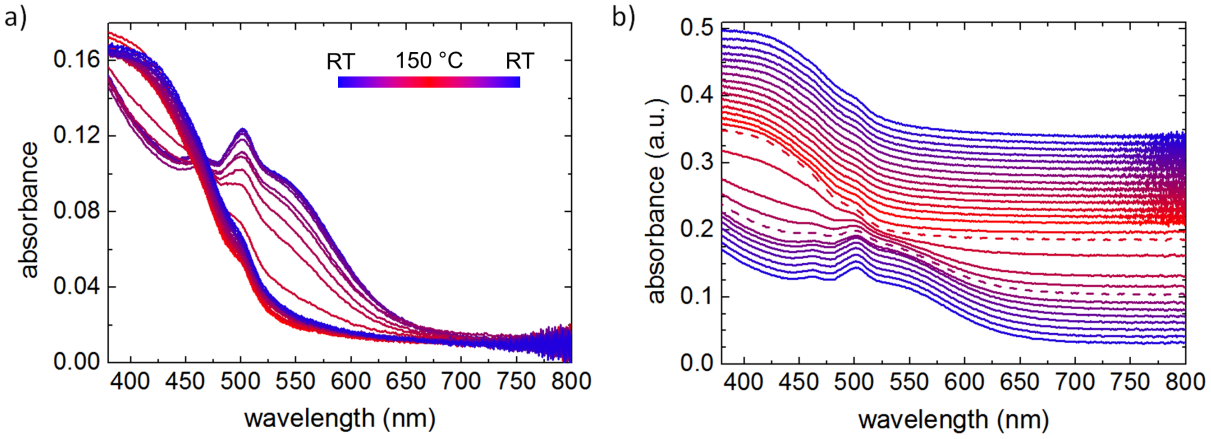

Figure 5.2: *a) Absorbance evolution with temperature of a PBST3HT thin film. The color gradient depicts the evolution from RT to 150 °C and back. b) Shifted spectra from bottom to top for clarity of the presentation. Dashed lines display the absorbance curves at the two transition temperatures, 90 °C and 130 °C. Figure taken from* [16].

At around 90 °C the spectrum begins to change. It features an hypsochromic shift. This is an indicator that the optical band gap increases. The process of blue-shifting spans over approximately 40 K range, and ends at approximately 130 °C. Once the shift is completed the absorption onset lies at around 530 nm, corresponding to a larger optical band gap than before. Optically, the samples display a yellow color after the annealing. The observed shift in the absorption onset is ascribed to a reorganization process induced by self-assembly of the tellurium units. In the new state, the earlier soft transition at 460 nm becomes nearly invisible due to merging with the shifting main absorption feature. The spectra remain further unchanged upon cooling back to RT.

The relatively slow and traceable transitioning process observed in the absorption spectrum allows a certain degree of control of the absorption onset, and, consequently, the final material band gap. The combination of absorbance and thickness data allows for determination of the absorption coefficient $\alpha(\lambda)$, which at the same time allows for construction of the so-called Tauc plots $(\alpha(\lambda)E)^n$ vs. E, where E is the energy of the incoming photons. The process of calculation of the absorption coefficient is described in detail in section 3.2.1 and greater insight on the Tauc plot is provided in the literature.[156–158] The Tauc plot allows estimation of the optical band gap through interpolation to no-absorption of

the

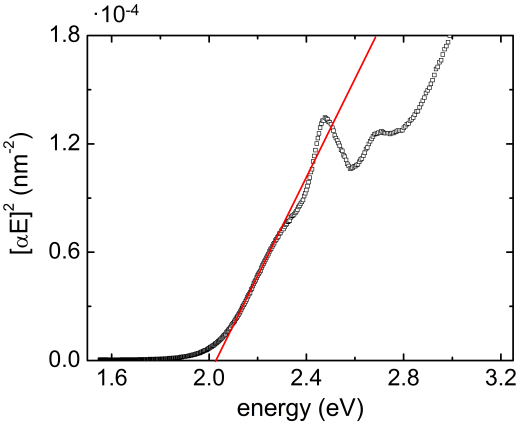

Figure 5.3: *Exemplary Tauc plot (black points) and the corresponding fitting of the absorption onset (red) line that allows for determination of the material optical bandgap.*

$\alpha(\lambda)E$ onset. An example of the Tauc plot and the corresponding fitting of the absorption onset for PBST3HT at RT is displayed in figure 5.3. Figure 5.4 shows the optical band gap obtained for PBS3HT as a function of temperature. At RT the band gap is estimated to be slightly above 2 eV. At 90 °C, the temperature that marks the beginning of the transition temperature range (indicated on figure 5.4a by the orange box), the band gap shows a strong increase, indicating the beginning of the reorganization process. The process ends up with an optical band gap of approximately 2.35 eV. The temperature step between 110 and 120 °C features the most abrupt band gap change, featuring by itself already a change of about 0.2 eV. The overall change in band gap, blue-shifting the overall absorption spectrum can as well be observed by naked eye in the color change of the deposited thin films (see figure 5.4b).

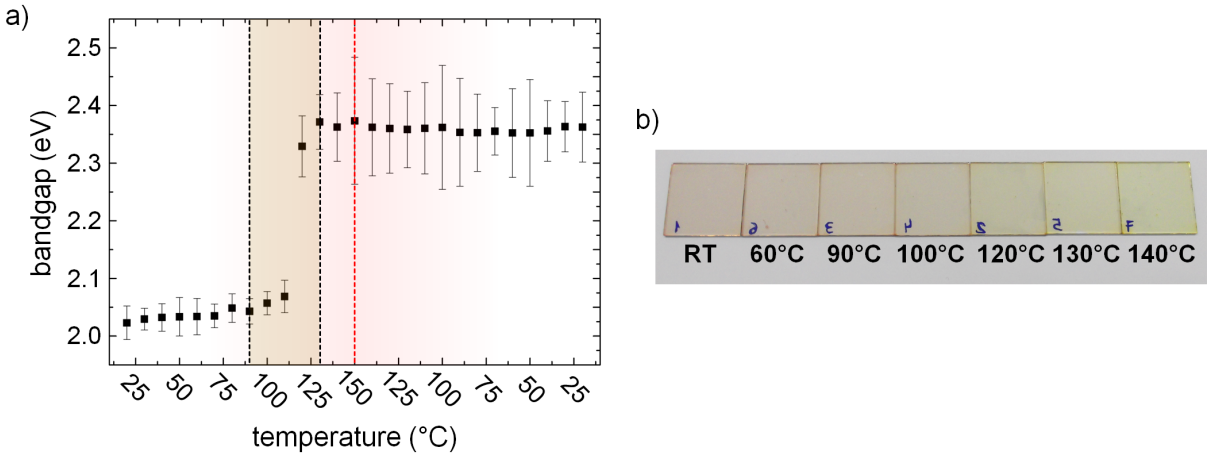

Figure 5.4: *a) Evolution with temperature of the PBST3HT optical band gap, according to the Tauc plot extrapolation obtained from UV/Vis data. The orange box depicts the temperature transition range between 90 and 130 °C. The red dashed line represents the transition between heating and cooling protocols. b) Color change of PBST3HT homogeneous films after annealing at different temperatures. Figure adapted from* [16].

Studies on polytellurophenes report that the energies of their molecular orbitals (and consequently, the absorption onsets and band gaps) can be controlled via coordination

chemistry on Te centers, e.g. by exposure to Br_2.[154] Hereby, Br_2 molecules coordinate around the Te centers, forming $TeBr_2$, drastically altering the HOMO and LUMO levels of the materials, and thereby allowing control of its optical properties.[159–161] Thus, the presently observed effect is not related to the presence of Br_2 and seems more related to the material morphology. This can be the tendency of Te atoms to coordinate via strong Te—Te intra- and/or intermolecular interactions, that have an influence on the overall solid-state morphology and cause the observed change in the material band gap.

5.2.2 Morphological changes in thin films upon annealing

Temperature [°C]	σ_{RMS} [nm]
RT	0.6±0.1
40	0.6±0.1
60	0.4±0.1
70	0.5±0.1
90	0.4±0.1
100	0.5±0.1
130	0.4±0.1

Table 5.1: *Root mean squared roughness (R_{RMS}) values of PBST3HT films annealed at different temperatures.*

The films, presenting thicknesses of around 60 nm, are measured with XRR (details of the measurement method in section 3.1.2). The obtained XRR data as well as the parameters and SLD profiles extracted from the corresponding fits are displayed in figure 5.5. The samples were annealed at different temperatures and scanned at RT. The modeling of the vertical SLD profile is done by assuming a main central bulk phase and two much thinner interfacial layers at the polymer-substrate and the polymer-air interfaces. The measurements at various temperatures present Kiessig fringes, indicating smooth sample surfaces. The root mean squared roughness (R_{RMS}) values for the top interface obtained from the fits are summarized in table 5.1. Fitting of the XRR curves provides as well information on the vertical SLD distribution, which is displayed in figure 5.5b. All samples display approximately the same bulk SLD of around $1.3 \cdot 10^{-5}$ Å. By increasing temperature, the SLD of the thin top layer seems to decrease, from starting values of almost $1.5 \cdot 10^{-5}$ Å for non-anealed (RT) samples down to values below $13 \cdot 10^{-6}$ Å for samples annealed at 130 °C. On the other hand, the thin layer modeled close to the silicon substrate does not seem to follow a clear trend.

High resolution SEM measurements (details of the method in section 3.1.1) are as well performed on the thin films to characterize potential morphology changes appearing upon temperature treatment. For SEM measurements, the films are spin coated on clean, non-etched ITO substrates (details in chapter 4).

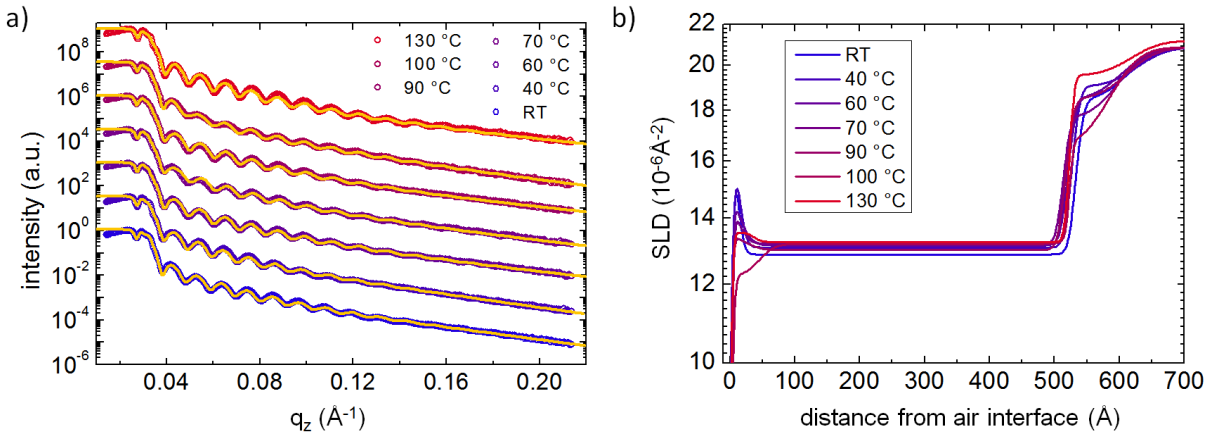

Figure 5.5: *a) PBST3HT XRR curves obtained for samples annealed at different temperatures. Colored circles correspond to the data whilst orange lines indicate the fit. b) Resulting SLD profile obtained from the fits to the XRR data. The origin of the x-axis correspond to the PBST3HT-air interface. Figure taken from [16].*

The SEM pictures are shown in figure 5.6. They show a drastic change in morphology in agreement with the UV/Vis data. At low T, a rather homogeneous morphology is obtained, with small and weak lighter regions assumed crystalline, and featuring as well some darker spots. Above 90 °C, the morphology displays a qualitative change. The contrast between the different phases in the film increases. The darker spots grow in size up to some tens of nm, and the assumed crystalline lighter regions grow for high temperatures, featuring sizes of up to several hundreds of nm, even reaching the μm range. Similarly to XRR, SEM samples were annealed by the temperatures indicated in figure 5.6 and afterward scanned at RT.

5.2.3 Morphological and crystalline development in the bulk

The observed changes in PBST3HT absorption spectrum involve a change in the material band gap, presumed to be morphology-related. After this correlation with the morphology has been observed from SEM measurements, the changes in the inner morphology of the material upon thermal annealing are recorded as well. This is accomplished via SAXS/WAXS transmission measurements in vacuum. Like in the UV/Vis characterization, SAXS/WAXS is performed with in-situ control of the sample temperature. The measurements are carried out on drop-cast thick films, starting at 25 °C and subsequently from 30 to 150 °C, with 10 °C step between measurements. Once the heating protocol is completed, the process is repeated in reverse down to 25 °C. The combined SAXS/WAXS q-range spans from $5 \cdot 10^{-3}$ Å^{-1} to 2 Å^{-1}. This allows for characterization of structures with sizes or characteristic distances ranging from few Angstroms to tens of nanometers. The obtained data sets and the corresponding fittings

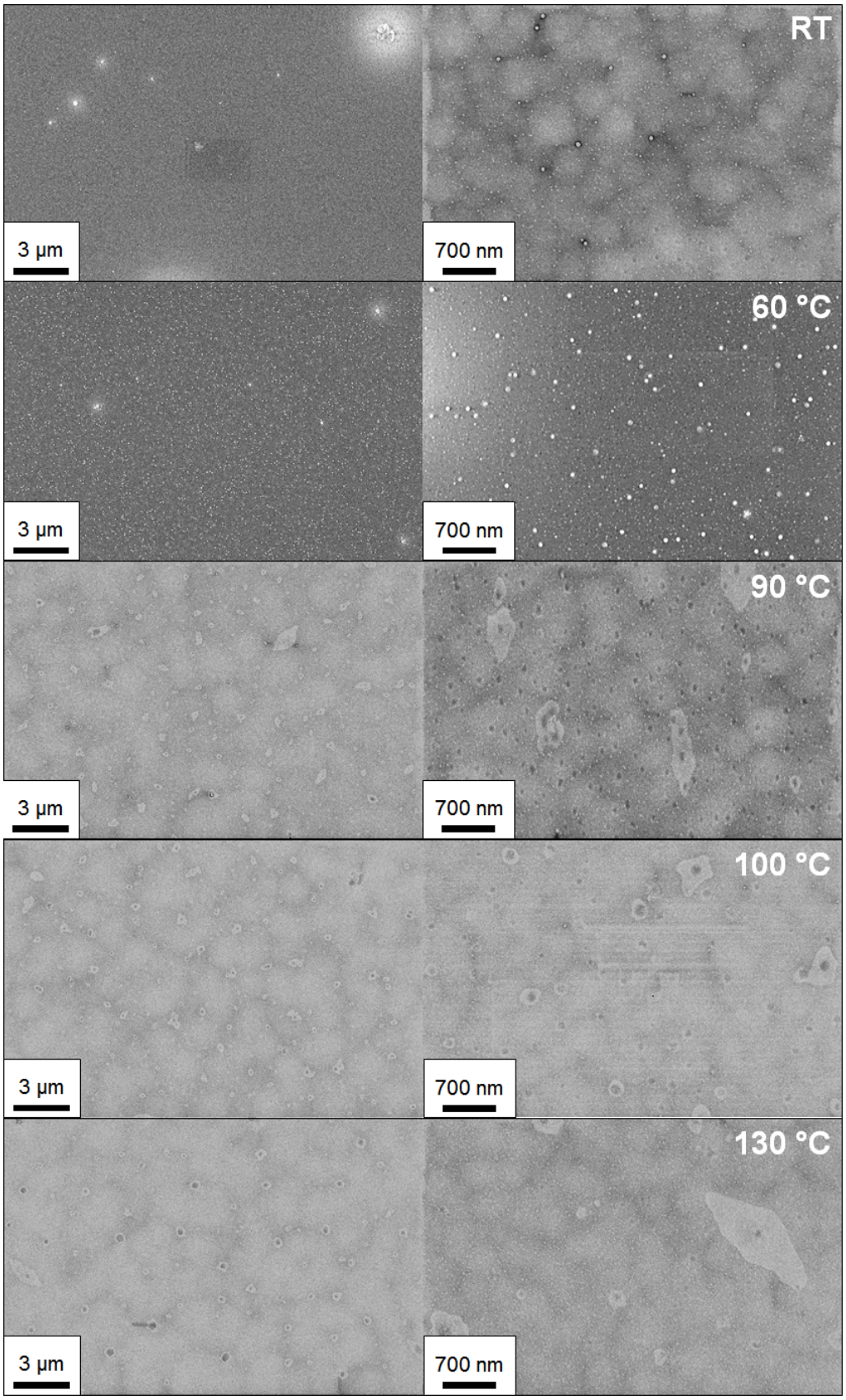

Figure 5.6: *Top-view SEM images for different magnifications of PBST3HT samples annealed at different temperatures. Figure taken from [16].*

are presented in figures 5.7 and 5.8. Details on the models used for the fitting are available in sections 2.4.2 and 2.4.3.

SAXS sections of the data are fitted, on the one hand with a Porod decay ($I_{Porod} \propto q^{-4}$) that accounts for the intensity contribution of big objects not resolvable with the used setup (below $q = 10^{-2}$ Å^{-1} in the main panel of figure 5.7). On the other hand, for low temperatures ($< 90°C$) the fitting includes as well an Ornstein-Zernike term with a size of 39.6 ± 0.9 Å. At 100 °C a remarkable feature appears in the q-range of $2 - 3 \cdot 10^{-2}$ Å^{-1}, indicated by the large arrow in the main panel of figure 5.7. It develops further for increasing temperatures, even developing a second-order shoulder, which indicates well-defined domains. Modeling of these domains has been attempted with form factors of different shapes, mainly cylinders, spheres and, finally, lamellae. The modeling has been only successful with spherical form factors, which indicates a certain degree of 3D isotropy in the domain formation.

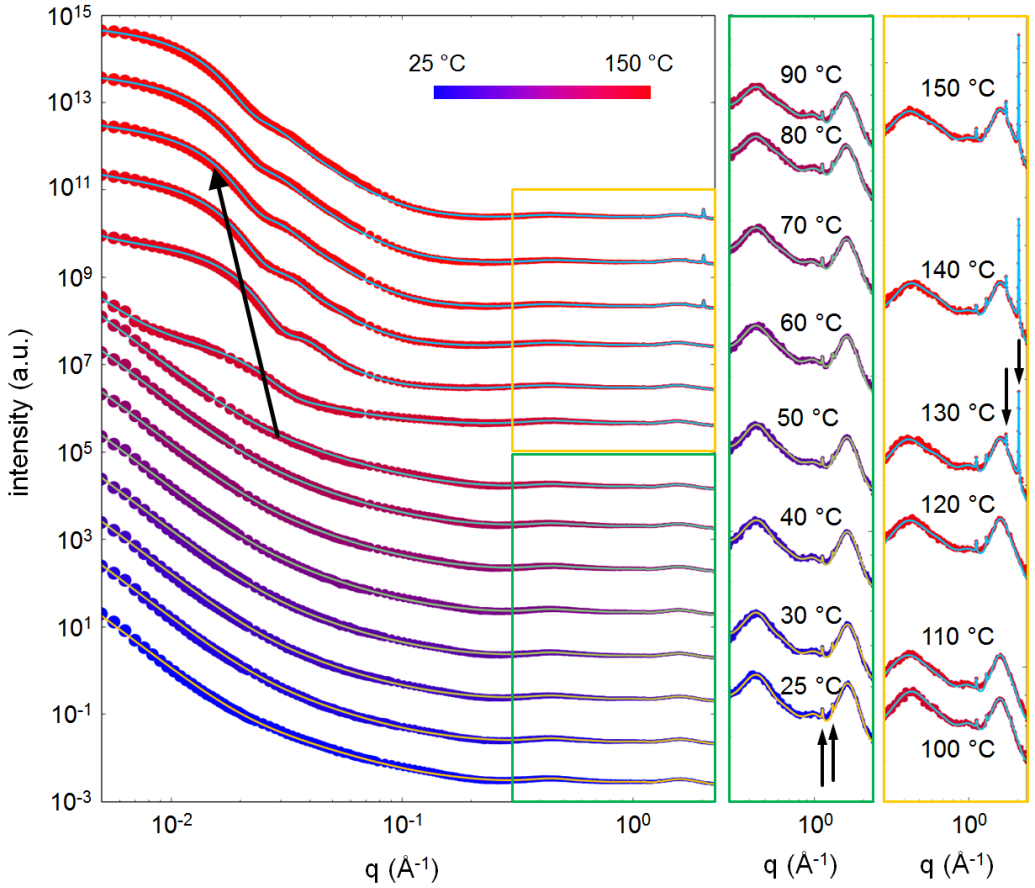

Figure 5.7: *SAXS/WAXS integrated data curves for in-situ annealing PBST3HT samples during the heating protocol. The green and yellow insets depict the WAXS region with greater detail. Points correspond to the data while the lines indicate the fit. Curves are vertically shifted for clarity. Figure adapted from* [16].

The change in mesomorphology of PBST3HT upon thermal treatment happens along with changes in the crystalline arrangement of the material as well. Both yellow and green insets in figure 5.7 display the WAXS sections of the x-ray scattering data for the heating run.

A crystalline structure featuring sharp Bragg peaks at 4.86 ± 0.02 Å and 5.60 ± 0.02 Å are present (indicated by the two black arrows on the 25 °C curve). These persist for the complete heating run. However, at 130 °C, observed as the end of the temperature transition range observed in UV/Vis, two new peaks appear, indicating the transition to a new crystalline phase.

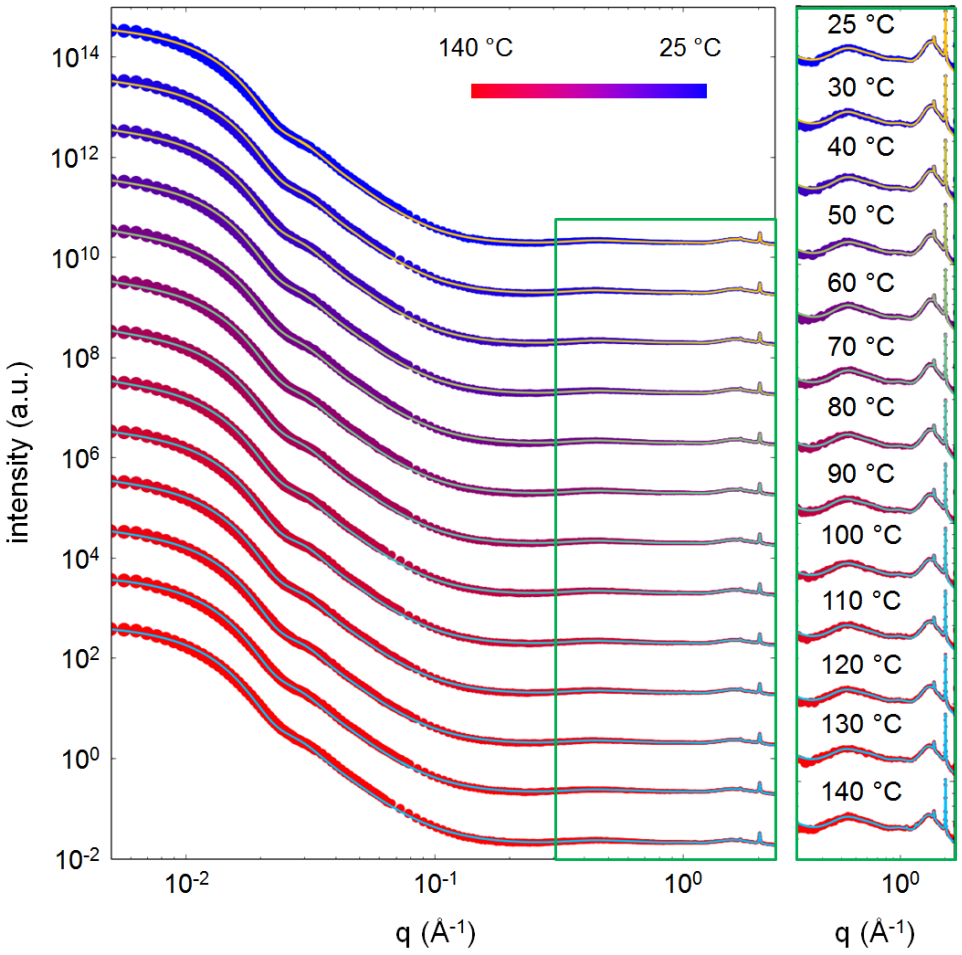

Figure 5.8: *SAXS/WAXS integrated data curves for in-situ annealing PBST3HT samples during the cooling protocol. The green inset depicts the WAXS region with greater detail. Points correspond to the data while the lines indicate the fit. Curves are vertically shifted for clarity. Figure taken from* [16].

Figure 5.8 shows the datasets obtained in the subsequent cooling procedure. The thermal

annealing has brought the system to a more stable morphology. Therefore, the meso-morphology data obtained from SAXS remains constant for the whole run. Regarding the crystallinity of the films, when cooled below 140°C, the crystalline phase originally present during the heating cycle from 25°C to 130°C, represented by the two Bragg peaks at 4.86 ± 0.02 Å and 5.60 ± 0.02 Å disappears completely. This indicates the completion of the irreversible crystalline transition.

Figures 5.9 and 5.10 display the summary of the obtained parameters in the SAXS/WAXS fitting. Figure 5.9 summarizes the emergence and development of the spherical domains in the mesoscale (SAXS) introduced above. As mentioned, the objects appear at 100 °C and grow in size and concentration up to a temperature of approximately 130 °C, after which both trends plateau. The obtained SLDs associated to the domains and to the polymer matrix are $1.89 \cdot 10^{11}$ cm^{-2} and $1.265 \cdot 10^{11}$ cm^{-2}, respectively. The starting value for the fitting of the SLDs of the polymer matrix was obtained from XRR measurements. Hereby, the final SLD value obtained for the matrix is lower than the starting one, and the final SLD of the spherical domains is about a 15% larger than the starting value obtained from XRR, thereby establishing a good agreement with XRR data. Moreover, the observed morphology transformation is as well in good accordance with the SEM investigations (see section 5.2.2), which show remarkable morphology changes from 90 °C on, displaying large structures of up to μm-size embedded in the PBST3HT films.

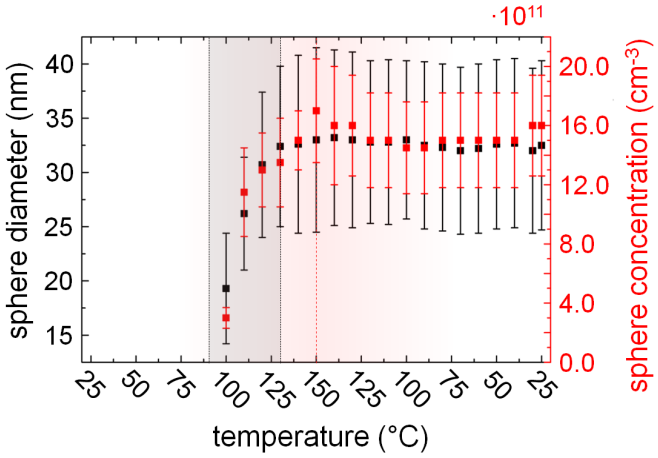

Figure 5.9: *Evolution with temperature of the mesostructure growth in PBST3HT samples. The gray box depicts the temperature transition range between 90 and 130 °C. The red dashed line represents the transition between heating and cooling protocols. Figure adapted from* [16].

The evolution of the crystalline Bragg peaks observed in the WAXS segments of the data curves are summarized in figure 5.10. The crystalline peaks are fitted with Lorentzian curves, out of which the corresponding lattice distances can be estimated (theoretical details in section 2.4.3). The crystallites present sizes of few tens of nanometers and, at RT, two Bragg peaks are visible, displaying lattice distances of 4.86 ± 0.02 Å and 5.60 ± 0.02 Å, indicated in figure 5.10 by the black and red hollow symbols.

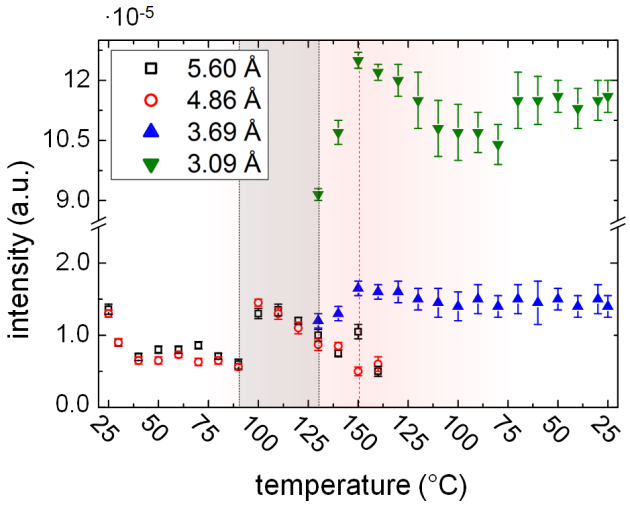

Figure 5.10: *Evolution with temperature of the Lorentzian fits to the WAXS crystalline peaks. The gray box depicts the temperature transition range between 90 and 130 °C. The red dashed line represents the transition between heating and cooling protocols. Figure adapted from [16].*

With increasing T, the intensities of both peaks decrease until approximately 40 °C, where they level off. The beginning of this previously spotted transition temperature range (90 °C, indicated by the gray box in figure 5.10) is marked by an intense jump in crystalline intensity, and subsequent decrease further until 150 °C, while the material band gap widens, as observed in the UV/Vis experiments. This sudden transition at 90 °C is as well in very good agreement with the SEM observation, in which for samples annealed at 90 °C already a very different morphology was observed, as compared to the original one obtained after film deposition at RT.

At the end of the crystalline transition (130 °C) a new crystalline phase appears, represented by two sharp peaks at 3.69 ± 0.01 Å and 3.09 ± 0.01 Å (blue and green solid symbols in figure 5.10). These newly appeared phase coexists with the previous one in the temperature range 130 °C - 150 °C, making this temperature range the one with highest crystallinity. When the cooling starts, the original crystalline phase completely disappears at 140 °C. The two new peaks are ascribed to $\pi - \pi$ interactions coming from reorganization of the tellurophene units. Their lattice distances lie within twice the van der Waals bond lengths for carbon (1.77 Å), selenium (1.90 Å) and tellurium (2.15 Å), in agreement with the hypothesis of $\pi - \pi$ coupling. Furthermore, Te-Te distances between 3.80 and 4.04 Å have been observed already in 3,4-dimethoxytellurophene, as well ascribed to $\pi - \pi$ interaction.[159] This new crystalline phase appears exactly when the band gap widening process observed in UV/Vis is completed, at 130 °C, and it stays upon cooling back of the system down to RT.

5.2.4 Modeled behavior

Computational studies have as well contributed to understanding the reaction of PBST3HT to temperature treatment. Experimentally, the absorption profile of PBST3HT presents

a main broad feature centered roughly at 400 nm, plus two additonal sharper transitions at 460 nm and 500 nm. Each transition cannot be individually ascribed to any of the particular chalcogenophene units. For this reason, monomeric as well as dimeric and trimeric units of PBST3HT are further simulated. The absorption energies are simulated using DFT, whereas the geometry optimization is carried at the MM2 and UFF levels of theory.[162] Calculation of the absorption energy for a monomer unit yields an absorption feature approximately at 340 nm, red-shifting to about 410 nm and to 450 nm upon simulation of longer units, i.e. upon switching from monomer to dimer and to trimer.[16] This suggests that the observed absorption profile might correspond to different PBST3HT phases presenting different average conjugation lengths, i.e. degrees of order, and that annealing of the system acts to the detriments of the longest segments.

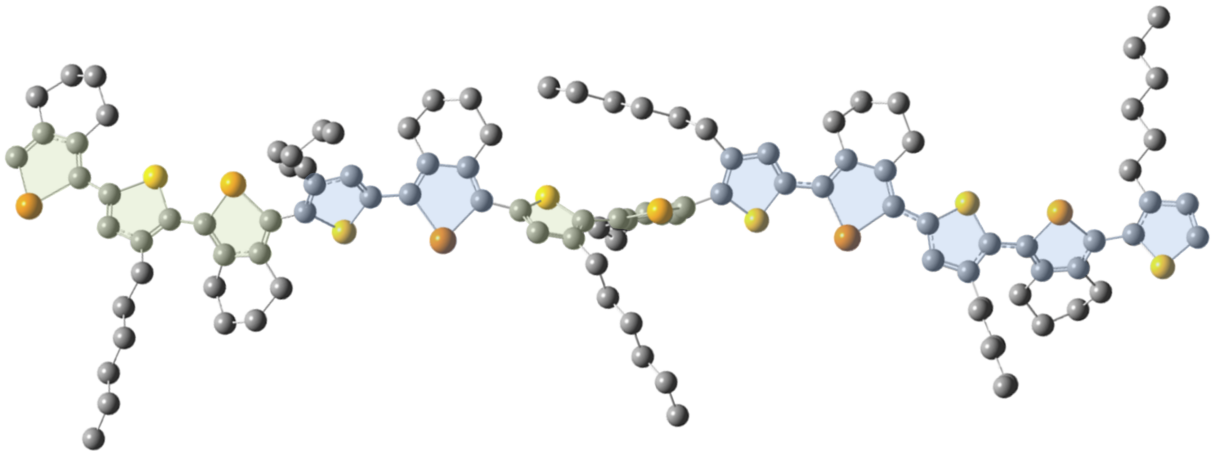

Figure 5.11: *3D representation of the energetically-optimized structure of a BST3HT trimer (tri-BST3HT). The calculations are done within the UFF level of theory in the gas phase. The alternatively colored regions indicate segments of the conjugated backbone eventually separated due to the severe backbone twists. Figure adapted from* [*16*].

On the other hand, and as mentioned in the beginning of the present characterization section 5.2, it is worth noting that in simulations of the PBST3HT monomer there is always a dihedral angle appearing along the backbone. MM2 geometry optimization yields a twist angle of 50°, whilst for UFF calculation the angle reaches 110°. This demonstrates the sensibility of this conjugation length-breaking parameter to the theory used for geometry optimization, as well as to the environment experienced by the molecule itself. Moreover, even though the particular choice of a force field (e.g. MM2 vs. UFF) can lead to different end angle values, the appearance of such a twist along the PBST3HT chain is recursive and irrespective of the chosen computational framework. Figure 5.11 displays the example of a energetically-optimized BST3HT trimer (tri-BST3HT), showing a backbone with repeated twists, thereby compromising the length along the backbone of π-delocalized regions.

Simulations suggest a morphology with twisted backbone for various levels of theory. Combined with the experiments, it all suggests a temperature transition featuring an energetic optimization of the system. This happens through an increased $\pi - \pi$ stacking, occurring to detriment of the conjugation length. Hence we observe a blue-shift in UV/Vis spectrum. The strong coordination tendency of tellurophene units is arguably the driving force behind the recrystallization process, and it presumably occurs through backbone twisting or folding, since simulations appoint θ as a firm candidate for crystallinity-driving parameter.

5.3 Behavior in devices and test solar cells

Fundamental characterization of PBST3HT in light of its promising properties compared to P3HT reveals interesting behavior, featuring strong changes in mesomorphology and crystallinity upon thermal treatment. These come along with drastic changes in its opto-electronic properties, like the observed optical bandgap. As discussed in the introduction of the present chapter, PBST3HT is expected to bring advantages related to light absorption and exciton/charge carrier transport derived from the presence of heavy chalcogen heteroatoms. In the following we discuss the results obtained from the first attempts of embedding this novel macromolecule in complex multilayer solar devices.

5.3.1 PBST3HT as electron donor and active layer

Amongst many, one of the advantages of substituting the sulfur heteroatom in a regular thiophene by a heavier chalcogen atom, like selenium, lies in the modifications that it brings to the overall material energy levels. Due to the higher ionization potential of Se as compared to S, the LUMO of the associated polymer is expected to lie at lower energies than in sulfur-based polymers. On the contrary, the similar electronegativities of the two heteroatoms lead to expectation of similar HOMO levels. In BHJ OSCs, the open-circuit voltage (which is one of the main bottlenecks of OPV technologies and will be discussed in detail in chapter 7) results primarily from the difference between the HOMO of the donor material and the LUMO of the acceptor. Hereby, the expectation is that the substitution of P3HT with PBST3HT in a conventional P3HT:PCBM BHJ device, which contains 25% more selenophene units than regular P3HT, will lead to a similar photovoltage and, at the same time, increase the amount of charge carriers, due to the improved absorption capabilities associated to its narrower band gap. This strategy, combined with the potentially elongated exciton lifetimes provided by the Te centers along the polymer backbone, makes PBST3HT an interesting candidate for improving performance of OSCs.

Therefore, we first attempt to fabricate PBST3HT:PCBM devices in order to quantify the magnitude of this expected advantages in real operating device environment. The solar cells were prepared by the standard procedure as described in chapter 4.

The results obtained in the I-V characterization of the OSCs are summarized in figure 5.12. Several J-V curves of both PBST3HT:PCBM cells as well as reference P3HT:PCBM OSCs manufactured simultaneously are displayed. Warm-colored J-V curves correspond to the reference P3HT:PCBM solar cells (and the corresponding current densities refer to the left red y-axis). In total, eight P3HT:PCBM J-V curves are displayed, presenting an average efficiency of (2.7 ± 0.3) %, featuring standard values of V_{OC}, but slightly low values for J_{SC} and FF, thereby yielding efficiencies below state-of-the-art values. On the other hand, cold-colored I-V curves indicate the seven PBST3HT:PCBM cells (their current densities refer to the right blue ordinate axis). The averaged efficiency amounts to (0.0016 ± 0.0011) %. At first sight, a clear non-diodic behavior is recognized from the new system, eventually revealing important degrees of exciton and/or charge carrier recombination. This gives rise to extremely low shunt resistances of (2.8 ± 0.6) $\Omega \cdot \mathrm{cm}^2$, i.e. almost no resistance. This reduces the fill factor down to around 25 %, which is characteristic of a straight J-V line (blueish curves in figure 5.12), and with it depicting a more linear rather than a diodic behavior.

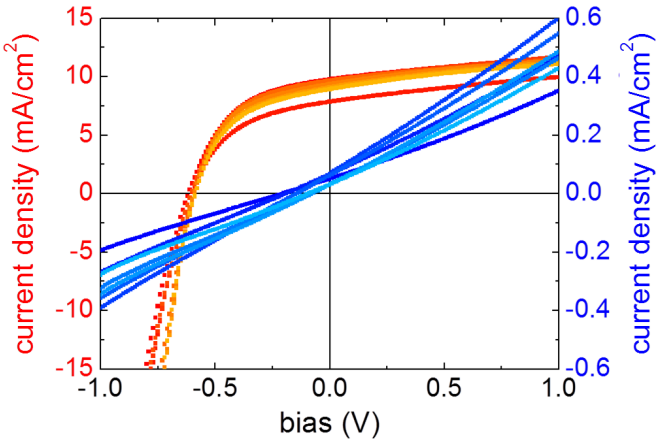

Figure 5.12: *Bias-current density (J-V) characteristics of P3HT:PCBM (warm colors) and PBST3HT:PCBM (cold colors) BHJ OSCs. Left red ordinate axis corresponds to P3HT:PCBM cells. Right blue ordinate axis corresponds to PBST3HT:PCBM cells.*

Another feature worth noting is the low J_{SC}s achieved by the PBST3HT:PCBM devices, displaying currents about 20 times lower than the reference P3HT:PCBM devices (compare the two ordinate scales for the two material systems). This is arguably related to a low intrinsic material conductivity. It is as well possible that the device recombination is so high that it suppresses an intrinsic good electrical conductivity. However, low conductivities for non-doped similar polytellurophenes have already been reported.[161,163]

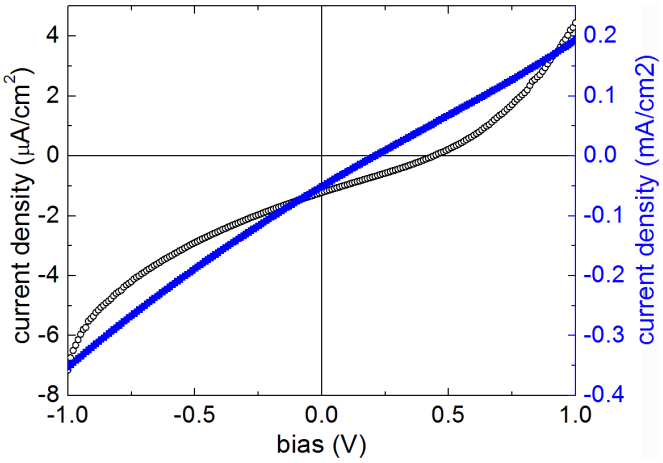

Figure 5.13: *Black: J-V characteristics of a PBST3HT single-component OSC. Blue: J-V characteristics of a BHJ PBST3HT:PCBM OSC for reference.*

In a similar way, the as well low V_{OC}s delivered by PBST3HT:PCBM OSCs likely arise from elevated recombination rates. One hint in this regard is that, independently of the material intrinsic band gap or the active layer optical band gap in combination with an acceptor molecule, alone the work function (WF) difference between the two device electrodes amounts to $WF_{Al} - WF_{ITO} = 0.5\ eV$. Thus, a device V_{OC} in this range is what should at least be expected from a non-ill functioning, not recombination-governed OSC. On the other hand, low V_{OC} values can as well arise from an unfavorable match of HOMO and LUMO levels between donor and acceptor, as well as between active materials and blocking layers and electrodes.

In order to gain further insight on potentially deficient exciton and/or polaron transport properties of PBST3HT, OSCs with PBST3HT as the only photoactive material are fabricated. Furthermore, study of PBST3HT-only devices help understanding the high recombination presented by PBST3HT:PCBM devices that results in low currents and photovoltages. Figure 5.13 shows an exemplary I-V curve of a PBST3HT-only device. On the one side, and regardless of the current ordinate scale, a better diodic behavior can be observed, indicating that, to some extent, the assumed recombination in PBST3HT:PCBM devices arises from incompatibilities in the partnership with PCBM. Moreover, the obtained V_{OC} in this case lies around 0.44 V, still inferior to the standard proxy $WF_{Al} - WF_{ITO} = 0.5\ eV$ and to standard P3HT:PCBM OSCs, but notably better than for BHJ PBST3HT:PCBM cells.

However, PBST3HT-only devices allow for better recognition of the expected problem of deficient exction/polaron transport within PBST3HT. As observed in figure 5.13, the current density scale is tuned to $\mu A/cm^2$, thereby yielding J_{SC} values somewhat four orders of magnitude lower than for reference P3HT:PCBM devices, or two orders of magnitude less than PBST3HT:PCBM cells. Hereby it is concluded that in the case of BHJ PBST3HT:PCBM OSCs most of the polaron-transport was carried out by the PCBM.

Overall the efficiency of this device amounts to 0.00015 %. Thus, we gain certainty about the main disadvantage observed for PBST3HT, i.e. low electrical conductivity. Studies on similar polytellurophenes or even macromolecules with alternating tellurophene and selenophene or thiophene units report almost insulating properties of the materials in their natural state. However, according to these, conductivity values can be improved upon I_2 uptake.[161,163]

Besides the performance of PBST3HT-only OSCs, observation of their time evolution in the first stages of device functioning, yields interesting results. Figure 5.14 displays the first 15 minutes of evolution of the main photovoltaic indicators of a PBST3HT-only device. Interestingly, the PCE delivered by the device shows an improvement during the first minute of work.

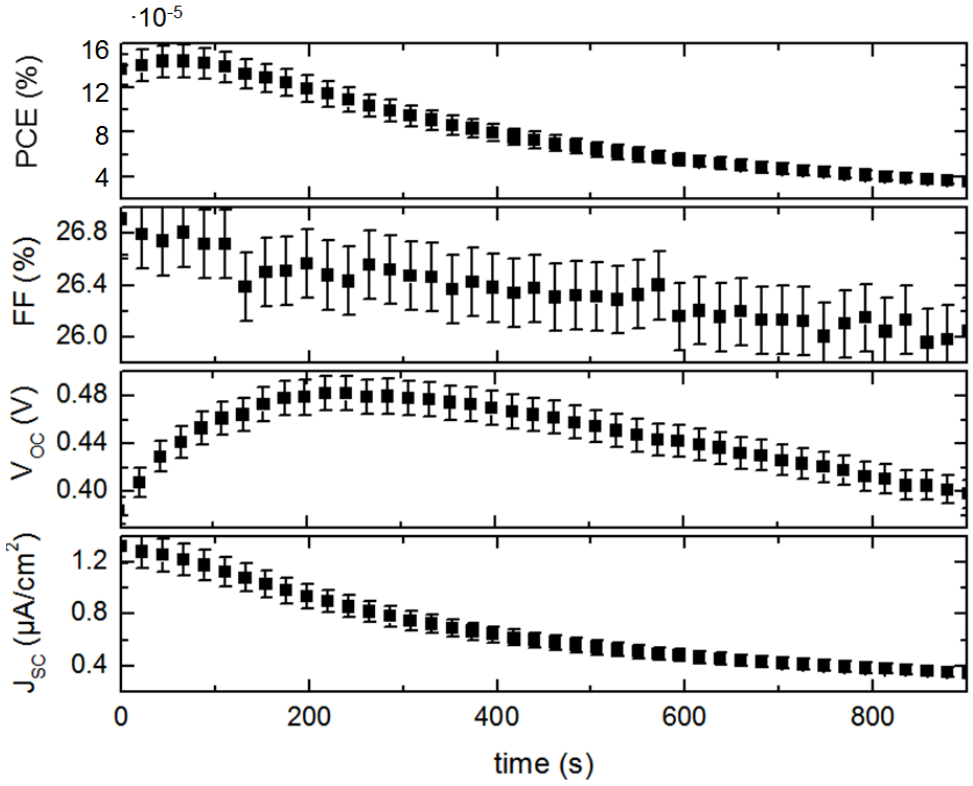

Figure 5.14: *Time evolution of the PCE, FF, V_{OC} andJ_{SC} for a PBST3HT-only OSC.*

It can be seen how this improvement is driven by an increase in the device photovoltage. An explanation for this effect is related to the already observed reorganization and re-crystallization process of PBST3HT upon thermal exposure, in this case provided by the heat produced by the UV radiation from the solar simulator. In the case of PBST3HT, we see how the exposure to heat can lead to a widening of the bandgap, which in turn leads to a broader optical bandgap. More generally, V_{OC}-increasing heat-triggered effects

associated with the crystalline evolution of the active layer of solar devices have been observed as well. They are studied in the frame of device aging studies in P3HT:PCBM OSCs and will be discussed in detail in chapter 7. On the other hand, FF and J_{SC} show a monotonous decrease, indicating worsening performance conditions. These are ascribed to the aging resulting from prolonged contact with air and UV radiation.

Despite the low conductivity of PBST3HT and, thus, the low efficiencies yielded by its associated devices, the interesting "recovering" behavior observed in time-dependent measurements poses the question whether this effect can be of use, maybe within different devices layouts. Following the presented experiences we experiment with incorporation of PBST3HT as third component in P3HT:PCBM solar cells. The goal is to take advantage of the interesting observed morphological, crystalline properties of PBST3HT as well as of its time-dependent behavior in devices. Hereby the time evolution of P3HT:PCBM devices is improved, in the first place regardless of the absolute performance values obtained.

5.3.2 PBST3HT as photoactive third component

In order to accomplish that, we prepare multiple P3HT:PCBM OSCs with different concentrations of PBST3HT, ranging from 0 wt.% up to 30 wt.% in steps of 5 wt.%. We look first at how PBST3HT affects the absolute performance of P3HT:PCBM solar devices, as well as its effect on individual device parameters. Afterwards we will similarly compare the evolution of those in time for different concentrations of PBST3HT.

Figure 5.15 depicts the evolution of PCE, FF, V_{OC} and J_{SC} with PBST3HT concentration. The initial reference P3HT:PCBM solar cells present a rather sub-standard performance, owing mainly to a low short-circuit current density J_{SC}. Moreover, the inclusion of PBST3HT affects negatively the absolute performance of ternary devices, as it is indeed expected, given the observed low PBST3HT intrinsic conductivity and the high device recombination introduced in partnership with PCBM, arguably owing to unfavorable HOMO/LUMO match. By 5 wt.% PBST3HT concentration, the PCE has fallen to approximately one third of the initial value. By 15 wt.% the PCE lies around 0.1 %, and the decrease proceeds up to 30 wt.%, where the performance falls one further order of magnitude. Unsurprisingly, the FF follows a similar evolution.

Furthermore, the evolution of the device photovoltage is of special interest. The photovoltage, as it was mentioned previously and will be discussed in greater detail in chapter 7, is intimately related to the recombination in the device. Interestingly, we see in the

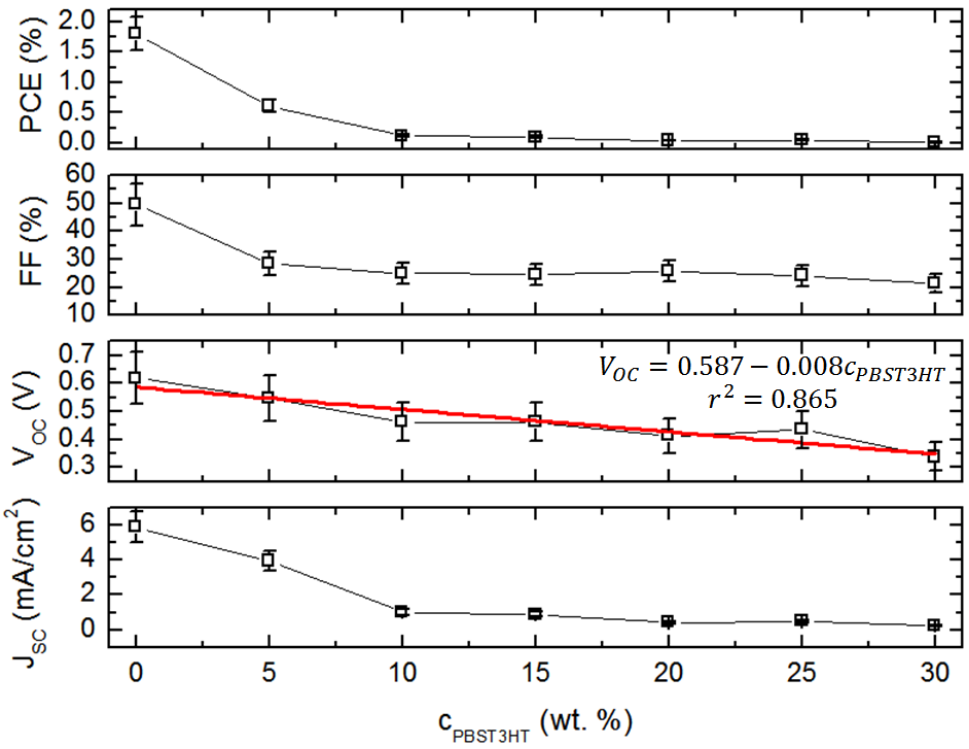

Figure 5.15: *PCE, FF, V_{OC} and J_{SC} measured for P3HT:PCBM solar cells with different concentrations of PBST3HT. Solid squares represent the data points. Black solid lines are a guide to the eye. For the V_{OC} the red solid line depicts the linear fit indicated by the function $V_{OC}(c_{PBST3HT})$.*

present set that the decrease of the V_{OC} depicts, to a very good level, a linear relation with the wt.% of PBST3HT, thereby further supporting the hypothesis of increasing recombination due to important mismatches between PBST3HT HOMO/LUMO levels and the relevant energy levels of the other layers composing the stack. On the other hand, observation of the evolution of J_{SC} also allows drawing of some hypotheses. Unlike V_{OC}, the J_{SC} decreases rapidly for the first 10 wt.% concentration range. By 10 wt.% the J_{SC} has decreased already to a 17 % of its initial value. This suggests that PBST3HT possibly enriches at some height in the device, thereby blocking the effective charge carrier collection due to its intrinsic low conductivity. If PBST3HT were distributed homogeneously within the active layer, it would be expected that the charge carriers were able to find percolation pathways to the electrodes within the P3HT (PCBM) phase.

Regardless of the absolute performance values obtained for different amounts of PBST3HT within the active layer, it is interesting to see whether this novel triple chalcogenophene improves the device resistance to aging by comparing the evolution of the main photovoltaic parameters to the initial ones. In this regard, figure 5.16 displays the evolution of PCE, FF, V_{OC}, J_{SC} for different PBST3HT concentrations, all normalized to the corresponding value at time $t = 0$.

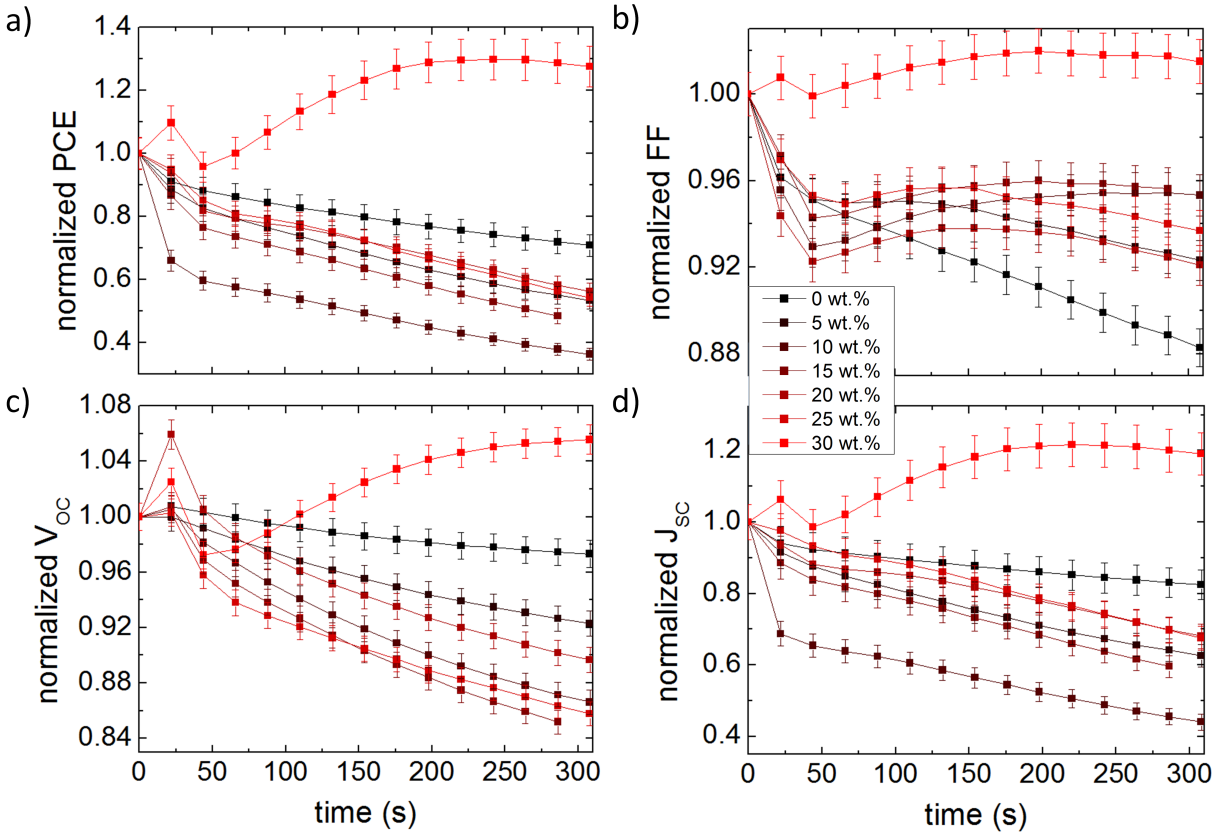

Figure 5.16: *Time evolution of the PCE, FF, V_{OC} and J_{SC} for different concentrations of PBST3HT in ternary P3HT:PBST3HT:PCBM solar cells. The solid squares represent data points. The solid lines are a guide to the eye.*

Clear qualitative changes in time-dependent behavior appear beyond a certain concentration threshold. In an attempt to establish comparisons with the previous case of PBST3HT-only cells, we can take a closer look at the V_{OC} of the ternary devices. As it will be presented and discussed later in chapter 7, the V_{OC} of regular non-encapsulated P3HT:PCBM devices can hold at higher than 90 % of the initial value for several hours under operation. In the present case, and after the first seconds of operation that show an improvement, the decrease rate of V_{OC} accelerates until its fastest rate at 15 wt.% PBST3HT. The nature of this early behavior will be as well addressed in detail. Approximately after this concentration an improvement in the aging behavior can be observed. Either in the form of a more prominent improvement in the initial "burn-in" phase and/or as a decreased rate of V_{OC} decay (compare the cases of PBST3HT concentrations of 15 and 25 wt.%). It is not until the highest concentration of 30 wt.% that, after some operation time, improved V_{OC} values compared to the starting ones can be first observed.

Similarly, the short-circuit current density J_{SC} decreases at its fastest at a PBST3HT con-

centration of 10 wt.% in the initial seconds of the burn-in phase. For higher PBST3HT concentrations it shows more stable development compared to the starting values within the first seconds. Again, it is at a PBST3HT concentration of 30 wt.% that the J_{SC} shows improvement upon functioning compared to the initial value.

The FF is the parameter which shows the most interesting time development, since already from 5 wt.% PBST3HT concentration the degradation profile after the first minute shows qualitative differences compared to the reference P3HT:PCBM devices. Indeed, for all devices containing PBST3HT in the active layer, the FF decays until around 50 s operation time, threshold after which the FF start either showing an improvement of staying relatively stable at the value reached after these 50 s. For 30 wt.% the FF after that 50 s threshold show clear improvements by up to over 20% compared to the initial FF.

As a combination of all studied parameters, the PCE evolution presents for almost all PBS3HT concentrations a qualitatively very similar degradation profile, featuring the same decay rate after the fast initial burn-in phase. This initial burn-in phase is especially severe for the device containing 15 wt.% PBST3HT, mainly driven by the degradation in J_{SC}. As it happens for all other parameters, at a PBST3HT concentration of 30 wt.% the PCE starts improving continuously after the initial burn-in phase, reaching improvements of up to 30 % compared to the initial performance.

5.4 Conclusions and outlook

In the present chapter we conducted an exhaustive analysis of some fundamental properties of a novel and custom-synthesized triple-chalcogenophene oligomer named PBST3HT. Preliminary tests in real solar cells for assessment of main bottlenecks and for identification of the material's main potentials have as well been conducted.

The triple chalcogenophene combination is expected to bring along varied advantages due to the presence of Se- and Te-based units. On the one hand, narrower bandgaps as compared to standard P3HT provide improved light absorption and, with it, higher exciton/polaron density. Moreover, Te is known to contribute to improved ISC in the system, which results in a higher share of triplet excitons and, thereby, longer average exciton diffusion lengths.

The fundamental characterization of PBST3HT shows interesting bandgap-adjusting prop-

erties upon thermal treatment, featuring tunable bandgaps from 2 eV up to 2.35 eV. These are accompanied by significant changes in morphology and crystalline arrangement, expectedly induced by the high coordination tendency of tellurophene units. The combination of optoelectronic and morphological characterizations with simulations suggest that temperature triggers the development of a more stable system morphology. It features enhanced $\pi - \pi$ stacking to detriment of the polymer conjugation length, thereby also inducing the observed widening of the band gap.

Implementation of PBST3HT in solar cells yields still unsatisfactory device performance as compared to the reference P3HT, arguably related to two main features of PBST3HT. The first one is its extremely low electrical conductivity in its natural state. This feature has been reported already multiple times for very similar systems, like polytellurophenes or selenophene/tellurophene copolymers.[161,163] In these mentioned cases, the conductivity improves significantly upon exposure to I_2. In this regard, measurements of electrical conductivity or even characterization of PBST3HT-based OSCs in presence of I_2 gas could help finding a way to dramatically improve PBST3HT performance in devices.

The second noteworthy drawback presented by PBST3HT is an eventually unfavorable energy level match with the standard acceptor PCBM. This prevents the right-away substitution of P3HT in solar devices. One of the original purposes of substituting sulfur with selenium is the fact that the resulting polymer can present lower LUMO levels with relatively unchanged HOMO energies, thereby increasing the effective light absorption without important losses in device V_{OC}. However, the introduction of tellurophene units presumably distorts this strategy, since the study of PBST3HT:PCBM and PBST-only devices shows very significant levels of charge-carrier recombination when in combination with PCBM. Likewise, combination of PBST3HT with P3HT is not expected to be beneficial, since it would mean the combination of two p-conducting polymers within a BHJ. In this regard, comprehensive ultra-violet photoelectron spectroscopy (UPS) measurements at different temperatures can reveal HOMO and LUMO positions at different stage of band gap switching, allowing for better allocation of proper n-conductive photoactive partners for OSCs. The search of proper photoactive partners of PBST3HT can be further complemented by the tuning of the intrinsic PBST3HT HOMO and LUMO levels allowed by the presence of Te-based units. This can be achieved by e.g. bromination, i.e. exposure to Br_2 vapor, as reported for similar materials.[161] Br_2 coordinates with Te centers forming $TeBr_2$. This produces major changes in the material HOMO and LUMO, mainly narrowing the material optical band gap. Therefore, potential experiments with Br_2-exposed OSCs could help finding out if a more beneficial HOMO/LUMO combination

can be achieved by such procedure, and/or if this approach allows for enough energetic adaptability of the material, so that it can partner with a broad range on n-conducting molecules. Nevertheless, technical and health concerns related to Br_2 exposure need to be taken into serious account. Bromine is volatile, releases suffocating vapors, is very corrosive to skin, tissue and metals, is highly toxic, accelerates the burning of combustible material and reacts in contact with water forming highly-corrosive hydrobromic acid HBr. Therefore, special precautions, technical challenges and security protocols must be foreseen and planned when engaging with such a line of research.

One further noteworthy feature of PBST3HT is related to the challenging synthesis of Te-based macromolecules. Most of Te-based macromolecules present very low degrees of solubility. This, combined in some cases with slow reaction kinetics decreases the efficiency of the polymerization process, generally leading to polytellurophenes presenting only low molecular weights, and thereby limiting the attainable narrow band gaps.[163,164] In the case of PBST3HT ($M_W \approx 4$kDa) the narrowest band gaps obtained lie around 2 eV, very similar to standard P3HT and, hence, the potential advantages of narrow band gap polymers cannot be fully exploited. However, some novel reports present already synthesis routes delivering polytellurophenes with molecular weights as high as $M_W = 25$kDa.[164]. In any case, the observed morphology transitions in PBST3HT that happen to detriment of the longest conjugated units may make the degree of polymerization not the main concern in the attempt of achieving low-band gap Te-based polymers.

On the other hand, inclusion of PBST3HT in P3HT:PCBM solar cells has yielded interesting results. Regardless of a worse absolute performance, the presence of PBST3HT induces an improvement in the aging behavior of PBST3HT:P3HT:PCBM ternary solar cells compared to initial values, showing even improvement during functioning for high loads of PBST3HT (30 wt.%). Further research as the proposed above, aiming to increase the electrical conductivity as well as to tuning the PBST3HT HOMO and LUMO levels in order to better partner with P3HT and PCBM, could eventually lead to better absolute performances in ternary P3HT:PBST3HT:PCBM devices while still taking advantage of the "recovery" properties observed upon inclusion of PBST3HT. This effect of improving OSC performance is arguably related to a heat-triggered morphological and crystalline reorganization, as observed for neat PBST3HT. Upon heating of the system due to exposure to sunlight, the system moves towards an equilibrium state for the P3HT:PBST3HT:PCBM ternary system, inducing a different equilibrium configuration and, hence, a different time evolution for different PBST3HT concentration.

Further study of the recovering of PBST3HT-based solar devices can as well yield substantial fundamental knowledge that can eventually help better understanding and avoiding OSC aging. However, the particular use of PBST3HT as OSC third component seem yet far from application, and the use of iodine or bromine for eventually tackling some of its bottlenecks poses some important technical, health and security challenges. In the following, we will explore new approaches to improve OSC efficiency through improved exciton spin statistics, lifetime and diffusion length.

Chapter 6

Superparamagnetic Fe_3O_4 nanoparticles in P3HT:PCBM organic solar cells

The content of this chapter features the first comprehensive morphological as well as optoelectronic characterization performed on P3HT:PCBM BHJ OSCs modified with Fe_3O_4 NPs. Morphological as well as optoelectronic characterization of thin films and full solar devices suggest an extension of exciton lifetime on the basis of an increased ISC, ultimately leading to an enhanced device efficiency. Furthermore, the influence of a magnetic field on the performance of the modified devices is investigated. The article *"Improved power conversion efficiency of P3HT:PCBM organic solar cells by strong spin-orbit coupling-induced delayed fluorescence"*, cited in this thesis as reference [14], has been published as a result of part of the work presented in the following. Parts of the work discussed in this chapter are originally presented in the master thesis *"Enhancing triplet exciton population in organic solar cells"* by Florian Dreher.[117]

6.1 Introduction

In the previous chapter we studied the properties of PBST3HT, as well as assessed its capabilities in solar devices in its natural, non-doped state. PBST3HT constitutes one further attempt in the yet rather immature field of combining triplet-emitting properties with high-molecular-weight macromolecules. In this regard, we have developed PBST3HT-based solar cells. To the best of our knowledge, the PBST3HT-based OSCs presented and discussed in the previous chapter are the firsts successfully fabricated with a Te-based oligomer. Despite the fact that the results of the first experiments are promising, in the case of the used PBST3HT system, as discussed at the end of the previous chapter, still some bottlenecks need to be addressed in order to unlock attainment of high-performing OSCs. These bottlenecks prevent immediate substitution of P3HT with PBST3HT in

BHJ OSCs. The remaining challenges are mostly related to a deficient electrical conductivity of Te-based polymers in their natural state. Hereby, study of the effect of doping, iodination, bromination, etc. as well as further innovation in the field of synthesis can show the correct path to keep up the good progress. Moreover, PBST3HT has shown band gap-adjustment behavior upon exposure to different temperatures, eventually allowing for HOMO and/or LUMO change during OSC fabrication process. Similar to the issue of low conductivities, this can be addressed via multiple synthesis and/or device fabrication procedure approaches (see section 5.4).

Hence, we develop in parallel further approaches to increase the exciton diffusion length in common and well-known systems. An interesting approach consists of the addition of NPs. In general, inorganic nanoparticles have proven to provide multiple advantages that can be used in photovoltaic technology, such as surface plasmon resonance, band gap-tuning in hybrid PV systems, acceleration of exciton splitting in the case of nanocrystals, modification of work functions for improved carrier-blocking properties, or improving interlayer contacts, amongst others.[165–168] Furthermore, NPs can be used for increasing the ISC in the solar device photoactive medium. The NPs used for this purpose are superparamagnetic and feature small remanent magnetizations. These create small local magnetic fields in their vicinity, increasing the ISC in the neighboring molecules, given that the magnetic field induces spin rephasing (see section 2.3 for detailed discussion on the corresponding theoretical background).

The current approach involving NPs presents some advantages. In contrast to the approach presented in the previous chapter, introduction of superparamagnetic NPs is a more straight-forward method for a handful of reasons. On the one hand, control and parametrization of BHJ morphologies upon NP addition is generally a better-studied and accessible area, making this approach more immediately usable. Furthermore, synthesis, functionalization and inclusion of NPs in solar devices is a by far cheaper method than custom-engineering novel macromolecules, in which the aimed properties generally imply low-efficiency synthesis routes or require full development of new synthesis strategies. This makes the approach with nanoparticles commercially attractive, especially, taking into account that they can be easily implemented in otherwise well characterized photoactive systems.

This way of approaching exciton diffusion length elongation is still relatively novel, as there exist just few reports on improved PCE via this method.[14,169,170] In 2011, Zhang et al. suggested that this effect is achieved by the introduction of superparamagnetic

Fe_3O_4 NPs, reporting devices efficiencies improved by about 18% in a study based exclusively on analysis of device performance.[169] Our work, presented in this thesis, was the next one building on top of that first report, with results in very good agreement with the work of Zhang,[169] improving efficiencies by up to 11 %.[14] Moreover, our study was the very first one featuring comprehensive investigations on the effect of NP addition on the system performance in devices, mesomorphology, crystallinity and optoelectronic response, supporting the argument of elongated exciton lifetimes, and offering broader insight on the NP-assisted increased ISC for the first time. Shortly thereafter, further work by Jaramillo et al., featuring more developed approaches with core-shell Fe_3O_4@ZnO NPs reported efficiency improvements of by up to 25 %.[170]

In the present chapter, we study the effect of Fe_3O_4 NPs in the otherwise well-characterized active layer system P3HT:PCBM.[171] The presented research features more detailed morphological and optoelectronic characterization of the many effects that the presence of NPs could have in OSCs, compared to the just preliminary device comparison reported by Zhang et al.. First, the effect of NPs in the performance and other device parameters is examined. Afterwards, morphology changes upon NP addition are cross-checked to conclude which and to which extend of the observed effects can be explained by morphological/crystalline arguments. Finally, we estimate exciton lifetimes via PL spectroscopy. Overall, the whole picture supports the hypothesis of an elongated exciton diffusion length by the ISC enhancement induced by the NPs.

In the second part of the chapter, the effect of additional external magnetic fields on the performance of solar devices is explored. The presence of external fields further magnetizes the NPs beyond their remanence, thereby having a further influence on the device performance. Indeed, our study with additional magnetic fields yield further improvements in PCE and, under some conditions, on FF. These indicate a further reduction in the charge carrier recombination. The attainment of the setups necessary for generating the required magnetic fields and to accommodate the characterization of the investigated solar devices required itself some technical developments. In this regard, the setups used, their layouts, construction, calibration and features are described in the appendix A at the end of this thesis.

6.2 Influence of nanoparticles on P3HT:PCBM bulk heterojunction solar cells

The work starts by attempting to improve the PCE via the inclusion of NPs, whereby studies of the device performances are carried out. Upon attainment of reproducible PCE improvements at low Fe_3O_4 concentrations, in-depth structural characterization is performed in order to ensure non-changing morphology. Moreover, optoelectronical characterizations of NP-modified photoactive thin films lead to estimates on the variations of exciton lifetimes, providing greater insight into the reasons for PCE improvement.

6.2.1 OSC efficiency improvement

Following up the study first reported by Zhang et al.[169] several OSCs are built with different concentrations of Fe_3O_4 NPs. The preparation routes are described in chapter 4. The resulting devices are measured under an AM1.5g illumination with an irradiation density of 1000 $^{W}/_{m^2}$. The obtained device PCEs and the corresponding FFs are displayed in figure 6.1. The presented parameters are calculated using the software *IValuator*, based on the formalism described in section 3.2.3. The mean values and their corresponding standard deviations are calculated from the results obtained from the multiple OSCs fabricated on each substrate (see section 4.4).

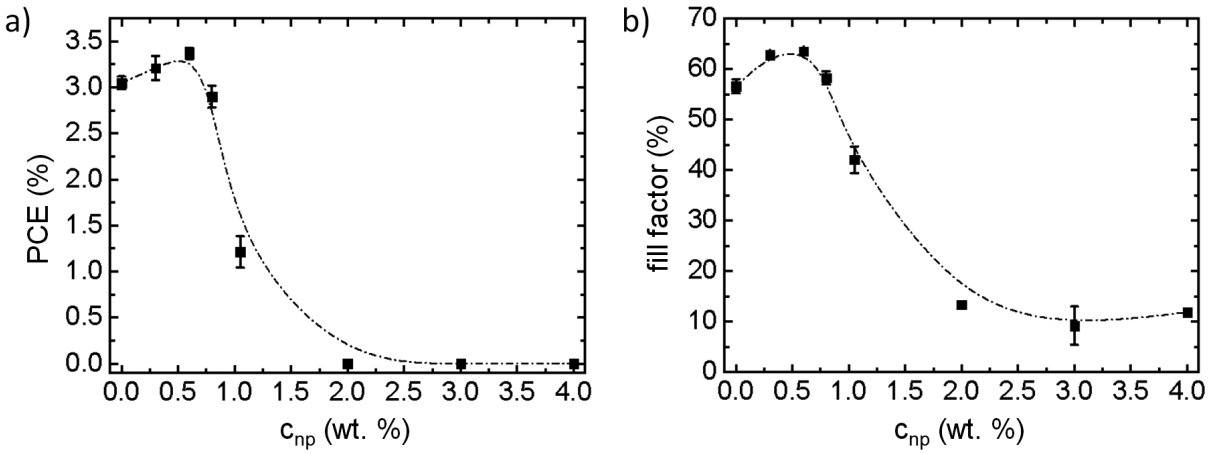

Figure 6.1: *a) PCE and b) FF of the fabricated P3HT:PCBM OSCs expressed as a function of Fe_3O_4 NPs weight percentage. Dashed lines are guides to the eye.*

The devices show a consistent increase in performance upon inclusion of the NPs only up to low NP concentrations. The data are in good agreement with the previous report by Zhang et al., who reported a PCE increase by a factor of up to 1.18 compared to the non-modified reference devices. They reported attainment of the maximum efficiency at

NP concentrations of 1 wt.%, although their study presented coarser Fe_3O_4 concentration steps.[169]

In our investigation, we study the evolution of the OSC parameter with Fe_3O_4 concentrations up to 4.0 wt.%. The devices present as well a monotonous increase in PCE up to 0.6 wt.%, thereby yielding an 11 % improvement compared to unmodified OSCs (starting from 3.05 % up to 3.37 %). The evolution of the PCE is closely related to that of the FF, displayed in figure 6.1b. The PCE and the FF show the same trend, whereby a maximum FF is observed for a concentration of 0.8 wt.% with a corresponding FF improvement factor of 1.12 compared to the reference device (from 56.5 % to 63.5 %).

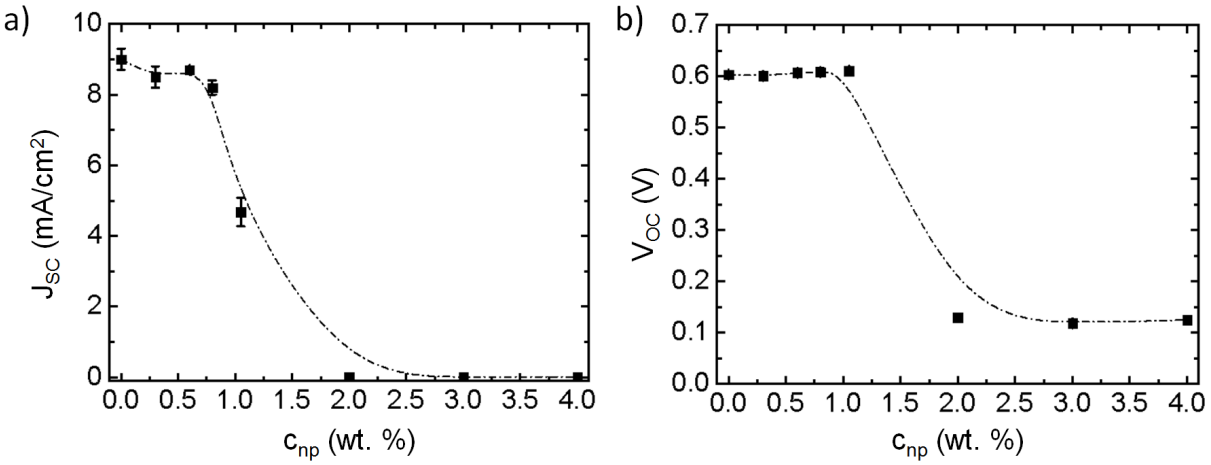

Figure 6.2: *a) J_{SC} and b) V_{OC} of the fabricated P3HT:PCBM OSCs fabricated with different concentrations of Fe_3O_4 NPs expressed as a function of Fe_3O_4 weight percentage. Dashed lines act as guide to the eye.*

The apparent conflict between the maximum performances of PCE and FF, which do not happen at the same wt.%, is caused by the other OSC parameters. Figure 6.2 displays the dependence of the J_{SC} and the V_{OC} with the NP concentration. J_{SC} (figure 6.2a) shows a mild decrease of around 1 $^{mA}/_{cm^2}$ in the range from 0 to 0.8 wt.%, which causes the disagreement between the PCE and FF. Beyond the 0.8 wt.% threshold, J_{SC} shows a dramatic decrease. Similarly, the V_{OC}, which up to a NP concentration of 1.05 wt.% showed consistent yet slight improvement, drops suddenly for higher Fe_3O_4 NP weight percentages. The sudden drop in V_{OC}, coincident with an as well dramatic decreases in both J_{SC} and FF, depicts a significant enhancement of leakage currents throughout the device. This fact is as well confirmed by the notable drop in shunt resistance R_{SH}. An overload of Fe_3O_4 NP within the system is the reason for this behavior. Fe_3O_4 is a strong electrical conductor that displays conductivity values up to six times higher than just regular hematite (Fe_2O_3). This enhanced conductivity comes as a result of electron

exchanges between Fe^{3+} and Fe^{2+} centers.[172] Therefore, higher concentrations of Fe_3O_4 enable alternative percolation paths throughout the device for charge carriers. Strong increase in conductivity in polythiophene films introduced by OA-capped Fe_3O_4 NPs was already observed in literature.[173]

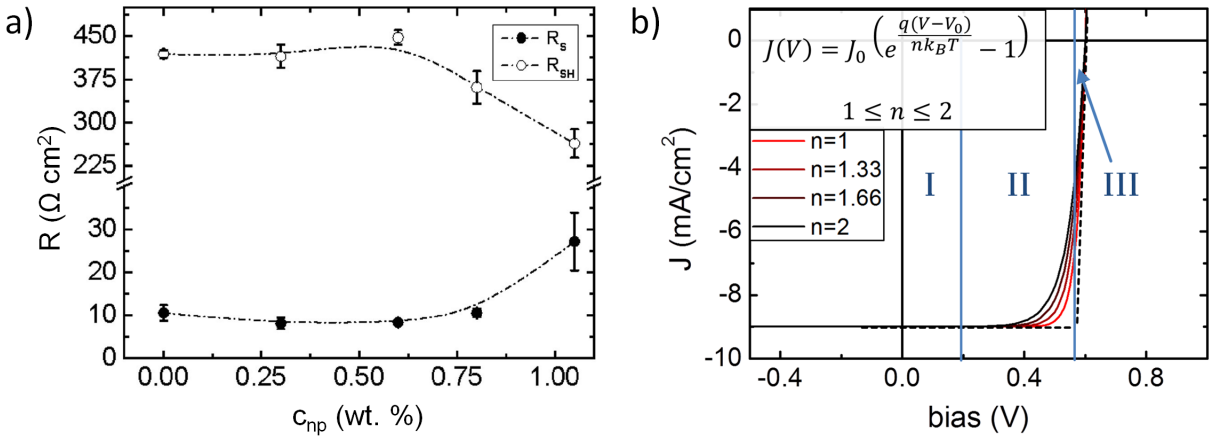

Figure 6.3: *a) R_S (solid circles) and R_{SH} (hollow circles) resistances of the P3HT:PCBM OSCs fabricated with different concentrations of Fe_3O_4 NPs expressed as a function of Fe_3O_4 wt.%. Dashed lines act as guide to the eye. b) Simulated exemplary set of offsetted (indicating illumination) ideal diode J-V curves. The curves have been generated with the insetted ideal diode equation by tuning the ideality factor n between 1 and 2. An increase in FF without modification of R_S and R_{SH} is depicted. The forward bias region is divided in three regions: I: shunt region, II: diode region, III: series region. The blue arrow indicates the location of the region III between the diode region and the V_{OC}.*

The evolution of the R_S and R_{SH} resistances is displayed in figure 6.3a. Both R_S and R_{SH} stay constant during the concentration range of device improvement, i.e. up to 0.8 wt.%. It is important to note that, in general, not all variations of FF can be directly ascribed to a reduced charge carrier recombination, since variations in e.g. R_S due to the resistance of the contacts can as well modify the FF by changing the slope at the open-circuit region of the diagram (see region III in figure 6.3b).[174] Thus, the fact that the FF improves without major variation of both R_S and R_{SH} is of capital importance, since it displays that the increase in FF must happen in the so-called diode region (region II in figure 6.3b). As an illustration, a simulation of ideal diode J-V curves with constant R_S ($R_S = 0\ \Omega\ \mathrm{cm}^2$) and R_{SH} ($R_{SH} = \infty\ \Omega\ \mathrm{cm}^2$) but with different ideality factors is displayed in figure 6.3b. The two extreme cases correspond to an ideality factor $n = 1$ on the one hand, corresponding to a device completely governed by diffusion current, and on the other hand $n = 2$ displays a device where the J-V curve is dominated by recombination.[174] Similar to what happens for our Fe_3O_4 NP-modified devices, J-V simulations on figure 6.3b show how all changes in FF due to a lowered ideality factor, i.e. a reduced recombination, happen in the region II with no effect of both resistances. Hereby it can be concluded that low

concentrations of Fe_3O_4 NPs induce a lowering of the recombination current in the device.

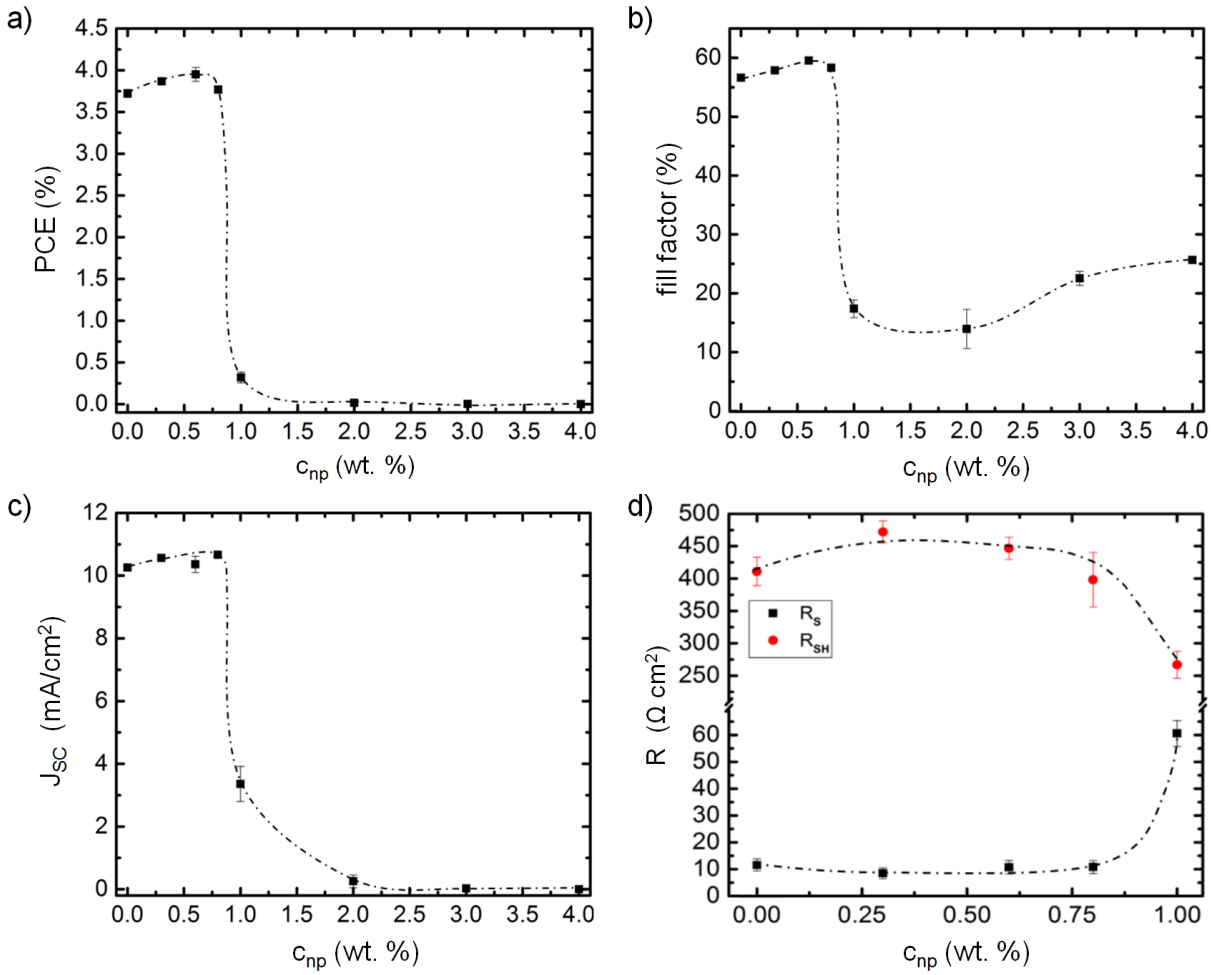

Figure 6.4: *OSC performance indicators of the optimized P3HT:PCBM OSCs fabricated with different concentrations of Fe_3O_4 NPs expressed as a function of Fe_3O_4 weight percentage. Dashed lines act as guide to the eye.*

Further tests and batches of OSCs following the same procedures yielded optimized devices. These are summarized in figure 6.4. Hereby, the overall performances are significantly improved, displaying PCEs over a 0.5 % better. The qualitative behavior remains essentially unchanged, further confirming the reproducibility of the results obtained. PCE increases in the range of low Fe_3O_4 load, mainly driven by increasing FF, whereas in the same wt.% range the photovoltage V_{OC} and both the R_S and R_{SH} resistances remain fairly constant. The PCEs improve from a starting average value of 3.72 % to a maximum average value of 3.95 %, reached at Fe_3O_4 NP concentrations of 0.6 wt.%. Similarly, the FF as well reaches at 0.6 wt.% NPs its maximum, with a value of 59.5 %.

Unlike in the previous case, here both the PCE and the FF reach their maximum at

the same Fe_3O_4 concentration. This is due to the fact that for these optimized OSCs, the short-circuit current density J_{SC} shows as well an improvement in the region of light NP incorporation, reaching improvements of by up to 4 % at concentrations of 0.8 wt.% NPs. This effect follows directly from the reduced device recombination, due to which the density of charge carriers is increased. Moreover, this effect has been as well observed and reported in similar experiments, featuring P3HT:PCBM OSCs modified with superparamagnetic NPs, as well reaching maximum values for NP loads of slightly under 1 wt.%.[169,170] Both the R_S and R_{SH} resistances behave as in the first OSC sets, showing the same qualitative behavior and taking the same absolute values, which reinforces the reproducibility of the research.

Thus, the repeatedly observed reduced recombination displayed by improvements of the device FF in the diode region in combination with slightly improved J_{SC}s, yield improved PCEs. This is attributed to the sought enhancement of triplet exciton population, brought by the higher degree of ISC introduced in the photoactive medium by the NPs.

6.2.2 Structural characterization

The study of the solar cell behavior upon addition of Fe_3O_4 NPs shows an improvement in performance through a reduced exciton recombination. This reduction complies with the hypothesis of the work, by which the inclusion of NPs induces an enhancement of ISC, which in turn elongates the average exciton lifetime and thereby its diffusion length. Nevertheless, to ensure comprehensiveness and to avoid misinterpretation, other potential changes in the OSC upon introduction of the NP need to be discarded. In particular, the incorporation of third components in BHJ blends is expected to alter the demixing behavior and, potentially, as well the arrangement scale.[175,176] It is obviously of importance to discard this factor, since an altered demixing scale and, consequently, a different mean distance between D-A interfaces can as well affect the exciton splitting rate. In this regard, GISAXS experiments (details in sections 2.4.5 and 3.1.4) are conducted in order to probe the film structure. The probed sample area is approximately of the same size as the device area, allowing for a direct comparison between the inner film structure and the electrical device function.[108] Figure 6.5 displays the 2D GISAXS patterns obtained for P3HT:PCBM BHJ films with Fe_3O_4 NPs concentrations between 0 and 4.0 wt.%. The specularly-reflected intensity is shielded by a round-shaped beamstop to protect the detector electronics. The black stripes at $q_z = 1.2$ nm^{-1} and $q_y = 0.4$ nm^{-1} correspond to the horizontal and vertical inter-module gaps of the Pilatus 1M detector, respectively.

From the 2D patterns it can be seen how the contrast along the vertical direction is

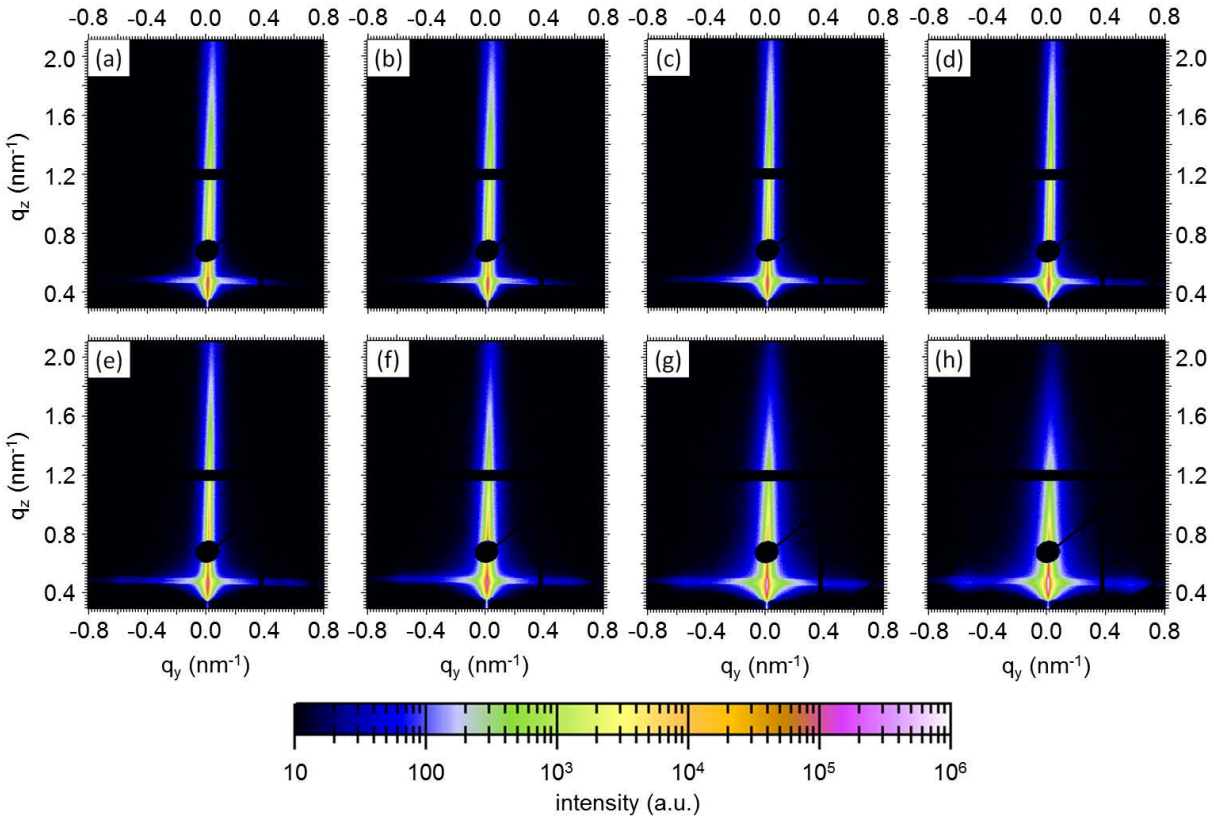

Figure 6.5: *2D GISAXS patterns of P3HT:PCBM BHJ thin films with different concentrations of Fe_3O_4 NPs: a) 0.0 wt.% b) 0.1 wt.% c) 0.6 wt.% d) 0.8 wt.% e) 1.05 wt.% f) 2.0 wt.% g) 3.0 wt.% h) 4.0 wt.%. The round beamstop protects the detector from specularly-reflected x-ray radiation. Black stripes at $q_z \approx 1.2$ nm^{-1} and $q_y \approx 0.4$ nm^{-1} are the inter-module gaps of the Pilatus 1M detector.*

continuously lost with increasing Fe_3O_4 concentration, whilst lateral structures appear. At around $q_z = 0.5$ nm^{-1} the horizontal signal extends into higher q_y values, and from 1.0 wt.% NPs (figure 6.5e) on the formation of small localized lateral structures becomes prominent.

Deeper insight into the effect of the NPs on the blend morphology is gained through analysis of the horizontal line cuts performed at the Yoneda peak position (further information in sections 2.4.5 and 3.1.4). The horizontal cuts provide information about the lateral structures within the film, such as domain sizes and neighbor-to-neighbor distances. The cuts are subsequently fitted following the protocols and models described in section 2.4.5. In the present case, four different sets of form and structure factors are required, whereby one of them refers to the NPs and the other three serve the reconstruction of the D-A inner film morphology. The cuts and the corresponding fits are displayed in figure 6.6a, whereby the Fe_3O_4 NP concentration increases from bottom to top, from 0.0 to 4.0 wt.%. From the horizontal line cuts already some structures can be recognized as shoulders or

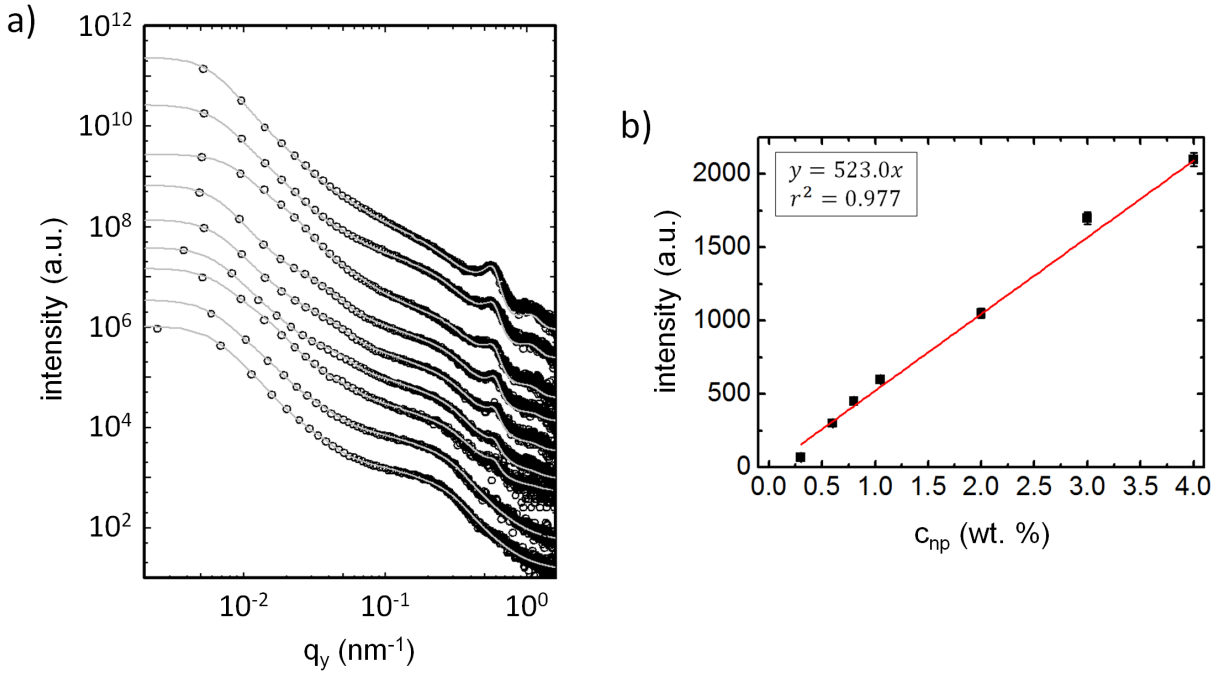

Figure 6.6: *a) Horizontal line cuts performed at the Yoneda peak position of the 2D GISAXS patterns with different Fe_3O_4 concentrations (increasing from bottom to top). Gray lines indicate the model fits. Cuts are shifted vertically for clarity of the presentation. b) Linear regression of the intensity of the GISAXS NP form factor versus the NP concentration. Black dots correspond to the data and the solid line indicates the linear fit.*

peaks. In particular, the lateral structure already visible in the 2D patterns becomes prominent beyond 1.0 wt.% and can be seen as a growing peak at around $q_y = 0.6$ nm^{-1}. The data obtained from the fitting clearly supports the assumption that it originates from the NPs (see section 2.4.5 for details on the fitting model). On the one hand the size parameters required for fitting the assumed NP structure, e.g. radius (4.9 ± 0.3) nm, are in very good agreement with the size provided by the supplier $((10 \pm 1)$ nm diameter). On the other hand, the intensity of the form factor needed for fitting the peak grows linearly with the NP concentration. As discussed in section 2.4.2, in the current grazing-incidence geometry the absolute value of the scattering cross section depends linearly on the concentration of scattering domains (see equations 2.53, 2.53 and 2.57). Therefore, assuming constant form and structure factors (which seems a reasonable assumption for almost monodisperse, solid NPs), an increase in scattering cross section and, hence, in scattering intensity, follows from an increase in concentration of scattering centers. Moreover the hypothesis of constant form and structure factors is supported by the values obtained through the fit, which stay nearly constant for the whole concentration range. Thus, the linear co-dependence between the recorded scattering intensity of the form factor and the NP concentration allows identification of NPs in the horizontal cut. The linear co-dependence and the respective regression is shown in figure 6.6b.

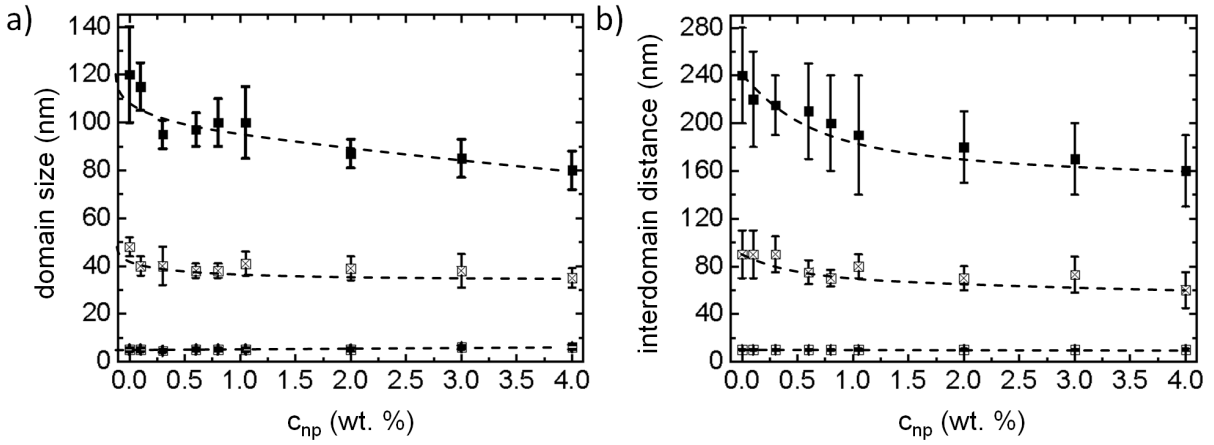

Figure 6.7: *Mean a) domain radii and b) inter-domain distances between organic domains as a function on NP concentration. The values are extracted from the fits. The dashed lines are a guide to the eye.*

Figure 6.7 displays the evolution of the remaining three form and structure factors describing the intermixing of P3HT and PCBM with Fe_3O_4 concentration. The biggest domains identified for the reference sample (0.0 wt.% Fe_3O_4) present sizes of (120 ± 20) nm. The domain size decreases with increasing NP concentration, to (80 ± 8) nm for a concentration of 4.0 wt.%. Similarly, the associated structure factor decreases over the same concentration range from initial values of (240 ± 40) nm to (160 ± 30) nm. The variation occurs with a very large overlap of the associated error bars, making it difficult to clearly identify the decay. Moreover, the large-sized domains formed are not expected to play any important role in the exciton separation, since the singlet exciton diffusion length is still far below the obtained values.

The medium and small scattering objects present only small-to-no variations in either size or neighbor-to-neighbor distances upon addition of NPs. The medium-sized domains change from (48 ± 4) nm (0.0 wt.%) to (35 ± 4) nm (4.0 wt%) in domain radius and from (90 ± 20) nm to (60 ± 15) nm over the same concentration range in center-to-center distance. The change occurs within error bar overlap of the intermediate points. Hence, the changes observed are negligible.

The small domains remain practically unchanged over the whole range (from (5.0 ± 0.8) nm to (6.0 ± 1.0) nm in radii and from (10.0 ± 0.5) nm to (10.0 ± 1.0) nm in structure factor). These small objects are regarded as PCBM domains, and they represent the closest mixing between P3HT and PCBM, being in a size range relevant for exciton dissociation.[171]

Thus, it is concluded that the improvements observed in device functioning upon addition of NPs cannot be explained by changes in the sample morphology, since the P3HT:PCBM

intermixing at the relevant exciton splitting scales do not show any prominent alteration. Moreover, the trend of slight changes observed in whichever size range does not correlate with that of the efficiency of any other photovoltaic parameter.

6.2.3 Spectral behavior

Following the morphology investigation carried out through GISAXS experiments, it is concluded that the improvement seen in OSC performance cannot be attributed to changes in the intermixing between donor and acceptor phases (section 6.2.2). Study of the J-V curves shows that the improvement in device performance is linked to a decrease in the device recombination (see section 6.2.1). It is anticipated that the reduced recombination arises from an extended exciton diffusion length introduced by the Fe_3O_4 NPs that enhance the ISC in the system. The correctness of this hypothesis can be tested through time-resolved PL measurements. When excited, the samples emit fluorescence (prompt or delayed) and/or phosphorescence signals. As the effect of the excitation disappears, the system response decays gradually with a certain timescale. Therefore, if the ISC indeed plays an active role in the exciton dynamics, longer exciton lifetimes are expected to increase the average decay timescale of the overall fluorescence signal. In other words, when the average exciton lifetime becomes longer, the ratio delayed-to-prompt fluorescence signals (DF-to-PF) increases.

Thin film P3HT:PCBM BHJ samples with different concentrations of Fe_3O_4 NPs are spin coated on Si substrates following the cleaning and deposition procedures described in chapter 4. The samples are excited with a wavelength of $\lambda = 485$ nm, slightly more energetic than the P3HT absorption's maximum (the mixture's main absorber). The photoluminescence response of the system is recorded between 600 and 850 nm. Five measurements are done on each sample: one prompt fluorescence (PF) measurement (recorded immediately after excitation) and four delayed fluorescence (DF) measurements with time delays of 10, 20 30 and 40 μs (gate time= 10 μs, flash count=1, cycle=20), whereby the measurements with 40 μs displayed again no intensity. All the signals are clearly identified as DF and not as phosphorescence due to the same spectral profile as the prompt fluorescence.[67] The obtained results are depicted in figure 6.8.

In figure 6.8 each point of both signals, PF (hollow squares) and DF (solid squares), corresponds to the integrated intensity over the whole scanned range (600 to 850 nm). In the case of DF, the measurements that yield a signal are as well combined. First of all, it can be already seen from the integrated PL intensities that the overall PL signal consistently decreases in the concentration region of improvement of OSC performance,

both for PF and DF. This higher level of quenching indicates a reduced recombination, since less intensity means less exciton decay per unit time.

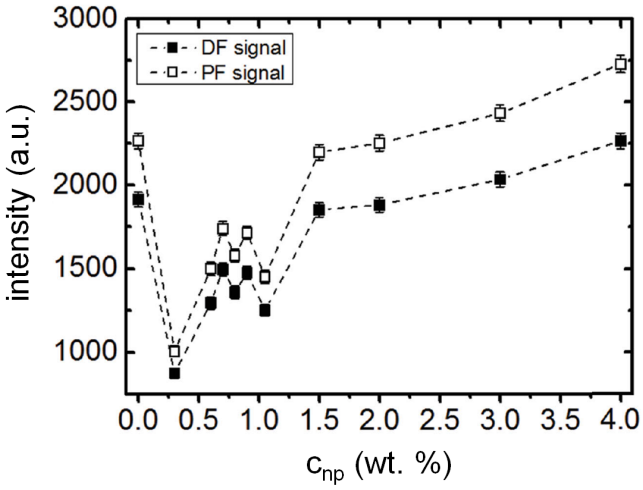

Figure 6.8: *Integrated PF (open symbols) and DF (full symbols) for different Fe_3O_4 concentrations.*

In order to gain insight into the underlying mechanisms of this reduced recombination, figure 6.9a shows the evolution of the ratio of DF-to-PF signals. The enhanced DF-to-PF ratio in the range of low NP content indicates, as discussed earlier, a higher degree of ISC. Thus, the elongated overall lifetime is related to the triplet-shifted exciton wave function, as discussed above in the beginning of the present section 6.2.3. Another way to see it is that the overall exciton lifetime is elongated through the contribution of those excitons that, once excited, migrate to the triplet manifold for later jumping back to the singlet excited state via triplet-triplet annihilation (TTA) prior to the radiative decay (details are provided in section 2.3). The DF-to-PF ratio is enhanced for low Fe_3O_4 NP concentrations with respect to the unmodified reference values (slightly above 0.84). Beyond 1.5 wt.% the ratios are back to the initial values and below. Moreover, since the DF measurements are performed with four different delay times, the signal decay in time is modeled as an exponential decay and can be used to extract a time constant. Despite the low time resolution of our experiment we are able to obtain an indicator related to the exciton lifetime τ_{eff}. Thus, the τ_{eff} value for each Fe_3O_4 NP concentration is calculated from the exponential fitting of the integrated PF and DF intensities:

$$I(t) = I_0 e^{-\frac{t}{\tau}} \;\Rightarrow\; ln(I) = ln(I_0) - \frac{1}{\tau}t \tag{6.1}$$

We can fit the logarithm of the decaying intensity with a linear regression $y = ax + b$, where $y = ln(I)$, $b = ln(I_0)$ and $a = -\frac{1}{\tau}$. Consequently, the error in τ_{eff} is derived from the error associated to the slope of the linear regression. The error of the slope a reads:

$$\delta a = \delta_{y_{reg}} \sqrt{\frac{N}{\Delta}} \tag{6.2}$$

where N is the number of fitted points, $\Delta = N \sum_i x_i^2 - (\sum_i x_i)^2$, and $\delta_{y_{reg}}$ is the standard deviation of each point of the fit:

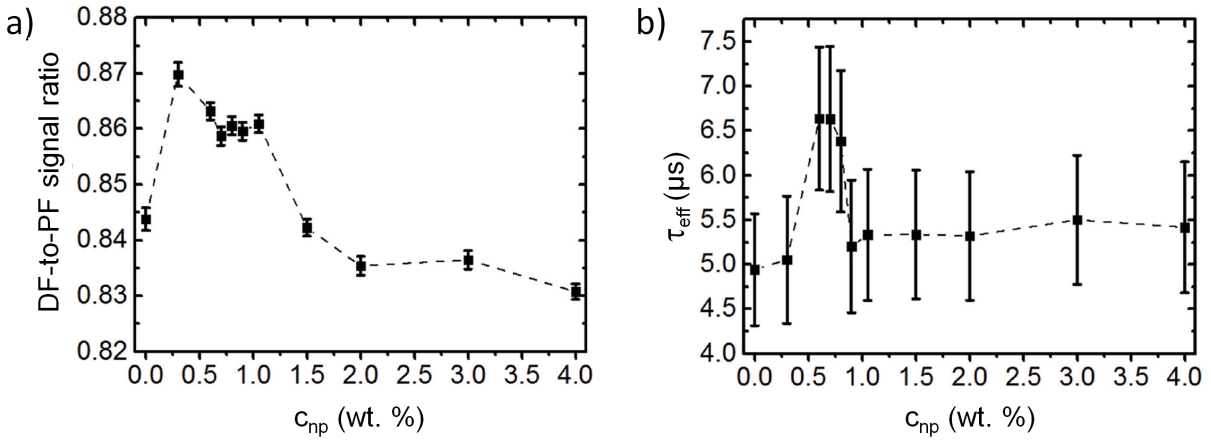

Figure 6.9: *a) Delayed-to-prompt fluorescence ratio and b) τ_{eff} versus NP concentration. Black squares are data points. Dashed lines are a guide to the eye.*

$$\delta_{y_{reg}} = \sqrt{\frac{1}{N-2}\sum_i (y_i - (ax_i + b))^2} \tag{6.3}$$

Once the uncertainty associated to the slope is calculated, propagation of errors yields the uncertainty on τ_{eff}:

$$\delta a = \frac{\partial a}{\partial \tau}\delta\tau = \frac{1}{\tau^2}\delta\tau \rightarrow \delta\tau = \tau^2 \delta a \tag{6.4}$$

Therefore:

$$\delta\tau_{eff} = \frac{\delta a}{a^2} \tag{6.5}$$

The evolution of τ_{eff} with the NP concentration is displayed in figure 6.9b. The error associated to each point is extracted from the fitting.

As it can be seen from figure 6.9b, τ_{eff} increases by more than 34 % at NP concentrations between 0.6 and 0.8 wt.% compared to the reference values (from 4.9 to 6.6 μs). It is noteworthy that τ_{eff} does not depict the intrinsic exciton lifetime. τ_{eff}, the time constant obtained from the exponential decay fitting, depends on a bunch of parameters combined together, such as the above-mentioned PL measurement protocol itself, or to recombination mechanisms that do not correlate with the exciton lifetime, like the non-geminate recombination (non-geminate recombination does not depend on the exciton dynamics since it happens between already independent polarons. See section 2.2.5 for further discussion). As a result of all these factors combined we obtain τ_{eff} and, although conclusions on the absolute time values obtained are not to be drawn, the study allows for comparison between samples where the measurement protocol has been kept constant

throughout the whole sample batch (as it is the present case) and throughout which the D-A morphology remains statistically unchanged. This last condition is confirmed by the GISAXS measurements.

The results obtained from the PL measurements support the hypothesis of extended average exciton lifetimes as origin of the observed improved OSC performance. Shorter exciton lifetimes as consequence of higher recombination rates have been already reported for small molecule BHJ OSCs, an effect that plays against the extraction of charge carriers in a solar device.[177] Besides of the evidence obtained from optical investigation, the improvement in OSC performance cannot be ascribed to morphology issues.

The decrease in DF-to-PF ratio and, consequently, in τ_{eff} for higher NP concentrations is ascribed to an increase in the rate of TTA events and, thereby, recombination. TTA is the primary decay mechanism for triplet excitons in organic media. In this recombination process two triplet excitons meet and, as a result of the annihilation process, one exciton comes out following spin statistics (meaning it will be a triplet exciton 75% of the times and a singlet the remaining 25%), whereas the second one decays non-radiatively to the singlet ground state, therefore, resulting in at least the net loss of one triplet exciton.[178,179] The efficiency of the TTA mechanism grows quadratically with the population of triplet excitons.[179] Thereby, at high NP concentrations, the magnitude of this mechanism is already expected to be significant, inducing a rapid destruction of the generated triplets and forcing one quarter of the remaining excitons back into the singlet manifold within short time scales. Hence, arguably shortening the overall decay time observed in PL measurements.[179,180]

6.2.4 Influence of P3HT crystallite behavior on short-circuit current density

To complete the characterization performed on P3HT:PCBM BHJ thin films with different concentrations of Fe_3O_4 NPs, GIWAXS experiments are performed. The inclusion of NPs could alter the crystalline phase in OSC active layers, thereby affecting device parameters such as the electrical conductivity. In this regard, GIWAXS allows us to track the sample's crystalline evolution. GIWAXS measurements are performed at the P03 beamline, at the PETRA III storage ring at DESY, Hamburg (DE). The x-ray energy is 13 keV, the incident angle 0.15° and the SDD 153 mm. The scattering signals were recorded on a Pilatus 1M detector. The collected 2D patterns for P3HT:PCBM blends with varied Fe_3O_4 NP concentrations are displayed in figure 6.10.

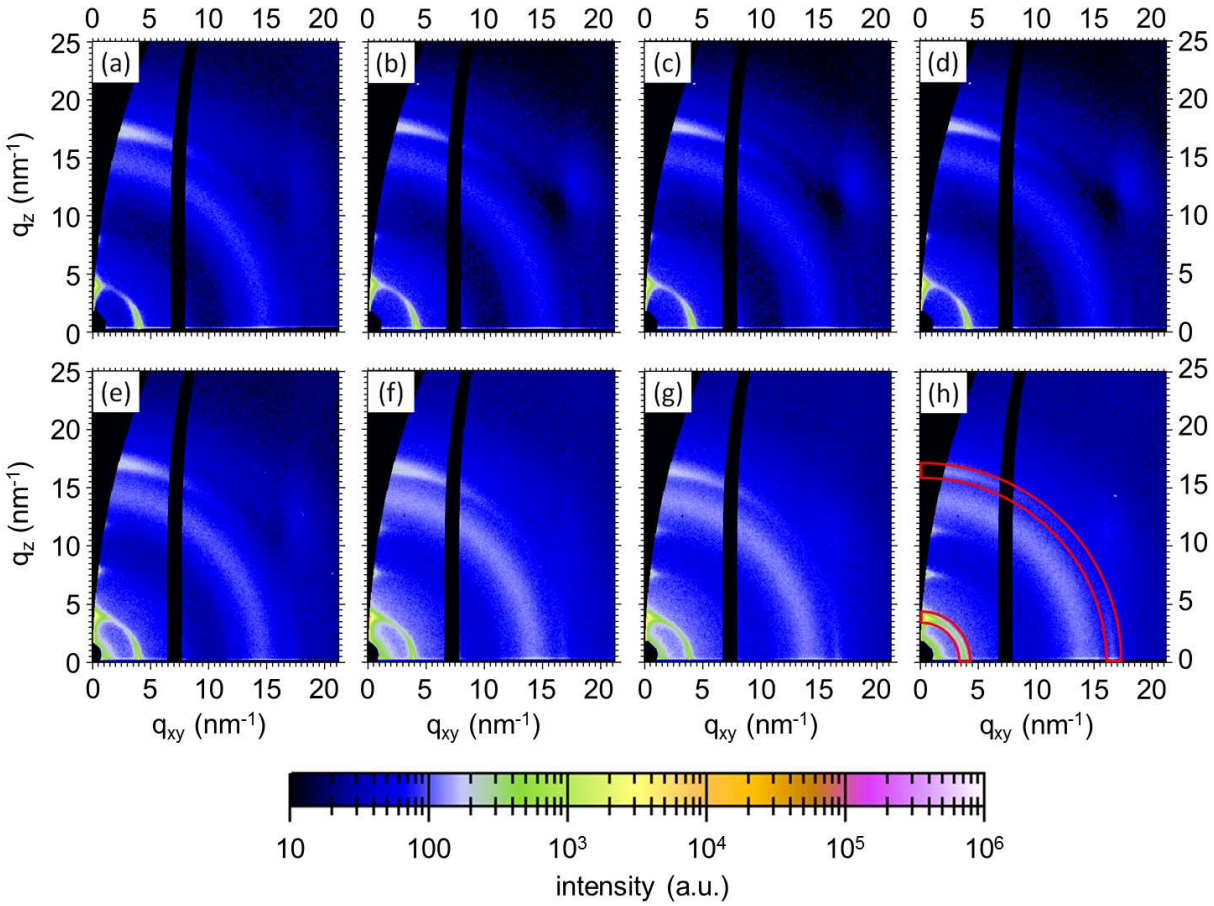

Figure 6.10: *2D GIWAXS patterns of P3HT:PCBM BHJ thin films with different concentrations of Fe_3O_4 NPs: a) 0.0 wt.% b) 0.1 wt.% c) 0.6 wt.% d) 0.8 wt.% e) 1.05 wt.% f) 2.0 wt.% g) 3.0 wt.% h) 4.0 wt.%. Images are corrected for q_{xy} vs. q_z representation. Tube cuts in h) indicate the areas selected for radial integration around the crystalline families (100) and (020) for study of the P3HT crystallite orientation.*

Already from the 2D GIWAXS data the Bragg peak arising from the P3HT $\pi - \pi$ stacking is visible at $|q| \approx 17$ nm^{-1}. This crystalline family is the (020) (indicated in figure 6.10h by the outer red ring) and plays an important role in the conductivity of P3HT. In polymer crystals such as P3HT, the highest conductivity values correspond to the (h00) polymer backbone direction, followed by the relatively high conductivity through $\pi - \pi$ stacked planes along the (0k0) crystal direction. Here the (020) shows a preferential orientation perpendicular to the substrate for 0.0 wt.% (along $q_{xy} = 0$ nm^{-1}). Upon addition of NPs the vertical (020) feature becomes wider, thereby indicating a more isotropic orientation of crystallites. The same is observed for the (100) family, which relates to the backbone spacing within one stacking plane of a P3HT crystallite (inner red ring in figure 6.10h). The (100) Bragg peak shows for 0 wt.% NPs strongly-oriented crystallites both parallel and perpendicular to the sample substrate, for afterwards becoming a more

ring-shaped feature upon addition of NPs, meaning a more isotropic orientation of crystallites. Moreover, the increase in Fe_3O_4 NP concentration reveals as well an improved edge-on orientation (i.e. $\pi - \pi$ planes stacked perpendicular to the sample substrate, while polymer backbones are oriented parallel to it. See section 3.1.4). This is indicated by the increasing intensity of the (100) higher orders, i.e. (200) and (300). As discussed above, an increase in edge-on orientation to detriment of the face-on is expected to have a negative effect on the device vertical conductivity, since the polaron mobility across stacked planes is higher than along hexyl side chains, where the lack of conjugated bonds makes the conductivity almost negligible.[181,182]

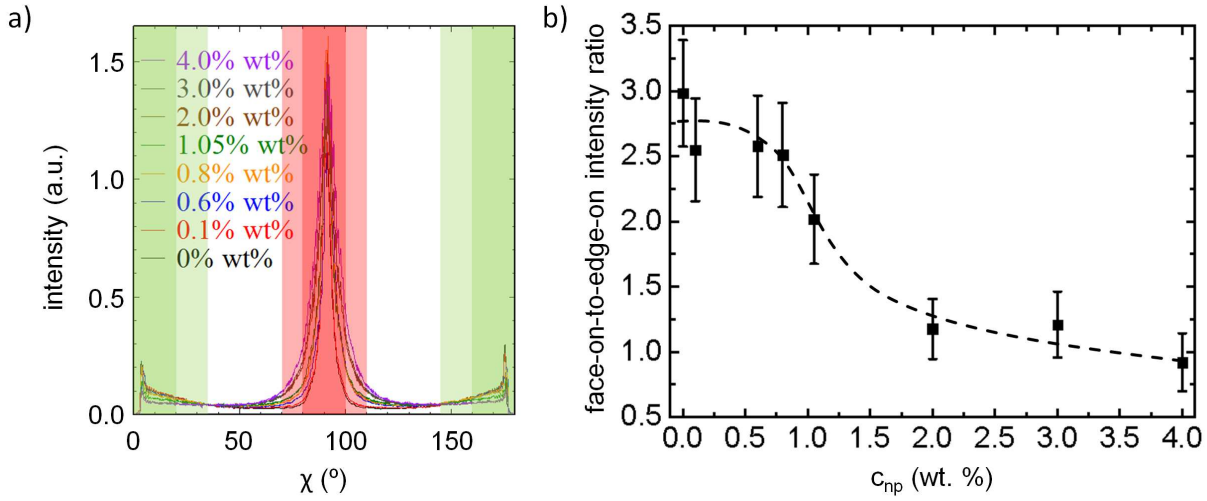

Figure 6.11: *a) Tube cuts of the P3HT (100) plotted versus the angle χ. The red areas indicate edge-on orientation, whereas green areas are considered as face-on orientation. Light- and dark-colored ranges indicate the tolerance in the definition of the different orientations. b) Face-on-to-edge-on ratios calculated from the (100) tube cuts. The dashed line is a guide to the eye.*

Tube cuts along the (100) Bragg peak for all possible crystalline orientations are performed to gain further insight into the evolution of P3HT orientation with Fe_3O_4 content. These are displayed in figure 6.11a, where it can already be seen how the face-on orientation (at the two green sides of the graph) decreases with NP content. By selecting different angular ranges associated to pure face-on (in green) and edge-on (red) orientations and integrating the corresponding intensities under the curves, we are able to estimate face-on-to-edge-on ratios. The angle thresholds defining which sections of the cuts are regarded to as face-on or edge-on orientations are multiple, being the broadest and narrowest cases indicated in figure 6.11a as lighter and darker highlighted regions, respectively. This multiple selection on the position of the edge-on and face-on borders is done in order to ensure that the obtained trends do not depend on a particular choice. The resulting face-on-to-edge-on ratios are displayed in figure 6.11b, and the multiple

choice of orientation threshold provide the error bars associated to each ratio.

As it can be seen from figure 6.11b, the ratio remains reasonably constant below 1.0 wt.% NPs, the region of solar cell improvement. This further discards device improvement due to any modification of the crystalline phase, giving further credit to the anticipated extended exciton diffusion length that has been already supported by all previous characterization methods. Beyond 1.0 wt.% of NPs the face-on-to-edge-on ratio of P3HT decreases down to about one third of the initial value for concentrations of 4.0 wt.%. In addition to a lowered face-on-to-edge-on ratio and a general isotropic crystallite reorientation, it can as well be seen from the tube cuts in figure 6.11a how specifically the edge-on orientation itself broadens with Fe_3O_4 NP presence, indicating a worsening orientation of stacked planes perpendicular to the sample substrate. For a more quantitative analysis on this loss of orientation definition the edge-on orientation of the tube cuts is fitted with Lorentzian functions. The results are depicted in figure 6.12. The loss of definition in edge-on oriented crystals is noticeable from the fitting. The FWHM of the fitted Lorentzian curves is displayed versus the NP content in figure 6.12b. It remains approximately unchanged for low Fe_3O_4 NP concentrations (below 1.0 wt.%), whereby beyond this limit the FWHM rapidly increases, surpassing at 3.0 wt.% the double of the initial value.

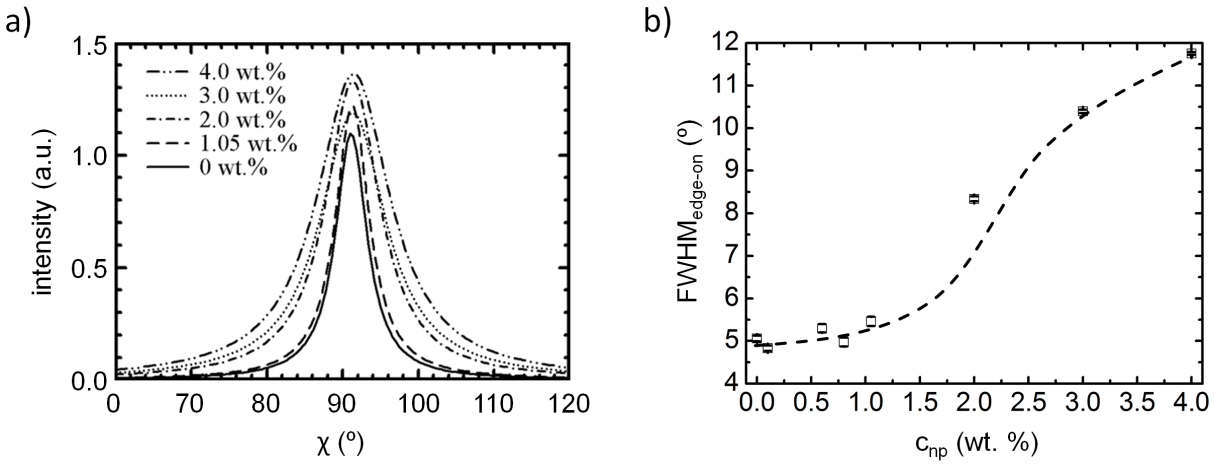

Figure 6.12: *a) Lorentzian fits to the tube cuts of the P3HT (100) Bragg peaks plotted versus the angle χ. b) FWHM of the Lorentzian fits plotted versus the NP wt.%. The dashed line is a guide to the eye.*

Interestingly, it is possible to compare the evolution of the degree of the edge-on orientation with that of the short-circuit current of the resulting solar devices. The inverse of the FWHM obtained from the fit to the edge-on maxima is plotted versus the NP wt.% together with the device J_{SC} in figure 6.13.

The plot of both parameters shows a good agreement, especially in the range of low Fe_3O_4 content. The relation between active layer morphology and J_{SC} has already been reported, including as well studies that suggest that face-on orientation is beneficial for photovoltaic applications.[179,183,184] Given that the changes in mesomorphology observed in the present study are negligible, we ascribe the evolution of the device J_{SC} to the worsening ordering of the P3HT aggregated regions. This correlation is especially good in the range of low NP content, where below 1.0 wt.% J_{SC} presents a mild decay. For high concentrations, as discussed earlier, the conductive paths enabled by the massive presence of NPs are expected to significantly contribute to the drastic decay in J_{SC}.

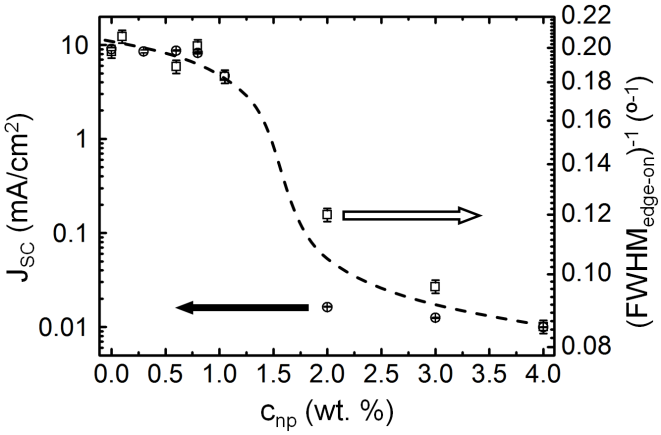

Figure 6.13: *Inverse FWHM of the Lorentzian fits to the P3HT (100) family along with the device J_{SC} plotted versus the NP content. Open and full symbols are data points. The dashed line is a guide to the eye.*

6.3 Effect of additional external magnetic fields

The investigations presented in 6.2 on the effect of superparamagnetic NPs on the performance of P3HT:PCBM OSCs yielded striking results, displaying reduced charge carrier recombination and increasing PCEs in the regime of low Fe_3O_4 content, up to concentrations of 0.8 wt.%. The only appointable reason for this reduction in recombination is the increase in ISC introduced in the photoactive layer by the NPs. Effects pointing to this reduced recombination were directly observed in the behavior of solar devices, as discussed in section 6.2.1. Moreover, spectral and structural characterization closed the eventual improvement of OSC performance due to optimized active layer morphology, thereby reinforcing the assumption of longer exciton diffusion lengths through higher triplet exciton population, induced by an increased ISC.

Furthermore, the round-shaped superparamagnetic NPs are further magnetized under the influence of an external magnetic field, creating a stronger inhomogeneous field distribution in their vicinity than they have in absence of external fields. Saturated Fe_3O_4 NPs with a size of 10 nm can generate a magnetic gradient of 60 $^{mT}/_{nm}$, larger than usual hyperfine coupling, and much larger than any inhomogeneities that can be generated

with macroscopic external setups, like coils or permanent magnets.[73] Following this line of thought, the next step is to explore the effects on OSC performance upon additional magnetization. According to the supplier, the NPs present a magnetization > 45 emu/g under 4500 Oe at RT[185], and a saturation magnetization of (60 ± 25) emu/g, according to [186]. Nevertheless, the actual magnetization of the used NPs is expected to be lower than this latter value, given that the functionalization with OA decreases the overall saturation magnetization.[187] Thus, if the local magnetic field inhomogeneities are inducing the spin rephasing that leads to the improved OSC performance, it is the question whether this effect can be further magnified by an additional external magnetic field. The external field would bring the NPs towards saturation magnetization, increasing further the recombination reduction already observed in OSCs. It is noteworthy to mention that, throughout the thesis, for simplicity purposes, magnetic field intensities H are given as the equivalent magnetic flux density in vacuum (or air) B, whereby $B = \mu_0 \mu_r H$. Hence, the field intensity is expressed in mT, whereby the conversion factor to SI magnetic field intensity units reads: 1 mT = 10 Oe $\approx$ 795.77 A/m.[188]

In the present section we explore the effect on device performance of different applied magnetic field intensities. First, a study featuring weak but finely-adjustable field intensities is presented. This is achieved by a Helmholtz coil setup, featuring homogeneous and practically one-dimensional fields. Finally, a second setup with a permanent magnet is presented, in an attempt of reaching saturation magnetization. Thereby, challenges related to technical implementation and comprehensiveness of the obtained data still remain. In this regard, detailed discussion on the setups, their construction, features and calibration are provided in the appendix A at the end of this thesis.

6.3.1 Weak magnetic fields

Weak magnetic fields are generated via a custom-made Helmholtz coil, able to generate magnetic fields up to 11 mT. The setup is calibrated to ensure homogeneity of the field, as well as to guarantee that the generated magnetic fields do not affect the surrounding electronics or the moving charge carriers outside the solar device, i.e. in the wiring attached to the OSC during operation. Confirmation of the field one-dimensionality is important, as Lorentz forces derived from non-parallel magnetic fields and flow of charge carriers could affect the current flow within the cables and, consequently, affect the obtained data.

The influence of magnetic fields on the performance of OSCs with NP loads between 0.3 and 0.8 wt.% is studied, given that higher concentrations already did not show an im-

provement in the absence of field. Reference devices without NPs were fabricated and used as calibration, as these are supposed to remain unaffected given their lack of NPs. The results corresponding to OSCs without NPs and their use for calibration purposes are discussed in the appendix A.

The main challenge to overcome was the fact that the non-encapsulated lab devices degrade over time, mainly owing to contact with O_2 in combination with UV radiation. Therefore, consecutive measurements of OSCs subjected to different magnetic field intensities yield results depicting decreasing absolute performances. The reason for that is that the improvement due to magnetic field is way smaller than the device degradation between consecutive measurements. Therefore, the improvement in performance provided by the magnetic field cannot be observed directly with the used OSC layout.

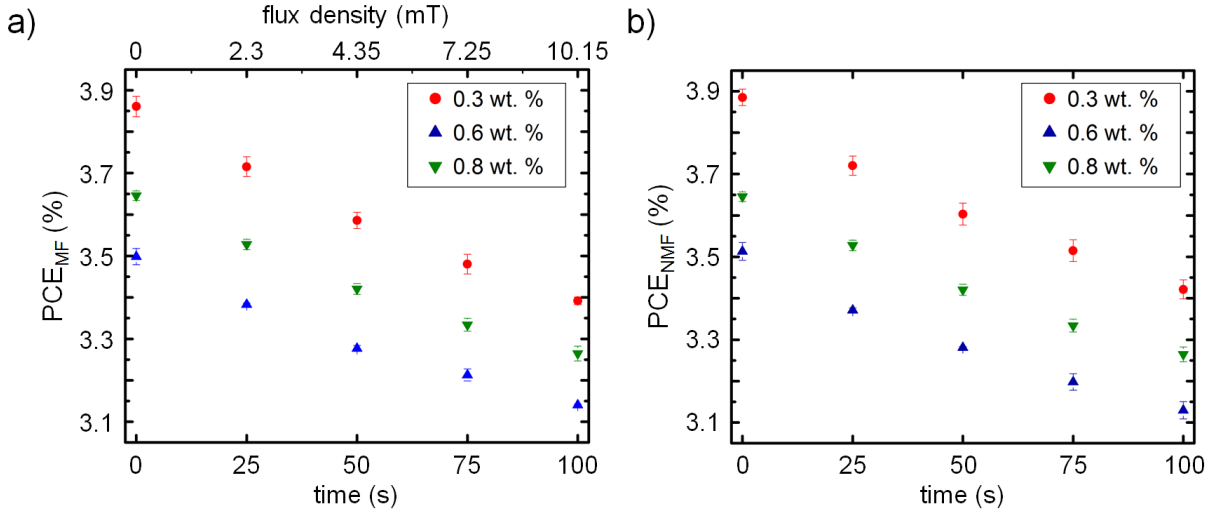

Figure 6.14: *a) Time development of efficiencies of OSCs with various NP contents for different intensities of the applied external magnetic field. b) Time development of efficiencies of OSCs with various NP contents in absence of applied external magnetic field for normalization purposes.*

Thus, to quantify the influence of the magnetic field, the measurements performed at different field intensities need to be decoupled from their time-dependent degradation. The workaround employed at this stage is to fabricate identical devices and to subject them to identical measurement protocols, while keeping the field intensity constantly to zero. The reference devices reproduce the aging behavior between measurements and during waiting times. Thus, their time behavior is used to normalize the photovoltaic parameters of the devices studied in presence of external field. Figure 6.14 exemplary shows the corresponding sets of data for the evolution of the PCE. Figure 6.14a displays the decay in PCE with time and flux density as depicted by the double x-axis. The upper x-axis shows the field intensity at which each measurement is taken. The lower x-axis displays the elapsed time between measurements, which is intentionally kept constant at 25 s. Fig-

ure 6.14b shows solely the time evolution of the reference devices, which were fabricated under the exact same conditions as those in figure 6.14a, but measured in absence of magnetic field. It can be seen how the absolute performances of the corresponding data sets are almost identical, thereby justifying the subsequent normalization, which eliminates the degradation-over-time dependency. The normalization is done via $r(B) = \frac{PCE_{MF}(B,t)}{PCE_{NMF}(t)}$. Thus, the obtained normalized photovoltaic indicator depends exclusively on the intensity of the magnetic field, and its evolution can be observed directly.

Figure 6.15 illustrates the normalized evolution of the main extracted photovoltaic parameters with magnetic field intensity for OSCs with different Fe_3O_4 concentrations. The error bars associated to each point are calculated from the distribution of values obtained from the different solar cells fabricated on each substrate. The green (red) areas indicate clear improvement (worsening) with respect to the initial values, whereas the yellow areas mark the uncertainty range associated to each first data point, hereby defining a region of ambiguous interpretation.

The evolution of the PCE (figure 6.15a) depicts an improvement with increasing magnetic field for OSCs with 0.8 wt.% NPs. The increase is monotonous and tops at a field of 10.15 mT, displaying an improvement of 2.56 % with respect to the initial reference value. Nevertheless, devices with lower Fe_3O_4 content do not display any clear trend for increasing magnetic strength. Given that the improvement expected for these two concentrations is lower than for the one with 0.8 wt.% (in accordance with the NP concentration) one possible explanation is that the effect generated for the samples with 0.3 and 0.6 wt.% is too small for the sensibility of the setup. Moreover, very small variations in PCE or any other OPV parameters due to the effect of the magnetic field are at risk of getting lost through the time-decoupling normalization procedure.

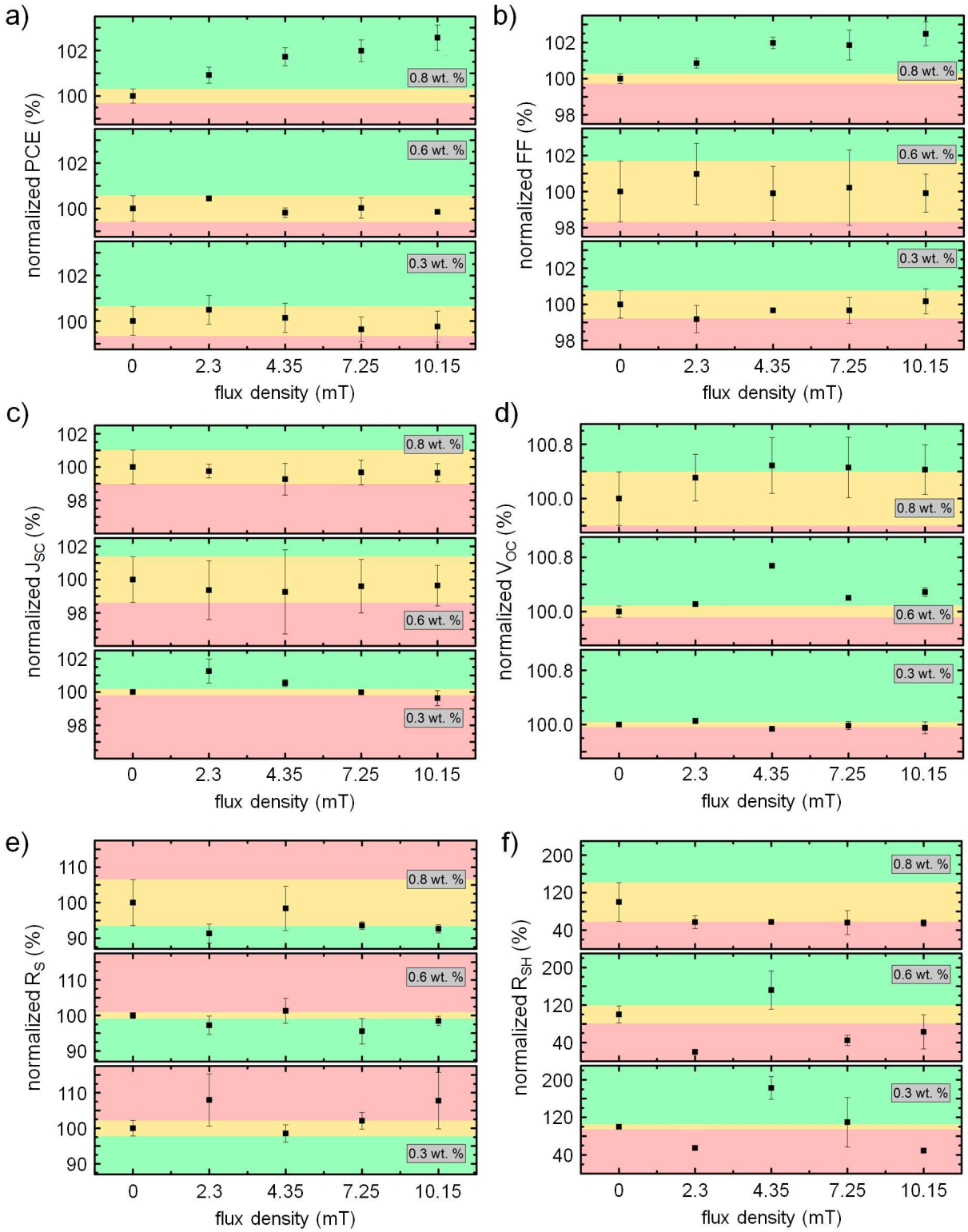

Figure 6.15: *Normalized a)PCE, b)FF, c)J_{SC}, d)V_{OC}, e)R_S and f)R_{SH} obtained for NP-modified P3HT:PCBM OSCs as a function of the applied external magnetic field. The yellow areas are defined by the error bars of the data points from OSCs measured in absence of field. These are taken as the range for which no parameter change is considered. Green areas indicate improvement, whilst red areas indicate parameter worsening.*

Similar to the effect observed upon incorporation of NPs (section 6.2.1), the normalized FF (figure 6.15b) depicts the same trend as the PCE. As discussed earlier in this chapter, an increase in FF combined with a flat development of both the R_S and the R_{SH} (figures 6.15e and f) indicates that the improved performance owes to a reduced device recombination. This happens in the case of solar cells containing 0.8 wt.% NPs, where the increase in FF is as well monotonous, showing an improvement of 2.48 % at a field strength of 10.15 mT, compared to the initial value.

The clear reduction of recombination observed for the sample with 0.8 wt.% Fe_3O_4 concentration is further confirmed by the mild increase in normalized photovoltage (figure 6.15d). The V_{OC} features an increase with a certain overlap with the yellow area (improvement factor 0.49 %), but qualitatively increasing with field strength. Compared to the reference, the OSCs with 0.6 wt.% NPs present improved normalized V_{OC} for all applied fields. The V_{OC} features a maximum for a field strength of 4.35 mT, which means an improvement of 0.68 % compared to the no-field case. In the case of samples with a Fe_3O_4 load of 0.3 wt.% the normalized photovoltage remains rather stable, arguably indicating that the concentration of Fe_3O_4 is too low to yield effects observable at device scale. The effect of the charge carrier recombination on the V_{OC} are discussed in detail in chapter 7. Likewise, greater insight into the nature of the V_{OC} and the influence of recombination is provided in the literature.[189,190]

The evolution of J_{SC} does not show any clear trend for any of the investigated Fe_3O_4 concentrations. Only in the case of 0.3 wt.% NPs a certain increase in J_{SC} is observed, reaching a maximum at a field intensity of 2.3 mT. However, this outcome needs to be considered with caution, since the evolution of J_{SC} linked to, e.g. a decreasing device recombination, is not clearly supported by any of the other photovoltaic parameters. Overall, by comparing the different concentrations for the various tested field intensities, the J_{SC} can be regarded as constant.

Also both the series and the shunt resistances depict no clear trend, and are regarded as constant, since they mostly pivot around the starting values in absence of magnetic field. Either most of the data points for non-zero field stay within the uncertainty of the yellow area, as it happens for samples with 0.8 wt.% NPs, or present ever-changing behavior, alternatively better and worse than the staring values, resembling a rather flat behavior. In any case, no clear and monotonous increase (decrease) is observed in the shunt (series) resistances, that could refute the observed increase in FF due to a reduction in the exciton recombination.

Thus, the study with weak magnetic fields shows further device improvement owing to reduced device recombination on top of the improvement observed by the simple addition of superparamagnetic Fe_3O_4 NPs. Overall, for P3HT:PCBM OSCs the further magnetization of the NPs via a weak external magnetic field brought on top of the 11 % PCE improvement introduced by the sole inclusion of the NPs an additonal increase of over 2.5 %. In the next section, we test the role of the magnetized photovoltaic setup further towards its limits, featuring fields roughly forty times stronger than those applied so far.

6.3.2 Strong magnetic field

According to Goya et al.[186] Fe_3O_4 NPs with a diameter of 10 nm present a saturation magnetization of (60 ± 2) emu/g, which, according to their hysteresis curves, is achieved to approximately 90 % at a field intensity of 5000 Oe. In the previous section we explored the effect of finely tunable magnetic fields, featuring intensities of up to 110 Oe. The fine tunability of the setup allows us to recognize effects on solar devices related to the magnetic stress, like the monotonous increase of the FF or of the V_{OC}, which in turn have obviously an impact on an icreasing PCE as well. However, the fields used in the previous section were small compared to the NPs saturation field. Hence, their influence made the system to stay in the initial linear segment of the hysteresis curve, which in turn explains the observed behavior of the tracked photovoltaic parameters.

In this section we discuss the results obtained for the first attempts to study the effect of a magnetic field intensity of 4400 Oe, much more comparable to the saturation fields required by the used NPs. The strong fields presented in this section are achieved by a permanent magnet setup. Therefore, the data obtained for these experiments can only compare field to no-field cases, thereby making the observation of monotonous trends with varying field intensities impossible. Some technical issues related to this setup have to be kept in mind: the approximation of one-dimensional magnetic field and, consequently, the no disturbance by the field of the surrounding electronics cannot be guaranteed as in the previous case. Details about the setup and its calibration are provided in the appendix A.

The procedure used in this case to decouple the time dependence from the effect introduced by the external field is the same as the one presented in the previous section 6.3.1. As in the previous case of weak magnetic fields, the error bars associated to each measured parameter are obtained from the distribution of obtained values among the single OSCs on each substrate. Furthermore, the uncertainties associated to the presented normalized

parameters $\frac{P_{MF}}{P_{NMF}}$ are calculated via Gaussian propagation of errors:

$$\delta\left(\frac{P_{MF}(B,t)}{P_{NMF}(t)}\right) = \sqrt{\left(\frac{1}{P_{NMF}(t)}\delta P_{MF}(B,t)\right)^2 + \left(\frac{P_{MF}(B,t)}{P_{NMF}(t)^2}\delta P_{NMF}(t)\right)^2} \tag{6.6}$$

whereby $\delta P_{MF}(B,t)$ and $\delta P_{NMF}(t)$ are the uncertainties measured for the corresponding parameters with and without presence of magnetic field, respectively.

The obtained normalized data is summarized in figure 6.16. The color code used in the previous case of weak magnetic fields still holds. Thereby, green bars indicate parameter improvement compared to the situation in absence of external magnetic field, whereas red bars indicate a worsening. Unchanged parameter behavior is highlighted with yellow bars. Similarly to the case of weak magnetic fields, the study is carried out for the NP concentrations in which previously the sole inclusion of NPs featured an improved device performance (data corresponding to 0 wt.% and their use for calibration purposes is presented in the appendix A).

Generally, the efficiencies of all investigated samples show an increase, irrespective of the NP concentration. The increase seems to be slightly larger for a Fe_3O_4 load of 0.8 wt.%, showing a performance improved by 2.3 % compared to the no-field situation. However, the associated errors bars for all three concentrations make it difficult to extract meaningful trend-like behavior, as they depict a significant overlap. Regarding the obtained efficiencies, the results are unexpected for two reasons: on the one hand, the average increase in PCE is in the same range as the one obtained in the case of weak magnetic fields. On the other hand, no clear unambiguous trend can be observed throughout the different Fe_3O_4 concentrations. In principle, both effects indicate that, even if according to their hysteresis cycle the NPs are not yet supposed to have reached saturation, the effect on the device performance of the applied magnetic field tops already at lower field intensities. However, all devices showed an improvement in the average PCE upon presence of magnetic field and increase monotonously with NP concentration, a fact which was expected and proven.

In the present case of strong magnetic field, the increase in PCE is clearly linked to an increase in J_{SC} (figure 6.16c), as high as over 3 % in the case of 0.3 wt.% NP-modified OSCs. Thereby, no clear correlation with the Fe_3O_4 concentration is recognizable. Nevertheless, the increase in J_{SC} (and consequently in PCE) due to a lowered exciton recombination was observed in section 6.2.1 in experiments without external magnetic field, as well as it is reported in the literature.[169,170]

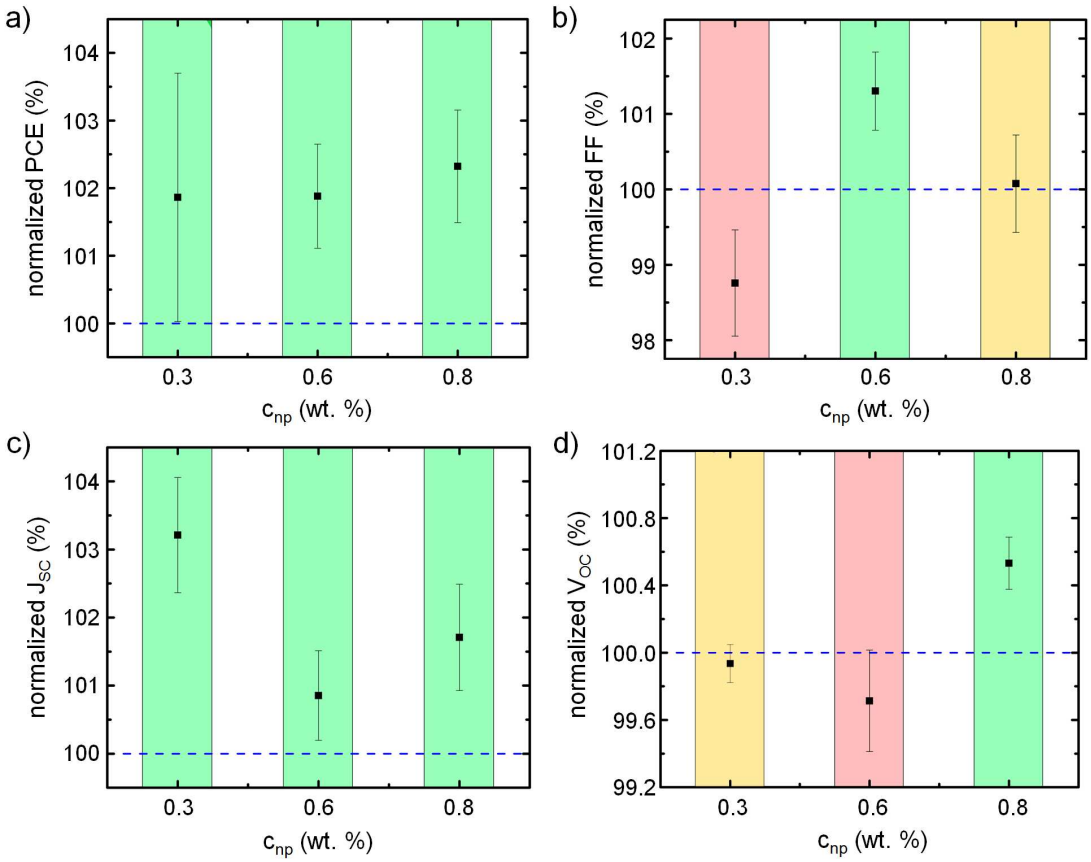

Figure 6.16: *Normalized a) PCE, b) FF, c) J_{SC} and d) V_{OC} obtained for modified P3HT:PCBM OSCs for an externally applied magnetic field of 440 mT, normalized to the no-field case, which is indicated by the dotted lines. Data points within green bars indicate improvement upon presence of magnetic field. Points in red bars indicate a worsening. Points within yellow bars indicate unchanged photovoltaic parameters.*

The other main OSC proxy for lowered device recombination, the FF (figure 6.16b), does not show the expected behavior, i.e. neither does it increase with the intensity of magnetic field nor does it correlate with the evolution of the PCE. The variation in FF upon presence of magnetic field is small: a worsening is found for 0.3 wt.% samples, an improvement is seen for 0.6 wt.%, and no clear change for 0.8 wt.% is observed. Hereby, none of the variations exceed 1.3 % in percentage. Similarly, the V_{OC} (figure 6.16d) shows a relative improvement only in the case of 0.8 wt.% NP concentration, whereas the other two concentrations depict a decrease in photovoltage. Nevertheless none of the changes exceed 1 % with respect to the no-field case.

In summary, an increase in PCE is observed upon deployment of a strong magnetic field for all NP concentrations. This increase seems to be driven by an increase in J_{SC}, which

is in agreement with previous experiments and with the literature. However, the FF provides an indication for an inverse correlation with the J_{SC}. This stands in contradiction with the experience gathered in no-field or weak-field situations. Moreover, it is difficult to observe trends amongst the recorded parameters, owing to the fact that the nature of the setup only allows field or no-field comparisons, discarding the possibility of performing field-dependent studies in the strong-field regime. In order to gain further insight in the system response to magnetic fields from no-field up to saturation, setups achieving homogeneous and one-dimensional strong fields in a continuous fashion are desirable.

6.4 Summary and conclusions

In the present chapter we have explored novel ways to enhance the performance of P3HT:PCBM organic solar devices through the inclusion of Fe_3O_4 NPs. The improvement in PCE appears at low concentrations (below 1.0 wt.%), mainly as a result of a higher FF. The NPs create in their vicinity weak magnetic fields due to their magnetic remanence, contributing to the relaxation of the spin selection rule. The resulting exciton spin rephasing leads to an increased ISC. The higher contribution of triplet states to the average exciton wave function induces a reduction in the efficiency of the radiative decay mechanism, as observed in fluorescence experiments (section 6.2.3). Hereby, longer average exciton lifetimes (τ_{eff}) are observed and, consequently, longer diffusion lengths. Longer diffusion lengths allow excitons to reach farther interfaces and, thereby, the recombination of excitons which are not reaching an interface within their lifetime is reduced, improving the efficiency of the solar device.

The improvement in the FF that leads to enhanced performance happens in the diode region of the J-V curve. This means a reduction in the device ideality factor without alteration of the series (R_S) and shunt (R_{SH}) resistances. R_S and R_{SH} stay constant throughout the NP concentration range of improved OSC performance. The increase is directly linked to a reduced recombination in device operation. Moreover, optimized devices showed as well a monotonous increase in J_{SC} as a result of the lowered recombination. This effect was previously observed by Zhang et al., and posterior experiments by Jaramillo et al. observed as well an increase in device J_{SC} upon recombination decrease due to presence of superparamagnetic NPs,[169,170] in good agreement with our observations.

The optoelectronic characterization shows an improved delayed-to-prompt fluorescence (DF-to-PF) ratio, supporting the assumption of longer τ_{eff} arising from higher ISC for

NP-modified devices. In this regard, estimation of the decay rate through DF measurements of different delay times show an elongation of τ_{eff} by up to 34% as compared to unmodified P3HT:PCBM reference cells. Comprehensive analysis of the bulk nano- and mesomorphology via GISAXS and GIWAXS experiments show no prominent changes in the crystallinity or the D-A arrangement that could explain the observed reduction in recombination and subsequent improved performance. Hence, the hypothesis of decreased recombination as a result of longer exciton diffusion lengths in modified OSCs is reinforced.

For high NP content above 1.0 wt.%, the OSCs present short-circuited behavior. This is ascribed to shunt paths enabled by the highly conducting Fe_3O_4, which is supported by the rapidly dropping device R_{SH} (beyond NP concentrations of 1.0 wt.%). Finally, the first stages of J_{SC} reduction upon low Fe_3O_4 content show very good agreement with the loss of order of edge-on-oriented P3HT crystallites, according to GIWAXS investigations.

The effect of additional external magnetic fields on Fe_3O_4-modified solar cells is additionally investigated. Two different setups are built, capable of generating two different magnetic fields. On the one hand, a Helmholtz coil setup achieves weak magnetic fields of up to 11 mT, though, finely adjustable, homogeneous, and highly one-dimensional. On the other hand, a permanent magnet setup presents much lower standards in terms of field adjustability and one-dimensionality. However, it is able to achieve fields of 440 mT, bringing the NPs close to their saturation magnetization, according to calculations based on other reports.

For weak magnetic fields, in the linear regime of the hysteresis curve and far from the saturation, a monotonous increase with magnetic field intensity is found in the PCE for samples with a Fe_3O_4 load of 0.8 wt.%. At 10.15 mT the PCE tops at a 2.56 % improvement as compared to the case in absence of magnetic field. As in the previous experiments with NPs and no external field, the improvement in PCE is intimately related to the improvement in FF, signalizing the desired reduced device recombination. For samples with lower Fe_3O_4 content, no significant variations or recognizable trends were observed. This is ascribed to the fact that the sought effects are either too small for the sensitivity of the setup, or they get lost in the applied normalization, time-decoupling process.

In experiments featuring intense magnetic fields of 440 mT, increases in efficiencies by between 2 and 3 % were found for all NP concentrations. These increases are driven by the J_{SC}, in accordance with previous experiments and with the literature, supporting the interpretation of reduced exciton recombination. Nevertheless, in the case of intense

magnetic fields, the device FF did not show consistent improvement. This fact is in contradiction with previous knowledge from the no-field or weak-field scenarios. In spite of the promising obtained results, in this case of strong magnetic fields, parameters of the setup and of the created magnetic field can benefit from a technical improvement iteration. Ideally, technical improvements should lead to an enhanced one-dimensionality of the generated field, avoiding feared Lorentz forces in the wiring and circuitry around the studied OSCs that could eventually affect the measurement. Nevertheless, calibration measurements with NP-free P3HT:PCBM OSCs showed good behavior, making the obtained results reliable, yet preliminary (more details in the appendix A).

To overcome the challenges met in the implementation of field-dependent experiments, the goal would be to achieve setups technically capable of achieving comparatively high flux densities. Flux densities of around 0.5 T in vacuum (air), adjustable in a continuous manner and featuring high one-dimensionality are desirable. Moreover, better approaches for eliminating the time-dependency due to device aging need to be found. As an example, experiments with encapsulated devices could be conducted.

Overall, the experience with PCE improvement and reduced exciton recombination investigated in this chapter yielded very positive results. Deployment of magnetic fields has proven to be able to tune the exciton spin statistics and to revert positively on the OSC performance. It is noteworthy to mention that the work presented here is pioneer in terms of its novelty and comprehensiveness. The study of the effect of magnetic fields on OSC charge carrier statistics and device performance is still a young field of research. Despite the understanding already available, complementary work is intended in order to gain further insight on the physics governing the device behavior at various field intensities.

Regarding its potential for immediate use in industrial applications, we can divide the presented work in two parts. The first one corresponds to the sole inclusion of superparamagnetic NPs in device active layers. It is an easy process, and the work carried out already provides great insight into the understanding of the underlying physical processes. Moreover, it grants as well reproducibility at low implementation costs. The second part corresponds to the further increase in efficiency through the use of external magnetic fields. Hereby, a further improvement is possible. However, the technical requirements for achieving such improvements are considerable (see appendix A), and the improvement gained is in return moderate (below the increase obtained by only introducing NPs). Therefore, further study of the effect of magnetic fields will provide valuable contributions to fundamental knowledge, but is rather unlikely to end up being generally

cost-effective in industrial or daily applications, at least based on the current approach.

Provided that the setting up of massive magnetic fields around solar cells might not be profitable from a large-scale, industrial point of view, in the next section we will investigate the influence of NPs on another aspect crucial in regard of commercial profitability; namely, the device lifetime. Material and device aging causes and paces are capital for determining integrated efficiencies over large periods of time. Efficiencies considered over functioning time are significant for deciding to which extend a technology is profitable. In this regard, besides of improving device PCEs, we explore whether the inclusion of Fe_3O_4 NPs has as well an impact on the device degradation. This research will ultimately lead to deeper fundamental study of the intrinsic behavior of device aging, providing greater understanding of the physics of OSC device degradation in general, and into the early "burn-in" aging phase in particular.

Chapter 7

Device aging of Fe_3O_4-modified P3HT:PCBM OSCs

After the investigation of the impact of NPs and of additional external magnetic fields on the performance of Fe_3O_4-modified P3HT:PCBM OSCs, we further explore the effect of such NPs on device aging under exposure to O_2 and UV radiation. The study of the changes in degradation speed as a result of NP inclusion reveals a need for further research about the links between the time-dependent behavior of solar cell operation and the changes in the crystalline morphology of the device active layer.

The article *Codependence between crystalline and photovoltage evolutions in P3HT:PCBM solar cells probed with in-operando GIWAXS*, cited in this work as the reference [15], has been published as a result of part of the work presented in this chapter. Parts of the chapter have been extracted from the master's thesis *"Enhancing triplet exciton population in organic solar cells"* by Florian Dreher.[117]

7.1 Introduction

The studies presented in the previous chapters, aimed at decreasing charge the carrier recombination via an ISC-assisted elongated exciton diffusion length, have yielded a promising scope for further research and development. Ambitious approaches involving polymers with chemically-embedded heavy post-transition elements (PBST3HT, see chapter 5) presented very interesting properties, including their outlandish response to temperature. Nevertheless, PBST3HT implementation in OSCs still requires further research iterations. In contrast, alternative approaches taking advantage of magnetic field gradients using Fe_3O_4 NPs have yielded very positive results (chapter 6). The introduction of NPs yielded *PCE* improvements of up to 11 % as compared to unmodified reference

devices. This represents an easy and inexpensive approach to improve the efficiency of known systems, such as the model system P3HT:PCBM. Moreover, further experiments studying the effect of external magnetic fields on Fe_3O_4-modified OSCs yielded further improvements in performance.

The improvements seen in such studies are linked to a reduced charge carrier recombination. The magnetic field gradient created by the NPs facilitates the spin rephasing between exciton components, thereby increasing the rate of ISC. This can be observed in the evolutions of the device PCE and FF, which increase linearly with the magnetic flux density (see section 6.3). This provides valuable insight into the fundamental working principles of optoelectronic devices under magnetic stress, as well as unveils new potential avenues to further increase device efficiencies. Nevertheless, for the studied P3HT:PCBM system, the PCE improvement at field intensities of up to saturation magnetization amount to ≈ 3 %, compared to the performances in the absence of external field. These relatively humble improvements, compared to the technical requirements necessary to achieve such fields, makes such approaches rather unappealing from an application point of view. At least in their current shape.

Hence, we focus our effort on studying the influence of NPs on another key parameter which severely affects OSC device device profitability: the device lifetime. The device lifetime quantifies the OSC's service life, projecting how long devices can operate. This time-dependent behavior is of paramount importance. Solar devices can turn unprofitable in a time-integrated calculation of the power generation if their service life is too short, despite a very high initial PCE. The study and understanding of degradation is of great interest especially in the case of OPV, since their relatively poor long-term stability is one of the main barriers to commercial application.[191] According to some studies, OPV could be competitive upon attainment of modules with service lifetimes ranging from five to ten years.[12,13] The degradation of solar cells arises from a complex interplay of several factors, such as photochemical degradation, oxidation of the top electrode, and morphological changes of the individual films composing the stack, amongst others.[58,60,192]

In the present chapter we explore the effect of Fe_3O_4 NPs on the device lifetime of lab-scale non-encapsulated P3HT:PCBM BHJ OSCs. We assess if there is a positive impact on the device degradation time evolution, in addition to the improvement in the device PCE. The results of the investigation raise further questions regarding the underlying causes of material aging and device parameter evolution. The NP-modified devices show a faster degradation and, in some instances, a qualitative change in the device behavior. This

ultimately leads to further fundamental exploration of the intrinsic mechanisms behind device degradation, with focus on the structure-performance relation. This is achieved by a time-resolved in-operando GIXS investigation. As a result, comprehensive insight into the relation between the crystallinity of the device active layer and the resulting performance is obtained. In particular, the in-operando investigation provides insight into the decisive early degradation stages, commonly referred to as the *burn-in phase*.

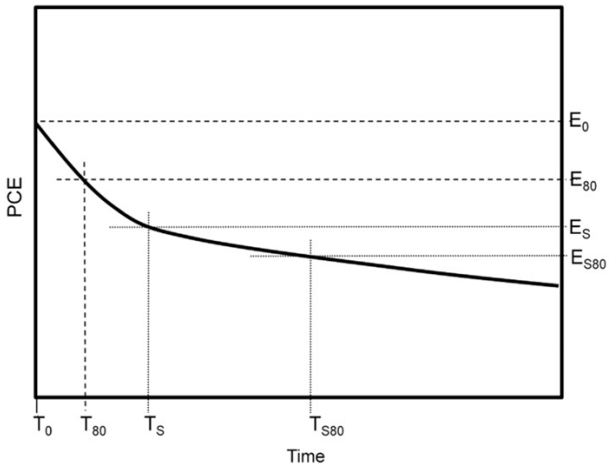

Figure 7.1: *Schematic time development of the PCE for aging characterization. The early faster burn-in can be observed. Four key time checkpoints and their associated efficiencies are generally used for describing the OSC aging behavior.* (E_0, T_0) *is the starting PCE.* (E_{80}, T_{80}) *is the time that shows 80 % of the initial efficiency.* (E_S, T_S) *are the times and efficiencies displayed by the cell at the end of the burn-in phase.* (E_{S80}, T_{S80}) *represents the time at which the device presents 80 % of the efficiency displayed at* (E_S, T_S)*. Reprinted from* [193] *with permission from Elsevier.*

Typically, OSC temporal performance shows two distinct regimes: an initial fast decay followed by a linear decrease of slower pace. These are schematically depicted in figure 7.1. The initial stage is referred to as burn-in. The rapid decrease in performance is generally related to intrinsic effects of material's properties, impurities, blend morphology and of the layer stack. However, precise understanding of the processes governing the burn-in phase is not yet achieved.[194] Aging experiments performed under standardized laboratory conditions reveal that burn-in generally does not happen in the dark, pointing to illumination and/or electrical stress as potential causes.[194]

In order to quantify the lifetime of a device, there are several indicators commonly used in the PCE-vs.-time chart. The first one is the initial device efficiency E_0, which occurs at the initial time $T_0 = 0$ s. The main indicator of the initial degradation speed associated with this initial performance is the (E_{80}, T_{80}) point, the time at which the OSC has lost 20 % of its initial PCE.[61] Another important point in the diagram is the (E_S, T_S), which is the time threshold at which the initial burn-in stage is considered to be over. Beyond time $t = T_S$ the decrease in PCE enters the second stage, featuring generally a linear decay with a lower slope, as compared to the previous burn-in phase. Additionally, there is the (E_{S80}, T_{S80}), where the device displays 80 % of the efficiency achieved at the (E_S, T_S) point. These four in-

dicators allow parametrization of the aging behavior of an OSC in the two main regimes. These are schematically depicted in figure 7.1. Due to its slightly arbitrary nature, the exact location of the (E_S, T_S) point is subjective. However, some groups have suggested bi-exponential fittings of the initial burn-in PCE decay, which provide a more objective definition of the decay scale.[194]

In general, device lifetime is not used uniformly in the literature. Often the lifetime refers to the T_{S80} time.[195] However, some reports use the T_{80} time. Some groups suggest more refined lifetime quantification mechanisms, based on fitting parameters that allow more objective comparisons among time-integrated parameters. One example is the *"lifetime energy yield"* suggested by Roesch et al..[194] They suggest integration of the power delivered by the OSC between $t = 0$ s and T_{S80} as a device figure of merit. This seems to be an intelligent approach to start studying the efficiencies of OSCs integrated over time. Nevertheless, this approach is not yet an extended practice.

7.2 Influence of Fe_3O_4 NPs on device aging

As discussed in the introduction of the present chapter (section 7.1), we first explore the influence of Fe_3O_4 NPs on the time evolution of modified P3HT:PCBM OSCs degradation. The devices are built following the standard procedures described earlier in chapter 4, using the materials presented in chapter 3. As in the study of the effect of external magnetic fields (section 6.3), the study is conducted for P3HT:PCBM BHJ OSCs with Fe_3O_4 loads up to 0.8 wt.%, which are the ones showing an improvement compared to unmodified devices.

7.2.1 Accelerated burn-in

Characterization of OSCs is carried out with a solar simulator at both ambient temperature and humidity. The samples were continuously illuminated under AM1.5g conditions with an irrandiance of 100 $^{mW}/_{cm^2}$. During the parametrization of device aging, one measurement is taken every 157 seconds, whereby the total device tracking time spans up to 700 minutes. The usual photovoltaic indicators are gathered and are studied as a function of time. To study the relative variations upon degradation, the parameters are normalized to their initial values. The obtained data are summarized in figure 7.2.

At first sight, a negative impact of the Fe_3O_4 NPs on the aging time profile of the studied OSCs is visible. The pristine, unmodified P3HT:PCBM OSCs present the longest T_{80} time, (370 ± 3) min. Unmodified, non-encapsulated P3HT:PCBM cells lose 20 % of

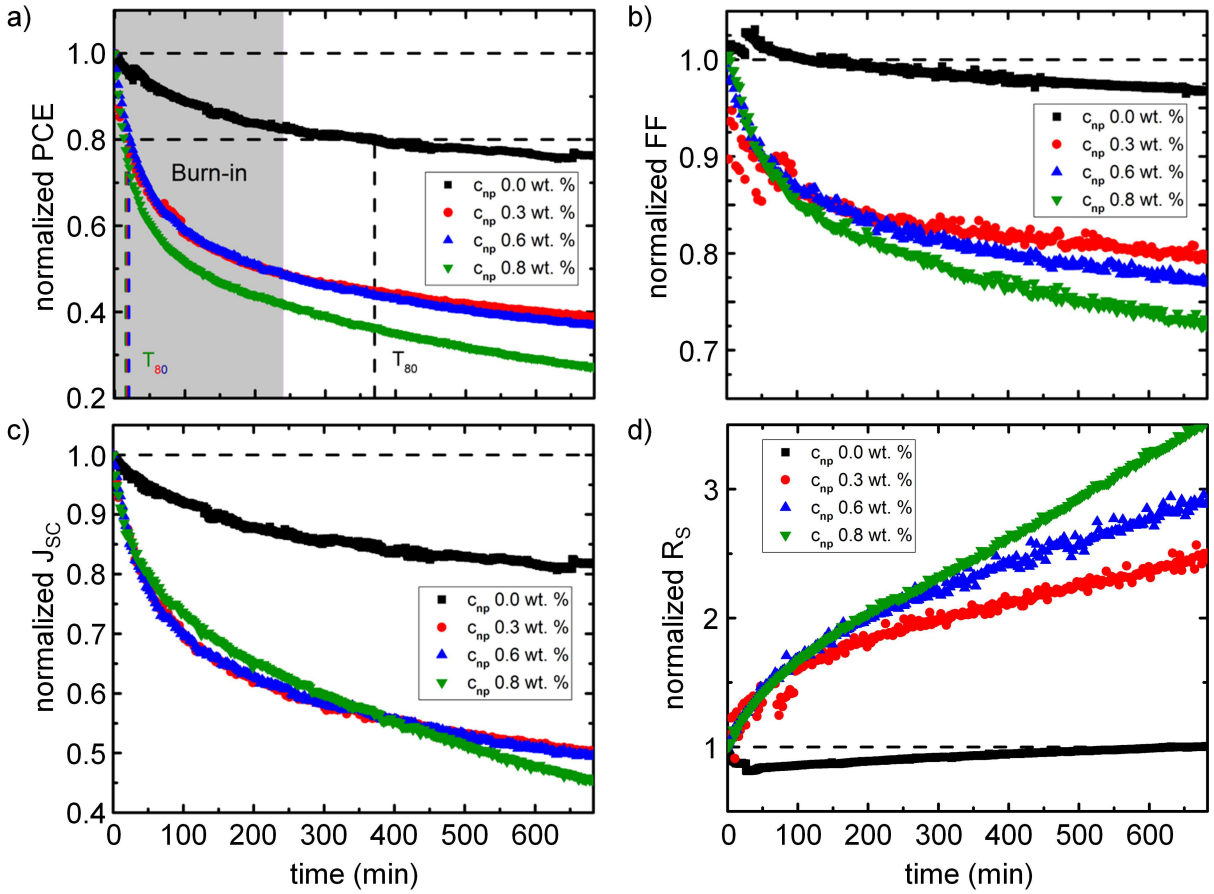

Figure 7.2: *Evolution of the performance indicators of P3HT:PCBM OSCs fabricated with different concentrations of Fe_3O_4 NPs expressed as a function of the illumination time: a) PCE, b) FF, c) J_{SC} and d)R_S.*

their efficiency only after six hours of continuous illumination. In contrast, the values for Fe_3O_4-modified devices are (18 ± 3) min for a NP content of 0.3 wt.%, (21 ± 3) min for 0.6 wt.% NPs, and (13 ± 3) min for a Fe_3O_4 NP load of 0.8 wt.%. This significant difference in aging speed represents an acceleration of the degradation process by approximately a factor seventeen. Interestingly, this acceleration of the degradation pace occurs mostly in the burn-in phase (colored in gray in figure 7.2a). The end of the burn-in phase is taken to be around 240 min. In the subsequent linear decay phase, all cells present a similar decay slope. Nevertheless, the aging process still seems to be mildly accelerated with increasing NP content. At the end of the burn-in phase, the unmodified P3HT:PCBM device has lost around 18 % of its initial performance, whereas the values are 51 %, 51 % and 58 % for NP contents of 0.3, 0.6 and 0.8 wt.%, respectively.

Figure 7.2b displays the evolution of the cells' normalized FF. An important difference between the presence and the absence of Fe_3O_4 NPs in the devices' active layers is visible.

In absence of NPs, the FF falls to about 95 % of the initial value, whereas for cells with some NP content this figure falls to between 70 and 80 %. Similarly to PCE, the largest erosion in FF occurs in the early illumination stages corresponding to the burn-in phase. Later on, the rate of FF loss slows and stays comparable to the degradation in unmodified devices. However, again a mild increase in the degradation speed can be observed in the linear, post-burn-in phase.

Figure 7.2c shows the evolution of the J_{SC} with illumination time. This is the main factor that drives the overall decay in PCE. At the end of the experiment, after 670 min, J_{SC} has fallen to 80 % of the initial value for cells with no NP content, whilst for NP-containing devices the J_{SC} decays to around 45 to 50 %. Again, the initial burn-in sets the greatest difference between NP-modified and unmodified OSCs. The J_{SC} of the devices containing 0.3 and 0.6 wt.% NPs follow an almost identical degradation profile. In contrast, for 0.8 wt.% NPs, an acceleration of the current density loss can be observed, in good agreement with the other inspected photovoltaic parameters. A similar trend can be observed for device R_S (presented in figure 7.2d). While the unmodified OSC shows a rather steady R_S, virtually constant for the duration of the experiment, the cells with NP content exhibit qualitatively different behavior. In this case, R_S increases at a high rate in the first minutes of illumination, afterwards entering a linear regime. Again, a clear increase of the linear R_S growth regime with Fe_3O_4 NP content can be seen. At the end of the experiment, cells with NPs depict R_S between two to over three times their initial values.

Overall, it can be seen that the presence of NPs speeds up degradation. Given the complex interplay of several factors, it is difficult to determine the causes of the increased rate of degradation upon inclusion of NPs. As mentioned above, it can be seen from picture 7.2 that the J_{SC} is arguably the main parameter responsible for the accelerated aging of modified cells. Different reports have addressed the reduction of J_{SC} as a result of device aging. Amongst others, the main factors proposed are the oxidation and/or delamination of top metallic contacts, and the physical reorganization of the BHJ within the device active layer.[48,58] This latter effect, of significant importance, attributes the loss in J_{SC} to a change in the thermodynamic equilibrium of the photoactive components, thereby leading to changes in the demixing behavior. This has been thoroughly investigated by Schaffer et al., and simulations of domain coarsening reproduce the measured J_{SC} decay with excellent agreement.[58] Thus, in view of the fact that Fe_3O_4 NPs turn the original P3HT:PCBM BHJ into a ternary system (P3HT:PCBM:Fe_3O_4), the thermodynamic equilibrium point of the new system is anticipated to lie elsewhere in the phase

diagram. Therefore, the speed at which aging occurs is affected. One fact in favor of this argument is that the parameter evolution for modified and unmodified devices generally presents qualitative differences, whereas the NP-modified devices usually show only small differences between themselves, scaled to the corresponding NP concentrations. This is particularly clear, for instance, in the evolutions of the FF and the R_S, depicted in figures 7.2b and 7.2d.

To further support the view that the morphological instabilities lead to faster or slower OSC aging, very insightful work published by Kong et al. demonstrates the major influence of chain polydispersity in the time degradation profile.[191] Reportedly, polydisperse PCDTBT is separated in different M_W components. On the one hand, PCDTBT:PCBM devices fabricated with high-M_W low-polydispersity PCDTBT lead to almost complete suppression of the burn-in phase and much slower post-burn-in decay. On the other hand, devices including low-M_W components show more pronounced burn-in phases and, thus, shorter device lifetimes. Interestingly, low-polydispersity high-M_W PCDTBT samples show almost no morphological changes upon annealing, as compared to as-cast samples. In contrast, low-M_W PCDTBT samples present very significant morphological changes upon temperature treatment. Thus, they conclude that low-M_W components are the responsible for morphological instabilities leading to marked burn-in phases and fast performance decay rates.[191] In the process of D-A domain coarsening, which assists the reduction in J_{SC}, an increase of exciton recombination arises. This increase in recombination contributes to the reduction of the device FF as it was observed by Schaffer et al. and also in the present investigation (figure 7.2b).[58]

Another possible cause for accelerated degradation is related to the photo-oxidation of P3HT. One mechanism responsible for the solid state degradation of P3HT, or poly(3-alkylthiophene)s (P3ATs) in general, is the formation of strongly-oxidizing singlet molecular oxygen $O^*_2(^1\Delta_q)$, hereafter referred to as $^1O^*_2$. $^1O^*_2$ interacts with thiophene units through a Diels-Alder reaction at the thiophene positions one and four, forming endoperoxydes. The formed endoperoxydes, besides ending up decomposing into various products (e.g. carbonyl or olefinic functional groups), break the conjugated polymer backbone. This process (schematically depicted in figure 7.3) disturbs the molecular π-conjugation and reduces light absorption, which in turn leads to a reduction of the current generated by the OSC.[55] Molecular oxygen presents a triplet ground state ($^3O_2$), and the formation of excited singlet oxygen is normally achieved by chemical methods (e.g. using sodium hypochlorite/hydrogen peroxide[55]). However, its formation can also be achieved by energy transfer from a molecular (P3HT) triplet exciton. Further details are available in

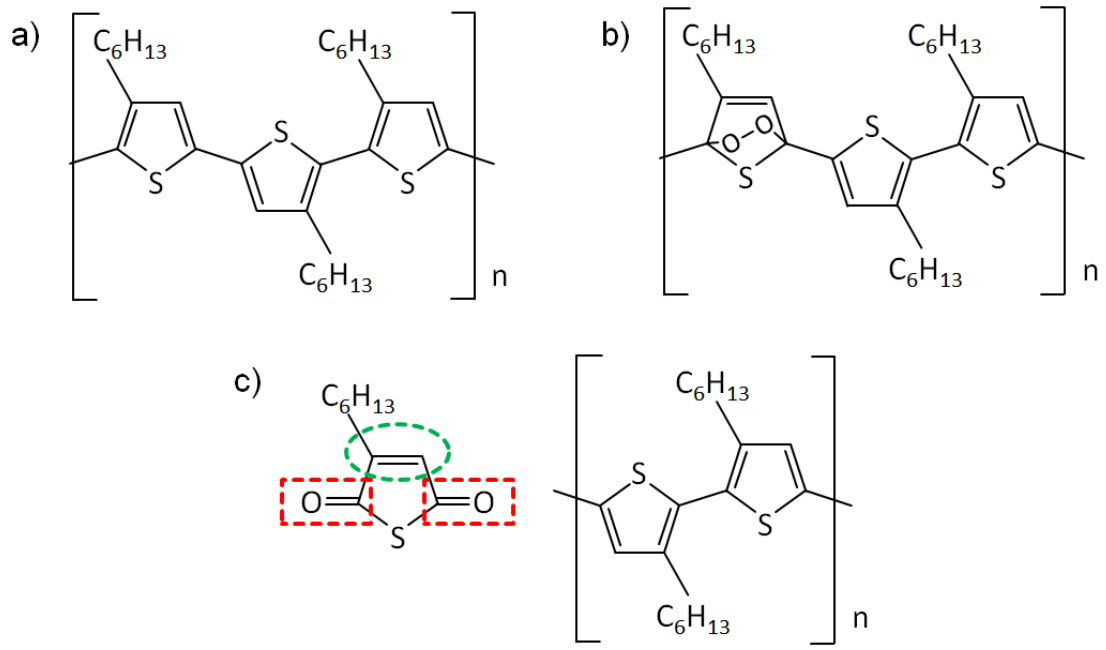

Figure 7.3: *Schematic depiction of the singlet oxygen $^1O^*_2$-induced degradation of a) a P3HT chain. b) An excited $^1O^*_2$ molecule undergoes 1,4 Diels-Alder addition, forming an endoperoxyde to detriment of the conjugated bonding in the thipohene ring. c) The unstable endoperoxyde leads to an olefinic ring (olefinic group highlighted in green) with carbonyl side groups (in red), thereby detaching the original 3-hexylthiophene unit from the polymer backbone, reducing the conjugation length.*

the literature.[196,197] This effect is generally regarded as unlikely, given the low quantum yield of triplet formation in regular P3HT ($<10^{-6}$).[198,199] Nevertheless, the efficiency of this oxidation mechanism is arguably increased in our case, given the increased presence of triplet excitons owing to the presence of Fe_3O_4 NPs. In addition, $^1O^*_2$ interacts with hexyl side chains, forming carbonyl adducts that results in energetic traps for molecular singlet excitons, leading to higher rates of non-radiative relaxation.[60,200] Nevertheless, some experiments based on direct exposure of P3HT to chemically-generated $^1O^*_2$ suggest that $^1O^*_2$ may not be the main trigger of P3HT photo-oxidation, making the real role of $^1O^*_2$ in film aging still unclear.[51,55]

7.2.2 Effect on photovoltage

Figure 7.4 depicts the evolution with illumination time of the open-circuit voltage V_{OC} for different concentrations of Fe_3O_4 NPs. V_{OC} presents, compared to the other parameters examined, the most outlandish behavior. For solar cells without NPs the V_{OC} evolution resembles the usual trend also observed for other parameters, mainly characterized by an initial strong decay in the burn-in phase. Afterwards, it stays stable for several hours at around 96 % of the initial value. On the other hand, the evolution of V_{OC} of NP-containing samples feature unexpected behavior even in the burn-in phase. At early times strong

relative V_{OC} decays are observed, followed by unusual partial recoveries. This behavior is especially clear in the 0.3 wt.% case, where the V_{OC} hits a minimum of around 96 % after approximately 20 min, subsequently recovering and stabilizing at a greater value. Furthermore, it stabilizes at a relative value greater than that of the devices without NPs after approximately 500 min illumination. This, in spite of the as yet not understood behavior taking place in the burn-in phase, indicates a beneficial effect on the V_{OC} degradation time dependence upon addition of Fe_3O_4 for 0.3 and 0.6 wt.% NPs. These being the NP concentrations at which the overall device PCE is also highest (see section 6.2 for details). At a concentration of 0.8 wt.% NPs the samples behave qualitatively similar to the 0.3 and 0.6 wt.% cases, yet the V_{OC} loss in the burn-in phase is much more significant, dropping to around 82 % of its initial value. Therefore, the 0.8 wt.% sample seems to set an upper threshold of NP content for potential V_{OC} improvement, in accordance to what was seen for other photovoltaic indicators (see section 6.2). For all NP concentrations the V_{OC} shows a stable behavior beyond the burn-in phase, thereby highlighting the importance of the burn-in phase in improving the degradation behavior of modified OSCs.

The behavior of V_{OC} is difficult to address, given the intricate nature of the parameter itself, and its multiple dependencies on several material, layer and device properties. Often the fine structure of the V_{OC} behavior in the burn-in phase is not carefully accounted for, and it is often approximated by a constant.[194] In general, many reports point to a close relationship between the V_{OC} and the morphological/crystalline state of the films composing the OSC, which in turn is affected by multiple factors including fabrication procedure, temperature, humidity, etc.[201] In the next section we focus on this structure-function relation for the active layer of a P3HT:PCBM OSCs, paying special attention to the behavior of the photovoltage V_{OC} and to the early burn-in phase. This is achieved via in-operando GIWAXS experiments that allow us to monitor the evolution of the main OSC photovoltaic indicators simultaneously with the evolution of the samples morphology.

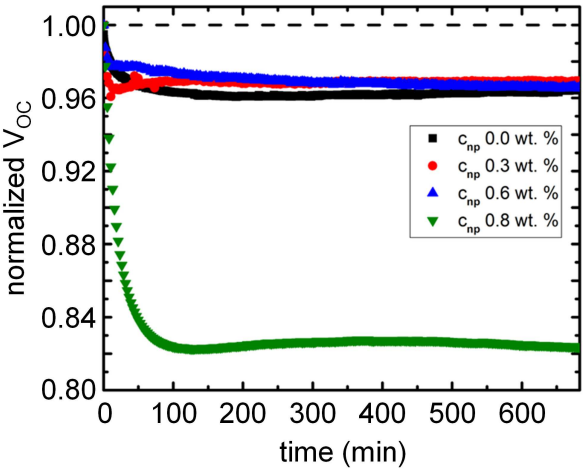

Figure 7.4: *Evolution of the V_{OC} of P3HT:PCBM OSCs fabricated with different concentrations of Fe_3O_4 NPs expressed as a function of the illumination time.*

7.3 Structure-function relation in P3HT:PCBM device aging

In the last section it has been shown that NPs accelerate the degradation of P3HT:PCBM solar devices. This acceleration happens especially in the burn-in phase, and two potential reasons are identified. First, the presence of NPs changes the thermodynamic equilibrium of the P3HT:PCBM system, thereby accelerating the photoactive domain coarsening, which is one of the main causes of J_{SC} reduction during illumination.[58] Second, it is argued that the enhanced ISC and the increased population of triplet excitons favors the appearance of more molecular oxygen in the excited singlet state ($^1O^*_2$, see section 7.2.1), which accelerates the physical degradation of P3HT.

In general, all OSC parameters show the most significant changes during the burn-in phase. In this regard, the behavior observed for the V_{OC} is especially outlandish, since the introduction of NPs qualitatively alters the behavior of the V_{OC} with time. NP-containing devices exhibit a minimum in the V_{OC} during the burn-in phase, followed by a partial recovery. As it is reported e.g. for the J_{SC} and other photovoltaic parameters, the behavior of the V_{OC} with illumination time is related to morphological and structural parameters of the layers composing the device. In the present section we take a closer look at the behavior of the OSC photovoltaic parameters in general, and of the V_{OC} in particular, along with their relation to the morphological and crystalline parameters of the active layer system. This investigation is performed in a time-resolved in-operando GIWAXS experimental campaign, through which we gain further insight into the burn-in device degradation phase.

7.3.1 The origin of V_{OC}

The device V_{OC} is the result of a complex interplay of several factors, including recombination rates, the DOS shape and the charge carrier and exciton mobilities, amongst other factors.[190,202,203] Within this complex interplay, the crystalline state of the active layer is of special importance.[40,204,205] As an example, a relationship between the charge transfer energy (and therefore V_{OC}) and the crystalline fraction in a solution of photoactive materials has been thoroughly studied by Vandewal et al..[206]

V_{OC} is primarily determined by the energy of the BHJ optical band gap, this is the energetic difference between the donor's HOMO and acceptor's LUMO. The V_{OC} and the optical bandgap depict a clear linear relation, and, given that the V_{OC} is strongly conditioned by the polaron recombination, it suggests that this recombination must happen

mainly at the D/A interface. Nevertheless, the HOMO and LUMO levels are not sharp energy levels, but rather energy distributions. This is due to the nature of polymers themselves, which in most cases can only achieve semi-crystalline states, showing only partial aggregation (see section 2.1.2 for further details). This is the result of uneven conjugation lengths, polydispersity, chemical defects, etc. The corresponding effect on the energy distribution is schematically depicted in figure 7.5.

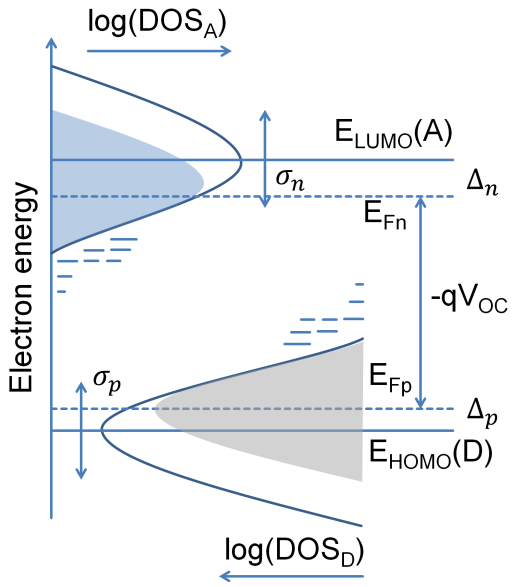

Figure 7.5: *Schematic representation of the optical band gap for a BHJ. The blue lines represent the Gaussian DOS distributions centered at the $E_{HOMO}(D)$ and $E_{LUMO}(A)$ energies, respectively. The colored areas correspond to the respective occupied states. σ_p and σ_n indicate the Gaussian energy deviations. E_{F_p} and E_{F_n} indicate the respective quasi-Fermi energies. The energetic offset between the optical band gap and the photovoltage $qV_{OC} = E_{F_p} - E_{F_n}$ is indicated by Δ_p and Δ_n. Adapted with permission from ref [15]. Copyright 2017. American Chemical Society.*

Usually this effect is referred to as *Gaussian disorder* and its broadness is characterized by the standard deviations σ_n and σ_p.[40,190] Furthermore, it is also important to consider the occupation of these Gaussian DOSs. Typically, when the device is illuminated, the occupied states lie somewhat two orders of magnitude below the available states.[190] In figure 7.5 the occupied states are indicated by the blue- and gray-colored regions within the LUMO and HOMO DOSs, respectively. As it can be seen, this actually leads to a situation in which the mean energies of the occupied distributions are closer to each other than the actual energetic distance between HOMO and LUMO mean energies (the difference between the two magnitudes is indicated by the Δ_n and Δ_p offsets). As a result, under illumination, the occupation of available energy states is mostly restricted to the DOS tails. Even at high irradiances, where exciton and, therefore, charge carrier generation is increased, the situation persists, since the recombination rates increase as well. Especially in the case of non-geminate recombination the recombination rate increases quadratically with the carrier density (see section 2.2.5).[207,208]

Thus, the resulting device V_{OC} is lower than the voltage associated with the optical band gap of the BHJ (compare the optical band gap with the photovoltage in figure 7.5: $BG_O = -qV_{OC} + \Delta_n + \Delta_p$). More comprehensive discussion of the relation between the

device V_{OC} and the Gaussian disorder is available in the literature.[190,209] Further effects related to the energetic landscape of the active layer and to the stability of the composing layers have an influence on the V_{OC}, such as trap-assisted recombination or failure of the device electrodes.[48,191,192]

In summary, the V_{OC} scales with the splitting of the negative and positive quasi-Fermi levels. The balance reached between generation and recombination rates determines the occupancies and, thus, the offset between the optical band gap and the actual V_{OC}. Interestingly, the dynamics of exciton and polaron transport and recombination, as well as DOS shapes are closely related to the arrangement of the materials composing the photoactive BHJ.[40,204,210–212] In this sense, features such as the degree of crystallinity, crystallite grain sizes and lattice parameters exert an important influence on sample properties, such as conjugation length uniformity (and, therefore, DOS sharpness), exciton and polaron mobilities and, thus, recombination rates.[203]

7.3.2 In-operando crystalline tracking of device aging

In order to approach the direct observation of the link between the crystalline evolution of an OSC and the corresponding photovoltaic parameters, in-operando GIWAXS measurements are performed. The real-time measurements follow the crystalline evolution of the device active layer via scattering under shallow incident angle. At the same time, the OSC is placed inside a sample environment that allows I-V tracking during illumination. A detailed description of the chamber and the in-situ GIWAXS experiments is provided in section 3.1.5. In an attempt to reproduce real working conditions, OSCs are tracked as a function of time under air atmosphere and with no external control of the device temperature. However, the evolution of the device temperature with illumination time is recorded.

The device temperature has an impact on charge carrier statistics and, consequently, on the OSC parameters extracted during I-V tracking. Overall, the heating induced in the setup and the sample due to the illumination of the portable solar simulator induces a mild temperature increase from 26 to 32 °C. High temperatures induce re-arrangement of the organic domains in the active layer, similar to the effects observed in PBST3HT homofilms and P3HT:PBST3HT:PCBM ternary films (see chapter 5). Similarly, the charge-carrier statistics is affected by temperature, through e.g. heat-induced impurities emerging in organic chains, formation of fullerene crystals or P3HT "crystallite melting".[127,213] Figure 7.6a shows the evolution of the temperature of the copper block as recorded during the in-operando experiment. A Pt100 temperature sensor is embedded in the copper block (see figure 3.7 in section 3.1.5) and allows real-time monitoring of the block temperature.

The temperature is measured in the copper block due to the impossibility of measuring it directly at the back of the sample, as this would block the path of the x-ray scattering experiment. Thus, in order to ascertain the temperature of the sample, ex-situ calibration measurements are done. These reproduce the environment and illumination conditions of the real in-operando experiments. In this case the sample is substituted by a glass substrate with an additional Pt100 temperature sensor. This way, the temperature of the sample for a given temperature of the copper block can be obtained. The relation between the two magnitudes is presented in figure 7.6b. The two temperatures depict a bi-linear relation ($r^2 = 0.81$ and $r^2 = 0.98$ for the first and second sections, respectively). The linear correspondence is especially accurate after the temperature has initially stabilized. This second stage begins between 500 s and 1500 s after the start of the experiment, as indicated by the blue-shaded area in figure 7.6a. Combination of the sets of data presented in figures 7.6a and 7.6b allows us to state that the temperature rose during the experiment to temperatures slightly below 32 °C in the stable regime.

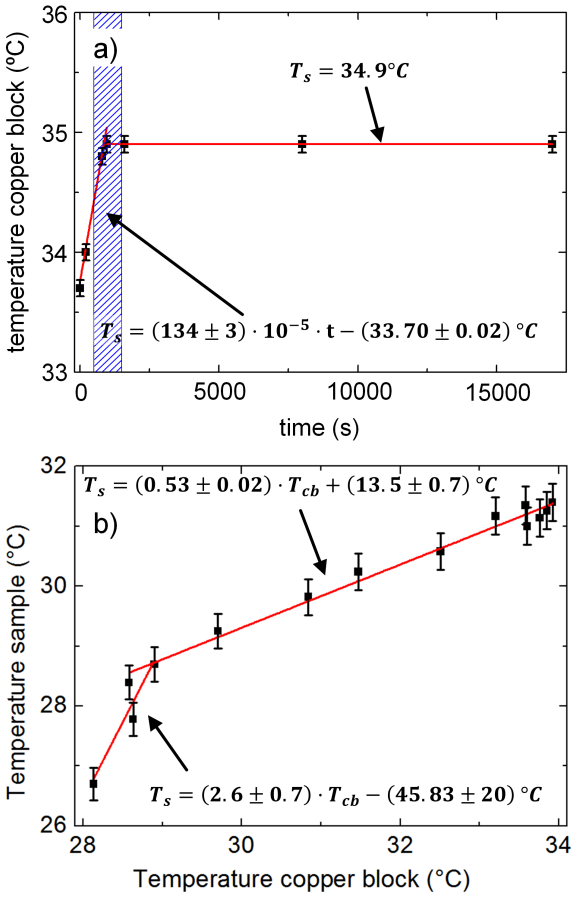

Figure 7.6: *a) Temperature of the copper block as a function of illumination time. b) Temperature of the sample as a function of the temperature of the copper block. Black squares are data points. Straight red lines are linear fits, whose corresponding temperature functions are indicated. The blue shaded area indicates the time window of temperature stabilization. Adapted with permission from ref [15]. Copyright 2017. American Chemical Society.*

P3HT:PCBM GIWAXS measurements present two main signals. First, a signal related to PCBM randomly-oriented crystallites, which do not experience changes during the whole experiment. Second, the GIWAXS signal exhibits a strong P3HT (100) peak, as is common for P3HT-based systems and has been described previously in section 6.2.4. These reflections allow parametrization of the crystalline state of P3HT.[108] As in the case of films formed using most high boiling-points-solvents, most of the (100) intensity

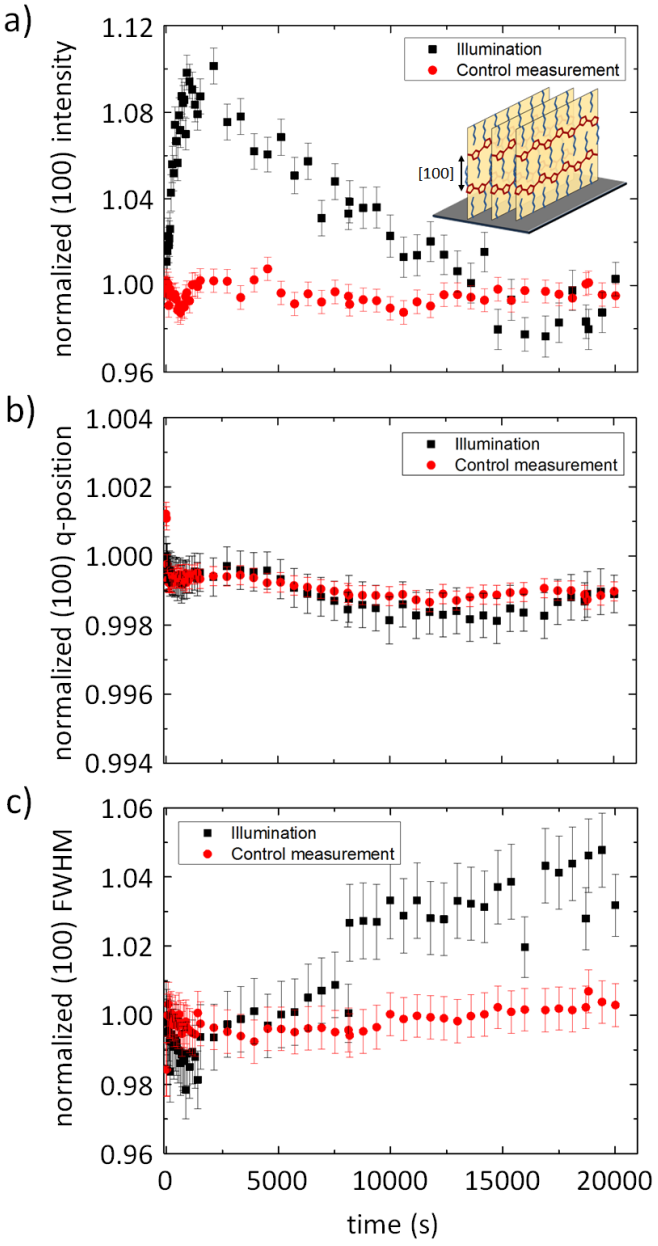

Figure 7.7: *Evolution with time of the edge-on (100) P3HT crystalline family, both during illumination (black squares) as well as during the control experiment (red circles). a) Peak intensity. b) Peak center position. c) Peak FWHM. The displayed magnitudes are normalized to starting values. The inset in a) depicts a P3HT edge-on-oriented crystal standing on the sample substrate, indicated by the underlying gray surface. Adapted with permission from ref [15]. Copyright 2017. American Chemical Society.*

appears along the q_z-axis, indicating predominant edge-on orientation.[214] In P3HT, the [100] lattice vector corresponds to the spacing between adjacent polymer backbones. In the edge-on configuration, the side chains of P3HT are standing perpendicular to the sample substrate. An edge-on-standing P3HT crystal is depicted in the inset of figure 7.7 for clarity. More detailed general discussion of the morphology of P3HT crystals is available elsewhere.[108]

Figure 7.7 displays the evolution of the peak parameters extracted from the Gaussian fittings of the edge-on (100) peak. The data are presented for the case of device illumination as well as for the control experiment, in the dark and in absence of voltage sweep. The initial stages of device operation (black squares in figure 7.7) are marked by an increase in signal intensity that spans the first 15 min, indicating an increase in the total degree of crystallization (figure 7.7a). After this initial stage, the intensity reaches a maximum, and the process starts reversing, indicating a partial loss of the crystalline phase. This is directly linked to illumination from the solar simulator, as the data associated to the control experiment remained constant over the course of the experiment. This is in agreement with the behavior obtained for the edge-on (100)

FWHM, shown in figure 7.7c. Similarly, during illumination, the initial stage is characterized by a reduction of the FWHM, which is associated with an increase in the average crystallite grain size. This process culminates after approximately 15 min, synchronized with the evolution of the peak intensity. The FWHM of the control experiments stays constant within the associated experimental errors. Finally, the average edge-on (100) peak center stays fairly constant in all cases throughout the experiment (shown in figure 7.7b). This is not surprising, as a generalized change in the packing distance between P3HT chains due to solar illumination is rather unexpected.

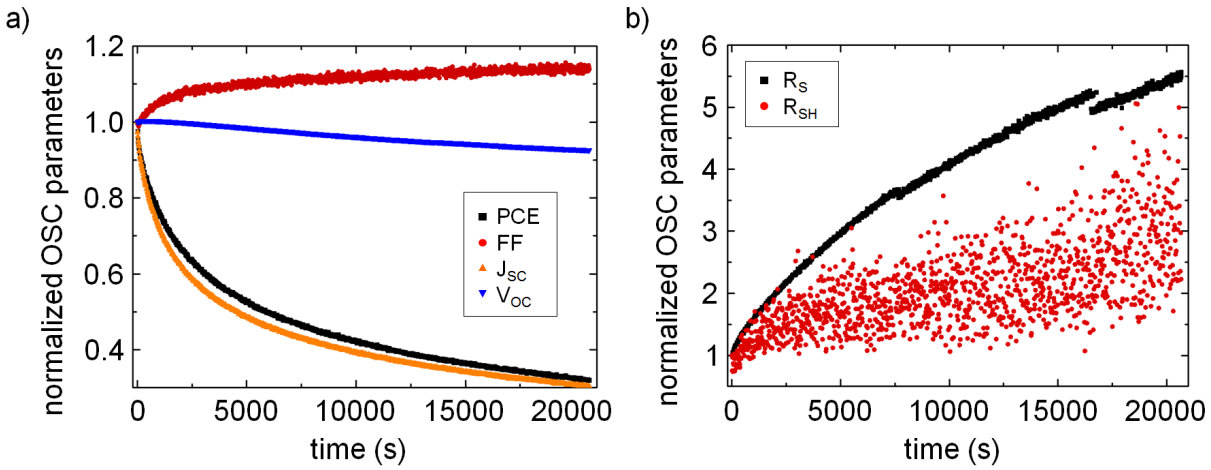

Figure 7.8: *Evolution of the a) PCE, FF, J_{SC} and V_{OC} and of the b) R_S and R_{SH} of the OSC characterized in-situ during functioning. Y-axes indicate the variation normalized to the initial values. Adapted with permission from ref [15]. Copyright 2017. American Chemical Society.*

In parallel, the evolution of the device J-V characteristics are tracked. The main OSC photovoltaic indicators (PCE, FF, J_{SC}, V_{OC}, R_S and R_{SH}) are plotted versus the time and displayed in figures 7.8a and 7.8b. The device shows a humble initial performance. The initial J_{SC} amounts to 1.91 $^{mA}/_{cm^2}$, which is about one fifth of the vale expected for a normal-functioning P3HT:PCBM BHJ OSC. Similarly, the device FF (28.05 %) exhibits a significant reduction compared to a fresh device. The drastic reduction in FF affects the values of R_S and R_{SH}, which amount to 161.2 $\Omega \cdot cm^2$ and 218.9 $\Omega \cdot cm^2$, respectively. Nevertheless, the device V_{OC} does not suffer from this degradation process and presents the same value as a fresh-prepared P3HT:PCBM device (0.60 V). This is particularly significant in the research presented here, as it will mainly focus on the role of the V_{OC} and its link with the crystallinity of the device active layer. The observed poor device performance is a result of transport conditions and the significant time elapsed between device fabrication and characterization at the synchrotron light source. Further details are provided in section 3.1.5.

The PCE decreases with illumination time. The decay is mainly governed by the J_{SC}. The main causes for the lowering J_{SC} are first, the physical reorganization of the bulk, as first observed by Schaffer et al. in in-situ OSC experiments, as discussed previously in section 7.2.1.[58] Second, the contact of the solar device with oxygen-rich atmosphere is known to lead to failure of the device electrodes.[48,58] Both effects are supported by the evolution of R_S (see figure 7.8b), which increases with the illumination time, indicating worsening device transport properties. Furthermore, shorter conjugation lengths and decreasing chain planarity as a result of long exposures to sunlight lead to exciton and polaron trapping with the residues of the photodegaradation. These phenomenon has been reported by Deschler et al., also negatively impacting the J_{SC}.[215]

The early stages of device functioning show an increase in the device FF by approximately 10 to 15 %. This indicates a reduction in device recombination, which is primarily ascribed to the observed increase in temperature. In organic semiconductors, due to the hopping nature of the charge transport, increasing temperature leads to more efficient charge carrier mobility. At the same time, it favors the appearance of thermal defects, which ultimately can result in generation of additional polarons, thereby improving the device FF.[216] Comparison of the FF and temperature evolutions reveals stabilization at similar time scales (figure 7.6a). Moreover, the reduction in recombination is further supported by the continuously increasing R_{SH} (see figure 7.8b).[174]

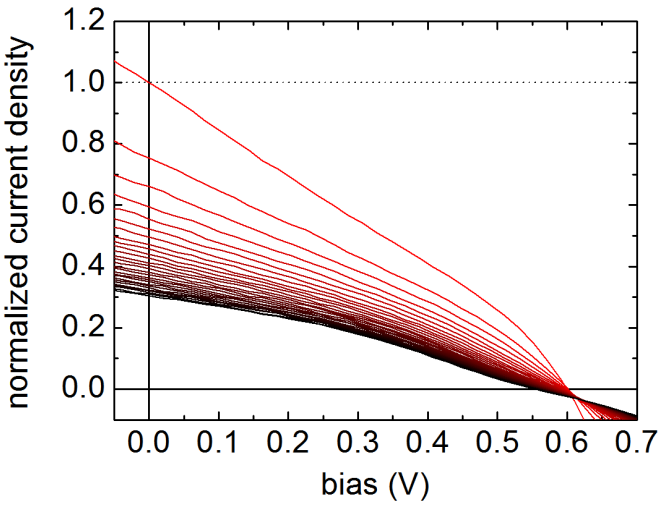

Figure 7.9: *First quadrant close-up of 27 time-equidistant J-V curves between the beginning of the in-situ experiment and five hours illumination. The time gap between two consecutive curves is of 13 minutes. The time progress is color-coded in a red-to-black gradient. Adapted with permission from ref [15]. Copyright 2017. American Chemical Society.*

Nevertheless, another factor might be playing a role in the shaping of the FF time evolution, namely the already discussed time decay of the J_{SC}, which develops on similar time scales. As displayed in figure 7.9, the current density decay happens faster in the first stages (also visible in figure 7.8a). This decay, combined with a comparatively stable V_{OC}, eventually induces an increase in the ideality of the shape of the J-V curve. Therefore,

a higher ratio $(V_{MPP}\ J_{MPP})/(V_{OC}\ J_{SC})$ is achieved, despite the fact that the absolute delivered power decreases with time.

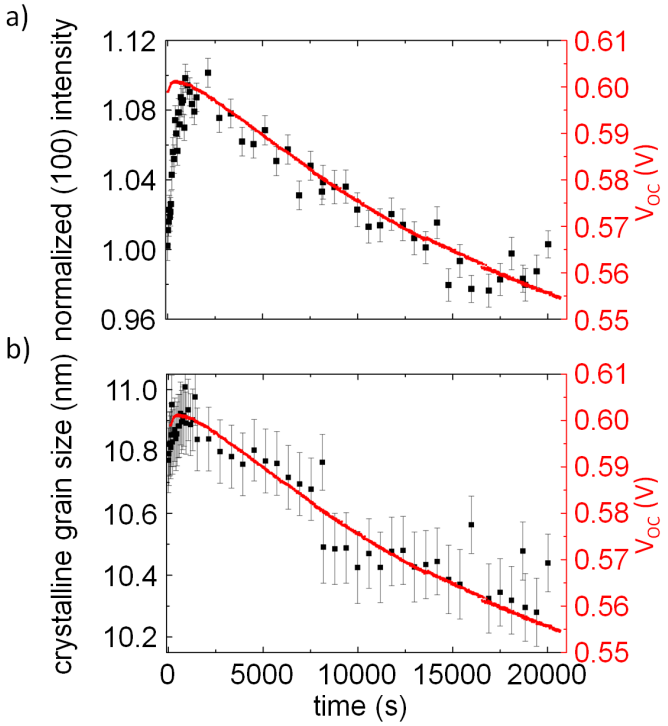

Figure 7.10: *Temporal comparison of the recorded device V_{OC} and a) the P3HT edge-on (100) intensity and b) the P3HT edge-on (100) estimated crystallite grain size. Adapted with permission from ref [15]. Copyright 2017. American Chemical Society.*

The device V_{OC} presents roughly a linear decay, falling to around 93 % of the starting value after 20000 s. Nevertheless, a closer examination of its time evolution yields a tight correlation with that of the observed GIWAXS trends. This is summarized in figure 7.10. Figure 7.10a compares the time developments of the P3HT edge-on (100) intensity with the relative variation of the device V_{OC}. Both magnitudes increase in their early stages with respect to their initial values. Both reach a maximum at the same time, for afterwards decaying linearly. Moreover, figure 7.10b compares the same time evolution of the photovoltage with that of the crystallite grain size, showing excellent agreement. The crystalline grain size is estimated from the FWHM of the (100) edge-on P3HT intensity with the help of the Scherrer equation (see equation 2.73 in section 2.4.3).

The data presented here constitute direct evidence of the co-dependence between the crystalline state of the active layer of a BHJ P3HT:PCBM solar cell and the delivered device photovoltage V_{OC}. With in-situ techniques we are able to directly observe the parallel evolution of both magnitudes in real time. However, the inter-dependence of these two magnitudes has been described previously in several ex-situ pieces of research involving several material and device parameters. Zimmerman et al. reported comprehensive investigations on the effects of different post-treatments on the performance of DPSQ:C_{60} OSCs, highlighting the capital role of the photoactive layer morphology in the process.[203] The dependence of the V_{OC} on device morphology can be isolated. In this regard, they reported that a disordered bulk morphology prevents the overlap of donor and acceptor

molecular orbitals, which has a notable impact in deminishing the non-geminate recombination. However, the exciton transport properties of disordered BHJs are rather poor, favoring geminate recombination. Contrary to this, highly crystalline phases exhibit good carrier transport properties, but suffer from increased recombination at D/A interfaces. The high recombination results from the high degree of D/A molecular orbital overlap resulting from the high regularity of the interface. Thus, they propose and implement an optimum morphology, consisting of highly crystalline domain bulk, combined with a disordered D/A interface. This arrangement combines a low D/A orbital overlap with good bulk exciton transport properties, thereby favoring the reduction of both types of recombination (increasing R_{SH}). Consequently, this configuration yielded the highest V_{OC} values obtained.

Other studies, like the reported by Vanlaeke et al., study the effect of annealing and blend composition on the crystallinity of neat P3HT and of P3HT:PCBM BHJ films. The crystallinity not only leads to improved spectroscopic properties (which positively affect device performance), but also has a direct impact on the P3HT hole transport properties.[204] Moreover, thorough work done by Spano, featuring experiments as well as simulations, provides great insight into the intimate relation between the crystallinity, lamellar aggregate morphologies, chain correlation lengths and the associated energetic disorder, impacting the sharpness of the associated UV/Vis transitions.[40,210]

The examples above summarize the research carried out on the interrelations between the key concepts of polymer system crystallinity, the subsequent effect on the energetic disorder of the material and, finally, on the effect on the V_{OC} delivered by the corresponding solar device. This, up to now, patch-wise research involving everything from the nanoscale morphology of the polymer active layer up to the macroscopic device V_{OC} allows us to build a framework of parameter interdependence. Nevertheless, the in-situ investigations provided here allow us to take one step further and gain a more comprehensive understanding of the fundamental processes governing device function.

In our in-situ characterization of device aging, we first observe a decrease in device recombination. This decrease is assisted by the increase in device temperature caused by the illumination, as it has been shown earlier in the present section. This decrease in recombination and its link to the evolution of device temperature can be identified from the time evolution of the FF. Reduced recombination leads to an increasing occupancy of the DOSs on the two sides of the optical band gap. As discussed in the previous section 7.3.1, this induces a separation of the quasi-Fermi levels, which ultimately leads to the

initial increase in V_{OC}. In parallel, the increased temperature helps activating polymer chain mobility, and enables system relaxation towards equilibrium, similar to what usually happens in thermal annealing processes.[204] Hereby, the aggregation of P3HT improves, resulting in a higher volume fraction of P3HT (100) edge-on crystallites, as shown by the increasing GIWAXS intensity (compare the first stages of figure 7.10a). Additionally, the enhanced crystallinity is displayed by the increase of the crystallite grain size in this early time evolution phase (figure 7.10b) and the lowering P3HT (100) edge-on FWHM values (figure 7.7c). These two latter parametters also indicate a more even distribution of backbone spacings and conjugation lengths, arguably contributing to the narrowing of the HOMO and LUMO energy distributions, which in turn reduce the DOS tails and improve the charge carrier occupation statistics.[127,217]

After the first stage, the system's temperature stabilizes and the crystalline intensity, the grain size and the photovoltage reach a maximum. This long-term exposure to sunlight and elevated temperature activates thermal stress, which triggers degradation mechanisms, such as oxidation or photobleaching, amongst others. These phenomena negatively impact the crystallinity of P3HT, as proven systematically by Hintz et al. in photodegradation studies.[52] The increased chain mobility provided by temperature destabilises the P3HT aggregates, leading to "crystallite melting".[127] In the GIWAXS data, this can be observed in both the evolution of the crystalline signal as well as in that of the grain size. In detailed studies of the effect of annealing and, more generally, of elevated temperatures on polymer films, Motaung et al. reported the same trends for P3HT:PCBM blends. Upon exposure to elevated temperatures, they observe an increase in film crystallinity, a trend which experiences reversion after some time.[127] The destruction of the crystalline phase after long exposures to heat was confirmed by Raman and XRD characterizations. The investigations showed the formation of non-crystalline material, as well as a reduction in the polymer conjugation length. This last effect was also observed in UV/Vis measurements of P3HT samples. For long annealing times, the samples displayed a blue-shift, indicating shortening conjugation length for weakly-coupled H-aggregates, such as P3HT.[218,219] Furthermore, after long times the polymer phase undergoes physicochemical degradation, featuring the modification of the chemical structure of the molecular chromophores, mainly consisting of the detachment of light units, like C-S groups of hexyl chains.[57]

The fading of crystallites contributes to an increase in energetic disorder of the photoactive medium. This leads to a broadening of the DOS, allowing the occupation of deeper energetic states, and thereby reducing the splitting of the quasi-Fermi levels. Beiley et al.

already highlighted the dependence of trap formation on the morphology of photoactive PCDTBT films, stating that structural defects and disorder contribute to the broadening of the energetic trap-width.[220] For long illumination times, the splitting (and, thus, the V_{OC}) is further reduced by the effect of additional degradation effects, like photobleaching. This reduces the material's intrinsic absorption and, consequently, the concentration of photogenerated charge carriers, reducing in turn the DOS occupancies.[52] These processes take place in parallel with the physical reorganization of the BHJ, which reduce the amount of D/A interface. With it, the chance for exciton splitting is also reduced, increasing the geminate recombination and, thus, contributing to a further decrease in V_{OC}.[58]

7.4 Conclusions and outlook

In the first half of this last chapter, in addition to the observed improvement in PCE, we investigate the effect of Fe_3O_4 NPs on the OSC service life. As in the study carried out exploring the application of different intensities of magnetic field, we focus on aging of devices containing loads of Fe_3O_4 that lead to an improvement as compared to non-modified P3HT:PCBM cells, i.e. between 0 and 0.8 wt.% Fe_3O_4 NPs. The aging pace is dramatically accelerated upon addition of NPs. The T_{80} time falls from (370 ± 3) min for non-modified cells to T_{80}s between (13 ± 3) min and (21 ± 3) min for NP-modified cells with different concentrations. The main parameters signaling the accelerated decay are the FF, the R_S and, in particular, the J_{SC}. According to existing investigations, the decay in PCE responds mainly to failure of the device contacts and the morphological re-arrangement of the BHJ components, which is in good agreement with the marked increase in the R_S in the early burn-in phase.[48,58]

In some of the tracked parameters (especially the R_S and the V_{OC}) a qualitative change in the time behavior is observed. Moreover, a decrease in cell stability is observed with increasing Fe_3O_4 NP content. The main causes of the accelerated aging are, first, the alteration of the thermodynamic equilibrium through addition of NPs, which can induce the acceleration of the physical BHJ aging. This strong effect of the sample morphology and composition on thermodynamic equilibrium and its effect on device degradation speed has been reported by Kong et al..[191] They observed a strong influence of polymer M_W and polydispersity on OSC degradation. Accordingly, the observed NP-dependent degradation speeds for different Fe_3O_4 loads in P3HT:PCBM BHJ devices highlight the vital structure-function link that is further investigated in-operando (see section 7.3.2).

Secondly, the reducing cell stability observed with increasing NP content can additionally be related to P3HT photo-oxidation through increased presence of singlet excited oxygen states, resulting from the increased triplet excitons in the organic phases. In order to further test the suitability of the hypothesized underlying causes, an in-operando GISAXS characterization on P3HT:PCBM devices with different NP concentrations would enable the observation of qualitative differences in the domain evolution and/or accelerated domain coarsening. The evolution of the mesomorphology should correspond to the observed accelerated J_{SC} decay, in reproduction of the work carried out by Schaffer et al..[58] Furthermore, spectroscopic studies of the P3HT degradation products and potential changes in e.g. composition upon addition of NPs can help elucidate the importance of singlet oxygen $^1O^*_2$ in Fe_3O_4 NP-modified systems.

Amongst the observed photovoltaic indicators, V_{OC} shows a rather interesting behavior upon inclusion of NPs. The pristine P3HT:PCBM device shows a strong decay of V_{OC} in the burn-in phase, while devices containing Fe_3O_4 feature more complicated time profiles, containing early minima followed by partial recoveries. In some cases, the V_{OC} stabilizes after several hours at higher relative values than in the case of unmodified devices.

It is worth highlighting that the acceleration of degradation mostly occurs during the burn-in phase for all observed parameters. Moreover, the behaviors observed for the J_{SC} and the V_{OC} suggest that parameter evolution can be linked to morphological changes. Furthermore, the V_{OC} of modified devices stabilizing at higher values than pristine P3HT:PCBM implies that NPs change the point of thermodynamic equilibrium of the ternary system as compared to unmodified P3HT:PCBM, arguably leading to a change in the morphological evolution. Thus, in the second half of the chapter, to further examine the reasons for the observed aging, including the burn-in phase, and in order to deepen the understanding of the V_{OC}, an in-operando GIWAXS characterization is performed.

Interestingly, the device V_{OC} shows a very clear correlation with the evolution of the crystallinity recorded in GIWAXS. This observation supports the link with film morphology, anticipated from the V_{OC} behavior observed in the aging experiments with different loads of Fe_3O_4 NPs. The photovoltage, similar to the P3HT (100) edge-on intensity and the crystallite grain size calculated from the same Bragg reflection, increases in the early stages of increasing temperature. Upon stabilization of the device temperature, crystallite intensity, grain size and V_{OC} reach a maximum and the trends revert. In the long run, degradation mechanisms such as photobleaching and crystallite melting further assist the decrease in crystallinity, grain size and photovoltage. We argue that the evolution of the

observed parameters results from the competition of two main mechanisms. First, the crystallinity enhances in the early stages due to the increasing temperature provided by the sample illumination. Second, radiation-induced aging leads to losses in crystallinity. The influence of crystallinity in the energetic disorder, DOS shape, material transport properties and recombination dynamics provides the link between the GIWAXS signal and the photovoltage.

Determination of the mechanisms behind the behavior of V_{OC} has often been a difficult task, especially during the complex initial burn-in phase. In time-dependent aging experiments, the V_{OC} is parametrized as nearly constant, neglecting the outlandish behavior shown in the first operation stages. Even comprehensive models parametrizing the fine structure of the aging behavior for other OPV parameters regard the photovoltage as constant.[194] In this regard, the present research constitutes the first direct evidence of the link between P3HT:PCBM device photovoltage and the crytallinity of its active layer, achieved with help of an in-operando combination of GIWAXS and I-V tracking. Furthermore, the presented work takes a step further into understanding the nature of V_{OC} and its evolution during aging. More generally, the knowledge about the device photovoltage, its link with system crystallinity and its control grows continuously. As an example, successful approaches involving ternary active layers that enable control of photovoltaic parameters (including V_{OC}) through fine adjustment of aggregation, packing distances and crystallite orientations are available.[221]

According to the insight gained from the data, the unexpected behavior observed for the V_{OC} in P3HT:PCBM OSCs upon addition of Fe_3O_4 NPs is arguably related to different crystalline developments. Consequently, the V_{OC} stabilizing at different values for different Fe_3O_4 NP weight percentages is ascribed to different crystalline equilibrium states, which aligns with the earlier assumption of the NPs altering the thermodynamic equilibrium as compared to pristine P3HT:PCBM devices. In this regard, further in-operando GIWAXS characterization of devices featuring different NP concentrations can confirm the presented hypothesis. To further explore the correlation between the crystallinity and the performance decay in pace and shape, in-operando GIWAXS offer a perfect follow up to the work by Kong et al. observing in real time the influence of film crystallinity on the already spotted link between the polymer polydispersity and the severity of the PCE decay within the burn-in phase.[191]

The present chapter sheds light on the effect of NP inclusion on P3HT:PCBM device aging, thereby highlighting the aspects that are as yet poorly understood or require further

improvement. Moreover, in-operando investigations have proven to be a powerful tool for providing insight into the nature of the burn-in phase and, in turn, into the nature of relevant photovoltaic parameters, such as the V_{OC}. The high-precision setup combined with synchrotron radiation allows unprecedented time resolutions, which unveil material and device behavior even in the very first moments of operation Thus, this breakthrough constitutes a great avenue to study the effect of NPs on the morphology and thermodynamics of polymer systems, and to correlate them to OSC performance. Further knowledge on the factors governing OSC functioning through the link to material morphology can be gained via in-operando experiments featuring different types and concentrations of NPs and/or photoactive systems, as well as tailored temperature, pressure or moisture conditions.

Chapter 8

Conclusions and outlook

The main aim of the broader research to which the present work belongs is to explore the possibilities of improving OSC performance via a modification of the device charge-carrier statistics in nominal, relative and time-aggregated terms. The central idea of the investigated approach is to learn to control the rate of exciton ISC in the photoactive medium and increase it in a tailored manner. This way, photogenerated singlet excitons are more likely to shift their wavefunctions towards the triplet spin manifold, thereby reducing the overall efficiency of the exciton radiative decay. Consequently, the device geminate exciton recombination is reduced. This leads to higher exciton diffusion lengths and, consequently, to higher exciton splitting rates, improving the overall device performance. The present thesis approaches this idea from different perspectives.

The first approach picks up the principles employed in OLED research, in which triplet emitters with heavy metallic elements embedded in the chemical structure increase the rate of ISC. In this sense, we put to test the novel donor material PBST3HT, a thiophene-based macromolecule including selenophene and tellurophene units, featuring a period-five semi-metal, tellurium. In the effort of merging heavy-metal heteroatoms with long molecular weights, which has been and still is an important synthesis bottleneck, very insightful results are obtained. The temperature response of the material (an important behavior since temperature is a key parameter in device fabrication) is characterized by a change in the band gap. This is driven by significant changes in the crystalline packing of the polymer aggregates and, to a lesser extent, to changes in its meso-morphology. The process is arguably driven by the high coordination of the Te atoms. In combination with temperature, it induces the development of stable crystalline morphologies, featuring an increased $\pi - \pi$ stacking to the detriment of the crystallinity along the backbone.

The band gap-tuning behavior via simple thermal annealing opens the possibility to make

PBST3HT compatible with a broad range of acceptor materials in devices. Nevertheless, the immediate substitution of P3HT with PBST3HT in P3HT:PCBM BHJ devices needs to be improved. The low performances obtained are mainly linked to the low polaron conductivity of PBST3HT in its natural, undoped state, as is common for tellurophenes. In this regard, further research to implement PBST3HT in devices can involve fundamental material morphological as well as optoelectronic characterization under exposure to I_2. A study of the OSC behavior in a controlled I_2 atmosphere and the possibility to relate the device behavior to the material morphology is also expected to provide better insight. Moreover, our investigations on the PBST3HT optoelectronic properties reveal strongly condition-dependent HOMO and LUMO levels. These are highly sensitive to temperature and to the halogenation processes (iodination, bromination) related to the needed increase in the polaron conductivity. Hence, a comprehensive knowledge of the PBST3HT energetic landscape for different temperatures and halogen exposure treatments will be of great importance and can be achieved by means of e.g. ultraviolet-photoelectron and impedance spectroscopy.

On the upside, PBST3HT cells have shown the interesting effect of performance improvement in the first minutes of illumination. This is arguably related to morphological changes observed under increased temperature. This structure-relation link can be further researched, and optimally, controlled. In the present work it has been shown that this behavior can be transferred into P3HT:PCBM devices by building ternary P3HT:PBST3HT:PCBM cells. Despite a reduced device absolute performance resulting from the poor conductivity of PBST3HT, the result combined with the improvements in the PBST3HT properties and a better control of its energy levels could lead to e.g. an improved device aging response of P3HT:PBST3HT:PCBM ternary systems.

The second approach employed in this work to improve the PCE via an increased ISC relies on the use of small superparamagnetic nanoparticles. The magnetic remanence of the NPs creates a strong magnetic field gradient in the material surroundings of each NP. The coupling of excitonic spins with the magnetic field results in a spin rephasing, which favors the singlet-to-triplet transition and, thus, the ISC. The incorporation of Fe_3O_4 NPs in P3HT:PCBM devices leads to a reduced charge carrier recombination, as observed in the analysis of the corresponding J-V curves. This behavior is confirmed by an additional optoelectronic characterization of photoactive films, which in turn allowed for estimation of the average lifetime. An additional bulk GIXS characterization ruled out the possibility of significant morphological or crystalline changes in the system which contributed to the improvement in the device performance.

Additionally, the performance of OSCs modified with different Fe_3O_4 contents in the presence of an additional external magnetic field was also studied. In the weak magnetic field regime (linear region of the Fe_3O_4 NP hysteresis curve) an additional device improvement related to a lower rate of recombination was observed for low NP concentrations. The improvement shows a nearly linear growth with the magnetic flux density. In the strong field regime (close to magnetic saturation) improvements in the device performance were also observed. Nevertheless, these were not completely consistent in their nature with those observed with weak or no magnetic field. Combined with the impossibility of tuning the field intensity with the employed setup, invites to consider these results carefully, until further tests with more developed setups are possible. The further and more precise characterization of the influence of additional external magnetic fields along the whole hysteresis curve can benefit from a setup capable of generating highly linear and homogeneous fields of up to 0.5 T that allows for continuous or small-step adjustment of the magnetic flux density.

In general, experiments with magnetic fields (NPs or external) have yielded positive results. The sole inclusion of Fe_3O_4 NPs in P3HT:PCBM photoactive layers yields *PCE* improvement factors of up to 11 %. And the further deployment of external magnetic fields showed improvements of up to 3 %. It is worth noting that the work presented in this thesis is one of the first and most comprehensive studies available regarding the effect of magnetic fields on organic photoactive systems with special attention to its application in OPV. Compared to the first approach, featuring chemically-engineered macromolecules that include ISC-enhancing heteroatoms, the use of superparamagnetic NPs is a more industry-friendly approach. It avoids the controlled synthesis of complex novel materials, it can be applied to a broad variety of photoactive systems, different types of NPs fitting tailored needs can be used, and the process of incorporation is inexpensive.

Furthermore, regarding industry-friendliness, the research inexorably encountered the issue of device time behavior, an unavoidable aspect when assessing the commercial viability of OSCs. On the one hand, despite low absolute performances due to the issues discussed above, PBST3HT-only devices presented a "recovery" effect, showing improved performance values in the first minutes of device functioning compared to the initial values. A very positive and interesting result obtained is that this observed behavior has been successfully transferred to P3HT:PCBM devices by using PBST3HT as a third component in P3HT:PBST3HT:PCBM ternary-active-layer devices. Hereby, improvements in relative terms in the aging profiles compared to pristine P3HT:PCBM cells are obtained.

This behavior is ascribed to the morphological and crystalline dependence on temperature observed in the fundamental characterization.

On the other hand, despite the improved PCE and the pursued reduction in exciton recombination, the inclusion of Fe_3O_4 NPs has had so far a negative impact on the P3HT:PCBM device service life. The main reasons proposed are the promotion of singlet oxygen and the accelerated coarsening of domains within the BHJ upon Fe_3O_4 inclusion. Deeper research into the causes of accelerated aging led to time-resolved in-operando scattering characterization, which provided further insight on the relation between crystallinity and electrical performance (more specifically, the photovoltage V_{OC}). More generally, the link between structure and function is often one of the common denominators of the understanding of organic electronic devices. In this regard, GIXS characterization techniques for thin films proved to be a powerful tool in examining the fundamental physics governing material and device behavior. In particular, measurements employing high-flux x-ray radiation, characteristic of synchrotron light sources, have enabled the possibility to characterize systems in real time, allowing for real-time correlation of events and observation of degradation processes even in the very first seconds of device operation. Further research efforts in this regard featuring more material combinations and more- and better-controlled sample environments, amongst other possibilities, will be key in disentangling the complex ins and outs of the important structure-performance relation.

Overall, the presented work shows that research in OSC performance improvement via ISC control can be deployed at different, yet parallel dimensions. On the one hand, applied research closer to direct device implementation can offer progress in increasing PCEs by simple methods. For example, inclusion of NPs in photoactive D-A systems. This approach has proven to be straightforward and to deliver satisfactory results. Moreover, the obtained results still can be further improved by further testing new organic materials, NPs, fabrication environments, etc. On the other hand, more fundamental, long-term-oriented and less cost-efficient research stays one step ahead in the understanding of underlying physical and chemical principles, providing knowledge for subsequent technological breakthroughts. The promising results obtained in this work regarding band gap adjustability of PBST3HT and of further PCE improvements under the influence of strong external magnetic fields generated by expensive and bulky setups are good examples of promising long-term studies. Overall, the combination of the two approaches allows for mutual feedback, guaranteeing the introduction of new fundamental knowledge in the process of novel device design, at the same time that technical progress is underpinned by

a solid understanding of the underlying physical, chemical and engineering challenges.

Appendix A

Magnetic field-generating setups: layouts and calibration

In the second half of chapter 6, in section 6.3 the effect of external magnetic fields on the performance of P3HT:PCBM OSCs modified with Fe_3O_4 NPs is discussed. In order to generate the magnetic fields necessary for carrying out the presented study, two different setups are constructed. One of them is based on a Helmholtz double coil, capable of generating very homogeneous and one-dimensional weak magnetic fields. The second approach uses a permanent magnet, which generates a magnetic field on the probed sample of about 4400 Oe. In the present appendix, the necessary details about the setups, their construction and their calibration are provided. The content of this appendix is based on work presented in the masterthesis *"Enhancing triplet exciton population in organic solar cells"* by Florian Dreher.[117]

A.1 Helmholtz coil setup

The Helmholtz coil setup is designed to achieve low but finely adjustable magnetic fields. The core structure of the setup consists of a long varnished copper wire coiled around two ring-like shells. The shells are as well varnished in order to avoid electrical contact with the wiring. The copper wire itself has a diameter of 1 mm, whilst the total diameter, including the varnish layer amounts to 1.1 mm. Each of the coils has sixty-six wire windings, and an inner and outer diameters of 8 and 11 cm, respectively ($R \approx 4.75$ cm). Their middle planes are 4 cm apart. The double-coil system is fixed on a base consisting of a 22×22 cm^2 plate, designed to fit in the measuring stage of the solar simulator (see section 3.2.3). The plate has two recesses that leave in the middle of the plate a bridge, in the center of which the OSC sample is placed. The two recesses create the space necessary

for the two bars that hold the two coils immobile with respect to each other, so that the sample can be placed in between the coils and equidistant to both of them. Thus, the sample plane is perpendicular to the magnetic field. The system is designed in a way, that the measured OSC is placed in the region of the most homogeneous magnetic field. A concept-drawing as well as a picture of the real mounted setup are shown in figure A.1.

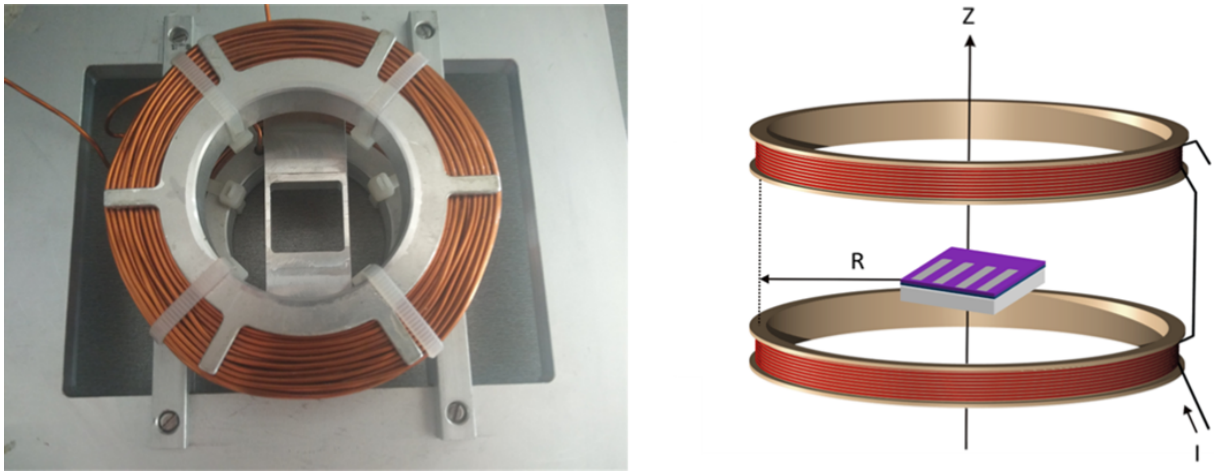

Figure A.1: *a) Top view of the mounted Helmholtz double-coil setup. The second coil lies below the plane of the main plate, which occupies the whole picture. The square hole in the geometric center is designed for placing the sample under investigation in its holder. b) Concept-drawing of the Helholtz coil setup. The sample under measurement lies in the geometric center of the setup. The space direction along the axes of the coils is regarded as the z-direction. Figure is adapted from* [222].

When voltage is applied to the setup the current flow generates a magnetic field according to the Biot-Savart law. The ring-like form of the wound cables generate a straight field parallel to the coil axis. Thus, since the setup consists of the superposition of two straight equal fields separated by a certain distance, the setup is able to generate an overall highly homogeneous and one-dimensional magnetic field.

The OSC is held in the center of the setup through a specially-designed PVC holder. The purpose of the holder (shown in figure A.2) is to ensure homogeneous contact throughout all the pixels of a solar cell, and to avoid magnetic distortions of the electric current flowing through the measuring cables. At one of its ends the holder has the sample stage. It consists of a pocket carved in a PVC cube with the exact size of one of our ITO substrates. The sample is placed with the pixels facing the interior, and they are individually contacted by gold-covered test pins. Each pin is partially inserted in an as well gold-capped capsule, which is contacted to the copper cables in the rear end. The test pins are pressed against the pixels via a spring (see figure A.2a), ensuring homogeneous contact. The substrates are held immobile against the force of the springs with a thin metallic plate, over which another plate with an illumination mask (a hole with the dimensions

of one pixel) slides through two guides laterally carved in the PVC block (see figure A.2b).

At the rear end of the golden measuring capsules, the cables going to the Keithley SourceMeter are soldered. They are mounted on a long PVC block and kept straight with silicone within carved rails for 20 cm. This is done to ensure that the charge carriers extracted from the device travel parallel to the magnetic field for a sufficient distance. This way, potential influence exerted by the Lorentz force in presence of the magnetic field is neutralized, and thereby the obtained measurement is not potentially corrupted.

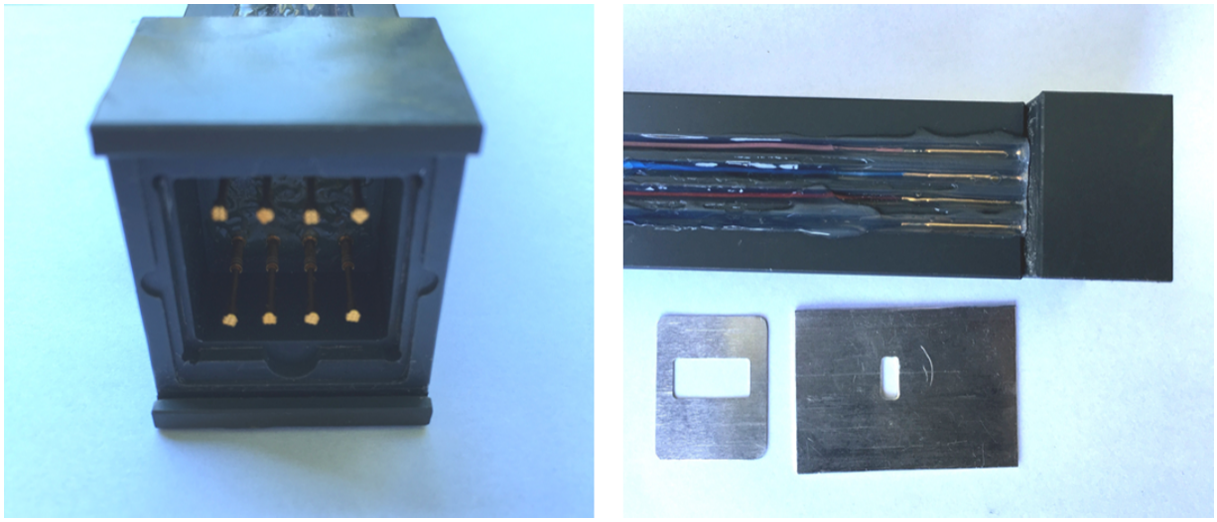

Figure A.2: *a) Front view of the sample stage of the PVC holder used in the measurements with the Helmholtz coil setup. The ends of the eight gold-capped test pins are visible in the center of the picture b) Detail of the wiring soldered to the rear end of the test pins. The cables are driven straight for 20 cm. Metallic thin plate for fixing the OSC within the holder, leaving all pixels visible through the sample glass, and outer sliding illumination mask for pixel selection.*

A.1.1 Characterization of the magnetic field

The current flowing through the coils is generated with a HQPOWERPS3010 DC POWER SUPPLY source, with a voltage compliance of 25 V and a current compliance of 7.5 A. The thereby generated magnetic fields are measured with an MMZ-2502-UH Hall sensor for different applied currents. The data readout was provided by a Lakeshore 460 3-channel gaussmeter. The field is characterized for most of the accessible volume between the two coils, to ensure field homogeneity over a large macroscopic space. The obtained field profiles for various z-points and distances from the coil-system axis are depicted in figure A.3 (azimuthal isotropy is assumed).

The high field homogeneity can be observed from the color maps. Along the double-coil

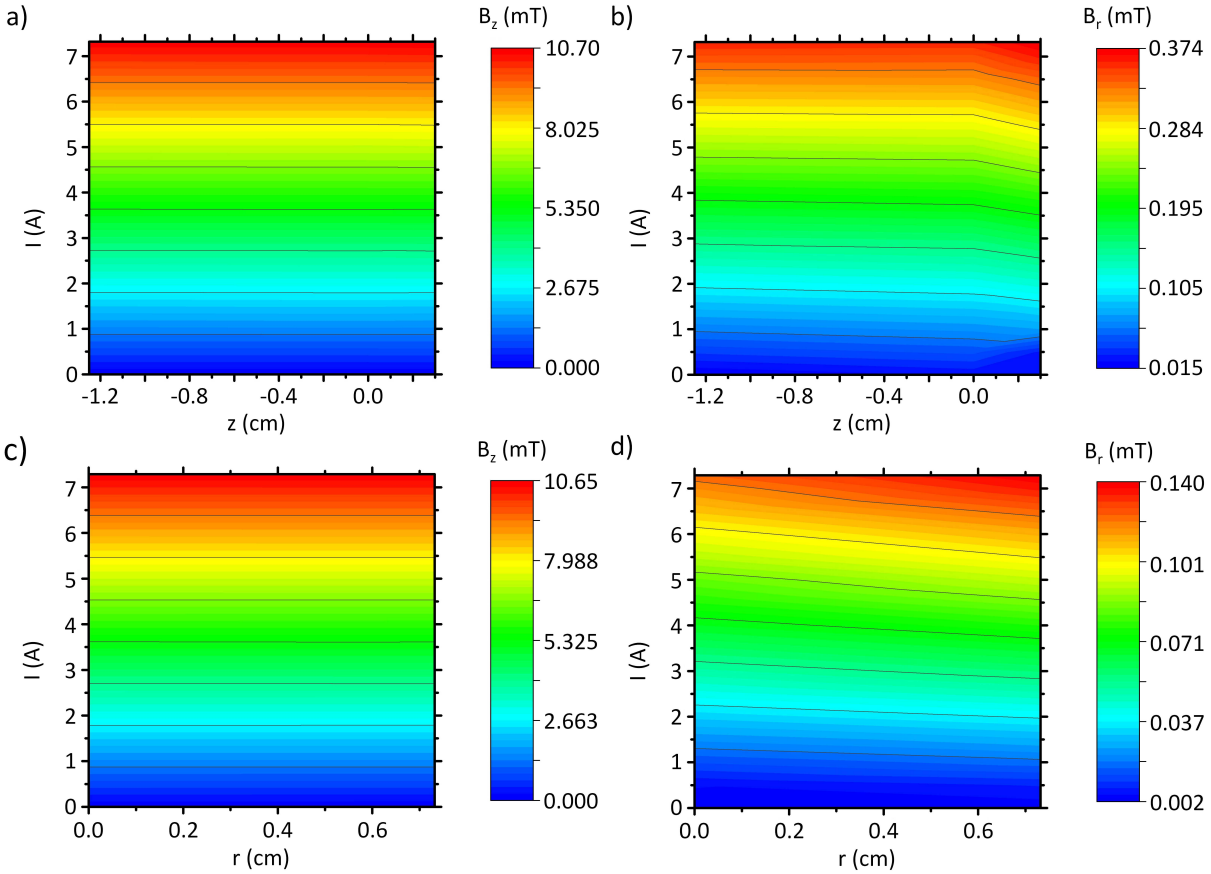

Figure A.3: *Magnetic field intensity vs. position vs. current obtained in the calibration of the Helmholtz coil system. a) z-profile of the field z-component at r=0. b) z-profile of the field radial component at r=0. c) radial profile of the field z-component at z=0. d) radial profile of the field radial component at z=0.*

axis, the z-component of the measured field (A.3a) amounts to a maximum of 10.70 mT and stays constant for a z-variation of 1.5 cm (for comparison, the active layers of the probed solar cells, which extend along the same direction, present thicknesses in the order of 100 nm). Along the same z-range, the radial component stays as well constant for most of the range and depicts a field intensity almost 30 times lower. Figures A.3c and A.3d depict the z- and radial components of the field at the z-height of the sample (z = 0). The field is characterized within a circular area of 1.5 cm size (the individual devices are approximately 2×5 mm^2). The z-component stays within the regarded area as well constant, whilst the radial component shows a small intensity increase as the sensor approaches the wires.

Overall, the largest field intensity variation within the probed cylindrical volume happens for the radial component and amounts to 4 %, whereby the radial component is two orders of magnitude lower than the z-component. Thus, the homogeneous field can be fitted and described as a function of the flowing current, namely:

$$B_r(I) = \left[(5 \pm 4) \cdot 10^{-2} I\right] \mathrm{mT} \tag{A.1}$$

$$B_z(I) = \left[(1.45 \pm 0.02) I\right] \mathrm{mT} \tag{A.2}$$

whereby the current is given in A.

A.1.2 Calibration with non-modified OSCs

Prior to use in experiments with Fe_3O_4-modified OSCs, proper calibration and test measurements need to be granted in order to ensure that none of the unwanted effects regarding Lorentz force or other inductive effects appear during device operation. In this regard, tests and calibration are carried out with non-modified pristine P3HT:PCBM solar cells. If the setup works properly, they should remain unaffected by the magnetic field, since they do not contain superparamagnetic agents and the measuring circuitry is designed to stay unaffected by the field.

To grant as well independence of the sign of magnetic flux variation, half of the pixel of each solar cells are measured from zero to maximum fields and back to zero, and the other half are measured in the opposite way. Waiting time between consecutive measurements is kept constant at the same as for the case with modified OSCs (see section 6.3).

The obtained results are summarized in figure A.4. Evolution of the PCE, FF, J_{SC}, V_{OC}, R_S and R_{SH} normalized to the first value are shown. The black data set corresponds to the pixels measured with increasing-decreasing magnetic flux variation protocol, whereas the red points indicate the pixels measured in decreasing-increasing mode. It must be noted that the worsening of the parameters observed arises from the device aging due to contact with O_2 and UV radiation, given that between consecutive measurements a certain amount of time elapses, i.e. field and time axes are coupled.

The corresponding data sets overlap very good for most of the magnetic range, featuring only small variations on localized graph positions, and only for certain parameters. These variations between mean values, however, still lie within the uncertainty range defined by the corresponding error bars. Hence, after the successful calibration, we consider the Helmholtz coil setup to function properly and not to affect non-modified devices, as it is desired.

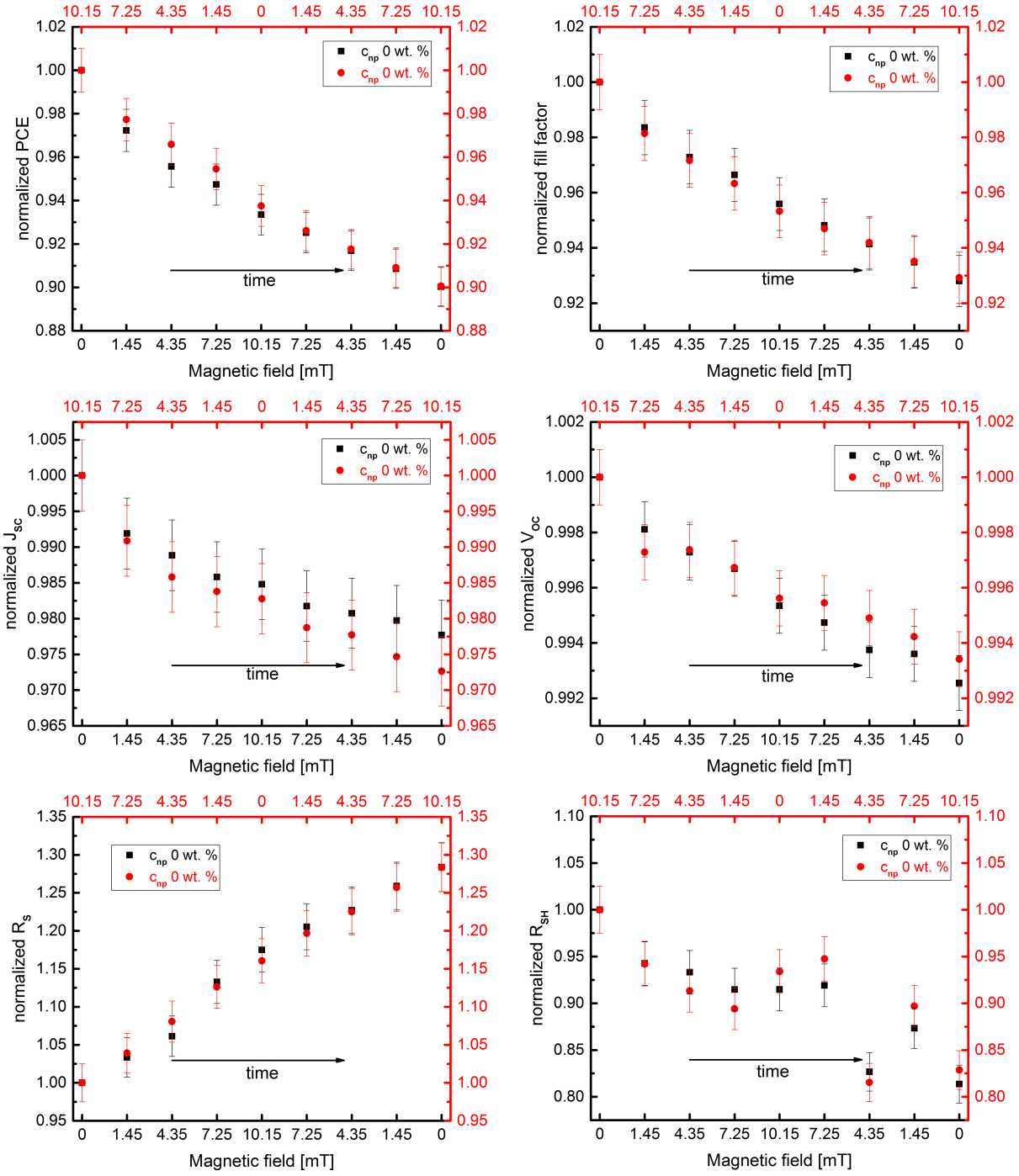

Figure A.4: *Normalized PCE, FF, J_{SC}, V_{OC}, R_S and R_{SH} obtained for the calibration measurements with non-modified P3HT:PCBM OSCs for weak magnetic fields generated with the Helmholtz coil setup. To ensure symmetry with respect to the sign of magnetic flux variation, one set of measurements is performed from zero to maximum field intensity and back (black data points), and a second set of pixels is measured following the opposite protocol (red data points). The decrease in performance arises from the prolonged contact with atmosphere and UV radiation (indicated by the time arrows).*

A.2 Permanent magnet setup

As discussed previously in section 6.3, despite the high homogeneity and one-dimensionality of the field generated by the Helmholtz coil setup, the field intensities that the setup is able to generate are limited. Thus in order to enable the study of the OSC response to field intensities that bring the NPs closer to saturation magnetization, another setup is required. In order to achieve on the solar device fields of ≈ 4500 Oe, a setup based on a strong cuboid neodym permanent magnet is constructed. The magnet (shown in figure A.5a) was purchased from *magnet-shop.de*, its dimensions are $30 \times 12 \times 12\text{mm}^3$ and has a magnetization of N52, corresponding to a remanence of 1.42 to 1.47 T.

Figure A.5: *a) Permanent cuboid neodym magnet used for the construction of the strong field-generating setup. b) Close-up of the modified empty PVC holder with larger distance between the test pin rows and two recesses for insertion of the neodym magnet. c) Front view of the assembled holder with the magnet and without the sample and the illumination mask mounted.*

The setup consists basically of a modification of the PVC device holder presented for the previous Helmholtz setup (displayed in figure A.5b). In this case, however, the two rows of gold-capped test pins are further apart from each other, leaving room in between for inserting the elongated magnet through recesses of the size of the magnet section ($12 \times 12\text{mm}^2$) bored on both lateral walls of the holder. The rest of the setup and its usage regarding to device characterization is identical to the previous mentioned one (see previous section A.1). As depicted in figure A.5c, the lower surface of the magnet in the fully assembled holder lies 1 mm away from the surface of the OSC, generating a magnetic flux density in vacuum of 440 mT at the position of the device. Thus, the field generated by this setup cannot be adjusted like in the case of the Helmholtz double-coil.

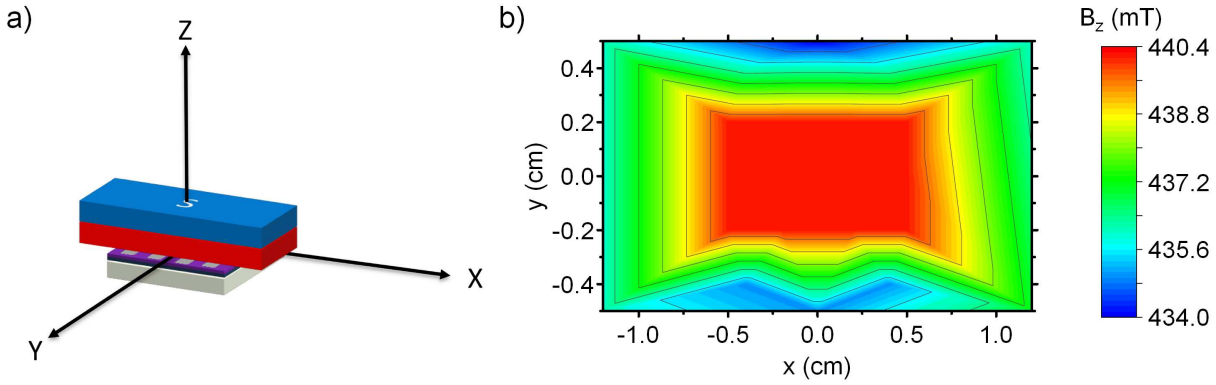

Figure A.6: *a) Schematic depiction of the magnet-sample relative configuration within the assembled holder. Similar to the case of the Helmholtz setup, the z-direction is defined as perpendicular to the sample plane. b) Magnetic field intensity vs. x/y-position obtained in the calibration of the permanent magnet system. Measurements are carried out at a height of z=0, i.e. the distance between magnet and OSC surfaces is 1 mm.*

A.2.1 Characterization of the magnetic field

In this case, once the whole system consisting of holder and magnet is assembled, there are no mobile parts, and the position of the device pixel under characterization is fixed with respect to the magnet. Hence, the characterization of the magnetic field is performed only for one z-position, i.e. the position of the cell within the holder, 1 mm away from the magnet surface. Figure A.6a depicts schematically the position of the measured sample with respect to the magnet and its polarity.

Figure A.6b displays the intensity of the generated field as a function of the x and y positions. The maximum magnetic flux density achieved amounts to 440.4 mT in air, and its field intensity stays constant within a rectangular area with approximate dimensions of $6 \times 12\text{mm}^2$. Beyond the limits of this area, the field intensity decays down to a minimum of 434 mT. Thus, the largest percentile intensity variation is only 1.4 %. Hence, an homogeneous field of 440 mT intensity is considered.

A.2.2 Calibration with non-modified OSCs

For the permanent magnet setup, calibration based on the study of the behavior of non-modified OSCs was as well carried out. Similarly to the previous case, one pristine P3HT:PCBM solar cell is measured with and without the mounted magnet successively. Furthermore, an additional OSC containing no NPs is measured, first with the magnet and later without it. The results obtained are summarized in figure A.8. Again an overall worsening of the photovoltaic indicators is obtained as a result of the device ageing caused by the contact with O_2 and UV radiation. As before, the time elapsed between measure-

ments is held by 25 s. In general a good overlap within error bar tolerance is obtained. In the case of the V_{OC}, the overlap is a bit worse. However, the variations between the two mean values obtained represents just a 0.2 %.

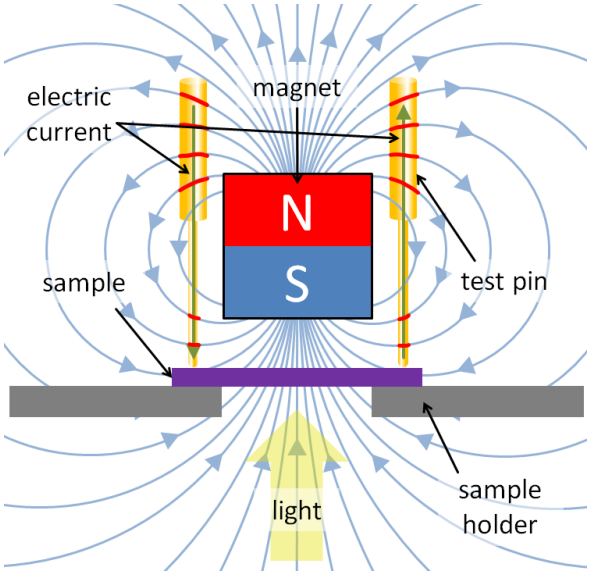

Figure A.7: *Schematic depiction of the field generated by the neodym magnet assembled into the measuring setup. Eventual meeting points between the recorded electric current and the magnetic field with a non-negligible perpendicular component that could arguably have an effect on the OSC characterization are indicated in red.*

According to the suggested calibration procedure, the permanent magnet setup can be considered to function properly, as the effect of the magnetic field on non-modified OSCs seems negligible. This positively contributes to the meaningfulness of the results obtained for Fe_3O_4-containing devices in section 6.3. However, judgment of the quality of the calibration in this case is based on very few data points, which still makes an overall reasonable doubt to remain present. It can be argued that, even if the magnetic field generated by the magnet does affect the charge carriers in the wiring of the measurement setup, this effect will remain the same for all samples. Thus, this effect could lead to a systematic error for the measurement, which could yield an offset in the obtained data. Nevertheless, a qualitative comparison amongst differently fabricated devices is still valid. However, the magnetic field generated by the permanent magnet setup must be kept in mind. It shows non-negligible components perpendicular to the test pins, as depicted in Figure A.7 (contentious meeting spots highlighted in red). Thus, the charge carrier could be influenced. This is an issue that it should be further looked into.

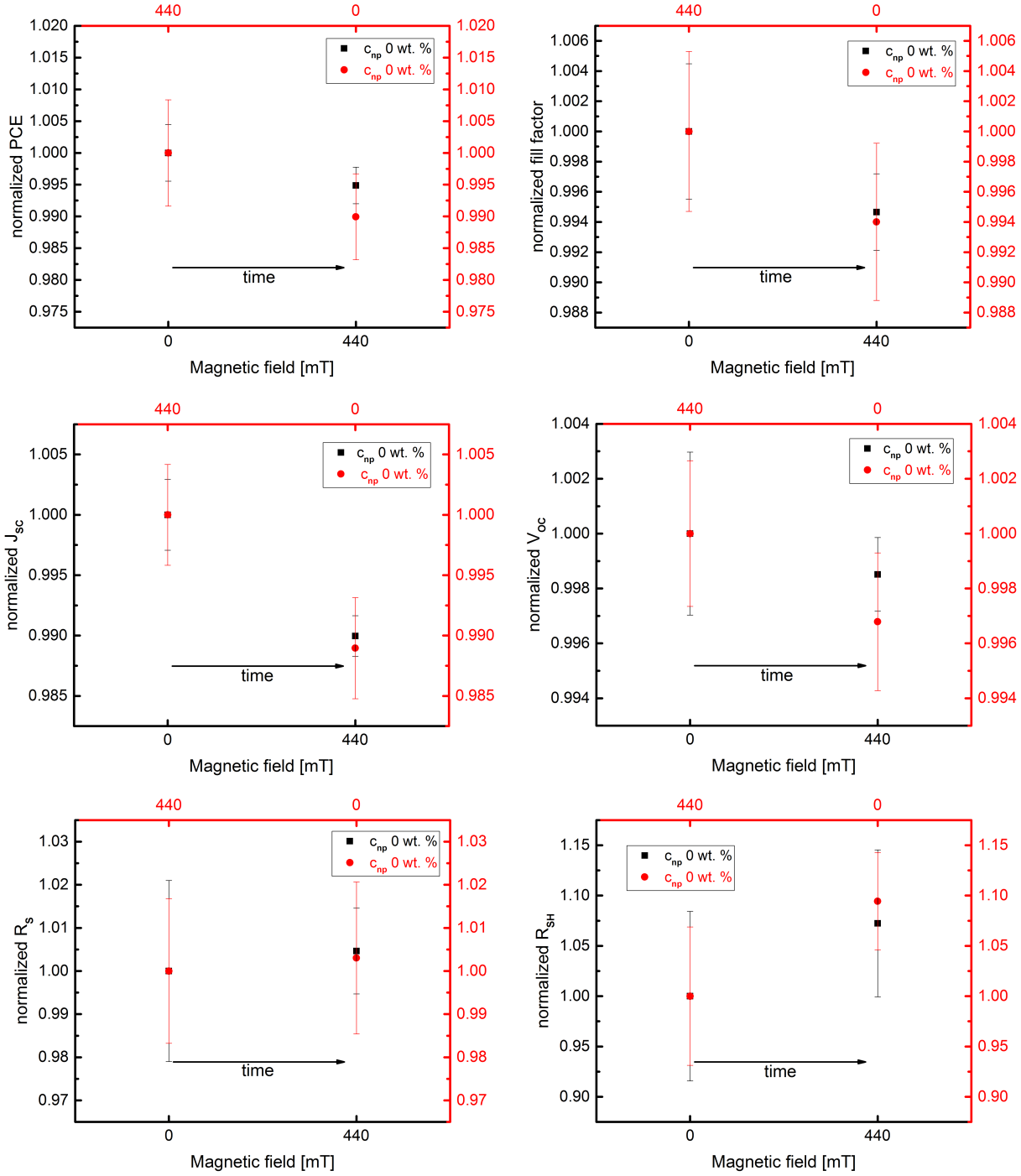

Figure A.8: *Normalized PCE, FF, J_{SC}, V_{OC}, R_S and R_{SH} obtained for the calibration measurements with non-modified P3HT:PCBM OSCs for strong magnetic fields generated with the permanent magnet setup. To ensure symmetry with respect to the sign of magnetic flux variation, one set of measurements is performed from zero to maximum field intensity and back (black data points), and a second set of pixels is measured following the opposite protocol (red data points). The decrease in performance arises from the prolonged contact with atmosphere and UV radiation (indicated by the time arrow).*

Bibliography

[1] U.S. Energy Information Administration. *International Energy Outlook*, 2011.

[2] International Energy Agency. *Medium-Term Renewable Energy Market Report*, 2016.

[3] J. R. Moreira and A. D. Poole. *Renewable Energy: Sources for Fuels and Electricity.* Island Press, 1992.

[4] M. Z. Jacobson and C. L. Archer. Saturation wind power potential and its implications for wind energy. *Proc. Natl. Acad. Sci. U. S. A.*, 109(39):15679–15684, 2012.

[5] B. Goldstein, G. Hiriart, R. Bertani, C. Bromley, L. Gutiérrez-Negrín, E. Huenges, H. Muraoka, A. Ragnarsson, J. Tester, and V. Zui. *IPCC special report on renewable energy sources and climate change mitigation.* Cambridge University Press, Cambridge, 2011.

[6] P. Meisen and A. Loiseau. Ocean energy technologies for renewable energy generation. Global Energy Network Institute, 2009.

[7] S. B. Darling and F. You. The case for organic photovoltaics. *RSC Adv.*, 3:17633–17648, 2013.

[8] M. A. Green, K. Emery, Y. Hishikawa, W. Warta, and E. D. Dunlop. Solar cell effciency tables (version 48). *Prog. Photovolt: Res. Appl.*, 24(7):905–913, 2016.

[9] P. Sommer-Larsen, M. Jørgensen, R. R. Søndergaard, M. Hösel, and F. C. Krebs. It is all in the pattern - high efficiency power extraction from polymer solar cells through high-voltage serial connection. *Energy Technol.*, 1(1):15–19, 2013.

[10] National Renewable Energy Laboratory. *Best research-cell efficiencies*, https://www.nrel.gov/pv/assets/images/efficiency-chart.png, 2016.

[11] B. Azzopardi, C. J. M. Emmot, A. Urbina, F. C. Krebs, J. Mutale, and J. Nelson. Economic assessment of solar electricity production from organic-based photovoltaic modules in a domestic environment. *Energy Environ. Sci.*, 4(10):37413753, 2011.

[12] G. Dennler, M. C. Scharber, and C. J. Brabec. Polymer-fullerene bulk-heterojunction solar cells. *Adv. Mater.*, 21(13):1323–1338, 2009.

[13] R. Gaudiana and C. Brabec. Organic materials: Fantastic plastic. *Nat. Photon.*, 2:287–289, 2008.

[14] D. Moseguí González, V. Körstgens, Y. Yao, L. Song, G. Santoro, S. V. Roth, and P. Müller-Buschbaum. Improved power conversion efficiency of P3HT:PCBM organic solar cells by strong spin-orbit coupling-induced delayed fluorescence. *Adv. Energ. Mater.*, 5(8):1401770 (1–10), 2015.

[15] D. Moseguí González, C. J. Schaffer, S. Pröller, J. Schlipf, L. Song, S. Bernstorff, E. M. Herzig, and P. Müller-Buschbaum. Codependence between crystalline and photovoltage evolutions in P3HT:PCBM solar cells probed with in-operando GI-WAXS. *ACS Appl. Mater. Interfaces*, 9(4):3282–3287, 2017.

[16] D. Moseguí González, K. N. Raftopoulos, G. He, C. M. Papadakis, A. Brown, E. Rivard, and P. Müller-Buschbaum. Bandgap-tuning in triple-chalcogenophene polymer films by thermal annealing. *Macromol. Rapid Commun.*, 38(11):1700065 (1–6), 2017.

[17] G. Strobl. *The Physics of Polymers*. Springer-Verlag Berlin Heidelberg, 2007.

[18] A. D. Jenkins, P. Kratochvíl, R. F. T. Stepto, and U. W. Suter. Glossary of basic terms in polymer science (IUPAC recommendations 1996). *Pure Appl. Chem.*, 68(12):2287–2311, 1996.

[19] G. Beaucage, R. S. Stein, T. Hashimoto, and H. Hasegawa. Tacticity effects on polymer blend miscibility. *Macromolecules*, 24(11):3443–3448, 1991.

[20] Ling Chang and E. M. Woo. Tacticity effects on glass transition and phase behavior in binary blends of poly(methyl methacrylate)s of three different configurations. *Polym. Chem.*, 1:198–202, 2010.

[21] Y. Kim, S. Cook, S.M. Tuladhar, S.A. Choulis, J. Nelson, J.R. Durrant, D.D.C. Bradley, M. Giles, I. McCulloch, C. Ha, and Ree M. A strong regioregularity effect in self-organizing conjugated polymer films and high-efficiency polythiophene:fullerene solar cells. *Nat. Mater*, 5(3):197–203, 2006.

[22] R. Mauer, M. Kastler, and Laquai F. The impact of polymer regioregularity on charge transport and efficiency of P3HT:PCBM photovoltaic devices. *Advanced Functional Materials*, 20(13):2085–2092, 2010.

[23] J. H. Hildebrand. *The solubility of non-electrolytes.* John Wiley & Sons, New York, 1936.

[24] M. G. Bawendi and K. F. Freed. Systematic corrections to Flory-Huggins theory. polymer-solvent-void systems and binary blend-void systems. *J. Chem. Phys.*, 88(4):2741–2756, 1988.

[25] Z. Horák, I. Fortelný, J. Kolařík, D. Hlavatá, and A. Sikora. *Encyclopedia of polymer science and technology*, chapter Polymer blends. John Wiley & Sons, 2005.

[26] L. H. Sperling. *Introduction to physical polymer science.* John Wiley & Sons, 2006.

[27] G. Strobl. Colloquium: Laws controlling crystallization and melting in bulk polymers. *Rev. Mod. Phys.*, 81(13):1287–1300, 2009.

[28] R. Becker. Die keimbildung bei der ausscheidung in metallischen mischkristallen. *Ann. Physik*, 424(1-2):128–140, 1938.

[29] M. V. Massa and K. Dalkoni-Veress. Homogeneous crystallization of poly(ethylene oxide) confined to droplets: the dependence of the crystal nucleation rate on length scale and temperature. *Phys. Rev. Lett.*, 92(25):255509 (1–4), 2004.

[30] B. Wunderlich. *Macromolecular physics vol. 2. Crystal nucleation, growth, annealing.* Academic Press New York, 1976.

[31] W. P. Su, J. R. Schrieffer, and A. J. Heeger. Solitons in polyacetylene. *Phys. Rev. Lett.*, 42(25):1698–1701, 1979.

[32] C. M. Palumbiny. *Polymer PEDOT:PSS electrodes for organic electronics: Understanding the conductivity-structure relation.* PhD thesis, Technical University of Munich, 2015.

[33] R. A. Marcus. On the theory of oxidation reduction reactions involving electron transfer. *J. Chem. Phys.*, 24(5):966–978, 1956.

[34] R. A. Marcus. Electron transfer at electrodes and in solution: comparison of theory and experiment. *Electrochim. Acta*, 13(5):995–1004, 1968.

[35] A. Miller and E. Abrahams. Impurity conduction at low concentrations. *Phys. Rev.*, 120(3):745–755, 1960.

[36] H. Bässler. Charge transport in disordered organic photoconductors. a Monte Carlo simulation study. *Phys. Status Solidi*, 175(1):15–56, 1993.

[37] E. U. Condon. The Franck-Condon principle and related topics. *Am. J. Phys.*, 15(5):365–374, 1947.

[38] F. Spano. Emission from aggregates of oligo-phenylene vinylenes: a recipe for superradiant h-aggregates. *Chem. Phys. Lett.*, 331(1):7–13, 2000.

[39] F. Spano. Absorption and emission in oligo-phenylene vinylene nanoaggre- gates: the role of disorder and structural defects. *J. Chem. Phys.*, 116(3):5877–5891, 2002.

[40] F. C. Spano. Modeling disorder in polymer aggregates: the optical spectroscopy of regioregular poly(3-hexylthiophene) thin films. *J. Chem. Phys.*, 122(23):234701, 2005.

[41] F. Spano and C. Silva. H- and J-aggregate behavior in polymeric semiconductors. *Annu. Rev. Phys. Chem.*, 65(1):477–500, 2014.

[42] D. Hertel and H. Bässler. Photoconduction in amorphous organic solids. *ChemPhysChem*, 9(5):666–688, 2008.

[43] J. E. Kroeze, T. J. Savenije, M. J. W. Vermeulen, and J. M. Warman. Contactless determination of the photoconductivity action spectrum, exciton diffusion length, and charge separation efficiency in polythiophene-sensitized tio2 bilayers. *J. Phys. Chem. B*, 107(31):7696–7705, 2003.

[44] L. Lüer, H. J. Egelhaaf, D. Oelkrug, G. Cerullo, B. H. Lanzani, G. Huisman, and D. de Leeuw. Oxygen-induced quenching of photoexcited states in polythiophene films. *Org. Electron.*, 5(1-3):83–89, 2004.

[45] C. L. Braun. Electric field assisted dissociation of charge transfer states as a mechanism of photocarrier production. *J. Chem. Phys.*, 80(9):4157–4161, 1984.

[46] R. A. Street, M. Schoendorf, A. Roy, and J. H. Lee. Interface state recombination in organic solar cells. *Phys. Rev. B*, 81(20):205307 (1–12), 2010.

[47] J. C. Scott and G. G. Malliaras. Charge injection and recombination at the metalorganic interface. *Chem. Phys. Lett.*, 299(2):115–119, 1999.

[48] E. Voroshazi, B. Verreet, T. Aeronuts, and P. Heremans. Longterm operational lifetime and degradation analysis of P3HT:PCBM photovoltaic cells. *Sol. Energy Mater. Sol. Cells*, 95(5):1303–1307, 2011.

[49] H. Hintz, H. J. Egelhaaf, H. Peisert, and T. Chassé. photooxidation and ozonization of poly(3-hexylthiophene) thin films as studied by UV/VIS and photoelectron spectroscopy. *Polym. Degrad. Stab.*, 95(5):818–825, 2010.

[50] S. Chambon, M. Manceau, M. Firon, S. Cros, A. Rivaton, and J.-L. Gardette. Photo-oxidation in an $^{18}O_2$ atmosphere: a powerful tool to elucidate the mechanism of UV-visible light oxidation of polymers-Application to the photodegradation of MDMO-PPV. *Polymer*, 49(15):3288–3294, 2008.

[51] M. Manceau, A. Rivaton, J.-L. Gardette, S. Guillerez, and Lemaître. The mechanism of photo- and thermooxidation of poly(3-hexylthiophene) (P3HT) reconsidered. *Polym. Degrad. Stab.*, 94(6):898–907, 2009.

[52] H. Hintz, H.-J. Egelhaaf, L. Lüer, J. Hauch, H. Peisert, and T. Chassé. Photodegradation of P3HT - a systematic study of environmental factors. *Chem. Mater.*, 23(2):145–154, 2011.

[53] M. S. A. Abdou and S. Holdcroft. Mechanisms of photodegradation of poly(3-alkylthiophenes) in solution. *Macromolecules*, 26(11):2954–2962, 1993.

[54] S. Chambon, A. Rivaton, J.-L. Gardette, M. Firon, and L. Lutsen. Aging of a donor conjugated polymer: photochemical studies of the degradation of poly[2-methoxy-5-(3,7-dimethyloctyloxy)-1,4-phenylenevinylene]. *J. Polym. Sci. Pol. Chem.*, 45(2):317–331, 2007.

[55] M. Manceau, A. Rivaton, and J.-L. Gardette. Involvement of singlet oxygen in the solid-state photochemistry of P3HT. *Macromol. Rapid Commun.*, 29(22):1823–1827, 2008.

[56] S. Chambon, A. Rivaton, J.-L. Gardette, and M. Firon. Reactive intermediates in the initiation step of the photo-oxidation of MDMO-PPV. *J. Polym. Sci. Pol. Chem.*, 47(22):6044–6052, 2009.

[57] D. E. Motaung, G. F. Malgas, and C. J. Arendse. Correlation between the morphology and photophysical properties of P3HT:fullerene blends. *J. Mater. Sci.*, 45(12):3276–3283, 2010.

[58] C. J. Schaffer, C. M. Palumbiny, M. A. Niedermeier, C. Jendrzejewski, G. Santoro, S. V. Roth, and P. Müller-Buschbaum. A direct evidence of morphological degradation on a nanometer scale in polymer solar cells. *Dav. Mater.*, 25(46):6760–6764, 2013.

[59] F. C. Krebs. *Stability and degradation of organic and polymer solar cells.* John Wiley & Sons, 2012.

[60] N. Grossiord, J. Kroon, R. Andriessen, and P. Blom. Degradation mechanisms in organic photovoltaic devices. *Org. Electron.*, 13(3):432–456, 2012.

[61] M. Jørgensen, K. Norrman, S. A. Gevorgyan, T. Tromholt, B. Andreasen, and F. C. Krebs. Stability of polymer solar cells. *Adv. Mater.*, 24(5):580–612, 2012.

[62] H. C. Liao, C.-C. Ho, C.-Y. Chang, M.-H. Jao, S. B. Darling, and W.-F. Su. Additives for morphology control in high-efficiency organic solar cells. *Mater. Today*, 16(9):326–336, 2013.

[63] Y. Yang, K. Mielczarek, M. Aryal, A. Zakhidov, and W. Hu. Nanoimprinted polymer solar cell. *ACS Nano*, 6(4):2877–2892, 2012.

[64] T. Pfadler, M. Coric, C. M. Palumbiny, A. C. Jakowetz, K.-P. Strunk, J. A. Dorman, P. Ehrenreich, C. Wang, A. Hexemer, R.-Q. Png, P. K. H. Ho, P. Müller-Buschbaum, J. Weickert, and L. Schmidt-Mende. Influence of interfacial area on exciton separation and polaron recombination in nanostructured bilayer all-polymer solar cells. *ACS Nano*, 8(12):12397–12409, 2014.

[65] C.-M. Yang, C.-H. Wu, H.-C. Liao, K.-Y. Lai, H.-P. Cheng, and S.-F. Horng. Enhanced photovoltaic response of organic solar cell by singlet-to-triplet exciton conversion. *Appl. Phys. Lett.*, 90(13):133509 (1–3), 2007.

[66] R. R. Lunt, N. C. Giebink, A. A. Belak, J. B. Benzinger, and S. R. Forrest. Exciton diffusion lengths of organic semiconductor thin films measured by spectrally resolved photoluminescence quenching. *J. Appl. Phys.*, 105(5):053711 (1–7), 2009.

[67] B. Xu and S. Holdcroft. Phosphorescence and delayed fluorescence of poly(3-hexylthiophene) films. *Thin Solid Films*, 242(1-2):174–177, 1994.

[68] M. A. Baldo, D. F. O'Brien, M. E. Thompson, and S. R. Forrest. Excitonic singlet-triplet ratio in a semiconducting organic thin film. *Phys. Rev. B*, 60(20):14422–14428, 1999.

[69] H. Najafov, B. Lee, Q. Zhou, L. C. Feldman, and Podzorov. Observation of long-range exciton diffusion in highly ordered organic semiconductors. *Nat. Mater.*, 9(11):938–943, 2010.

[70] N. Matsusue, S. Ikame, Y. Suzuki, and H. Naito. Charge-carrier transport and triplet exciton diffusion in a blue electrophosphorescent emitting layer. *J. Appl. Phys.*, 97(12):123512 (1–5), 2005.

[71] M. Samiullah, D. Moghe, U. Scherf, and S. Guha. Diffusion length of triplet excitons in organic semiconductors. *Phys. Rev. B*, 82(20):205211 (1–6), 2010.

[72] B. H. Bransden and C. J. Joachain. *Physics of atoms and molecules*. Longman Scientific & Technical and John Wiley & Sons., 1983.

[73] A. E. Cohen. Nanomagnetic control of intersystem crossing. *J. Phys. Chem. A*, 113(41):11084–11092, 2009.

[74] R. Kaptein. Chemically induced dynamic nuclear polarization. VIII. spin dynamics and diffusion of radical pairs. *J. Am. Chem. Soc.*, 94(18):6251–6262, 1972.

[75] R. Kaptein and D. Hollander. Chemically induced dynamic nuclear polarization. X. magnetic field dependence. *J. Am. Chem. Soc.*, 94(18):6269–6280, 1972.

[76] Z. G. Yu. Spin-orbit coupling and its effects in organic solids. *Phys. Rev. B*, 85(11):115201 (1–18), 2012.

[77] J. Behrends, A. Sperlich, A. Schnegg, T. Biskup, C. Teuloff, K. Lips, V. Dyakonov, and R. Bittl. Direct detection of photoinduced charge transfer complexes in polymer fullerene blends. *Phys. Rev. B*, 85(12):125206 (1–6), 2012.

[78] J. Niklas, S. Beaupré, M. Leclerc, T. Xu, L. Yu, A. Sperlich, V. Dyakonov, and O. G. Poluektov. Photoinduced dynamics of charge separation: from photosynthesis to polymerfullerene bulk heterojunctions. *J. Phys. Chem. B*, 119(24):7407–7416, 2015.

[79] S. D. Dimitrov, B. Schroeder, C. B. Nielsen, H. Bronstein, Z. Fei, I. McCulloch, M. Heeney, and J. Durrant. Singlet exciton lifetimes in conjugated polymer films for organic solar cells. *Polymers*, 8(1):14 (1–12), 2016.

[80] A. L. Buchachenko. Magnetic effects in chemical reactions. *Russ. Chem. Rev.*, 45(5):375–390, 1976.

[81] P. W. Atkins and T. P. Lambert. The effect of magnetic fields on chemical reactions. *Annu. Rep. Prog. Chem. Sect. A*, 72:67–88, 1975.

[82] A. Köhler and D. Beljonne. The singlettriplet exchange energy in conjugated polymers. *Adv. Funct. Mater.*, 14(1):11–18, 2004.

[83] N. J. Turro. *Modern Molecular Photochemistry*. University Science Books, Sausalito, CA, USA, 1991.

[84] R. P. Groff, R. E. Merrifield, A. Suna, and P. Avakian. Magnetic hyperfine modulation of dye-sensitized delayed fluorescence in organic crystal. *Phys. Rev. Lett.*, 29(12-18):823–825, 1972.

[85] K. Schulten and P. G. Wolynes. Semiclassical description of electron spin motion in radicals including the effect of electron hopping. *J. Chem. Phys.*, 68(7):3292–3297, 1978.

[86] S. Cook, A. Furube, and R. Katoh. Analysis of the excited states of regioregular polythiophene P3HT. *Energy Environ. Sci.*, 1(2):294–299, 2008.

[87] M. Tolan. *X-Ray Scattering from Soft-Matter Thin Films*, volume 148. Springer Berlin Heidelberg, 1999.

[88] J. Als-Nielsen and D. McMorrow. *Elements of Modern X-ray Physics*. John Wiley & Sons, Ltd., 2nd edition, 2011.

[89] M. Kotlarkchyk and S.-H. Chen. Analysis of small angle neutron scattering spectra from polydisperse interacting colloids. *J. Chem. Phys.*, 79(5):2461–2469, 1983.

[90] D. G. Greene, D. V. Ferraro, A. M. Lenhoff, and N. J. Wagner. A critical examination of the decoupling approximation for small-angle scattering from hard ellipsoids of revolution. *J. Appl. Cryst.*, 49:1734–1739, 2016.

[91] N. W. Ashcroft and N. D. Mermin. *Solid state physics*. Saunders College, Fort Worth, 1988.

[92] E. Burkel. Introduction to x-ray scattering. *J. Phys. Condens. Matter*, 13:7477–7498, 2001.

[93] A. Guinier. *X-ray Diffraction in Crystals, Imperfect Crystals, and Amorphous Bodies*. Dover Publications, Inc., 1994.

[94] P. Müller-Buschbaum. *Polymer Surfaces and Interfaces: Characterization, Modification and Applications*. Polymer Surfaces and Interfaces: Characterization, Modification and Applications., 2008.

[95] H. Kiessig. Interferenz von Röntgenstrahlen an dünnen Schichten. *Annalen der Physik*, 402(7):769–788, 1931.

[96] L. G. Parrat. Surface studies of solids by total reflection of x-rays. *Physical Review*, 95(2):359–369, 1954.

[97] L. Nevot and P. Croce. Caractérisation des surfaces par réflexion rasante des rayons x. application à l'étude du polissage de quelques verres silicates. *Revue de Physique Appliquée*, 15(3):761–779, 1980.

[98] P. Müller-Buschbaum. *A basic introduction to grazing incidence small angle X-ray scattering*. Springer, Berlin, 2009.

[99] A. Hexemer and P. Müller-Buschbaum. Advanced grazing-incidence techniques for modern soft-matter materials analysis. *IUCrJ.*, 2(1):106–125, 2015.

[100] P. Müller-Buschbaum. Grazing incidence small-angle x-ray scattering: an advanced scattering technique for the investigation of nanostructured polymer films. *Anal. Bionanal. Chem.*, 376(1):3–10, 2003.

[101] Y. Yoneda. Anomalous surface reflection of x rays. *Phys. Rev.*, 131(5):2010–2013, 1963.

[102] G. Renaud, R. Lazzari, and F. Leroy. Probing surface and interface morphology with grazing incidence small angle x-ray scattering. *Surf. Sci. Rep.*, 64(8):255–380, 2009.

[103] R. Lazzari. IsGISAXS: a program for grazing-incidence small-angle x-ray scattering analysis of supported islands. *J. Appl. Crystallogr.*, 35(4):406–421, 2002.

[104] R. Hosemann, W. Vogel, D. Wieck, and F. J. Baltá-Calleja. Novel aspects of the real paracrystal. *Acta Crystallogr. Sect. A*, 37(1):85–91, 1981.

[105] j. L. Baker, L. H. Jimison, S. Mannsfeld, S. Volkman, S. Yin, V. Subramanian, A. Salleo, A. P. Alivisatos, and M. F. Toney. Quantification of thin film crystallographic orientation using x-ray diffraction with an area detector. *Langmuir*, 26(11):9146–9151, 2010.

[106] Z. Jiang. Gixsgui: a matlab toolbox for grazing-incidence x-ray scattering data visualization and reduction, and indexing of buried three-dimensional periodic nanostructured film. *J. Appl. Crystallogr.*, 48(3):917–926, 2015.

[107] Z. Jiang. *Documentation for GIXSGUI - 1.6.1.*

[108] P. Müller-Buschbaum. The active layer morphology of organic solar cells probed with grazing incidence scattering techniques. *Adv. Mater.*, 26(46):7692–7709, 2014.

[109] A. Buffet, A. Rothkirch, R. Döhrmann, V. Körstgens, M. M. A. Kashem, J. Perlich, G. Herzog, M. Schwarzkopf, R. Gehrke, P. Müller-Buschbaum, and S. V. Roth. P03, the microfocus and nanofocus x-ray scattering (MiNaXS) beamline of the petra III storage ring: the microfocus endstation. *J. Synchrotron Rad.*, 19:647–653, 2012.

[110] G. Santoro, R. Buffet, A. abd Döhrmann, S. Yu, V. Körstgens, P. Müller-Buschbaum, U. Gedde, M. Hedenqvist, and S. V. Roth. Use of intermediate focus for grazing incidence small and wide angle x-ray scattering experiments at the beamline P03 of petra III, DESY. *Rev. Sci. Instrum.*, 84(4):043901 (1–9), 2014.

[111] G. Benecke, W. Wagermaier, C. Li, M. Schwartzkopf, G. Flucke, R. Hoerth, I. Zizak, M. Burghammer, E. Metwalli, P. Müller-Buschbaum, M. Trebbin, S. Förster, O. Paris, S. V. Roth, and P. Fratzl. A customizable software for fast reduction and analysis of large x-ray scattering data sets: applications of the new DPDAK package to small-angle x-ray scattering and grazing-incidence small-angle x-ray scattering. *J. Appl. Cryst.*, 47:1797–1803, 2014.

[112] J. Perlich, J. Rubeck, S. Botte, R. Gehrke, S. V. Roth, M. A. Ruderer, S. M. Prams, M. Rawolle, Q. Zhong, V. Körstgens, and P. Müller-Buschbaum. Grazing incidence wide angle x-ray scattering at the wiggler beamline BW4 of HASYLAB. *Rev. Sci. Instrum.*, 81:105105, 2010.

[113] http://www.genplot.com, January 2017.

[114] M. Kira, F. Jahnke, S. W. Koch, J. Berger, D. Wick, T. Nelson, G. Khitrova, and H. Gibbs. Quantum theory of nonlinear semiconductor microcavity luminescence explaining "boser" experiments. *Phys. Rev. Lett.*, 79(25):5170–5173, 1997.

[115] M. Kira and S. W. Koch. *Semiconductor Quantum Optics.* Cambridge University Press, 2011.

[116] S. Alexander, C. Laermans, R. Orbach, and H. M. Rosenberg. Fracton interpretation of vibrational properties of cross-linked polymers, glass and irradiated quartz. *Phys. Rev. B*, 28(8):4615–4619, 1983.

[117] F. Dreher. Enhancing triplet exciton population in organic solar cells. Master's thesis, Technical University of Munich, 2016.

[118] Y. H. Kim, C. Sachse, M. L. Machala, C. May, L. Müller-Meskamp, and K. Leo. Highly conductive PEDOT:PSS electrode with optimized solvent and thermal post-treatment for ITO-free organic solar cells. *Adv. Funct. Mater.*, 21(6):1076–1081, 2011.

[119] M. Vosgueritchian, D. J. Lipomi, and Z. Bao. Highly conductive and transparent PEDOT:PSS films with a fluorosurfactant for stretchable and flexible transparent electrodes. *Adv. Funct. Mater.*, 22(2):421–428, 2012.

[120] G. He, L. Kang, W. Torres Delgado, O. Shynkaruk, M. J. Ferguson, R. McDonald, and E. Rivard. The marriage of metallacycle transfer chemistry with SuzukiMiyaura cross-coupling to give main group element-containing conjugated polymers. *J. Am. Chem. Soc.*, 135(14):5360–5363, 2013.

[121] http://www.chem.ualberta.ca/∼ erivard/index.html, March 2017.

[122] S. G. Kwon, Y. Piao, J. Park, S. Angappane, N. M. Jo, Y. andHwang, J. G. Park, and T. Hyeon. Kinetics of monodisperse iron oxide nanocrystal formation by heating-up process. *J. Am. Chem. Soc.*, 129(41):12571–12584, 2007.

[123] S. Sun and H. Zeng. Size-controlled synthesis of magnetite nanoparticles. *J. Am. Chem. Soc.*, 124:8204–8205, 2002.

[124] P. Müller-Buschbaum. influence of surface cleaning on dewetting of thin polystyrene film. *Eur. Phys. J. E Soft Matter*, 12(3):443–448, 2003.

[125] D. W. Schubert and T. Dunkel. Spin coating from a molecular point of view: its concentration regimes, influence of molar mass and distribution. *Materials Research Innovations*, 7(5):314–321, 2003.

[126] R. P. Meier. *Novel Structuring Routines for Organic Photovoltaics*. PhD thesis, Technical University of Munich, 2012.

[127] D. E. Motaung, G. F. Malgas, and C. J. Arendse. Insights into the stability and thermal degradation of P3HT:C60 blended films for solar cell applications. *J. Mater. Sci.*, 46(14):4942–4952, 2011.

[128] T. M. Clarke, A. M. Balantyne, J. Nelson, D. D. C. Bradley, and J. R. Durrant. Free energy control of charge photogeneration in polythiophene/fullerene solar cells: the influence of thermal annealing on p3ht/pcbm blends. *Adv. Funct. Mater.*, 18(24):4029–4035, 2008.

[129] Y. Kim, S. A. Choulis, J. Nelson, D. D. C. Bradley, S. Cook, and J. R. Durrant. Device annealing effect in organic solar cells with blends of regioregular poly(3-hexylthiophene) and soluble fullerene. *Appl. Phys. Lett.*, 86(6):63502, 2005.

[130] `http://www.pv-tech.org/news/verified_heliatek_organic_solar_cell_achieves_record_12_conversion_efficien`, May 2014.

[131] G. Yu, J. Gao, J. C. Hummelen, F. Wudl, and A. J. Heeger. Polymer photovoltaic cells: enhanced eficiencies via a network of internal donor-acceptor heterojunctions. *Science*, 270:1789–1791, 1995.

[132] S. E. Shaheen, C. J. Brabec, Sariciftci N. S., F. Padinger, Fromherz T., and J. C. Hummelen. 2.5 *Appl. Phys. Lett.*, 78(6):841–843, 2001.

[133] P. E. Shaw, A. Ruseckas, and I. D. W. Samuel. Exciton diffusion measurements in poly(3-hexylthiophene)). *Adv. Mater.*, 20(18):3516–3520, 2008.

[134] W. Chen, M. P. Nikiforov, and S. B. Darling. Morphology characterization in organic and hybrid solar cells. *Energy Environ. Sci.*, 5(8):8045–8074, 2012.

[135] M. A. Ruderer, S. Guo, R. P. Meier, H.-Y. Chiang, V. Körstgens, J. Wiedersich, J. Perlich, S. V. Roth, and P. Müller-Buschbaum. Solvent-induced morphology in polymer-based systems for organic photovoltaics. *Adv. Funct. Mater.*, 21(17):3382–3391, 2011.

[136] K. Sarkar, C. J. Schaffer, D. Moseguí González, A. Naumann, J. Perlich, and P. Müller-Buschbaum. Tuning pore size of ZnO nano-grids via time-dependent solvent annealing. *J. Mater. Chem. A*, 2(19):6945–6951, 2014.

[137] W. Ma, C. Yang, X. Gong, K. Lee, and A. J. Heeger. Thermally stable, efficient polymer solar cells with nanoscale control of the interpenetrating network morphology. *Adv. Funct. Mater.*, 15(10):1617–1622, 2005.

[138] F. Padinger, R. S. Rittberger, and Sariciftci N. S. Effects of postproduction treatment on plastic solar cells. *Adv. Funct. Mater.*, 13(1):85–88, 2003.

[139] D. Spoltore, W. D. Oosterbaan, S. Khelifi, J. N. Clifford, A. Viterisi, E. Palomares, M. Burgelman, L. Lutsen, D. Vanderzande, and J. Manca. Effect of polymer crystallinity in P3HT:PCBM solar cells on band gap trap states and apparent recombination order. *Adv. Energy Mater.*, 3(4):466–471, 2013.

[140] R. P. Meier, C. Birkenstock, C. M. Palumbiny, and P. Müller-Buschbaum. Efficiency-improved organic solar cells based on plasticizer assisted soft embossed pedot:pss layers. *Phys. Chem. Chem. Phys.*, 14(43):15088–15098, 2012.

[141] B. P. Rand, C. Girotto, A. Mityashin, A. Hadlpour, J. Genoe, and P. Heremans. Photocurrent enhancement in polymer:fullerene bulk heterojunction solar cells doped with a phosphorescent molecule. *Appl. Phys. Lett.*, 95(17):173304 (1–3), 2009.

[142] Y. Zhang, T. P. Basel, B. R. Gautam, X. Yang, D. J. Mascaro, F. Liu, and Z. V. Vardeny. Spin-enhanced organic bulk heterojunction photovoltaic solar cells. *Nat. Commun.*, 3(1043):1–7, 2012.

[143] E. P. Yao, Y. J. Tsai, and W. C. Hsu. Investigation of organic photovoltaics improvement via extension of exciton lifeime. *Phys. Chem. Chem. Phys.*, 17(8):5826–5831, 2015.

[144] S. M. Parke, M. P. Boone, and E. Rivard. Marriage of heavy main group elements with π-conjugated materials for optoelectronic applications. *Chem. Commun.*, 52(61):9485–9505, 2016.

[145] Hartmut Yersin. *Triplet Emitters for OLED Applications. Mechanisms of Exciton Trapping and Control of Emission Properties*, pages 1–26. Springer Berlin Heidelberg, Berlin, Heidelberg, 2004.

[146] M. Heeney, W. Zhang, D. J. Crouch, M. L. Chabinyc, R. Higgins S. J. Gordeyev, S. Hamilton, I. McCulloch, P. J. Skabara, D. Sparrowe, and S. Tierney. Regioregular poly(3-hexyl)selenophene: a low band gap organic hole transporting polymer. *Chem. Commun.*, (47):5061–5063, 2007.

[147] A. Patra, Y. H. Wijisboom, S. S. Zade, M. Li, Y. Shenyin, G. Leitus, and M. Bendikov. Poly(3,4-ethylenedioxyselenophene). *J. Am. Chem. Soc.*, 130(21):6734–6736, 2008.

[148] A. Patra and M. Bendikov. Polyselenophenes. *J. Mater. Chem.*, 20(3):422–433, 2010.

[149] H. Yersin. Organometallic triplet emitters for oled applications. controlling of emission properties by chemical variation. *Proc. SPIE*, 5214:124–132, 2004.

[150] H. Yersin, A. F. Rausch, R. Czerwieniec, T. Hofbeck, and T. Fischer. The triplet state of organo-transition metal compounds. triplet harvesting and singlet harvesting for efficient oleds. *Coord. Chem. Rev.*, 255(21-22):2622–2652, 2011.

[151] M. A. Baldo, D. F. O'Brien, Y. You, A. Shoustikov, S. Sibley, M. E. Thompson, and S. R. Forrest. Highly efficient phosphorescent emission from organic electroluminescent devices. *Nature*, 395:151–154, 1998.

[152] V. Cleave, G. Yahioglu, P. Le Barny, R. H. Friend, and N. Tessler. Harvesting singlet and triplet energy in polymer leds. *Adv. Mater.*, 11(4):285–288, 1999.

[153] P. C. Srivastava, S. Bajpai, S. Bajpai, C. Ram, R. Kumar, J. P. Jasinski, and R. J. Butcher. Telluranes: potential synthons for charge-transfer complexes (involving hypervalent tei bonds) and serendipitous synthesis of the first triphenyl methyl phosphonium salts containing $[C_4H_8TeI_4]^{2-}$ and $[TeI_6]^{2-}$ anions. *J. Organomet. Chem.*, 689(1):194–202, 2004.

[154] A. A. Jahnke, G. W. Howe, and D. S. Seferos. Polytellurophenes with properties controlled by tellurium-coordination. *Angew. Chem. Int. Ed.*, 49(52):10140–10144, 2010.

[155] T. M. McCormick, A. A. Jahnke, J. Lough, and D. S. Seferos. Tellurophenes with delocalized π-systems and their extended valence adducts. *J. Am. Chem. Soc.*, 134(7):3542–3548, 2012.

[156] J. Tauc, R. Grigorovici, and A. Vancu. Optical properties and electronic structure of amorphous germanium. *Phys. Stat. Sol.*, 15(2):627–637, 1966.

[157] O. Stenzel. *The physics of thin film optical spectra*, volume 44 of *Springer series in surface sciences*. Springer International Publishing, 2016.

[158] J. Tauc. Optical properties and electronic structure of amorphous Ge and Si. *Mat. Res. Bull.*, 3(1):37–46, 1968.

[159] E. I. Carrera and D. S. Seferos. Semiconducting polymers containing tellurium: perspectives toward obtaining high-performance materials. *Macromolecules*, 48(2):297–308, 2015.

[160] A. A. Jahnke, B. Djukic, T. M. McCormick, E. Buchaca Domingo, C. Hellmann, Y. Lee, and D. S. Seferos. Poly(3-alkyltellurophene)s are solution-processable polyheterocycle. *J. Am. Chem. Soc.*, 135(3):951–954, 2013.

[161] A. A. Jahnke and D. S. Seferos. Polytellurophenes. *Macromol. Rapid Commun.*, 32(13):943–951, 2011.

[162] A. K. Rappé, C. J. Casewit, K. S. Colwell, W. A. Goddard III, and W. M. Skiff. UFF, a full periodic table force field for molecular mechanics and molecular dynamics simulations. *J. Am. Chem. Soc.*, 114(25):10024–10035, 1992.

[163] A. A. Jahnke. *Polytellurophenes as solution processable materials for applications in organic electronics*. PhD thesis, Department of Chemistry. University of Toronto, 2014.

[164] S. Ye, M. Steube, E. I. Carrera, and D. S. Seferos. What limits the molecular weight and controlled synthesis of poly(3-alkyltellurophene)s? *Macromolecules*, 49(5):1704–1711, 2016.

[165] Sungmo Ahn, Devin Rourke, and Wounjhang Park. Plasmonic nanostructures for organic photovoltaic devices. *Journal of Optics*, 18(3):033001, 2016.

[166] R. Vogel, P. Hoyer, and H. Weller. Quantum-sized PbS, CdS, Ag_2S, Sb_2S_3, and Bi_2S_3 particles as sensitizers for various nanoporous wide-bandgap semiconductors. *J. Phys. Chem.*, 98(12):3183–3188, 1994.

[167] A. P. Alivisatos. Semiconductor clusters, nanocrystals, and quantum dots. *Science*, 271(5251):933–937, 1996.

[168] M.-H. Park, J.-H. Li, A. Kumar, G. Li, and Y. Yang. Doping of the metal oxide nanostructure and its influence in organic electronics. *Advanced Functional Materials*, 19(8):1241–1246, 2009.

[169] W. Zhang, Y. Xu, H. Wang, C. Xu, and S. Yang. Fe_3O_4 nanoparticles induced magnetic field effect on efficiency enhancement of P3HT:PCBM bulk heterojunction polymer solar cells. *Sol. Energy Mater. Sol. Cells*, 95(10):2880–2885, 2011.

[170] J. Jaramillo, B. W. Boudouris, C. A. Barrero, and F. Jaramillo. Design of superparamagnetic coreshell nanoparticles for enhanced performance of inverted polymer solar cells. *ACS Appl. Mater. Interfaces*, 7(45):25061–25068, 2015.

[171] M. A. Ruderer, R. P. Meier, L. Porcar, R. Cubitt, and P. Müller-Buschbaum. Phase separation and molecular intermixing in polymer-fullerene bulk heterojunction thin films. *J. Phys. Chem. Lett.*, 3(6):683–688, 2012.

[172] N. N. Greenwood and A. Earnshaw. *Chemistry of the Elements*. Butterworth-Heinemann , Oxford, UK, 2nd edition, 1997.

[173] Y. S. Kim, S. M. Lee, P. Govindaiah, S. J. Lee, S. H. Lee, J. H. Kim, and J. W. Cheong. Multifunctional Fe_3O_4 nanoparticles-embedded poly(styrene)/poly(thiophene) core/shell composite particles. *Synth. Met.*, 175:56–61, 2013.

[174] B. Qi and J. Wang. Fill factor in organic solar cells. *Phys. Chem. Chem. Phys.*, 15(23):8972–8982, 2013.

[175] Y. Yao, E. Metwalli, M. A. Niedermeier, M. Opel, C. Lin, J. Ning, J. Perlich, S. V. Roth, and P. Müller-Buschbaum. Nano- and microstructures of magnetic field-guided maghemite nanoparticles in diblock copolymer films. *Appl. Mater. Interfaces*, 6(7):5244–5254, 2014.

[176] Y. Lin, A. Böker, J. He, K. Sill, H. Xiang, C. Abetz, X. Li, J. Wang, T. Emrick, S. Long, Q. Wang, A. Balazs, and T. Russell. Self-directed self-assembly of nanoparticle/copolymer mixtures. *Nature*, 434(7029):55–59, 2005.

[177] Y. Zhang, X.-D. Dang, C. Kim, and Nguyen T.-Q. Effect of charge recombination on the fill factor of small molecule bulk heterojunction solar cells. *Adv. Energy Mater.*, 1(4):610–617, 2011.

[178] H. Sternlicht, G. C. Nieman, and G. W. Robinson. Triplet-triplet annihilation and delayed fluorescence in molecular aggregates. *J. Chem. Phys.*, 38(6):1326–1335, 1963.

[179] K. Murawski, K. Leo, and M. C. Gather. Efficiency roll-off in organic light-emitting diodes. *Adv. Mater.*, 25(47):6801–6827, 2013.

[180] B. H. Wallikewitz, D. Kabra, S. Gélinas, and R. H. Friend. Triplet dynamics in fluorescent polymer light-emitting diodes. *Phys. Rev. B*, 85(4):045209 (1–15), 2012.

[181] A. Salleo. Charge transport in polymeric transistors. *Mater. Today*, 10(3):38–45, 2007.

[182] Z. Masri, A. Ruseckas, E. V. Emelianova, L. Wang, A. K. Bansal, A. Matheson, H. T. Lemke, M. M. Nielsen, H. Nguyen, O. Coulembier, P. Dubois, D. Beljonne, and I. D. W. Samuel. Molecular weight dependence of exciton diffusion in poly(3-hexylthiophene). *Adv. Energy Mater.*, 3(11):1445–1453, 2013.

[183] G. Zhao, Y. He, and Y. Li. 6.5% efficiency of polymer solar cells based on poly(3-hexylthiophene) and indene-C_{60} bisadduct by device optimization. *Adv. Mater.*, 22(39):4355–4358, 2010.

[184] B. C. Thompson and J. M. J. Fréchet. Polymer-fullerne composite solar cells. *Angew. Chem., Int. Ed.*, 47(1):58–77, 2008.

[185] http://www.sigmaaldrich.com/graphics/cofainfo/sigmasapqm/spec/70/700312/700312-bulk_____aldrich__.pdf, March 2017.

[186] G. F. Goya, T. S. Berquó, and F. C. Fonseca. Static and dynamic magnetic properties of spherical magnetite nanoparticles. *J. Appl. Phys.*, 94(5):3520–3528, 2003.

[187] Y. Wei, B. Han, X. Hu, Y. Lin, X. Wang, and X. Deng. Synthesis of Fe_3O_4 nanoparticles and their magnetic properties. *Procedia Eng.*, 27:632–637, 2012.

[188] http://lqm.epfl.ch/page-79032-en.html, March 2017.

[189] S. D. Collins, C. M. Proctor, N. A. Ran, and T.-Q. Nguyen. Understanding open-circuit voltage loss through the density of states in organic bulk heterojunction solar cells. *Adv. Energ. Mater.*, 6(4):1501721 (1–11), 2016.

[190] G. García-Belmonte and J. Bisquert. Open-circuit voltage limit caused by recombination through tail states in bulk heterojunction polymer-fullerene solar cells. *Appl. Phys. Lett.*, 96(11):113301 (1–3), 2010.

[191] J. Kong, S. Song, M. Yoo, G. Y. Lee, O. Kwon, J. K. Park, H. Back, G. Kim, S. H. Lee, H. Suh, and K. Lee. Long-term stable polymer solar cells with significantly reduced burn-in loss. *Nat. Commun.*, 5(5688):1–8, 2014.

[192] M. O. Reese, A. J. Morfa, M. S. White, N. Kopidakis, S. E. Shaheen, G. Rumbles, and D. S. Ginley. Pathways for the degradation of organic photovoltaic P3HT:PCBM based devices. *Sol. Energy Mater. Sol. Cells*, 92(7):746–752, 2008.

[193] M. O. Reese, S. A. Gevogyan, M. Jørgensen, E. Bundgaard, S. R. Kurtz, D. S. Ginley, D. C. Olson, M. T. Lloyd, P. Morvillo, E. A. Katz, A. Elscher, O. Haillant, T. R. Currier, V. Shrotriya, M. Hermenau, M. Riede, K. R. Kirov, G. Trimmel, T. Rath, O. Inganäs, F. Zhang, M. Andersson, K. Tvingstedt, M. Lira-Cantu, D. Laird, C. McGuiness, S. Gowrisanker, M. Pannone, M. Xiao, J. Hauch, R. Steim, D. M. DeLongchamp, R. Rösch, H. Hoppe, N. Espinosa, A. Urbina, G. Yaman-Uzunoglu, J.-B. Bonekamp, A. J. J. M. van Breemen, C. Girotto, E. Voroshazi, and F. C. Krebs. Consensus stability testing protocols for organic photovoltaic materials and devices. *Sol. Energy Mater. Sol. Cells*, 95(5):1253–1267, 2011.

[194] R. Rösch, T. Faber, E. von Hauff, T. M. Brown, M. Lira-Cantu, and H. Hoppe. Procedures and practices forevaluating thin-film solar cell stability. *Adv. Energ. Mater.*, 5(1501407):1–24, 2015.

[195] C. H. Peters, I. T. Sachs-Quintana, J. P. Kastrop, S. Beaupré, M. Leclerc, and M. D. McGehee. High efficiency polymer solar cells with long operating lifetimes. *Adv. Energ. Mater.*, 1(4):491–494, 2011.

[196] A. Sperlich, H. Kraus, D. Deibel, H. Blok, J. Schmidt, and V. Dyakonov. Reversible and irreversible interactions of poly(3-hexylthiophene) with oxygen studied by spin-sensitive methods. *J. Phys. Chem. B*, 115(46):13513–13518, 2011.

[197] K. Kawaoka, A. U. Khan, and D. R. Kearns. Role of singlet excited states of molecular oxygen in the quenching of organic triplet states. *J. Phys. Chem.*, 46(5):1842–1853, 1967.

[198] B. Xu and S. Holdcroft. First observation of phosphorescence from pi.-conjugated polymers. *J. Am. Chem. Soc.*, 115(18):8447–8448, 1993.

[199] V. Wintgens, P. Valat, and F. Garnier. Photochemical generation of radical cations from thiophene oligomers. *J. Phys. Chem.*, 98(1):228–232, 1994.

[200] B. Paci, A. Generosi, V. R. Albertini, C. D. Spyropoulos, E. Stratakis, and E. Kymakis. Enhancement of photo/thermal stability of organic bulk heterojunction photovoltaic devices via gold nanoparticles doping of the active layer. *Nanoscale*, 4:7452–7459, 2012.

[201] Yang Shen, Louis Scudiero, and Mool C. Gupta. Temperature dependence of homo-lumo levels and open circuit voltage for p3ht:pcbm organic solar cells. *MRS Proceedings*, 1360:1–4, 2011.

[202] M. C. Scharber, D. Mühlbacher, M. Koppe, P. Denk, C. Waldauf, A. J. Heeger, and C. J. Brabec. Design rules for donors in bulk-heterojunction solar cells - towards 10% energy-conversion efficiency. *Adv. Mater.*, 18(6):789–794, 2006.

[203] J. D. Zimmerman, X. Xiao, C. K. Renshaw, S. Wang, V. V. Diev, M. E. Thompson, and S. R. Forrest. Independent control of bulk and interfacial morphologies of small molecular weight organic heterojunction solar cells. *Nano Lett.*, 12(8):4366–4371, 2012.

[204] P. Vanlaeke, A. Swinnen, I. Haeldermans, G. Vanhoyland, T. Aernouts, D. Cheyns, C. Deibel, J. D'Haen, P. Heremans, J. Poortmans, and J. V. Manca. P3HT/PCBM bulk heterojunction solar cells: relation between morphology and electro-optical characteristics. *Sol. Energy Mater. Sol. Cells*, 90(14):2150–2158, 2006.

[205] K. Vandewal, K. Tvingstedt, A. Gadisa, O. Inganäs, and J. Manca. On the origin of the open-circuit voltage of polymer-fullerene solar cells. *Nat. Mater.*, 8(11):904–909, 2009.

[206] K. Vandewal, W. D. Oosterbaan, S. Bertho, V. Vrindts, A. Gadisa, L. Lutsen, D. Vanderzande, and J. Manca. Varying polymer crystallinity in nanofiber poly(3-alkylthiophene):PCBM solar cells: influence on charge-transfer state energy and open-circuit voltage. *Appl. Phys. Lett.*, 95(12):123303, 2009.

[207] A. Foertig, A. Wagenpfahl, T. Gerbich, D. Cheyns, V. Dyakonov, and C. Deibel. Nongeminate recombination in planar and bulk heterojunction organic solar cells. *Adv. Energ. Mater.*, 2(12):1483–1489, 2012.

[208] G. García-Belmonte, P. P. Boix, J. Bisquert, M. Sessolo, and H. J. Bolink. Simultaneous determination of carrier lifetime and electron density-of-states in P3HT:PCBM organic solar cells under illumination by impedance spectroscopy. *Sol. Energy Mater. Sol. Cells*, 94(2):366–375, 2010.

[209] C. G. Shuttle, N. D. Treat, J. D. Douglas, J. M. J. Freéchet, and M. L. Chabinyc. Deep energetic trap states in organic photovoltaic devices. *Adv. Energ. Mater.*, 2(1):111–119, 2012.

[210] F. C. Spano. Absorption in regio-regular poly(3-hexyl)-thiophene thin films: Fermi resonances, interband coupling and disorder. *Chem. Phys.*, 325(1):22–35, 2006.

[211] M. D. Perez, C. Borek, S. R. Forrest, and M. E. Thompson. Molecular and mophological influences on the open circuit voltages of organic photovoltaic devices. *J. Am. Chem. Soc.*, 131(26):9281–9286, 2009.

[212] D. Credgington, R. Hamilton, P. Atienzar, J. Nelson, and J. R. Durrant. Nongeminate recombination as the primary determinant of open-circuit voltage in polythiophene:fullerene blend solar cells: an analysis of the influence of device processing conditions. *Adv. Funct. Mater.*, 21(14):2744–2753, 2011.

[213] S. Bertho, G. Janssen, T. J. Cleij, B. Conings, W. Moons, A. Gadisa, J. DHaen, E. Goovaerts, L. Lutsen, J. Manca, and D. Vanderzale. Effect of temperature on the morphological and photovoltaic stability of bulk heterojunction polymer:fullerene solar cells. *Sol. Energy Mater. Sol. Cells*, 92(7):753–760, 2008.

[214] E. Verploegen, C. E. Miller, K. Schmidt, Z. Bao, and M. F. Toney. Manipulating the morphology of the P3HT-PCBM bulk heterojunction blends with solvent vapor annealing. *Chem. Mater.*, 24:3923–3931, 2012.

[215] F. Deschler, A. De Sio, E. von Hauff, P. Kutka, T. Sauermann, H.-J. Egelhaaf, J. Hauch, and E. Da Como. The effect of ageing on exciton dynamics, charge separation, and recombination in P3HT/ PCBM photovoltaic blends. *Adv. Funct. Mater.*, 22(7):1461–1469, 2012.

[216] V. N. Prigodin and A. J. Epstein. Resonance quantum transport in doped conducting polymers: the improbable becomes possible. *Europhys. Lett.*, 60(5):750–756, 2002.

[217] L. H. Nguyen, H. Hoppe, T. Erb, S. Günes, G. Gobsch, and N. S. Sariciftci. Effects of annealing on the nanomorphology and performance of poly(alkylthiophene):fullerene bulk-heterojunction solar cells. *Adv. Funct. Mater.*, 17(7):1071–1078, 2007.

[218] Y. Gao, T. P. Martin, E. T. Niles, A. J. Wise, A. K. Thomas, and J. K. Grey. Understanding morphology-dependent polymer aggregation properties and photocurrent generation in polythiophene/ fullerene solar cells of variable compositions. *J. Phys. Chem. C*, 114(35):15121–15128, 2010.

[219] J. Clark, C. Silva, R. H. Friend, and F. Spano. Role of intermolecular coupling in the photophysics of disordered organic semiconductors: aggregate emission in regioregular polythiophene. *Phys. Rev. Lett.*, 98(20):206406, 2007.

[220] Z. M. Beiley, E. T. Hoke, R. Noriega, J. Dacuña, G. F. Burkhard, J. A. Bartelt, A. Salleo, M. F. Toney, and M. D. McGehee. Morphology-dependent trap formation in high performance polymer bulk heterojunction solar cells. *Adv. Energ. Mater.*, 1(5):954–962, 2011.

[221] S. Agbolaghi, F. Abbasi, and H. Gheybi. High efficient and stabilized photovoltaics via morphology manipulating in active layer by rod-coil block copolymers comprising different hydrophilic to hydrophobic dielectric blocks. *Eur. Polym. J.*, 84:465–480, 2016.

[222] https://upload.wikimedia.org/wikipedia/commons/8/8d/helmholtz_coils.png, March 2017.

List of publications

Publications related to this dissertation

- D. Moseguí González, K. N. Raftopoulos, G. He, C. Papadakis, A. Brown, E. Rivard, P. Müller-Buschbaum. *Bandgap-tuning in triple-chalcogenophene polymer films by thermal annealing.* Macromolecular Rapid Communications 38(11), 1700065 (2017). DOI: 10.1002/marc.20170065.

    - *Associated front cover:* D. Moseguí González, K. N. Raftopoulos, G. He, C. Papadakis, A. Brown, E. Rivard, P. Müller-BUschbaum. *Bandgap-tuning in triple-chalcogenophene polymer films by thermal annealing.* Macromolecular Rapid Communications 11/2017. DOI: 10.1002/marc.201770037.

- D. Moseguí González, S. Pröller, J. Schlipf, L. Song, S. Bernstorff, E. M. Herzig, P. Müller-Buschbaum. *Evidence of co-dependence between crystalline evolution and device performance in P3HT:PCBM solar cells characterized with in-operando GI-WAXS.* ACS Applied Materials & Interfaces 9, 3282-3287 (2017). DOI: 10.1021/acsami.6b15661.

- D. Moseguí González, V. Körstgens, Y. Yao, L. Song, G. Santoro, S. V. Roth, P. Müller-Buschbaum. *Improved power conversion efficiency of P3HT:PCBM organic solar cells by strong spin-orbit coupling-induced delayed fluorescence.* Advanced Energy Materials 5(8), 1401770 (2015). DOI: 10.1002/aenm.201401770.

    - *Associated front cover:* D. Moseguí González, V. Körstgens, Y. Yao, L. Song, G. Santoro, S. V. Roth, P. Müller-Buschbaum. *Improved power conversion efficiency of P3HT:PCBM organic solar cells by strong spin-orbit coupling-induced delayed fluorescence.* Advanced Energy Materials 08/2015. DOI: 10.1002/aenm.201570040.

Further publications

- S. Pröller, D. Moseguí González, C. Zhu, E. Schaible, C. Wang, P. Müller-Buschbaum, A. Hexemer, E. M. Herzig. *Note: Setup for chemical atmospheric control during in situ grazing incidence x-ray scattering of printed thin films.* Review of Scientific Instruments 88(6), 066101 (2017). DOI: 10.1063/1.4984130.

- L. Song, W. Wang, S. Pröller, D. Moseguí González, J. Schlipf, C. J. Schaffer, K. Peters, E. M. Herzig, S. Bernstorff, T. Bein, D. Fattakhova-Rohlfing, P. Müller-Buschbaum. *In situ study of degradation in P3HT-titania-based solid-state dye-sensitized solar cells.* ACS Energy Letters 2(5), 991-997 (2017). DOI: 10.1021/acsenergylett.7b00117.

- J. Cui, Á. Rodríguez-Rodríguez, M. Hernández, M.-C. García Gutiérrez, A. Nogales, M. Castillejo, D. Moseguí González, P. Müller-Buschbaum, T. A. Ezquerra, E. Rebollar. *On the laser-induced periodic structures of P3HT and of its photovoltaic blend with $PC_{71}BM$.* ACS Applied Materials & Interfaces 8(46), 31894-31901 (2016). DOI: 10.1021/acsami.6b09053.

- L. Song, W. Wang, V. Körstgens, D. Moseguí González, Y. Yao, N. K. Minar, J. M. Feckl, T. Bein, D. Fattakhova-Rohlfing, G. Santoro, S. V. Roth, P. Müller-Buschbaum. *Spray deposition of titania films with incorporated crystalline nanoparticles for all-solid-state dye-sensitized solar cells using P3HT.* Advanced Functional Materials 26(10), 1498-1506 (2016), DOI: 10.1002/adfm.201504498.

- Y. Yao, E. Mettwalli, B. Su, V. Körstgens, D. Moseguí González, A. Miasnikova, A. Laschewsky, M. Opel, G. Santoro, S. V. Roth, P. Müller-Buschbaum. *Arrangement of maghemite nanoparticles via wet chemical self-assembly in PS-b-PNIPAM diblock copolymer films.* ACS Applied Materials & Interfaces 7(23), 13080-13091 (2015). DOI: 10.1021/acsami.5b03308.

- V. Körstgens, S. Pröller, T. Buchmann, D. Moseguí González, L. Song, Y. Yao, W. Wang, J. Werhahn, G. Santoro, S. V. Roth, H. Iglev, R. Kienberger, P. Müller-Buschbaum. *Laser-ablated titania nanoparticles for aqueous processed hybrid solar cells.* Nanoscale 7(7), 2900-2904 (2015). DOI: 10.1039/C4NR06782G.

- W. Wang, S. Pröller, M. A. Niedermeier, V. Körstgens, M. Philipp, B. Su, D. Moseguí González, S. Yu, S. V. Roth, P. Müller-Buschbaum. *Development of the morphology during functional stack build-up of P3HT:PCBM bulk heterojunction solar cells with inverted geometry.* ACS Applied Materials & Interfaces 7(1), 602-610 (2015). DOI: 10.1021/am5067749.

- K. Sarkar, C. J. Schaffer, D. Moseguí González, A. Naumann, J. Perlich, P. Müller-Buschbaum. *Tuning pore size of ZnO nano-grids via time-dependent solvent annealing.* Journal of Materials Chemistry A 2(19), 6945-6951 (2014). DOI: 10.1039/CATA00489B.

- T. Linderl, T. Zechel, M. Brendel, D. Moseguí González, P. Müller-Buschbaum, J. Pflaum, W. Brütting. *Energy losses in small-molecule organic photovoltaics.* Advanced Energy Materials. Published online. DOI: 10.1002/aenm.201700237.

- L. Song, W. Wang, V. Körstgens, D. Moseguí González, F. C. Löhrer, C. J. Schaffer, J. Schlipf, K. Peters, T. Bein, D. Fattakhova-Rohlfing, S. V. Roth, P. Müller-Buschbaum. *In situ study of spray deposited titania photoanodes for scalable fabrication of solid-state dye-sensitized solar cells.* Nano Energy. Submitted (2017).

- W. Wang, L. Song, D. Moseguí González, D. Magerl, M. Philipp, J. F. Moulin, P. Müller-Buschbaum. *Influence of solvent additive on P3HT:PCBM films.* In preparation (2017).

Press releases

- D. Moseguí González et al. *Die Mischung macht's: Magnetische Nanopartikel steigern Leistung von Solarzellen.* Deutsches Elektronen-Synchrotrons Pressemeldung. 25.02.2015.

Scientific reports

- D. Moseguí González, F. Dreher, P. Müller-Buschbaum. *Nanoparticles enable polaron spin tuning in organic solar cells.* Jahresbericht. Lehrstuhl für funktionelle Materialien. Technische Universität München (2016).

- D. Moseguí González et al. *Nanoparticles increase efficiency of organic solar cells. A matter of spin.* DESY Photon Science. Highlights and Annual Report (2015).

- D. Moseguí González, C. J. Schaffer, S. Pröller, J. Schlipf, L. Song, S. Bernstorff, E. M. Herzig, P. Müller-Buschbaum. *In-situ tracking of crystalline evolution in P3HT:PCBM organic solar cells.* Jahresbericht. Lehrstuhl für funktionelle Materialien. Technische Universität München (2015).

- F. Dreher, D. Moseguí González, G. He, E. Rivard, P. Müller-Buschbaum. *Characterisation of thiophene-selenophene-tellurophene copolymer thin films for OPV*

applications. Jahresbericht. Lehrstuhl für funktionelle Materialien. Technische Universität München (2015).

- D. Moseguí González, V. Körstgens, Y. Yao, L. Song, G. Santoro, S. V. Roth, P. Müller-Buschbaum. *Improved performance of organic solar cells from a quantum point of view*. Jahresbericht. Lehrstuhl für funktionelle Materialien. Technische Universität München (2014).

- N. Hohn, D. Moseguí González, P. Müller-Buschbaum. *Solvent tuning of aqueous processed P3P6T/WS-C_{60} thin films for OPV applications*. Jahresbericht. Lehrstuhl für funktionelle Materialien. Technische Universität München (2014).

- D. Moseguí González, S. V. Roth, P. Müller-Buschbaum. *P3HT:PCBM solar cells functionalized with iron oxide nanoparticles: morphology characterization*. DESY Photon Science. Highlights and Annual Report (2013).

- D. Moseguí González, S. V. Roth, P. Müller-Buschbaum. *Performance of P3HT:PCBM solar cells modified with iron oxide nanoparticles: a morphology study*. Jahresbericht. Lehrstuhl für funktionelle Materialien. Technische Universität München (2013).

Conference talks

- D. Moseguí González, J. Lebert, S. Pröller. *Polymer Blends*. Polymer physics summer school. Lehrstuhl für funktionelle Materialien. Obertauern, Austria. June 2016.

- D. Moseguí González, C. J. Schaffer, S. Pröller, J. Schlipf, L. Song, S. Bernstorff, E. M. Herzig, P. Müller-Buschbaum. *Links between organic solar cell performance and morphological properties*. DPG-Frühjahrstagung. Regensburg, Germany. March 2016.

- D. Moseguí González, V. Körstgens, Y. Yao, L. Song, G. Santoro, S. V. Roth, C. J. Schaffer, S. Pröller, J. Schlipf, S. Bernstorff, P. Müller-Buschbaum. *Nanomorphology and crystallinity of P3HT:PCBM solar cells doped with iron oxide nanoparticles*. Synchrotron radiation in polymer science. Madrid, Spain. September 2015.

- D. Moseguí González, W. Wang. *Polymer-based solar cells*. Polymer physics summer school. Lehrstuhl für funktionelle Materialien. Obertauern, Austria. June 2014.

Conference posters

- D. Moseguí González, C. J. Schaffer, S. Pröller, J. Schlipf, L. Song, S. Berstorff, E. M. Herzig, P. Müller-Buschbaum. *Morphology and performance of organic solar cells studied with in-operando scattering techniques.* 6th colloquium of the Munich School of Engineering. Garching, Germany. July 2016.

- D. Moseguí González, V. Körstgens, Y. Yao, L. Song, G. Santoro, S. V. Roth, P. Müller-Buschbaum. *Performance of P3HT:PCBM solar cells modified with iron oxide nanoparticles.* 5th colloquium of the Munich School of Engineering. Garching, Germany. July 2015.

- D. Moseguí González, V. Körstgens, Y. Yao, L. Song, G. Santoro, S. V. Roth, P. Müller-Buschbaum. *Performance of P3HT:PCBM solar cells modified with iron oxide nanoparticles.* Nanosystems Initiative Munich summer retreat, Lenggries, Germany. July 2015.

- D. Moseguí González, V. Körstgens, Y. Yao, L. Song, G. Santoro, S. V. Roth, P. Müller-Buschbaum. *Performance of P3HT:PCBM solar cells modified with iron oxide nanoparticles.* 4th International Solar Technologies Go Hybrid-Workshop. Kloster Banz, Germany. March 2015.

- D. Moseguí González, V. Körstgens, Y. Yao, L. Song, G. Santoro, S. V. Roth, P. Müller-Buschbaum. *Performance of P3HT:PCBM solar cells modified with iron oxide nanoparticles.* DPG-Frühjahrstagung. Berlin, Germany. March 2015.

- Arbeitsgruppe P. Müller-Buschbaum. *Nanostrukturierte Polymergrenzflächen.* Nanosystems Initiative Munich nanoday. Munich, Germany. November 2014.

- D. Moseguí González, V. Körstgens, Y. Yao, L. Song, G. Santoro, S. V. Roth, P. Müller-Buschbaum. *Performance of P3HT:PCBM solar cells modified with iron oxide nanoparticles.* 4th colloquium of the Munich School of Engineering. Garching, Germany. July 2014.

- D. Moseguí González, V. Körstgens, Y. Yao, L. Song, G. Santoro, S. V. Roth, P. Müller-Buschbaum. *Performance of P3HT:PCBM solar cells modified with iron oxide nanoparticles.* 3rd International Solar Technologies Go Hybrid-Workshop. Wildbad Kreuth, Germany. April 2014.

- D. Moseguí González, V. Körstgens, Y. Yao, L. Song, G. Santoro, S. V. Roth, P. Müller-Buschbaum. *Performance of P3HT:PCBM solar cells modified with iron oxide nanoparticles.* DPG-Frühjahrstagung. Dresden, Germany. March-April 2014.

- D. Moseguí González, C. M. Palumbiny, M. A. Niedermeier, R. Meier, S. V. Roth, J. Perlich, . Müller-Buschbaum. *Characterization of patterned polymer thin films for the application in organic photovoltaics using GISAXS*. GISAXS 2013 Hamburg, Germany. October 2013.

- D. Moseguí González, C. M. Palumbiny, J. Perlich, S. V. Roth, P. Müller-Buschbaum. *Effect of patterning on film morphology and device performance of BHJ organic solar cells*. DPG-Frühjahrstagung. Regensburg, Germany. March 2013.

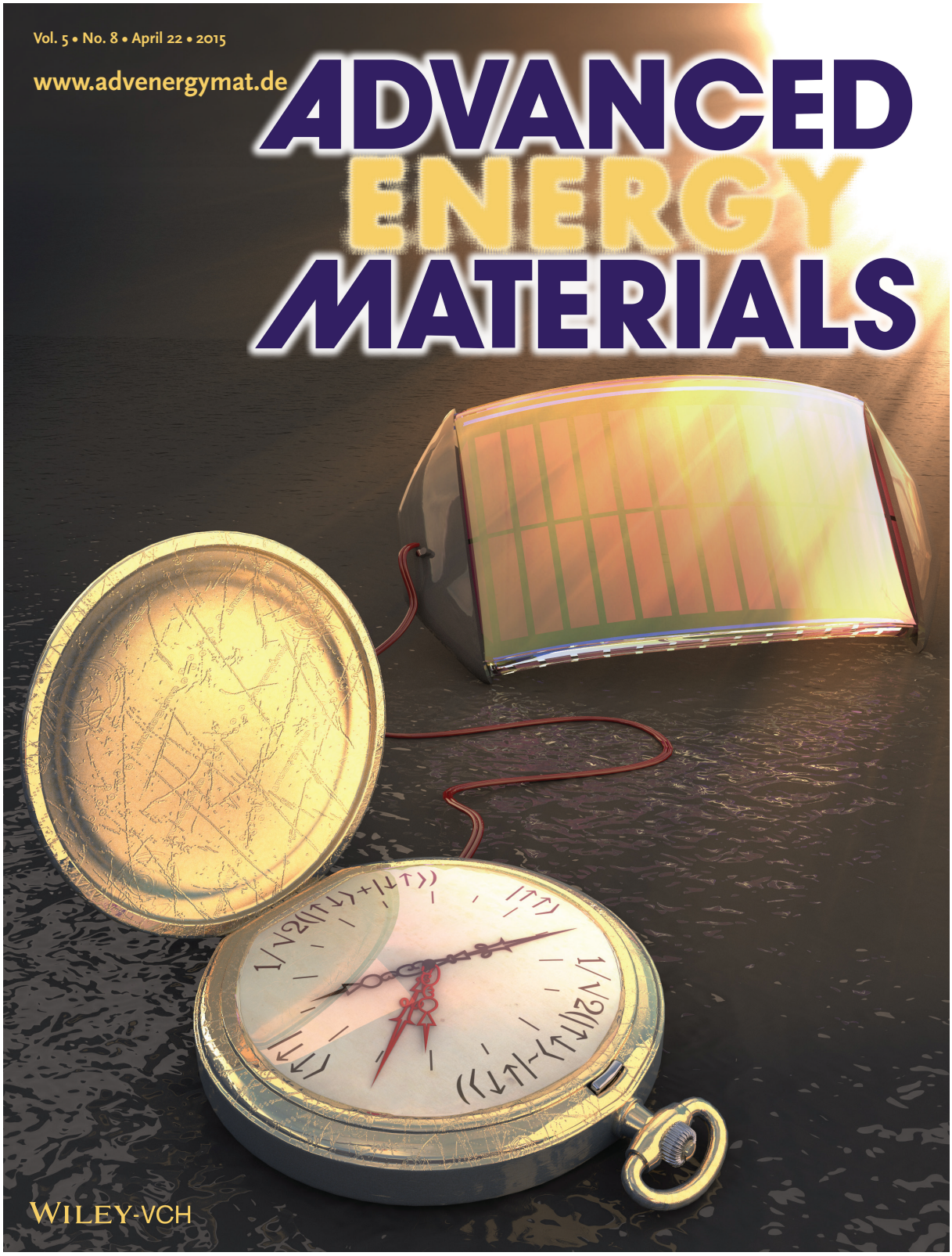

Cover picture featured on Advanced Energy Materials, Volume 5, Issue 8, April 2015.

Volume 38 • Number 11 • June 7, 2017 www.mrc-journal.de

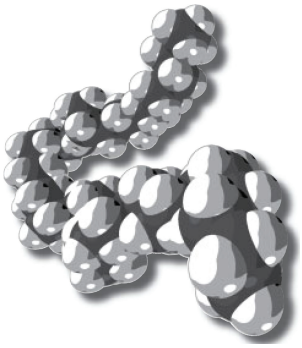

Macromolecular Rapid Communications

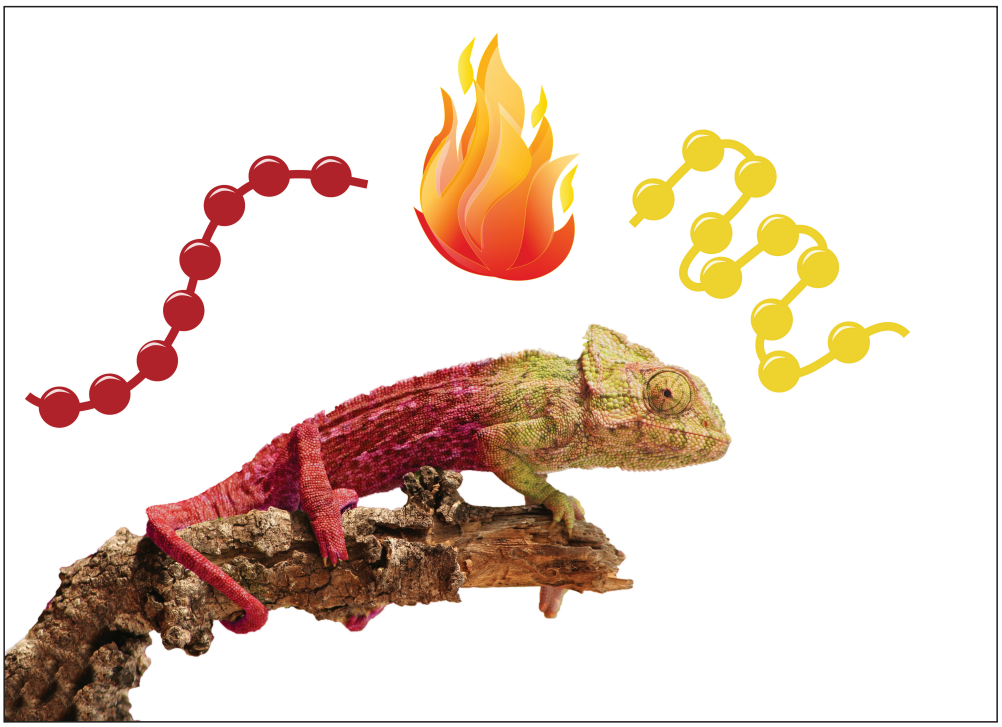

11/2017

WILEY-VCH

Cover picture featured on Macromolecular Rapid Communications, Volume 38, Issue 11, June 2017.

Acknowledgements

This thesis is the result of a considerable amount of work, but also a considerable amount of help, support and good advice from many sides and several people. The support and advice provided not only contributed to yield this dissertation as a result, but it also instilled ineradicable experiences and knowledge in me that made me grow considerably both in the professional and personal dimensions of my life. For all this I feel very thankful.

I would like to thank my thesis director in the first place, Peter Müller-Buschbaum, for giving me the chance of working in this exciting topic that taught me so much about material sciences and renewable energies. In spite of our repeated scientific and strategic disagreements you always kept an ear open and a good predisposition for discussion with me. Your active support during the hardest last stage of my PhD was highly valuable.

For active support, help and advice, which over time became some sort of informal supervision, I am thankful to my friend Kostantinos Raftopoulos. I was lucky to share some time with you, and your teachings in the professional and personal aspects of science helped me keeping my feet on the ground and gaining perspective. Our scientific and professional discussions always helped me remember the importance of being accurate on the one hand, and that science is indeed human, in the sense that is done by men and women, on the other.

I want to thank many of my current and former more senior colleagues, which were and are way more experienced than me, in the Chair for Functional Materials and other external institutions I had the pleasure to work with (DESY, MLZ, ILL, CSIC, ALS). They kindly accompanied me during some stage of my PhD and contributed to my further development as a scientist, besides of lots of help and assistance in everyday issues. I am thinking of Martin Niedermeier, Volker Körstgens, Weijia Wang, David Magerl, Shuai Guo, Martine Philipp, Ezzeldin Metwalli, Stephan Roth, Matthias Schwartzkopf, Gonzalo Santoro, Jean-Francois Moulin, Philipp Gutfreund, Tiberio Ezquerra, Alexander Hexemer and Cheng Wang.

I also want to thank my master students Nuri Hohn and Florian Dreher, and my students at the MSE. Working with you was an unforgettable experience in which I learnt a lot about science didactics, and especially about myself.

For their valuable help and wide experience, I am thankful to all the people who make science work behind-the-scenes: secretaries, technicians and clerks. Susanna Fink, Marion Waletzki, Carola Kappauf, Reinhold Funer, Raffael Jahrstorfer, Matthias Maier, Karin Lichtnecker, Maria Wassermann and all the others that I haven't even met, but still helped me, thank you very much for making our work so much easier.

I am grateful to all people working in the Chair for Functional Materials. You created and sustain an excellent working atmosphere that makes the work more enjoyable and grants help whenever one needs it. I am as well thankful to the Bavarian "Solar Technologies go Hybrid (SolTec)" research project through TUM.solar and to the "Nanosystems Initiative Munich (NIM)" for financial and logistic support.

More on the personal side, I am grateful to Stephan Pröller, Claudia Palumbiny, Nitin Saxena, Lorenz Bießmann, Christoph Schaffer, Gregory Tainter, Franziska Löhrer and Jenny Lebert. Thank you, not only for your support and help in my scientific path alongside yours, but also for the good quality time we spent together and we will keep spending.

For their tireless help in the scientific, professional, personal and emotional aspects of my PhD time, my development as a scientist and as a man, as well as for their nice friendship and invaluable company, I am especially thankful to my close friends Antonio Becerra Esteban, Borja Cirera Salinas, Pau Jorba Cabré, Johannes Schlipf and Kuhu Sarkar. Your company and friendship are and will remain one of the most memorable dimensions of my PhD time.

M'agradaria reservar els últims agraïments als meus pares i a la meva germana. Em vau veure marxar del vostre costat per acabar un projecte com aquest. La distància ha estat gran i perllongada, i això de vegades s'ha fet complicat. Ha passat molt de temps, i tant vosaltres com jo hem canviat al llarg del temps. Vosaltres no sempre heu entès el perquè de tot plegat, però m'heu recolzat, donat forces, i transmès la vostra experiència de la vida sempre que heu pogut i jo us ho he permès. Us he trobat i us trobo molt a faltar, i sovint penso que cada dia que passa estic un dia més a prop de tornar a estar amb vosaltres.

L'últim agraïment i el més sentit el deixo per a la dona de la meva vida. La dona generosa, carregada de paciència, amor i comprensió amb la que he tingut la inmensa sort d'ensopegar-me. Sempre preparada per ajudar-me en els moments difícils, per a aportar tranquil·litat i optimisme, per suportar el meu mal humor, de vegades gratuït, per donar-me perspectiva, per acompanyar-me, per estimar-me. T'estic molt agraït. M'hagués estat absolutament impossible aconseguir això sense la teva ajuda. Per molts anys més. T'estimo, Jasmin.